Lipid nanocapsules as a theranostic tool

Janske Nel

THESE DE DOCTORAT DE

L'UNIVERSITE D'ANGERS
et
L'UNIVERSITE CATHOLIQUE DE LOUVAIN
ECOLE DOCTORALE N° 605

Biologie Santé
Spécialité : Sciences Pharmaceutiques (Angers, UA)
Sciences Biomédicales et Pharmaceutiques (Louvain, UCL)

Par

Janske NEL

Lipid nanocapsules as a theranostic tool

Development of LNCs as an O_2 sensor for tumoural hypoxia using MR techniques

Thèse présentée et soutenue à Bruxelles (Louvain) le 14/01/2019 (défense privée) et en France (Angers) le 01/03/2019 (défense publique)
Unité de recherche : Micro et Nanomédecines Translationnelles (MINT), INSERM UMR-S 1066/CNRS 6021 et Biomedical Magnetic Resonance unit (REMA) in affiliation of the Louvain Drug Research Institute (LDRI)

Thèse N°: 139488

Rapporteurs avant soutenance:

Yves Michel FRAPART	Ingénieur de recherche, Université Paris Descartes
Myriam BERNAUDIN	Directrice de recherche CNRS, Université de Caen

Composition du Jury:

Yves Michel FRAPART	Ingénieur de recherche, Université Paris Descartes
Myriam BERNAUDIN	Directrice de recherche CNRS, Université de Caen
Fanny NOURY	Maître de Conférences, Université de Rennes
Président Anne DES RIEUX	Professeur des universités, Université de Catholique de Louvain
Directeur de thèse Laurent LEMAIRE	Ingénieur de Recherche, Université d'Angers
Co-directeur de thèse Bernard GALLEZ	Professeur des universités, Université de Catholique de Louvain

UNIVERSITE BIOLOGIE BRETAGNE SANTE LOIRE

université angers

UCLouvain

Titre: **Les nanocapsules lipidiques en tant qu'outil théranostique**

Mots clés: hypoxie ; nanocapsules lipidiques ; résonance paramagnétique électronique ; imagerie par résonance magnétique

Résumé: L'hypoxie est l'un des aspects les plus importants dans le microenvironnement tumoral. Ce phénomène, causé par une structure vasculaire anormale et un métabolisme perturbé, conduit à la formation de cellules hautement malignes résistantes aux thérapies cyto- et radio-toxiques. De ce fait, l'hypoxie est une préoccupation majeure et est à la base de notre nouvelle approche qui utilise des nanocapsules lipidiques (LNC) en tant que senseur d'oxygène. Il a été montré que les LNC sont d'excellents nanocarriers capables d'encapsuler des principes actifs à l'intérieur de leur cœur lipidiques et d'éviter le système immunitaire grâce au PEG de leur coque, permettant ainsi le traitement de tumeurs agressives. Nous avons émis l'hypothèse que le cœur lipidique des LNC pouvait être utilisé pour cartographier l'O_2 dans l'environnement tissulaire. En effet, la solubilité de l'O_2 étant supérieure dans les lipides que dans l'eau, le moindre changement d'oxygénation dans les tissus sera amplifié dans le cœur lipidique des LNC. Par conséquent, nous avons encapsulé une sonde paramagnétique lipophile, e.g. le tetrathiatriarylmethyl (TAM), et montré sa réponse *in vitro* à des variations en O_2 en utilisant la résonance paramagnétique électronique (RPE) montrant de ce fait la perméabilité des LNC à l'O_2. Nous avons utilisé les TAM-LNC dans un modèle *in vivo* de tissu normal (muscle murin gastrocnémien) et pathologique (sarcome). Sans LNC, le TAM a rapidement été réduit et aucune mesure en O_2 n'a été possible toutefois, notre système TAM-LNC présentait une demi-vie supérieure à une heure et permettait la mesure en temps réel lorsque les animaux respiraient soit de l'air soit du carbogène (95 % O_2, 5 % CO_2). Par ailleurs, la nature lipidique du cœur des LNC a été exploitée pour cartographier l'oxygénation des tissus grâce à l'imagerie par résonance magnétique (IRM) et plus précisément par l'utilisation de la séquence MOBILE qui permet d'imager la variation du temps de relaxation T_1 induite par l'O_2 dans les lipides. Avec une dose unique de LNC, nous avons été capables de représenter les changements de T_1 entre les différents modes de respiration et l'hétérogénéité de l'hypoxie dans des modèles de tissus murins sain et pathologique. En conclusion, nous avons apporté la preuve de faisabilité de l'utilisation des LNC en tant qu'outil diagnostique pour cartographier l'hypoxie dans des tissus sains et pathologiques.

Title: **Lipid nanocapsules as a theranostic tool**

Keywords: hypoxia ; lipid nanocapsules ; electron paramagnetic resonance ; magnetic resonance imaging

Abstract: Hypoxia is one of the most challenging aspects of the tumour microenvironment. The phenomenon occurs due to abnormal vasculature and an exacerbated metabolism, and leads to highly malignant cells resistant to radio- and cyto-toxic therapy. As such, hypoxia is of major concern and prompted our novel approach in using lipid nanocapsules (LNCs) as an oxygen sensor. LNCs have been demonstrated as excellent core-shell nanocarriers, capable of encapsulating drugs within their lipidic core and avoiding the immune system due to their PEGylated shell, thus enabling treatment of highly aggressive tumours. We hypothesised that the lipidic-core of LNCs could also be used to assess the O_2 environment in tissue. Indeed, because O_2 solubility is greater in lipids than in water, any subtle changes in tissue O_2 will be heightened in the lipidic LNC core. Consequently, we encapsulated a lipophilic paramagnetic probe, e.g. tetrathiatriarylmethyl (TAM), and demonstrated its response to variations in O_2 *in vitro*, using Electron Paramagnetic Resonance (EPR), indicating the permeability of LNCs to O_2. We applied the TAM-LNCs to an *in vivo* normal tissue model (gastrocnemius mouse muscle) and pathological model (sarcoma tumour). Herein, free TAM was rapidly reduced and no O_2 measurement was possible, however, our TAM-LNC system exhibited a half-life of over an hour and enabled real-time measurements whilst animals were breathing air and during a carbogen gas (95 % O_2, 5 % CO_2) breathing challenge. Moreover, the lipidic-core nature of the LNCs was exploited to image tissue oxygenation using Magnetic Resonance Imaging (MRI), specifically the MOBILE sequence which enabled the mapping of O_2-induced T_1 relaxation rate changes in lipids. Using a single dose of LNCs, we were able to portray the change in T_1 between air breathing and the carbogen challenge, and image the heterogeneous nature of hypoxia in murine normal tissue and pathological tumour models. In conclusion, we demonstrated the feasibility of using LNCs as a diagnostic tool for assessing hypoxia in both normal and pathological tissues.

Preface

This project was made possible through the collaborative effort between the European Commission Erasmus Mundus directive and the European Doctorate in Nanomedicine and Pharmaceutical Innovation (NanoFar) program, and stemmed from the combined efforts of the Université d'Angers and the Université Catholique de Louvain, with the research laboratories of Prof. SAULNIER (Micro et Nanomédecines Translationnelles [MINT]) and Prof. GALLEZ (Biomedical Magnetic Resonance unit [REMA]; an affiliation of the Louvain Drug Research Institute [LDRI]). We are also grateful for the monetary funds provided by the Fonds du Patrimoine (Secteur des Sciences de la Santé, UCLouvain, Belgium) and comité départemental de Maine et Loire de la Ligue Contre le Cancer (France).

Dedicated to my
inspiring parents and sister

Table of Contents

Abbreviations, Acronyms and Symbols

^{99m}Tc-HL91	Technetium-^{99m} hexamethylpropylene amine oxime
ANOVA	one-way analysis of variance statistical test
ARCON	accelerated radiotherapy combined with carbogen breathing and nicotinamide
ARDVARC	alternating relaxation delays variable acquisitions for reduction of clearance
ATP	adenosine triphosphate
B_S	a static external magnetic field
B_0	an oscillating magnetic field transverse to B_0
BMS-181,321	Technetium-^{99m} 2-nitroimidazole compound
BNIP3	Bcl-2/adenovirus E1B 19 kDa-interacting protein 3
BOLD	blood oxygen level dependent
BRU 59-21	Technetium-^{99m} 2-nitroimidazole compound
BW	bandwidth
C3H/HeJ	mouse strain
CA IX	carbonic anhydrase IX
CED	convection-enhanced delivery
CT	computer tomography
Cu-ATSM	diacetylbis(N(4)-methylthiosemicarbazonato) copper(II)
DCE-MRI	dynamic contrast-enhanced magnetic resonance imaging
DMEM	Dulbecco's modified Eagle's medium
DNA	deoxyribonucleic acid
DOS/T	diffuse optical spectroscopy and tomography
ECACC	the European collection of Authenticated Cell Culture
EF5	2-(2-nitro-1H-imidazol-1-yl)-N-(2,2,3,3,3-penta-fluoropropyl)-acetamide
EMT	epithelial-mesenchymal transition
EPO	erythropoietin

EPR	electron paramagnetic resonance
FAZA	fluoroazomycin arabinoside
FDG	fluorodeoxyglucose
FETA	fluoroetanidazole
FETNIM	fluoroerythronitroimidazole
FITC	fluorescein isothiocyanate
FLASH	fast low angle shot
FLOOD	flow and oxygenation dependent
FMISO	fluoromisonidazole
FOV	field of view
FREDOM	fluorocarbon relaxometry echo planar imaging for dynamic oxygen mapping
FRET	Förster resonance energy transfer
FSaII	syngenic fibrosarcoma murine cell line
G	Gauss
GFP	green fluorescence protein
GLUT	glucose receptor
Hb	deoxygenated haemoglobin (also referred to as rHb)
HbO_2	oxygenated haemoglobin (also referred to as $rHbO_2$)
HbT	total haemoglobin
HFB	hexafluorobenzene
HIF	hypoxia-inducible factor
HLDH5	human lactate dehydrogenase isoenzyme-5
IAZA	iodoazomycin arabinoside
IAZGP	^{124}I-iodoazomycin galactopyranoside
IAZP	iodoazomycin pyranoside
IAZXP	iodoazomycin xylopyranoside
IHC	immunohistochemistry

IMRT	intensity-modulated radiation therapy
IR FISP	inversion recovery fast imaging steady state precession
kDa	kilodalton
LiPc	lithium phatalocyanine
LNC(s)	lipid nanocapsule(s)
LOX	lysyl oxidase
LW	line width
MAPK/ERK	pathway enabling communication between cell receptors and its DNA
mG	milliGauss
MMPs	matrix metalloproteinases
MOBILE	mapping of oxygen by imaging lipids relaxation enhancement
mPa.s	millipascal-second
MR	magnetic resonance
MRI	magnetic resonance imaging
MTF-1	metal transcription factor-1
MWCO	molecular weight cut-off
N2IPA	1-(2-nitroimidazole-1-yl)-propanhydroxyiminoamide
NF-κB	nuclear factor- κB
NIRS	near-infrared spectroscopy
NMR	nuclear magnetic resonance
OCT	optical coherence tomography
OE-MRI	oxygen-enhanced magnetic resonance imaging
OPN	osteopontin
p53	tumour suppressor gene
PALI	photoacoustic lifetime imaging
PAT	photoacoustic tomography
PDI	polydispersity index

PDT	photodynamic therapy
PEG	polyethylene glycol
PET	positron emission tomography
PFC(s)	perfluorinated compound(s)
P-gp	glycoprotein P
PI3K/AKT/mTOR	cell cycle pathway relating to quiescence and proliferation
PISTOL	proton imaging of siloxanes to map tissue oxygenation levels
PIT	phase inversion temperature
PIZ	phase inversion zone
pO_2	partial pressure of oxygen
ppm	parts per million
PRESS	point resolved spectroscopy
R_1	inverse of T_1 ($=1/T_1$)
RARE	rapid acquisition with refocused echoes
RES	reticuloendothelial system
RF	radiofrequency
ROI	region of interest
$rStO_2$	relative tissue oxygen saturation
SD	standard deviation
SNR	signal-to-noise ratio
SPECT	single-photon emission computed tomography
SWOT	Strengths, Weaknesses, Opportunities and Threats analysis
T_1	spin-lattice relaxation time
T_1*	effective spin-lattice relaxation time
T_2	spin-spin relaxation time
T_2*	effective spin-spin relaxation time
TAM	a tetrathiatriarylmethyl radical, includes the names trityl and F15T-03

TAM-LNCs	TAM-loaded LNCs
TB	4-hydroy-TEMPO benzoate
TB-LNCs	TB-loaded LNCs
TE	echo time
TEMPO	2,2,6,6-tetramethylpiperidine 1-oxyl
TEMPO-LNCs	TEMPO-loaded LNCs
TR	repetition time
uPA-R	urokinase plasminogen activator receptor
USI	ultrasound imaging
VAPOR	variable power and optimised relaxation delays
VEGF	vascular endothelial growth factor
α	alpha
β	beta
ΔR_1	change in R_1

List of Figures

List of Tables

Statement of Original Authorship

The work contained in this thesis has not been previously submitted to meet requirements for an award at these or any other higher education institution. To the best of my knowledge and belief, the thesis contains no material previously published or written by another person except where due reference is made.

Signature: _____

Date: _____

Acknowledgements

I would like to extend my thanks to the many people, in many countries, who so graciously contributed to the work presented in this thesis.

Firstly, I would like to express my deep gratitude to Dr Laurent LEMAIRE and Prof Bernard GALLEZ, my research supervisors, for the opportunity to work on this project. But most importantly, for their guidance, encouragement and patience in teaching me the skills needed to become a researcher. I would also like to thank Dr Florence FRANCONI and Dr Nicolas JOUDIOU for their invaluable knowledge and technical support during the process of creating this thesis. Similarly, I am also grateful to Prof Frank BOURY, the coordinator of the European Doctorate in Nanomedicine and Pharmaceutical Innovation (NanoFar), Marion TOUCHETEAU, Sandrine WOLLANDERS and Ourega KOFFI, for their dedication to the NanoFar program and its students. Through their hard work they enabled many students, including myself, to realise the dream of pursuing a PhD, and I will be forever thankful.

I would like to thank the members of my dissertation committee; Prof. Anne DES RIEUX, Dr Myriam BERNAUDIN, Dr Yves Michel FRAPART, and Dr Fanny NOURY; for generously offering their time, expertise and guidance in review of my thesis.

My thanks to my colleagues in Belgium and France; it was a pleasure to work with them for three years and I am sincerely grateful for their professionalism and technical support. Specifically, I would like to thank Dr Céline M. DESMET and the staff at the Service Commun d'Animalerie Hospitalo-Universitaire (SCAHU, Angers, France) for their unfailing assistance and guidance.

Many thanks to my friends and colleagues in the NanoFar program, especially Valentina, Kita, Chiara, Bathabile, Maruthi, Surasa, Pauline, Natalija, Vincent, Audrey, Raneem and Mathie. Thank you for the coffee, delicious meals, and camaraderie that made my PhD so incredibly memorable.

I owe a great deal to my parents, Suzette and Marius NEL, as well as my sister, Sumari NEL, who have always encouraged and supported me no matter where in the world I am.

Finally, to Baptiste – thank you. An acknowledgement here cannot express how grateful I am to you for helping me attain something I thought was impossible.

Chapter 1:

Introduction

1.1 INTRODUCTION TO THESIS

Hypoxia is a characteristic feature of tumours. The phenomenon results from tissues increasingly consuming oxygen (O_2) whilst receiving a limited supply. Mounting evidence indicates that hypoxia plays a vital role in tumour development, angiogenesis, metabolism, and resistance to treatment. Alterations in the gene and protein expressions of tumours induced by hypoxia lead to more aggressive survival patterns and result in resistance to several forms of therapy, including radio-, immuno- photodynamic, and cytotoxic chemo-therapy. Thus, techniques to assess and image tumour hypoxia has become of crucial importance for the prediction of therapeutic outcomes.

Fortunately, the chemical and physical properties of O_2 facilitate a wide variety of methods for monitoring and imaging hypoxia. These methods involve electrochemical reduction, optical-based methods including spectroscopy and luminescence, nuclear-based methods including positron emission tomography, and magnetic resonance (MR) based methods including electron paramagnetic resonance (EPR) and magnetic resonance imaging (MRI). Unfortunately, no 'gold standard' amongst the methods exists as, although each method provides unique advantages, several limitations regarding the tumour microenvironment itself – such as tumour heterogeneity and necrosis – and the techniques – including invasiveness, use of ionising radiation, and poor spatial resolution – have stunted progress. Recent advances, however, have provided modern medicine with a new aid in the form of nanotechnology, which has emerged as an outstanding tool for the development of technologies for diagnosis, treatment and prevention of cancer. To this end, this thesis aims to demonstrate that lipid nanocapsules (LNCs), in combination with EPR and MRI techniques, can be used as an O_2 sensor to address these limitations. LNCs have been exemplified as excellent core-shell nanocarriers capable of encapsulating drugs within their lipidic core and avoiding the immune system due to their 'stealth' shell, thus enabling the treatment of highly aggressive tumours.

Firstly, in this thesis, LNCs will be used in combination with EPR oximetry. EPR oximetry enables repeated and direct O_2 quantification within tumours from the interactions between the unpaired electrons of molecular O_2 and a paramagnetic probe. These interactions lead to a decrease in spin-spin (T_2) relaxation rates and can be evaluated by the EPR signal line width (LW) which is directly proportional to O_2 tension. Unfortunately, paramagnetic probes can often be rapidly bioreduced and thus require encapsulation before their introduction into an *in vivo* system. Thus, in this thesis, LNCs were used to encapsulate and

protect paramagnetic probes and to demonstrate its response to variations in O_2 *in vitro* thus indicating the permeability of LNCs to O_2. We applied the successfully encapsulated LNC paramagnetic probes to an *in vivo* normal tissue model (gastrocnemius mouse muscle) and a pathological model (fibrosarcoma subcutaneous tumour).

Secondly, the lipidic-core nature of the LNCs was exploited using MRI, specifically using a sequence which enables the mapping of O_2-induced spin-lattice (T_1) relaxation rate changes in lipids (MOBILE). This sequence, however, requires a sufficiently high intrinsic amount of lipids to acquire an oxygenation map, which unfortunately does not always occur spontaneously within tissues. Thus, LNCs were used to increase the lipidic signal-to-noise ratio within normal (gastrocnemius mouse muscle) and pathological tissues (neoplastic models including fibrosarcoma subcutaneous and intracerebral glioblastoma tumours) within murine models, and using the MOBILE sequence, oxygenation maps were produced of tissues in which this was not previously possible.

1.2 AIMS AND OBJECTIVES

This thesis aims to investigate the feasibility and usefulness of the LNC therapeutic nanocarrier as a diagnostic O_2 sensor using EPR and MRI. The main objectives of the thesis are therefore:

¶ **When applying LNCs to the EPR technique:**

a) Can LNCs encapsulate paramagnetic EPR probes?

b) If so, can the LNCs protect the encapsulated probe from the biological milieu?

c) Once encapsulated, are the probe-loaded LNCs sensitive to O_2 variation *in vitro*?

d) Furthermore, can the probe-loaded LNCs serve as O_2 sensors by responding to O_2 variation achieved by a hyperoxic gas (95 % O_2 and 5 % carbon dioxide (CO_2); carbogen) breathing challenge within normal murine tissue?

e) Lastly, can the probe-loaded LNCs serve as an O_2 sensor within murine tumours?

¶ **When applying LNCs to MRI using the MOBILE sequence;**

a) Are the lipids within the LNCs detectable by MRI using the MOBILE sequence?

b) If so, do the lipids within the LNCs respond to O_2 variation *in vitro*?

c) Can the LNCs serve as O_2 sensors by responding to O_2 variation, achieved by a hyperoxic gas breathing challenge, within normal murine tissue using the MOBILE sequence? If so, can an oxygenation map be produced of the area?

d) Similarly, can the LNCs serve as O_2 sensors by responding to O_2 variation, achieved by a hyperoxic gas breathing challenge, within tumoural tissues; such as intracerebral glioblastoma and fibrosarcoma subcutaneous murine tumours? If so, can an oxygenation map be produced of the area?

1.3 THESIS OUTLINE

In the following chapter (Chapter 2), the background of the thesis will be presented and will include an overview of; tumour hypoxia and its relevance to malignancy and treatment resistance in oncology, the current techniques for assessing and imaging tumour hypoxia with emphasis on their advantages and limitations, an introduction to the theoretical basis of MR techniques and the working principles of EPR and MRI on which special interest will be focused on the specific issue faced for each technique. These specific limitations will be addressed by the introduction and discussion of LNCs which will serve as the nanoparticle employed in this thesis.

In chapter 3, the ability of LNCs to encapsulate paramagnetic EPR spin probes is investigated, as well as their ability to respond to *in vitro* and *in vivo* oxygenation variation.

In chapter 4, the ability of LNCs to increase the lipidic content sufficiently to enable the mapping of O_2 using the MRI MOBILE sequence is investigated in both normal and pathological tissues.

Following this, in Chapter 5, the conclusions in the previous chapters are presented and their implications are discussed. Additionally, the future work which could stem from this thesis is considered.

.

Chapter 2:

Background to the Research Area

2.1 INTRODUCTION TO CHAPTER 2

In this chapter, the literature relevant to the background of this thesis is reviewed. The aim is to provide a strong theoretical framework for the knowledge and context of this body of work, and identify previous work and their limitations pertaining to the assessment and imaging of tissue oxygenation.

In section 2.2, the general biology of the tumour microenvironment is introduced, and the relevance of hypoxia is described in regards to cancer progression and treatment. Several methods to assess and image tumour hypoxia *in vivo* have been previously developed and are described in section 2.3, with special attention given to their advantages and disadvantages. This section will highlight the need for novel non-invasive methods for tumour hypoxia assessment and imaging such as EPR and MRI. Next, in section 2.4, the governing principles of EPR oximetry and its development in oncology will be explored. Similarly, in section 2.5, MRI will be discussed, including its usage in O_2 determination in oncology. Then, in section 2.6, the development of LNCs as a therapeutic nanomaterial will be reviewed and its use as an O_2 sensor – and thus a potential theranostic tool – using EPR and MRI will be introduced.

2.2 THE TUMOUR MICROENVIRONMENT AND HYPOXIA

O_2 plays a critical role in cellular metabolism and is involved in the pathogenesis of several maladies including carcinogenesis and its treatment regimes. Consequently, the ability to measure O_2 in tissue with sufficient sensitivity, accuracy and simplicity would be immensely beneficial as it would enhance our understanding and therapeutic strategies of solid tumours. When low levels of O_2 persist (referred to as hypoxia); changes in the gene and protein expressions of cells occur which causes an increase in vasculature growth (angiogenesis) to supply the proliferating cancer cells with O_2 and nutrients, a switch to anaerobic metabolism to combat the low O_2 environment leading to an increase in the pH of the microenvironment, and ultimately gives rise to cells which are highly malignant, metastatic, and resistant to therapy. This cascade is, of course, an oversimplification of hypoxia pathogenesis as tumours are complex systems consisting of a plethora of different cells and heterogeneous microenvironments which are constantly in flux and influenced by temporal and local changes [1]. Thus, the following sections will provide an overview of hypoxia and the challenges researchers face in elucidating the O_2 content of the tumour microenvironment.

2.2.1 What is hypoxia?

The status of 'hypoxia' is characterised by physiologically low levels of O_2 in which tissues can no longer function optimally. These low levels of O_2 tension often arise when the O_2 supply in limited but its consumption is increased, causing genetic and proteomic changes [1]. Several pathologies, beside cancer, are also associated with low levels of O_2 tension, including vascular and pulmonary diseases [2]. Clinical investigations over the last three decades have clearly demonstrated that 50 – 60 % of locally advanced solid tumours [3] may exhibit hypoxic areas that are heterogeneously distributed within tumours larger than 1 mm^3. Such regions have been found in a wide range of malignancies including cancers of the breast, uterine, cervix, vulva, head and neck, prostate, rectum, pancreas, lung, brain tumours, soft tissue carcinomas, malignant melanomas, metastatic liver tumours and renal cell cancer [4–6].

Hypoxia-induced proteome and genome changes in the tumour may promote tumour progression via mechanisms enabling cells to overcome nutritive deprivation, to escape from the hostile environment, and favour unrestricted growth. Sustained hypoxia in a growing

tumour may also lead to cellular changes that can result in a more clinically aggressive phenotype [2]. It is therefore no surprise that hypoxia is an important physiological parameter, and the understanding of its pathogenesis requires consideration for tumour physiology and therapy.

2.2.2 The pathogenesis of tumour hypoxia

Cancer cells have a variety of mechanisms that enable them to adapt, evade and take advantage of their environment. The diversity of hypoxic stimuli within tumours is complex – several intracellular signalling pathways are activated in tandem amongst a variety of shared genes making it difficult to generalise on its effect on tumour biology because the interplay between the O_2 tension, hypoxia-induced signalling, genomic and proteomic reorganisation, and the prevailing cellular damage, is labyrinthine. Ultimately, however, these mechanisms are primarily mediated by a family of transcriptional regulators; hypoxia-inducible factor (HIF) [7]. Numerous pathways involving factors such as cytokines, chemokines, and growth factors, are also stimulated in a cascade of both hypoxia-dependent and independent manners which all eventually lead to the activation of the HIF pathway and, more specifically, the stabilisation of HIF-alpha (HIF-α).

HIFs are heterodimers consisting of two subunits, alpha (α) and beta (β). Whilst the β-subunit is not O_2 sensitive, HIF-α rapidly responds to low O_2 tension at the post-translational level causing an increase in its quantity [8]. Among the HIF protein family members, the role of HIF-1 is well-established in cancer progression. Importantly, several studies have associated HIF-1α expression with human cancer progression and its prognostic impact has been the subject of numerous studies. Histological analyses have indicated that increased intracellular levels of HIF-1α is associated with poor prognosis and resistance to therapy in breast [9–12], head and neck [13], oesophagus [14], stomach [15], lung cancers [16], and many other types [17,18]. The full pathway, mechanism and impact of HIFs is a fascinating and immense topic and cannot be fully covered in this thesis thus for a full review the work of Harris [19] is recommended.

It is important to note, however, that HIF-1 induces the expression of more than 30 known genes [2,6,19–25]; at O_2 partial pressure (pO_2) levels between 10 – 15 mmHg genes essential for angiogenesis are stimulated; at 10 mmHg or less decreased adenosine triphosphate (ATP) synthesis occurs leading to a change in energy metabolism; and at less than 1 mmHg hypoxia-induced apoptosis is stimulated (**Fig. 2-1**).

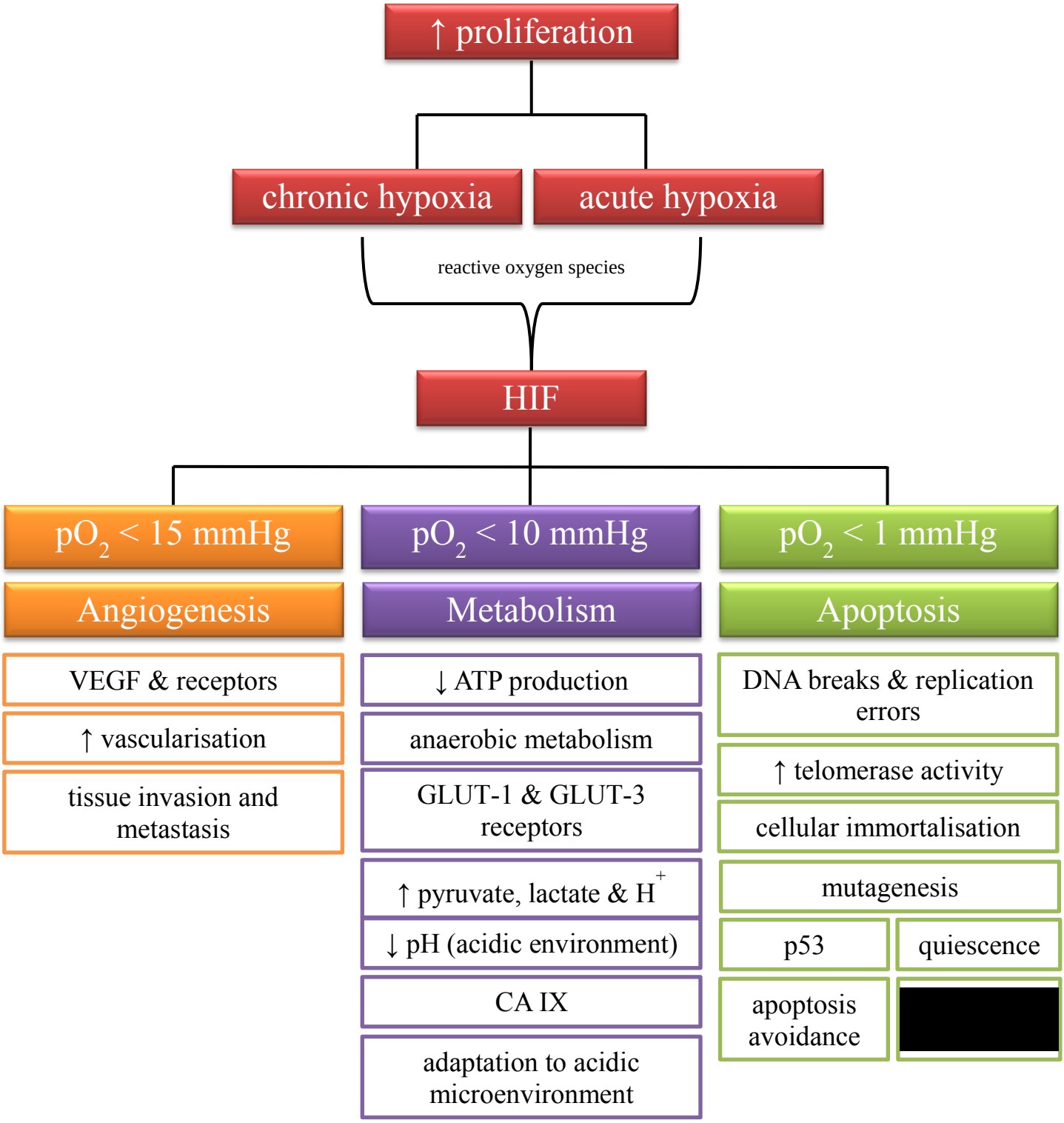

Figure 2-1. Schematic of tumoural progression and the effects on angiogenesis, metabolism and apoptotic pathways. Adapted from the following citations [2,6,19–25].

HIF, hypoxia-inducible factor alpha; pO_2, partial pressure of oxygen; VEGF, vascular endothelial growth factor; ATP, adenosine triphosphate; GLUT, glucose receptors, H^+, hydrogen proton; CA IX, carbonic anhydrase IX; p53, tumour suppressor gene.

2.2.2.1 Angiogenesis

Arguably, the most fundamental characteristic of cancer cells involves their ability to sustain persistent proliferation. Whilst normal tissues carefully control the production and release of growth promoting signals for homeostatic progression through the cell growth-and-division cycle, cancer cells dysregulate these signals. In cancer cells, signalling pathways are corrupted, negative-feedback loops are dampened, growth suppressors are evaded, and mechanisms of contact inhibition are suppressed; all of which enable the neoplastic cells to progress through the cell growth-and-division cycle and continuously increase in number and in size [1]. However, all cells require sustenance, even cancer cells. As such, tumour progression requires neovascularisation, which occurs either by the recruitment of circulating cells for the formation of blood vessels (vasculogenesis [26]) or by the sprouting of endothelial cells from nearby blood vessels (angiogenesis) in order to provide nutrients and O_2 and to remove catabolites from the expanding tumour mass. The 'angiogenic switch' is governed by a myriad of balanced, competing factors which either induce or oppose vascularisation, producing controlled and transient angiogenesis in normal tissue. For cancerous cells, however, this switch is tipped towards 'on' during the early development of the pre-malignant growth of the tumour mass and remains activated [27–29]. This activation is predominantly driven by vascular endothelial growth factor (VEGF), which is a well-known key angiogenic factor in normal tissues but with a markedly increased presence in several cancer types [30–32].

Despite the enhanced angiogenesis within a tumour mass, angiogenesis cannot keep up with the cancerous proliferation, thus median O_2 levels are significantly lower than normoxia (normal physiological levels of O_2 within a given tissue) and can even reach 0 % O_2 [33,34]. Furthermore, due to the haphazard growth of tumour cells and their associated vasculature, there is abundant evidence for the existence of substantial heterogeneity in the development and extent of tumour hypoxia due to pronounced intra- and inter-tumoural variability in vascularity, perfusion rates and regions of necrosis [35–39], thus scattered gradients of mild and severe hypoxia appear within the tumour. These gradients occur because O_2 delivery is impaired by structural abnormalities within the neovasculature, including; blood vessels growing as dilated or narrowed single branches, non-hierarchical and chaotic vascular networks, disturbed capillary architecture, leakiness, and incomplete vascular walls [40–43]. These abnormalities cause numerous functional impairments such as increased vascular permeability making the blood prone to clotting and local tissue oedema [44–46], interstitial

hypertension [47], and increased flow resistance. Furthermore, very often, tumour micro-vessels are perfused (at least transiently) by only plasma causing further stunting of O_2 delivery [48]. Thus, O_2 gradients can arise due to an increase in diffusion distances causing cells far away (> 70 μm) from blood vessels to receive less O_2 than needed. This is referred to as diffusion-limited hypoxia or chronic hypoxia. Acute or transient hypoxia occurs due to perfusion-limited O_2 delivery wherein the collapse, reversal of blood flow, and subsequent re-perfusion of these imperfectly formed blood vessels cuts off the O_2 supply intermittently [4]. Both chronic and acute hypoxia have been implicated to cause an increase in reactive oxygen species (ROS) [49] – due to the interruption of the mitochondrial oxidation process at low O_2 tension – leading to tissue damage, the activation of stress-response genes HIF-1 [50], and the subsequent stabilisation of HIF-1α. In turn, HIF-1α induces the transcription of several growth factors such as transforming growth factor r-β and platelet-derived growth factors [20,21,23,51], and of course, VEGF and its receptors [52]. But, notably, the expression of VEGF is not only influenced by hypoxia but also by glucose depletion [53,54] and an acidic extracellular pH [55].

2.2.2.2 Metabolism

During normal cellular metabolism, energy is harnessed in the form of ATP from the anaerobic processing of glucose into lactate (i.e. anaerobic glycolysis) and through the oxidation of glucose into CO_2 by mitochondrial respiration (i.e. aerobic mitochondrial oxidation). Notably, a phenomenon named the Warburg effect (also known as aerobic glycolysis) can occur in both normal and tumoural cells, wherein the uptake of glucose dramatically surges and, even in the presence of sufficient O_2 and functional mitochondria, the anaerobic formation of glucose to lactate is preferred [56] (**Fig. 2-2**). The Warburg effect has been hypothesised to benefit tumoural cells immensely as it allows for the rapid synthesis of ATP, increased biosynthesis through the pentose-phosphate pathway, enhances the disruption of tissue architecture and immune cell evasion, and allows for signal transduction through ROS [57,58]. This use of glycolysis and the pentose-phosphate metabolism seems counterintuitive; tumoural cells require large amounts of energy to keep proliferating whilst this metabolic switch provides considerably less energy. However, the glycolytic intermediate glucose-6-phosphate is used in the pentose-phosphate pathway to synthesise amino acids and nucleotides, which are essential for proliferation. Thus, not only is the use of the anaerobic metabolism an adaptive response for the tumour cells; it's an advantageous one.

At less than 10 mmHg, however, the O_2 content is no longer sufficient to supply ATP via mitochondrial respiration and the switch to anaerobic glycolysis is compulsory [59–63]. As a result of the glycolytic metabolism pyruvate, lactate and hydrogen ions are excreted from the tumoural cells into its surroundings, leading to an acidic microenvironment and the activation of HIF-1α. It, in turn, regulates the expression of all enzymes in the glycolytic pathway, as well as the activation of the glucose receptors (GLUT-1 and GLUT-3) which mediate cellular glucose uptake [64]. The overexpression of GLUT-1 is correlated with poorer outcomes in breast [65], head and neck [66], oesophagus [67], bladder [68], stomach [69], colorectal [70], ovarian [71], and lung cancer [72]. Tumour cells have also been shown to increase their glycogen storage in response to acute hypoxia to maintain cell viability and proliferation [73,74]. This metabolic switch, and associated enhanced glycolytic rates, is directly associated with increased lactate production which, of course, affects the overall pH of tumours. Unfortunately, this acidic

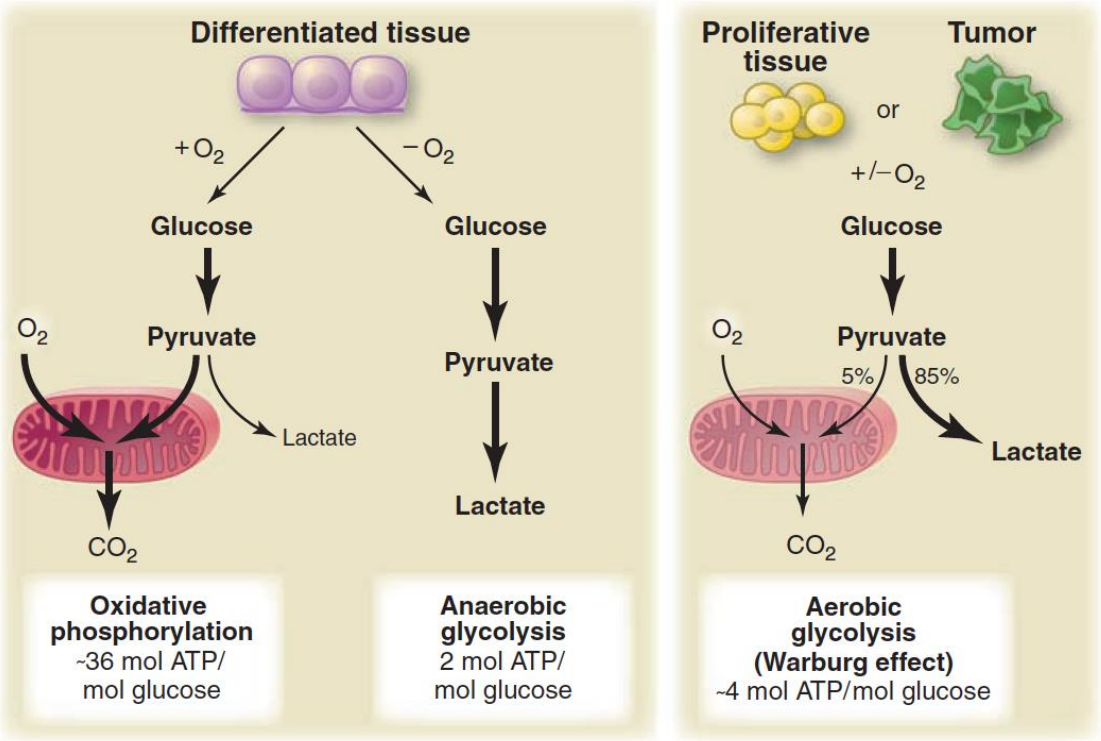

Figure 2-2. Schematic illustrating the difference between oxidative phosphorylation, anaerobic glycolysis, and aerobic glycolysis (Warburg effect). In the presence of O_2, non-proliferating cells (differentiated) preferentially metabolise glucose through the oxidative phosphorylation pathway, via the mitochondria. In this instance, because O_2 is the final electron acceptor to enable the complete oxidation of glucose, O_2 is essential for the process. However, when O_2 is limited, glycolysis can be used alternatively but results in fewer ATP than during oxidative phosphorylation. Conversely, in proliferating or tumoural tissue, although the mitochondria are functioning normally, the aerobic glycolysis pathway (Warburg effect) can be preferred. Image reproduced from Vander Heiden et al. [58].

environment is no deterrent for tumoural cells, who have adapted to growing in a much lower pH environment than their counterpart normal cells.

This adaptation is made possible by, among others, the enzyme carbonic anhydrase IX (CA IX) which is able to counteract the intracellular acidification caused by glycolysis by reversibly converting CO_2 and water into carbonic acid, as well as increasing the proton-extrusion capacity of cellular membranes, thus controlling the intracellular pH environment of the tumour cells. Several studies have correlated increased expression of CA IX with tumour cell survival [75], invasiveness [76], and poor outcomes in tumour therapy [68,77–81]. Notably, the full intricacies of the tumour metabolism is manifold and cannot be fully discussed in this section, thus the work of Eales [82] is highly recommended for a more complete understanding. But there is no doubt that a decreased pH is associated with hypoxia, and that CA IX is linked to the adaptive measures tumour cells employ to combat this acidification, as well as cell survival via apoptosis (a form of programmed cell death) avoidance [83,84].

2.2.2.3 Apoptosis

As much as proliferation is a key characteristic of cancer cells, so too is the avoidance of death and the continuation of cell survival. Apoptosis is induced in a number of HIF-1 dependent and independent pathways, and tumour cells have developed many mechanisms to evade these pathways. Under hypoxia, HIF-1α activates the expression of pro-apoptotic proteins [85–88], leading to the activation of the p53 gene; a tumour-suppressor gene which, once activated, causes a cascade of pathways leading to the apoptosis of the tumoural cell.

However, the relationship between p53, apoptosis and HIF-1 is not straightforward; hypoxia has been shown to induce p53 activation in some conditions but not in others, and the mechanisms by which this is controlled is not well understood [89,90]. What is known is that the severity and duration of the hypoxic condition plays a role. The endurance of chronic hypoxia by tumour cells, and the associated tissue damage via ROS, is correlated to a high frequency of DNA breaks and accumulation of DNA replication errors leading to genetic instability and mutagenesis in a variety of genes including p53 [91–93]. This enables the tumour cells to avoid apoptosis via the mutated p53 gene not activating the apoptosis pathways. Hypoxia also affects chromosomes to promote transformation via telomerases. Telomerases are ribonucleic enzymes that function to maintain telomere length – wherein increased

telomere length means increased cell survival – and their activity is suppressed in normal somatic cells, thus enforcing normal cell death following chromosome degradation. However, this safety feature – to self-destruct cells with damaged DNA – malfunctions in cancer cells. Instead, telomerase activity is increased and thus promotes cellular immortalisation [85]. Conversely, acute hypoxia leads to genomic instability due to a delay in the DNA damage response and p53-dependent apoptosis [94]. This encourages the cancer cells to enter quiescence; a state of cell-cycle arrest causing reduced cell proliferation and conferring a stem-cell like quality [95]. This would appear a paradox in the understanding of cancer cells seeing as their defining characteristic is uncontrolled proliferation; however, this reduced hibernation-like state is the perfect defence. By entering quiescence, cancer cells are able to conserve ATP supplies, avoid apoptosis (and senescence) and be protected from external stresses such as nutrition/O_2 deprivation and cancer therapies [96–99].

This interplay between HIF, p53 and hypoxia is complex and a more detailed description has been provided by Eales [82]. Hypoxia and its associated severities drive a physiological selective pressure in tumours for the expansion of cells that have lost their apoptotic potential and, in particular, for cells with p53 mutations, wherein cells lacking functional p53 are more susceptible to genomic instability and potential malignancy [100–102].

2.2.2.4 Other hypoxia-response factors

A number of other pathways are also stimulated during hypoxia including; the cell cycle pathway relating to quiescence and proliferation referred to as PI3K/AKT/mTOR [103,104], the receptor pathways relating to the communication between cell surface receptors and DNA referred to as MAPK/ERK [105–107], and a stress response pathway relating to cytokine production and cell survival controlled by nuclear factor- κB (NF-κB) [108]. These pathways, and many others, are activated and induces the activity of; metal transcription factor-1 (MTF-1; for increased iron metabolism), erythropoietin (EPO; for increased production of haemoglobin), human lactate dehydrogenase isoenzyme-5 (HLDH5; for lactate metabolism), Bcl-2/adenovirus E1B 19 kDa-interacting protein 3 (BNIP3; for apoptosis avoidance), matrix metalloproteinases (MMPs; for metastatic progression), urokinase plasminogen activator receptor (uPA-R; for metastatic progression), lysyl oxidase (LOX; for metastatic progression), osteopontin (OPN; for metastatic progression), and many more [1,109–112]. Hypoxia also regulates inflammatory mediators and growth factors to stimulate platelet,

leukocyte, and smooth muscle cell activity for immune-resistance and immune-suppression, helping the tumour cells escape surveillance and destruction [113,114]. Combined, all of these pathways form the critical steps involved in helping tumour cells persist and invade the body; the consequences of which include metastasis, increased malignancy and resistance to therapeutic interventions.

2.2.3 The consequences of tumour hypoxia

The increased proliferation of tumoural cells, and their associated chaotic and malfunctioning blood vessels, gives rise to the heterogeneous, hypoxic microenvironment associated with neoplasia. In turn, hypoxia induces a reduced stem-cell like proliferation, apoptosis avoidance, and cell-cycle arrest; all factors which contribute to the resistance of tumour cells to therapy (**Fig. 2-3**). These therapeutic problems apply to radio-, chemo-, photodynamic- and immuno-therapy due to the development of resistance in the tumoural cells [2,5,115–118].

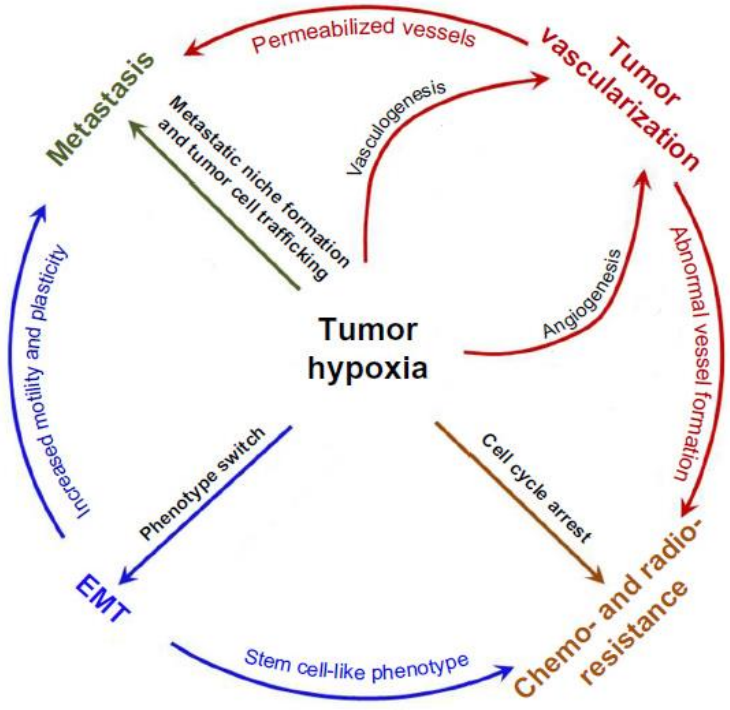

Figure 2-3. Schematic illustrating the role of hypoxia in cancer progression, angiogenesis, metastasis and, inevitably, resistance to therapy. Image reproduced from Muz et al. [6].

EMT, epithelial-to-mesenchymal transition.

This resistance is often the circumstance of the low O_2 tension itself. In the case of radio-therapy, sensitivity to the therapeutic regime is drastically reduced when the pO_2 in tissue is below 10 mmHg [119–125]. This is because O_2 is a potent radiosensitiser which, upon being bombarded with ionising radiation forms ROS (such as hydroxyl), and can produce single- and double-stranded DNA breaks within cells which facilitates cell death [126]. However, when O_2 levels are too low this mechanism cannot occur or occurs less effectively. This phenomenon is known as the 'O_2 enhancement effect'; wherein the radiation dose required to achieve the same biological effect is approximately three times higher in the absence of O_2 than in the presence of normal levels of O_2 [126,127]. Resistance is also compounded by the tortuous and chaotic vasculature network of the tumoural mass. Cells located distant from a functional blood supply can be resistant to drug therapy because of the limited penetration of the anti-cancer agents and thus its lower efficacy due to leaky vasculature and dead-ends associated with tumoural angiogenesis [128]; and the reduced rate of cell proliferation (i.e. quiescence) entered by cells further away from vasculature offers protection from the effects of chemotherapeutic agents whose activity is selective for rapidly dividing cell populations [128,129].

These resistance factors are prominently showcased in the chemo- and radio-therapeutic challenges faced in treating primary brain tumours (referred to as gliomas or glioblastomas). These neoplasms are extremely difficult to treat due to their increased proliferation, invasive nature, propensity for recurrence, and treatment resistance [130,131]. The standard treatment regime for newly diagnosed malignant gliomas involves surgical resection, and radio- and chemo-therapy [132–137], unfortunately however patient prognosis remains poor. The incurability of glioblastomas is underscored by the invasive, diffuse, and ill-defined borders of these tumours. Notably, image-guidance by MRI is routinely used as a guide for planning therapy strategies – including intensity-modulated radiation therapy (IMRT) – to help identify tumour location, oedema and necrosis, along with the tissue microstructural changes and regions displaying dysfunction of the blood-brain barrier [138–140]. Unfortunately, however, commonly used MRI sequences are not able to provide images that clearly delineate tumour boundaries and thus do not always correspond with sites of tumour infiltration or other molecular events, and provide only indirect information about tumour pathophysiology. This pathophysiology includes key factors that contribute to treatment failure such as tumour hypoxia. Current research strongly emphasises the need to study and determine the distribution of hypoxia in tumours for radiation treatment planning purposes. Ling et al. [141] proposed the concept of using functional imaging – based on known factors of

resistance (such as hypoxia) – to determine a heterogeneous multidimensional dose distribution of radiotherapeutics within tumours; this approach, closely related to IMRT, was named 'dose painting'. Using this method it is possible to apply a strategy of IMRT wherein higher doses of radiation are focused on areas of increased treatment resistance determined by functional imaging. To employ effective 'dose painting' strategies, the visualisation of tumour hypoxia *in vivo* would have a significant impact on the treatment strategy for tumours such as glioblastoma.

Notably, numerous studies have demonstrated that tumour hypoxia, in addition to diminishing therapeutic efficacy, plays a major role in metastasis [142] and malignant progression [143]. Hypoxia promotes these consequences by inducing the expression of HIF-1α, which in turn activates a metastatic cascade which provides a selection pressure for a more aggressive phenotype. This metastatic cascade and selective pressure involves the creation of favourable metastatic niches for tumoural cells and the trafficking of cells towards those locations. This is achieved by the expression of VEGF (essential for the dissemination of tumoural cells from the primary tumour cells) [144], the transition of epithelial cells to mesenchymal (EMT) (essential for invasive and migratory behaviour), and a trans-differentiation of cells to acquire plasticity (essential for mobility) [1,6,145]. Furthermore, hypoxic stress proteins and the loss of apoptotic potential can impart resistance to certain chemotherapeutic drugs [146–148]. Finally, the resistance of solid tumours to chemo-therapy may also be the result of another largely ignored perspective: that of fluctuations in blood flow such as seen in acute hypoxia. Acute hypoxia has significant implications for delivery of chemotherapeutic agents, cellular responsiveness to those agents, and the regrowth potential of the surviving tumour cells. Moreover, regions actively proliferating at one point in time may not have cells actively synthesising DNA at a different time [149,150]. This serves as a possible selection mechanism, wherein cells which survive this high-stress hypoxic environment, are likely to be a source of clonogenes which repopulates tumours with more malignant cells following radio-therapy [100,151,152]. Furthermore, tumour cells and their associated local microenvironment also change in response to anti-cancer treatments such as the transient changes in the oxygenation status of tumours induced by radiation [153]. It is important to emphasise that heterogeneities in tumour oxygenation vary throughout the tumoural microenvironment, thus there is a change in hypoxia both spatially and temporally. Furthermore, these changes differ between tumour types, patient, and from tumour to tumour. It is clear, therefore, that the challenges faced by researchers to develop methods to determine tumoural O_2 tensions are immense and of crucial importance.

2.3 EXISTING METHODS TO MEASURE HYPOXIA

Considering the severe consequences of hypoxia, it is no surprise that the measurement of O_2 tension in cancer represents a long-standing endeavour of medicine and biology. Because low O_2 tension is linked to such dire therapeutic outcomes, a collection of adjuvant therapeutic interventions involving increased O_2 administration have been proposed over the last several decades to improve the therapeutic outcomes of cancers. These include hyperoxic gas breathing – including the use of 100 % O_2, 95 % O_2/5 % CO_2 (carbogen gas) breathing and accelerated radiotherapy combined with carbogen gas breathing and nicotinamide (ARCON) – hypoxic cell-selective cyto-toxins, and IMRT [154–160]. However, despite the promising perspectives these therapeutic approaches have gained moderate success at the clinical level. This can be attributed to several factors, including the heterogeneity of hypoxia and a lack of accurate methods to characterise tissue O_2 levels *in vivo*. On these grounds, a more precise and robust measurements of the O_2 levels *in vivo* would allow a better selection of patients responding positively to hypoxia-directed treatments. The ideal properties of a hypoxia measurement technique should include; non-invasiveness, adequate spatial and temporal resolution, quantitative measurement, no O_2 consumption, adequate range of O_2 tension values measured, and if an exogenous agent is required, exhaustive knowledge of its toxicology and pharmacodynamics [161]. Unfortunately, there is currently no *in vivo* method that fulfils satisfactorily all these requirements. **Table 2-1** summarises the most relevant methodologies, together with their mechanisms, characteristics, advantages and limitations.

Table 2-1. Main characteristics of methods used to assess *in vivo* hypoxia.

	O_2 electrodes	IHC	Optical				Nuclear
Technique	**Polarographic electrodes**	**2-nitroimidazole**	**IR and NIR spectroscopy**	**PAT**	**OxyLite®**	**Luminescence quenching probes**	**PET/SPECT**
Mechanism	Current generated by reduction of O_2	Antibody/antigen, selective entrapment in hypoxic cells	Wavelength-dependent, Hb/HbO_2 ratio	Ultrasonic emissions, Hb/HbO_2 ratio	Phosphorescent lifetime measurements of dissolved O_2	Fluorescence quenching measurements of dissolved O_2	Radioisotopes, selective entrapment in hypoxic cells
Safety	Oedema & bleeding	Biopsy of tissue	None	None	Oedema & bleeding	Toxicity of injected probes	Ionising radiation, toxicity of injected probes
Spatial resolution	µm - mm	µm	mm - cm	mm	µm - mm	mm - cm	mm - cm
Temporal resolution	s	h	s - m	s	s	s	m - h
Necrosis detection	No	Yes	No	No	No	No	Yes
Chronic/acute hypoxia detection	No	No	No	Yes	No	No	Yes
pO_2 resolution	< 10 mmHg	< 10 mmHg	Hb/HbO_2 ratio	Hb/HbO_2 ratio	0 - 15 mmHg	< 15 mmHg	< 10 mmHg
Advantages	Direct O_2 measurement, high spatial resolution, extensive literature	Good spatial resolution	Non-invasive, inexpensive, repeatable	Non-invasive, repeatable	Direct O_2 measurement, does not consume O_2	Direct O_2 measurements, does not consume O_2, repeatable, all tumours measurable	Non-invasive, whole body detection, used clinically, all tumours measurable
Limitations	Invasive, consumes O_2, not repeatable, only accessible tumours	Not generally quantitative, not repeatable, only accessible tumours	Not measuring O_2 directly, poor spatial resolution, penetration depth issue	Not measuring O_2 directly, penetration depth issue	Invasive, no imaging, only accessible tumours	Penetration depth issue	Radiation risk with repeatability, poor spatial resolution

IHC, immunohistochemistry; PAT, photoacoustic tomography; PET, positron emission tomography; SPECT, single-photon emission tomography; Hb/HbO_2, deoxygenated and oxygenated haemoglobin ratio. Adapted from citations [162–166].

2.3.1 Electrode based methods

Assessment of the tumour oxygenation status by invasive and non-invasive procedures has been studied vigorously over the years. The most direct method, so far, for measuring hypoxia in solid tumours is the polarographic electrode measurement method. Polarographic electrodes (also known as Clark electrodes), which were introduced in the 1950s, were the first technology to allow for the accurate measurement of tissue oxygen levels. These electrodes measure the electric current formed at a cathode upon reduction of O_2, with the generated current being directly proportional to the pO_2 within the tissue [167]. The design generally includes a needle-like electrode, the tip of which is enclosed by a gas-permeable membrane. The pO_2 measurements made by the electrode are highly accurate, and was used extensively by Vaupel and colleagues to analyse tumour hypoxia in a range of models [118,168].

The technique offers high spatial resolution, and a direct method of assessing intratumoural pO_2 values (**Fig. 2-4**) [169].

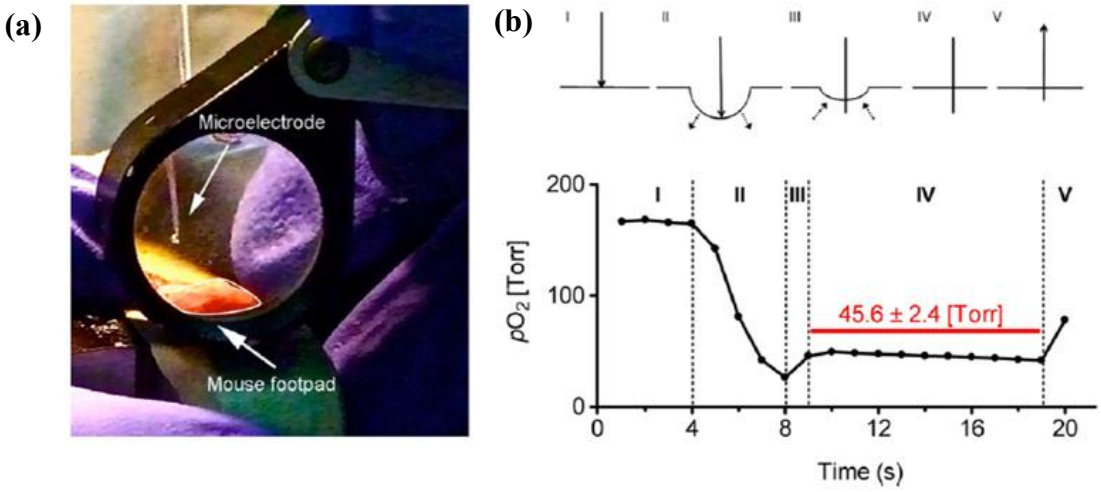

Figure 2-4. Determination of murine skin oxygen tension using the polarographic microelectrode technique. Note the diameter of the microelectrode tip (100 µm) shown in relation to the mouse footpad **(a)**. Figure **(b)** shows the time frame of measurements, performed over seconds, wherein (I) – (III) indicates the time wherein the tip is brought into contact and penetrates the skin. Time (IV) indicates the measurement of the oxygen tension. Note the decrease of pO_2 overtime due to the consumption of oxygen by the electrode. Image reproduced from Hofmann et al. [169].

Unfortunately, however, the use of the polarographic electrode technique includes several limitations and drawbacks; only tumours which are readily accessible can be measured, areas of necrosis cannot be identified, the technique is invasive and the insertion of the needle-like probes is not well-tolerated in human patients, the electrodes require careful calibration for each environment as many factors (e.g. temperature and ionic strength) affect performance, O_2 readings are highly location-dependent as the operator places the probe, the technique is destructive as it induces damage to capillaries and small blood vessels which further complicates matters of hypoxia and the microenvironment, and lastly, the electrode consumes O_2 during measurement [170].

To address some of these issues, the Eppendorf electrode system was developed, in which a computerised driver moves the electrodes to precise locations and depths [170]. Furthermore, recessed-tip microelectrodes were developed to reduce tissue damage and microcirculatory disturbance, providing faster responses and finer spatial resolution [171]. But, neither of these advances can eliminate the consumption of the O_2 within the tumour and the invasiveness of the technique. Recently, however, the concept of wearable, bio-conformable electronics was introduced to overcome this limitation [172]. Planar electrodes have been designed which enable the measurement and mapping of transcutaneous pO_2 by attachment of the probes to the skin surface [173]. However, the technique requires the elevation of the skin to 44 – 48 °C which perturbs the examined tissue. The Eppendorf polarographic measurement of tumoural pO_2 has been touted as the "gold standard" but is disputed. Often the pO_2 measurements are followed by a core biopsy of the tumour area (where the pO_2 determination occurred) to be processed with immunohistochemistry.

2.3.2 Immunohistochemistry (IHC) based methods

Regarding the development of suitable probes for tumour hypoxia, the nitroimidazoles have received particular attention. Originally, 2-nitroimidazole was developed as an antibiotic against anaerobic bacteria and protozoa in 1953 [174], but its unique behaviour in hypoxic environments propelled its popularity. In hypoxic conditions, nitro-aromatics are selectively reduced by nitro-reductase enzymes to form hydroxylamine intermediates that can bind irreversibly to cellular nucleophilic groups present in proteins and DNA [166]. This irreversible retention in cells is exploited to provide researchers with a microscopy based technique for visualising tumour hypoxia named immunohistochemistry (IHC) (**Fig. 2-5**) [175].

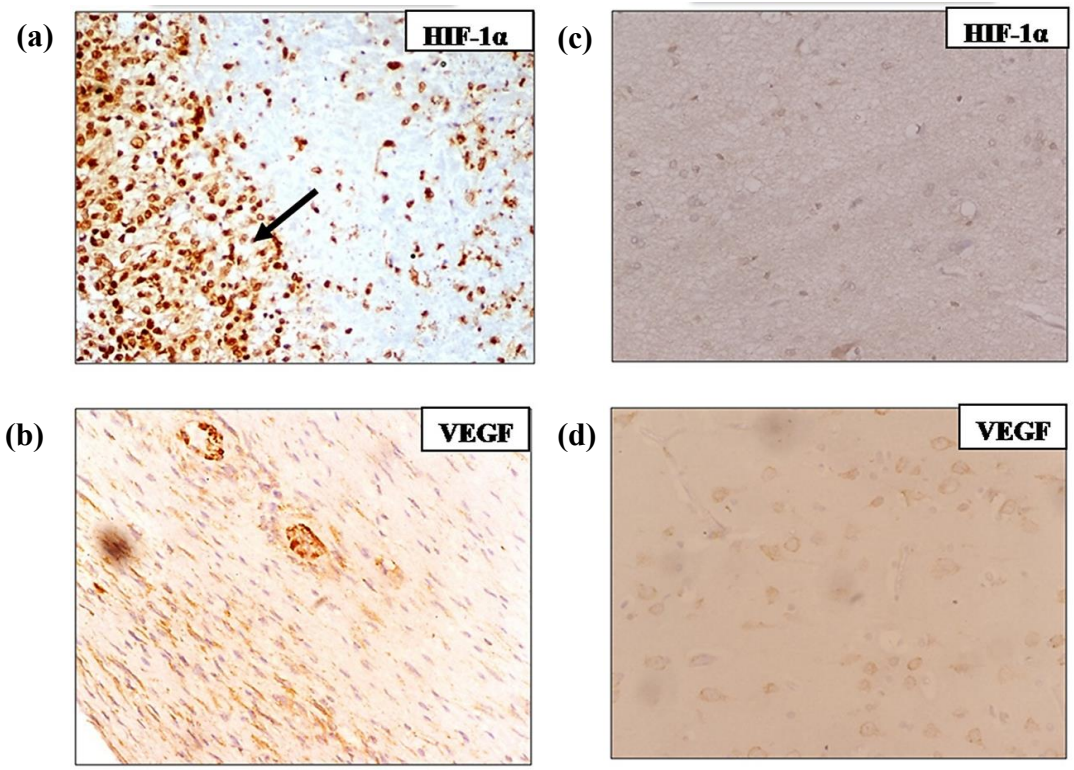

Figure 2-5. Example of immunohistochemical staining of HIF-1α and VEGF in glioblastoma tissue samples **(a)** and **(b)** and normal brain samples **(c)** and **(d)**. Arrow indicates area of necrosis within the sample. Image reproduced from Irshad et al. [175].

The detection of these exogenous hypoxia markers are based on antigen-antibody interactions which includes the injection of 2-nitroimidazole derivatives, such as pimonidazole or EF5 (pentafluoropropylacetamide), into the patient before biopsy of the tumour tissue and the detection of the reductants using antibodies conjugated with a

counterstain for detection. Importantly, due to the involvement of enzymes during the nitroimidazole reductions, the method only accounts for viable cells. Attempts to design optimised nitroimidazole molecules has been successful, enabling improved; stability, ability to attach moieties (such as isotopes) which enables multimodal imaging, solubility, tissue penetration and biodistribution [162,176]. Further improvements have enabled the vascular parameters of the hypoxic tissue to be related to O_2 concentration both *in vitro* [177,178] and *in vivo* [179,180]. It should be noted that nitroimidazole-based markers target highly hypoxic cells, such as cells with pO_2 below 1 mmHg, leading to cells with higher O_2 concentrations, but still deemed hypoxic, to be excluded [162]. Studies supporting the diagnostic significance of IHC have been published for soft tissue sarcoma [181], brain tumours [182], and head and neck cancers [183], however conflicting results have arisen, such as for cervical cancer [184].

IHC can also involve the use of surrogate markers of hypoxia, such as the endogenous makers for HIF-1, CAIX, VEGF and GLUT. Here, both exogenous and endogenous markers are used to provide information regarding the intercapillary distance, vascular density, and distance from tumour cells to the vessels, within the tumour microenvironment at a pO_2 of < 10 mmHg [185–187]. Several methods have been developed to directly measure HIF-1 activity using the introduction of transgenes with hypoxic response elements as promoter sequences coupled to reporter genes, such as luciferase [188,189] or green fluorescence protein (GFP) [190]. However, the heterogeneity of the tumour gene response makes HIF-1 a complex target; many studies have shown weak correlation between HIF-1α expression and the polarographic electrode technique [191,192]. Attempts to predict and quantify the re-oxygenation of acute hypoxia have been made using a combination of exogenous and endogenous probes [193]. However, although combination CA IX and proliferation markers can identify cells which are proliferating under hypoxic conditions, there is still no correlation between the amount of CA IX and direct O_2 measurements as compared to the polarographic electrode [194,195]. Markers such as VEGF and GLUTs have also been explored [196–198], and imaging strategies have been developed to reflect tumour vasculature and proliferation, however a direct relationship between pO_2 measurements and protein expression has not been established [199,200].

Thus, whilst IHC can provide important information regarding the tumour microenvironment, with only viable cells providing information at high spatial resolution and following a highly standardised technique, limitations include; invasiveness and limited sampling size, limited quantification of averaged hypoxic areas over sampled size, and a difficulty in performing repetitive measurements to monitor changes in oxygenation due to

the necessity for biopsy or surgical removal of the tumour tissue for evaluation thus hindering the ability to measure the heterogeneity of tumours. Furthermore, 2-nitroimidazole binds to keratinised tissue which could be partially responsible for unspecified staining thus explaining the disparities with other methods [201]. Although attempts have been made to use IHC techniques for chronic and acute hypoxia determination, overall the technique still provides only a snapshot in time of tumour dynamics [202–207].

2.3.3 Optical based methods

2.3.3.1 Fluorescence and near-infrared (NIR) spectroscopy

Both fluorescence and NIR spectroscopy enables the determination of haemoglobin saturation via the absorption and scattering of incident wavelengths in tissue. These techniques are non-invasive, and includes the used of near-infrared spectroscopy (NIRS), optical coherence tomography (OCT), and diffuse optical spectroscopy and tomography (DOS/T). These techniques enable the determination of haemoglobin saturation via the absorption and scattering of near-infrared wavelengths (400 – 1000 nm) which readily cross through biological tissues. This is achieved by the illumination of tissue, and the measurement of backscattered light as a function of wavelength, specifically when the haeme groups of haemoglobin bind O_2, their absorption spectrum changes and enables the differentiation between oxygenated (HbO_2) and deoxygenated (Hb) haemoglobin [208]. This differentiation can be expressed as the haemoglobin saturation fraction and can be related to the tissue pO_2 by using the haemoglobin dissociation curve [209,210]. For clinical studies, this method can be used under normal conditions without a major restriction of motion. Its main advantage is the ability to perform real-time measurements repeatedly [211].

For haemoglobin saturation measurements, four main applications of optical spectroscopy principles are used, namely; diffuse reflectance, hyperspectral imaging, and diffuse optic topography and tomography, all of which enables the quantification of light absorption and scattering to determine haemoglobin saturation in tissues. Bulk tissue oxygenation and the non-invasive monitoring of human intra-tumour chemotherapy response during treatment regimes can be determined via diffuse reflectance spectroscopy [212–214]. Window chamber models for high-resolution imaging of tumour microvasculature and haemoglobin saturation measurements have been achieved *in vivo* via hyperspectral imaging [215–217]. DOS/T involve

acquiring oxygenation measurements through the use of an array of NIR sources/detectors thus allowing for a relatively deep (tens of mm) measurement in tissue [218–220] (**Fig. 2-6**).

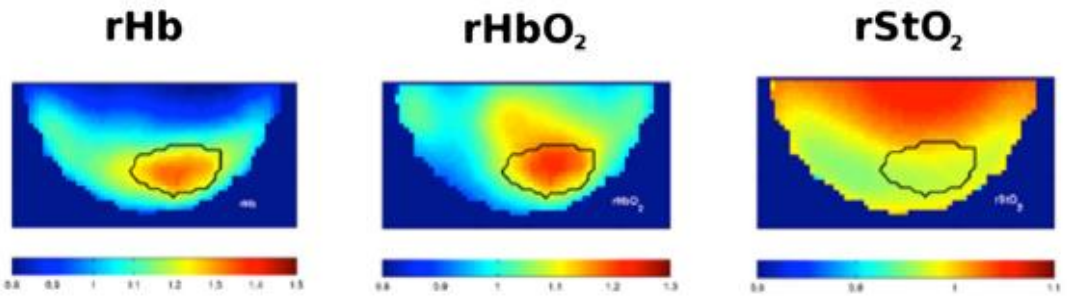

Figure 2-6. Example of diffuse optical tomography (DOT) imaging wherein an invasive ductal carcinoma is described in terms of relative deoxyhaemoglobin (rHb), oxygenated haemoglobin ($rHbO_2$), and relative tissue oxygen saturation ($rStO_2$). The black solid line indicates the region identified as the tumour. Notably, these parameters do not directly measure the tumoural pO_2 values. Image reproduced from Chung et al. [220].

Unfortunately, although fluorescence and NIR spectroscopy techniques are simple, low cost, and relatively non-invasive, they are fundamentally indirect methods for determining tumour pO_2 which depends on the tumours under investigation to have well-perfused vasculature. Direct spectroscopy methods are suitable to measure pO_2 from 20 to 100 mmHg, but suffer from a long response time (approximately 3 min) with relatively poor resolution (tissue scatters light strongly causing low absorption). To add to the complications, it should be noted that the useful lifetime of spectroscopy is short because the response to pO_2 is non-linear and not readily described mathematically, and pH and other gases, such as CO_2, can skew calculations. Regardless of this, a significant advantage of these optic techniques is that they are able to provide functional information regarding the tumour tissue [221–227].

2.3.3.2 Photoacoustic tomography (PAT)

The absorption of light by haemoglobin can also be directly detected by taking advantage of photo-thermal effects. For the use of the photoacoustic tomography (PAT) technique, laser energy is directed at a tissue sample, wherein the molecules absorb the light and converts it into heat, leading to a rapid but transient localised thermos-elastic expansion, generating an ultrasonic emission that can be detected. In this way, PAT enables the three-dimensional visualisation of the position of molecules within a tissue by absorption contrast. This contrast is largely determined by the wavelength-dependant changes in optical

absorption by a variety of endogenous chromophores, including melanin, Hb and HbO_2, or exogenous probes (e.g. NIR-absorbing dyes such as AlexaFluor 750 and indocyanine green).

PAT has shown potential in providing simultaneous structural, functional and molecular information in pre-clinical studies for visualising tumour location deep within tissue, and can provide information on tumour vasculature [228] and monitor angiogenesis [229]. PAT can also obtain information on haemoglobin oxygen saturation at high resolution and contrast without the use of exogenous contrast agents [230]. Another advantage of PAT is its compatibility with widely used ultrasound imaging (USI) techniques [231]; when combined, PAT and USI can simultaneously provide anatomical and functional information on tumours [232,233], enabling simultaneous imaging of cross-sections of blood vessels, the concentration and oxygenation of haemoglobin, as well as blood flow *in vivo* [232,234] (**Fig. 2-7**). These parameters can be used to quantify O_2 metabolism at a high spatial resolution without the requirement of an exogenous contrast agent. Photoacoustic imaging overcomes the diffusion limit of traditional optical methods by detecting ultrasound generated from light absorption [235], and can thus overcome the tissue scattering associated with most spectroscopy techniques [236].

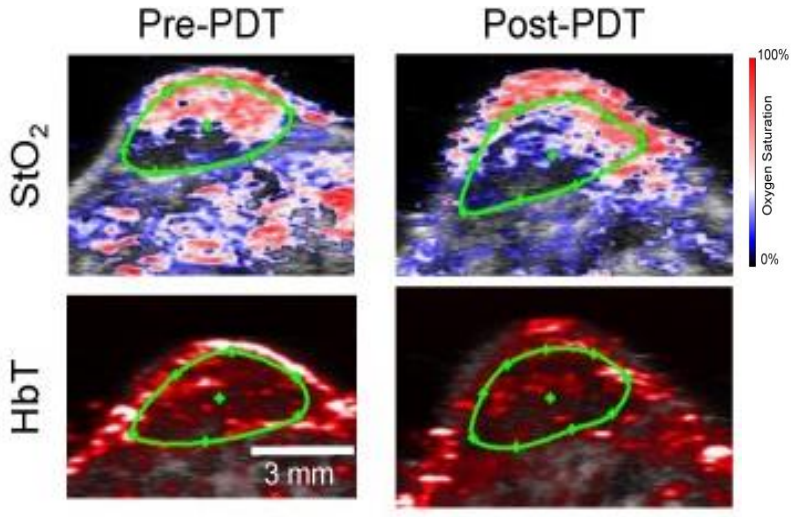

Figure 2-7. Combined ultrasound and photoacoustic images of subcutaneous tumours induced in nude mice before and after photodynamic therapy (PDT). Grayscale ultrasound images, presented in the top panel, are overlaid with oxygen saturation (StO_2) map where blue and red represent hypoxic and oxygenated regions. Similarly, the bottom panel is overlaid with a scale to represent the total haemoglobin (HbT). Image reproduced from Mallidi et al. [234].

By combining lifetime oxygen sensing and photoacoustic imaging, the technique PALI is able to reveal the distribution of pO_2 with the resolution determined by an ultrasound transducer, typically less than 1 mm, and a penetration depth of about 15 mm [237–239]. PALI utilises a series of two pulsed laser sources, one pulse excites the chromophores, and the other generates photoacoustic signals proportional to the transient absorption of the chromophores. Even though lifetime-based photoacoustic methods enable the measurement of pO_2, they require perfusion of exogenous contrast agents into the region of interests, which may raise concerns such as biosafety and biocompatibility [240].

Although PAT excels at providing high resolution, millimetre-deep imaging of the vasculature of tissue [232], this approach is considered an indirect method of pO_2 determination, and relies on the existence of blood and its perfusion, and does not reveal information regarding the concentration of O_2 within the tissues and cells themselves. Furthermore, a penetration depth issue is inherent in this technique. This limitation can be circumvented by using longer wavelengths but endogenous tissue chromophores have less optical absorption at these wavelengths thus creating a trade-off between imaging depth and resolution. Furthermore, absolute quantification for oxygenation in deep tissue remains a challenge, mainly due to unknown sources of optical influence.

2.3.3.3 Luminescence quenching probes

Optical-imaging approaches based on luminescence quenching enable the direct measurement, quantification and imaging of O_2 concentration within tissues, even in the absence of blood. Optical O_2 sensors based on luminescence quenching operate through energy exchange; excited state luminophores transfer energy to surrounding O_2 and thereby no longer emit. The quenching effect on the luminescence intensity and lifetime of a sensor is described by the Stern-Volmer equation. Many hundreds of different optical probes capable of sensing a myriad of different products have been designed, developed and applied in several applications [241–244].

Luminescence-intensity based approaches are advantageous in their simplicity and adaptability to assist existing imaging systems used to capture the distribution of phosphorescence intensity and quantify O_2 across two-dimensional surfaces [245,246]. Limitations such as inhomogeneous illumination and non-uniform distribution of the probes have been overcome by introducing O_2-independent references dyes that co-localise with the

phosphorescent sensor. In contrast, lifetime-based approaches are advantageous because they are independent of excitation energy, detector sensitivity, and probe concentrations. These methods have enabled a host of studies involving measurements of intravascular pO_2 values in various tissue types, including tumours, the brain, retina, and heart [247–250]. The most common, and oft used, example of O_2 dependent phosphorescent lifetime measurements is the OxyLite® probe. Since 1996, the assessment of tumoural oxygenation has been possible using fiber-optic O_2 sensors named OxyLite® [251]. Whereas the polarographic microelectrode provides static information of tissue oxygenation status, the fiber-optic technique used with the OxyLite® system, provides continuous pO_2 measurements. In this technique, the microelectrode probe is inserted within the concerned tissue for a prolonged period of time producing several repeated measurements in the same position and can directly image cell pO_2 within the range of 0 – 15 mmHg, as well as accurately map O_2 distribution [251–253]. Luminescent materials can be detected using a variety of optical imaging modalities, enabling a wide range of multi-modality capabilities. With regard to pre-clinical *in vivo* applications used to study tissue hypoxia, phosphorescence lifetime imaging has become increasingly important due to the capacity for successful three-dimensional spatial registration using confocal imaging [254] and diffuse tomography [255]. For example, phosphorescence lifetime imaging via OxyphorG2 was used to measure fluctuations in vascular pO_2 in fibrosarcomas, gliomas, and mammary adenocarcinomas grown in dorsal skin fold window chambers [256].

Aside from these two commonly used intensity- and lifetime-based O_2 determination systems, many other approaches, such as fluorescence anisotropy measurements, Förster resonance energy transfer (FRET), and two-photon excitation techniques have also been explored [249,257,258]. Various O_2 probes have been explored for decades and includes; transition metal Ru^{2+}-, Os^{2+}-, Ir^{3+}-complexes [259–262], organic dyes such as cyanine [263], rhodamine [264,265], fluorescein (including fluorescein isothiocyanate [FITC] and erythrosin B) [266–268], oxazine [269,270], and phosphorescent metalloporphyrins (Pt^{2+}, Pd^{2+}, and Zn^{2+}) [271–273] (**Fig. 2-8**).

These O_2 probes have been designed as complexes, films and foils, and encapsulated within nanoparticles, with each system bringing its own advantages and drawbacks. Due to the low cost, simple preparation and implementation, and their rapid and non-destructive characteristics, the use of optical O_2 probes is by far the largest sector of development as hypoxia sensors. However, the use of these probes come with some intrinsic disadvantages, including their poor chemical stability, poor photostability, cytotoxicity, perturbation of the host system, and poor spatial resolution due to high background noise [274].

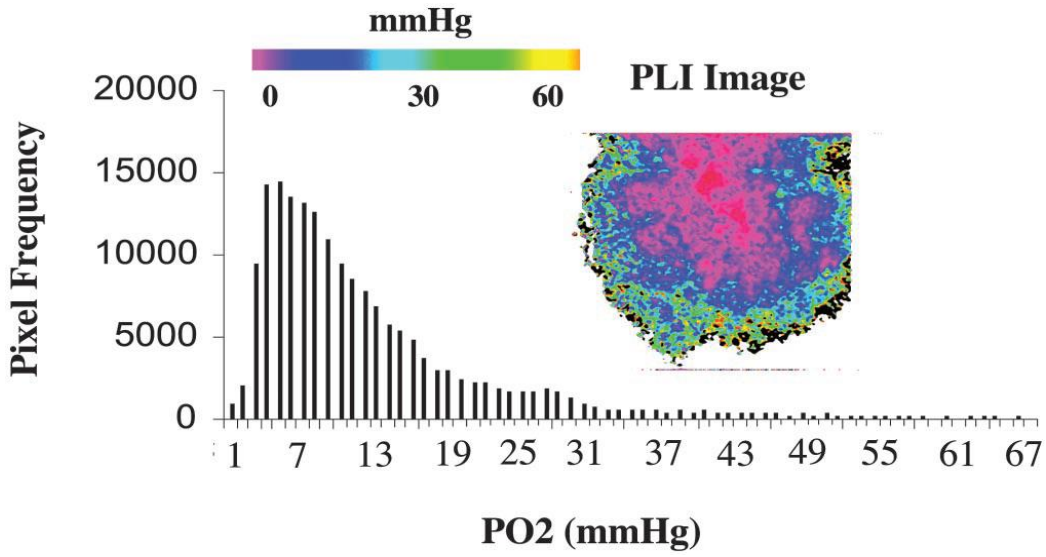

Figure 2-8. Example of a phosphorescence lifetime (PLI) image (using a Pd^{2+} porphyrin probe) and a pixel-pO_2 histogram of an *in vivo* tumour. Image reproduced from Erickson et al. [273].

2.3.4 Nuclear based methods

2.3.4.1 Positron emission tomography (PET)

One of the most widely used, and clinically applied, nuclear based techniques for hypoxia analyses and imaging in tumours is positron emission tomography (PET). PET, as the name suggests, is based on the positrons emitted as radioisotopes decay which, upon deceleration, encounters an electron causing the annihilation of both the electron and positron and the emission of a pair of gamma (annihilation) photons which are detectable by the PET equipment. The most common positron-emitting radioisotopes are ^{18}F, ^{124}I and $^{60/64}Cu$. These radioisotopes are attached to organic markers which includes; 2-nitroimidazoles, such as fluoromisonidazole (FMISO), 2-(2-nitro-1H-imidazol-1-yl)-N-(2,2,3,3,3-penta-fluoropropyl)-acetamide (EF5), and fluoroetanidazole (FETA); nucleoside conjugates, such as iodoazomycin arabinoside (IAZA); and copper compounds, such as Cu(II)-diacetyl-bis(N4-methylthiosemicarbozone) (Cu-ATSM) [275–277]. These markers specifically bind to viable hypoxic cells and form stable adducts, wherein the radioisotopes accumulate and are detected by a PET scanner.

The most popular hypoxia imaging agent for PET is 2-nitroimidazole, which is labelled with a radioisotope (e.g. [^{18}F]Fluoromisonidazole thus ^{18}F-FMISO) [166,275,278] and, is taken up by viable cells with <10 mmHg O_2 [279] in gradients (indicating the degree of adduct accumulation in the area). ^{18}F-FMISO has been used to demonstrate hypoxia in glioma, head

and neck cancer, renal tumours, soft-tissue sarcomas, and non-small cell lung cancer [279–281] but it is not suitable for all cancers [279,282]. Notably, ^{18}F-FMISO remains one of the most widely used radiotracer, specifically for glioblastomas, as it provides balance between sensitivity, specificity, tumour accessibility, imaging time, and invasiveness [283,284]. Second generation nitroimidazoles for PET have been developed including ^{18}F; -fluoroerythronitroimidazole ([^{18}F]FETNIM) [285,286], -fluoroetanidazole ([^{18}F]FETA) [287], -fluoroazomycin arabinoside ([^{18}F]FAZA) [288], and EF1/5 [289–291]. These markers have a relatively high lipophilicity, which ensured easy penetration of cell membranes and diffusion into tumour tissue, but limited the clearance of unbound tracer which leads to relatively low tumour-to-reference tissue ratios [292]. The iodinated analogues include iodoazomycin galactopyranoside (IAZGP) and IAZA, both of which are labelled with the long-lived radioisotope ^{124}I, thus allowing for delayed imaging. However, numerous studies have shown that delayed imaging provides no advantages as compared to the short half-life of ^{18}F, and rather demonstrated poor image resolution, higher doses of radiation, poor biodistribution, and reversible binding over time as compared to ^{18}F-compounds [293,294]. Other organic makers include the copper complexed dithiosemicarbazones (Cu-ATSM) for which the mechanism of hypoxia specificity is debated [295,296]. Regardless, Cu-ATSM can be an effective tracer for global hypoxia and is especially useful in situations where blood flow may be limited [297]. When compared to ^{18}F-FMISO, Cu-ATSM uptake is significantly higher in the target tissue than in non-hypoxic areas and occurs at a faster rate in animal models (10 – 15 min as compared to 2 – 4 h) [298,299]. Although Cu-ATSM has been successfully applied to several tumoural types for the detection of hypoxia [300–303], some preclinical data suggests that it may not be suitable for all tumour types [295,304,305]. Furthermore, opposite findings have observed between studies applying the same cell line to different animal species [306,307].

PET organic markers can also indicate glucose metabolism (e.g. ^{18}F-fluorodeoxyglucose [FDG]) (**Fig. 2-9**), or blood perfusion (^{15}O-labelled water). FDG is the most commonly used PET marker in oncology and, as previously discussed, under hypoxic conditions mitochondrial ATP synthesis is abandoned and glycolysis is used in compensation thus making the use of FDG a surrogate marker for tumour hypoxia [308,309]. However, as most cancer cells depend heavily on glycolytic ATP production even under well-oxygenated conditions, weak correlations between tumour hypoxia and FDG retention has been observed [308,309], thus the potential of the marker is limited. On the other hand, perfusion can be estimated with PET by using ^{15}O-labelled water. O_2 delivery to tumours occurs via the vascular supply, indicating that blood perfusion and hypoxia are related; poor perfusion will

increase the degree of chronic hypoxia, and changes in perfusion are responsible for acute hypoxia [310]. However, clinical studies using this approach have produced conflicting results [311]; high blood perfusion has been associated with metastasis and poor survival after radiotherapy [277], rather than the low perfusion one would expect to be indicative of hypoxia.

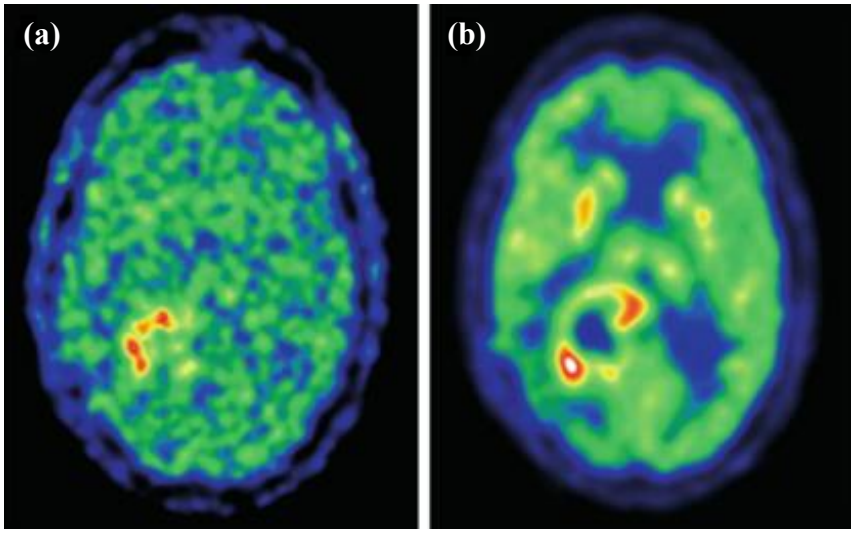

Figure 2-9. PET imaging of a high-grade glioma wherein the hypoxic regions (red) were assessed by ^{18}F-FMISO **(a)** and the high glucose metabolism (red) were determined by ^{18}F-FDG **(b)**. Note the lack of concordance between the two images, suggesting that a complex relationship exists between the two metabolic processes. Image reproduced from Lee and Scott [279].

2.3.4.2 Single-photon emission computed tomography (SPECT)

Whereas PET detects the emission of gamma ray pairs, the single-photon emission computed tomography (SPECT) technique simply relies on individually detected gamma ray photons. ^{123}I, iodinated azomycin arabinosides, was the isotope initially used for this purpose [312,313] but has shown inconsistent uptake into various tumours, thus efforts have been made towards its modification [314]. Newer agents include iodoazomycin pyranoside (IAZP), beta-*D*-iodinated azomycin galactopyranoside (IAZGP), and iodoazomycin xylopyranoside (IAZXP) based on the azomycin-nucleoside structure [315]. ^{99m}Tc is an isotope gaining popularity, with nitroimidazoles and non-nitroimidazoles labelled with ^{99m}Tc increasingly being used to study tumour hypoxia, such as; the nitroimidazole compounds BMS-181,321 and BRU 59-21; and complex ligands without the nitroimidazole group, such as N2IPA, and ^{99m}Tc-HL91 [315]. Unfortunately, BMS-181,321 suffer from instability, low clearance from the blood, and high background levels in normal tissues [316]. BRU 59-21 has greater stability *in vitro* and more

rapid clearance *in vivo* than BMS-181,321. This compound has shown good retention in tumours compared to muscle and blood, and has proven suitable for tumour hypoxia imaging, as confirmed by IHC staining [317]. Yutani et al. found a good correlation between ^{99m}Tc-HL91 retention and hypoxia, as measured by the polarographic electrode [318]. Thus, SPECT provides the advantage of being much simpler, less costly to acquire, and the ability to use a wide range of available gamma-emitting isotopes, however, its intrinsic spatial resolution is lower than that of PET.

Overall, PET and SPECT provide highly sensitive, relatively non-invasive information on viable hypoxic cells and can demonstrate O_2 gradients with high sensitivity. However, the use of radioactive compounds, with short half-lives, severely impedes the usage of the technique, as well as the variable uptake of the compounds in patients and tumours. Furthermore, one of the issues with PET markers is that the cells must be hypoxic for a significant period of time to be detected, which means that such markers are more likely to identify chronic rather than acute hypoxia. The major problem facing the application of PET and SPECT hypoxia markers however is one of resolution; often, the voxel size that would be identified in a PET scan is much larger than most of the hypoxic structures, thus the actual PET image does not accurately reflect the true hypoxia heterogeneity at the micro-regional level.

2.3.5 Magnetic resonance (MR) based methods

Having explored the developments, applications, advantages and limitations of electrode, immunohistochemistry, optical and nuclear based techniques for hypoxia analyses and imaging, the following sections will address the final technique: magnetic resonance (MR) based techniques as a major non-invasive technique capable of monitoring anatomy and tumour physiology. The phenomena of nuclear magnetic resonance (NMR) and EPR were discovered in the early 1940s, and was based on similar physical principles of interactions between protons or electrons with electromagnetic fields [319–321]. Notably, EPR spectroscopy utilises paramagnetic species containing unpaired electrons, such as free radicals and transition metals, whereas NMR spectroscopy detects the nuclei of non-zero nuclear spins such as ^{1}H, ^{31}P and ^{13}C. The interactions of these electron or non-zero nuclear species with an applied magnetic field give rise to the characteristic longitudinal (T_1) and transverse (T_2) relaxation times associated with MR based methods.

2.4 ELECTRON PARAMAGNETIC RESONANCE (EPR)

2.4.1 Development of EPR probes for oximetry

EPR is a non-invasive MR based technique, capable of making repeated measurements and provides direct O_2 quantification. EPR is the resonant absorption of radiation by paramagnetic systems in the presence of an applied magnetic field, which causes a separation in the energy fields of the unpaired electrons (i.e. Zeeman splitting [322]). Resonance absorption of electromagnetic radiation occurs when the applied energy exactly matches the energy level separation, and the degree of absorption is proportional to the number of free radicals in the material.

Notably, there are some differences between NMR and EPR. Firstly, as the magnetic moment of an electron is approximately 2000 times larger than that of protons, the extent of the external magnetic field required to separate the energies of the spin state to the same extent as that of protons, is correspondingly 2000 times lower in amplitude. Secondly, the spectral responses of the two spin systems also show some interesting differences. When perturbed from equilibrium by a pulse of radiation (at specific fields from microwave to RF), the spin system of protons returns to equilibrium with characteristic time constants, called T_1 and T_2. For protons, T_1 and T_2 are in the range of 1.0 to 0.1 seconds, and *in vivo* the T_1 and T_2 of protons vary depending on the tissue. In the case of electrons, T_1 and T_2 are occurring very rapidly in the range of 5 microseconds to 10 nanoseconds.

EPR oximetry is based on the paramagnetic characteristics of molecular O_2 which, in its ground state, possesses two unpaired electrons. As mentioned in the working principles of MR, macroscopic magnetisation occur when there is a net absorption of energy upon application of an external magnetic field; this absorption by the electron species is what is monitored by the EPR instrumentation (**Fig. 2-10**) and is converted into an EPR spectrum (**Fig. 2-11**). This spectrum indicates the simulated absorption for a system of electrons in a varying magnetic field. Furthermore, it should be noted, that electrons are not solitary in systems but instead are associated with one or more atoms. This causes several consequences, the most important of which is hyperfine coupling. This phenomenon occurs when the magnetic moment of a nucleus with a non-zero spin affects any unpaired electrons associated with that atom leading to the splitting of the EPR resonance signal into doublets, triplets, etc. This causes spectral lines to be either singular, or with several peaks and troughs.

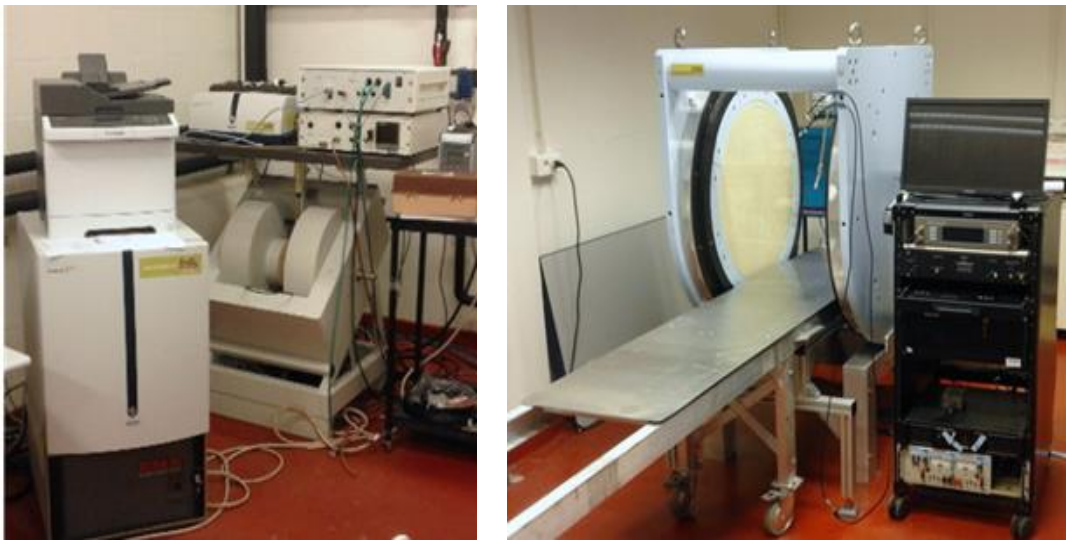

Figure 2-10. Examples of EPR instrumentation used in oximetry. Left: EPR X-band used for *in vitro* samples and, right: EPR clinical L-band used for *in vivo* work.

Importantly, however, EPR cannot measure O_2 itself. In the gas phase, at very low pO_2 (< 1 mmHg) it is possible to record an EPR spectrum of molecular O_2 with a conventional EPR spectrometer [323,324]. However, the T_1 for molecular O_2 dissolved in fluids was found to be 7.5 ps [325], making it much too short for measurement and making the direct measurement of O_2 impossible on current EPR spectrometers. Furthermore, in biological systems, direct EPR measurements cannot be achieved as the spectral lines are so broadened as to be undetectable. Hence the need for paramagnetic spin probes arose, whose measurements depend on T_1 and T_2, and can provide a direct indication of the concentration of O_2 [326,327,336,328–335].

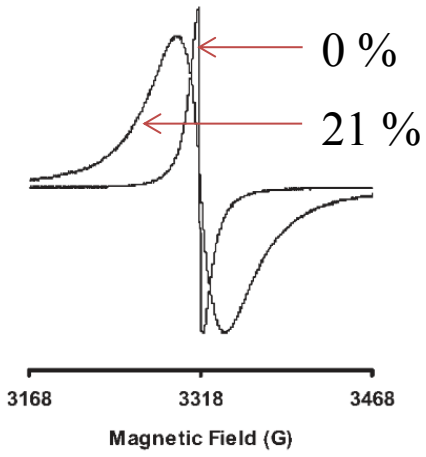

Figure 2-11. Example of EPR spectrum wherein the effect of O_2 on a paramagnetic species is demonstrated. The broad LW spectrum indicates measurement during 21 % O_2 and the thin LW spectrum indicates measurement during 100 % N_2. Image reproduced from Gallez et al. [341].

Another factor influencing EPR spectra is the interactions of unpaired electrons with its environment thus influencing line shape. Biomolecular collisions between O_2 and free radicals alter the resonance characteristics of the radical and consequently the EPR spectrum. Notably, molecular O_2 is an efficient relaxer (i.e. capable of shortening relaxation times) of other paramagnetic species. The enhancement of relaxation times scales linearly with the concentration of O_2, thus measurements that depend on T_1 and T_2 of EPR spin probes can provide a direct indication of the concentration of O_2. The most common method is to use the broadening of the principal hyperfine line (related to T_2). This line broadening occurs by direct biomolecular collisions between two paramagnetic species (with the rate of collision given by the Smoluchowski equation [337]) and by Heisenberg spin exchange [338].

Unfortunately, there is a lack of sufficient amounts of endogenous naturally occurring paramagnetic metal ions and free radicals to be detected directly by EPR *in vivo*. This deficiency makes it necessary to use exogenous paramagnetic materials, but not all paramagnetic substances are convenient for oximetry purposes. The main requirements for a suitable exogenous spin probe for oximetry applications are; a few narrow EPR lines in the EPR spectrum, good stability in biological media, and no pharmacotoxicity issues. Two types of probes are used; soluble probes that report the concentration of dissolved O_2, and particulate probes that measure pO_2 in tissue. Both have certain advantages and drawbacks.

Particulate probes include lithium phatalocyanine (LiPc) crystals and carbon-based products. LiPc aggregates have a single sharp EPR line, the width of which is highly sensitive to pO_2. LiPc crystals are implanted into the tissue of interest and the EPR spectra reflect the average pO_2 on the surface of each LiPc aggregate and enables the measurements of tumour pO_2 using only a few crystals [322,339–341]. Carbon-based materials include coals (such as fusinite [342,343] and gloxy [344]), chars [345,346], and carbon black [347] (India ink). These materials have been extensively used for *in vivo* EPR oximetry, with India ink thus far being the only spin probe approved for *in vivo* clinical use [347–350]. It should be noted that all particulate EPR probes require implantation into the tissue of interest several days before measurements can occur to allow the tissue damage caused by its insertion to be minimised, and can only measure pO_2 content at their site of implantation [339,351,352].

In contrast, soluble spin probes (e.g. nitroxides and triarylmethyl radicals) are chemically well-defined and can distribute evenly in tissues. Among soluble paramagnetic materials, two types of structures are particularly interesting: the nitroxides and the triarylmethyl radicals. Nitroxides are free radicals where the unpaired electron is delocalised

between nitrogen and O_2 and include 2,2,6,6-tetramethylpiperidine 1-oxyl (TEMPO) and 4-hydroy-TEMPO benzoate (TB) (**Fig. 2-12**). A number of different properties of nitroxides can be manipulated. For example, a charged nitroxide will not cross the plasma membrane and thus can be used to measure the concentration of O_2 in the extracellular compartment; a neutral nitroxide will be distributed throughout the intracellular and extracellular environments [353]. Moreover, nitroxides can be linked to carrier molecules to achieve tissue or organ selectivity [354,355]. The effect of O_2 on the LWs of these compounds is modest but sufficient for several applications. For most nitroxides, the LW in the absence of O_2 is approximately 1 Gauss. To increase the sensitivity to O_2, it is convenient to use perdeuterated nitroxides [326,335] for which the LW is lower than 200 mG. It is also possible to use nitroxides with a resolved super-hyperfine structure to increase sensitivity to O_2 [356]. This method is only valid at low O_2 because, at high a concentration of O_2, the super-hyperfine structure is not resolvable. Furthermore, nitroxides have the limitation of being metabolically converted to diamagnetic hydroxylamines thus rendering it unable to produce an EPR signal [357–360]. This limitation is compounded in strongly reducing systems, such as the low pH microenvironment of hypoxic tumours. A possible solution for these shortcomings is to encapsulate nitroxides in lipophilic environments. As O_2 is more soluble in organic solvents than in water, an increase in sensitivity has been demonstrated using these systems [337].

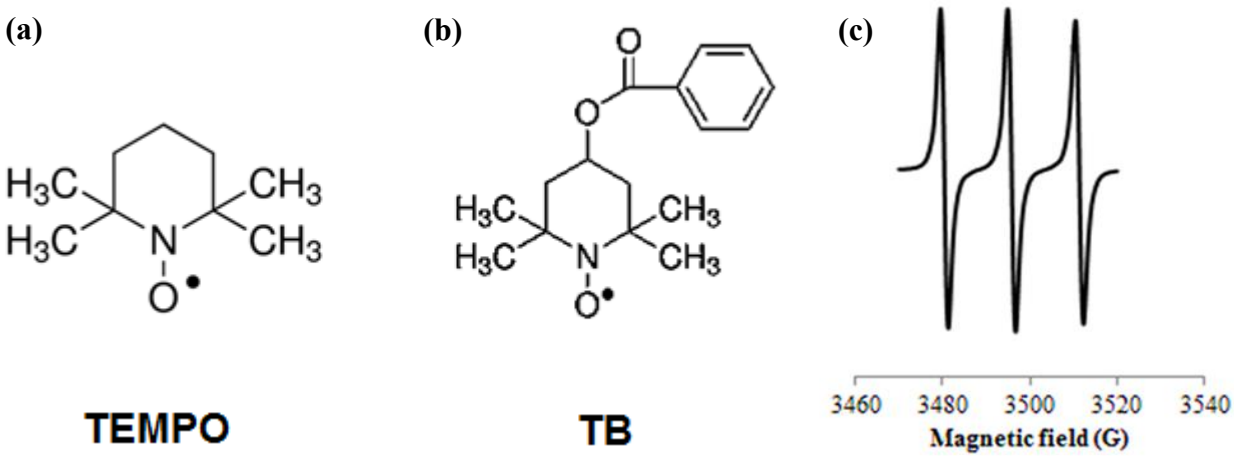

Figure 2-12. Chemical structures of two nitroxides; TEMPO **(a)** and 4-hydroy-TEMPO benzoate **(b)**, and the EPR spectrum of TEMPO under 21 % O_2 showing the characteristic 3 spectral lines of nitroxides **(c)**.

The second interesting group of soluble spin probes are the triarylmethyl (trityl or TAM) radicals. These radicals were first demonstrated by Gomberg in 1900 [361], and were further developed by Nycomed Innovations in the 1990s [362] by eliminating hyperfine coupling with hydrogen nuclei to achieve a single sharp EPR line, and thus became known as tetrathia-TAM radicals (**Fig. 2-13**). Salts of these trityl radicals have good water solubility as well as stability in the presence of reducing agents such as ascorbate and glutathione [363,364]. The EPR spectrum of these compounds displays one single line [365]. An important characteristic of triarylmethyl radicals is the narrowness of their EPR LW (typically less than 100 mG). As the signal intensity is inversely proportional to the square of the EPR LW, the sensitivity of detection is particularly convenient for *in vivo* applications using these compounds. Recent development of triarylmethyl radicals has significantly expanded their potential as O_2-sensitive free radicals in EPR [365–371]. In human blood, the stability of triarylmethyl radicals varies from a half-life of a few hours to one of more than 24 h depending on the particular structure of the compound. However, their oxygen sensitivity is affected by changes in viscosity and pH [364,371]. Additionally, when EPR measurements are performed in biological systems, the spin probes may lose their signal intensity – and thus their oxygen responsiveness – due either to; the removal of the probes from the site of introduction due to the vasculature; or from the interactions with tissues and cells; or by reduction of the unpaired electrons by chemical reactions or protein binding [372,373]. Notably, the presence of several fluorine atoms within the TAM (F15T-03 [374]) radical enable it to be easily emulsified or encapsulated within lipophilic environments which confers an excellent environment for both O_2 solubility and protection from the biological milieu [366,368,375].

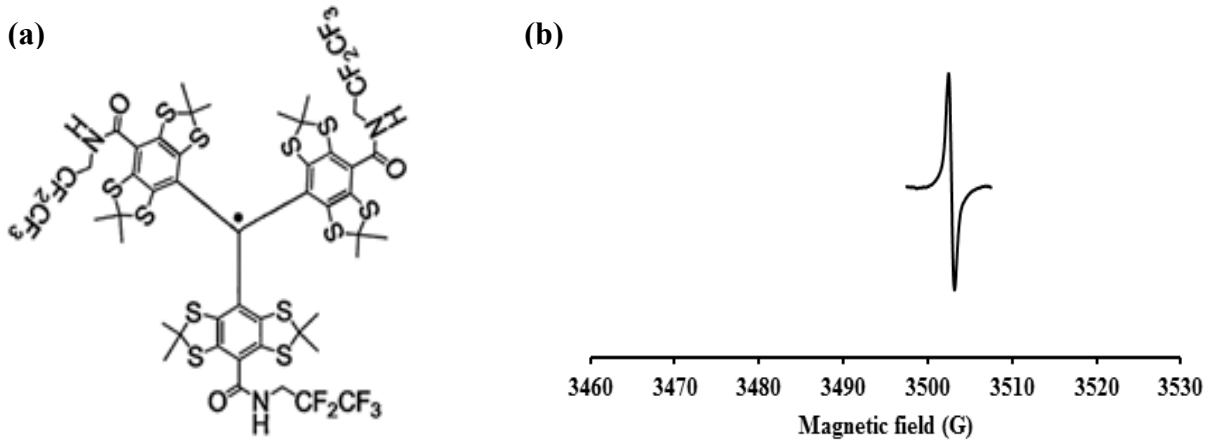

Figure 2-13. Chemical structure of a triarylmethyl EPR radical, namely TAM (F15T-03) **(a)**, and its associated EPR spectra **(b)** in 21 % O_2 showing the characteristic 1 spectral line of a triarylmethyl radical.

2.4.2 EPR oximetry in oncology

EPR oximetry is a technique that can provide repeated assessments of average tumour pO_2 with minimal perturbation to the microenvironment [376], and it has been extensively used for pO_2 measurements in animal models [377–379]. Importantly, EPR oximetry has been used to examine tumour re-oxygenation after radiation treatment in murine tumours [380,381] to determine tumour cure dependency on hypoxic fraction [333,382] and to examine changes in tumour oxygenation in response to vascular changes [383,384]. One of early applications of *in vitro* EPR oximetry was to measure the O_2 consumption rate in tumour cell suspensions [385] and to study O_2 transportation both across and within a lipid bilayer model membrane [338]. *In vivo* EPR applications, however, generally include the study of oxygenation of several tissues and organs (including the brain [386–390], heart [329,391–397], liver [351,398–403], kidney [344,404], gastrointestinal tract [405], skeleton muscles [337,339,342,344,406–410], and skin [347,411,412]) under various pathophysiological conditions (diabetes and wound healing [334,413,414]) of which, by far, the largest application is tumoural oximetry.

In several studies, measurements of tumour oxygenation using EPR have been designed as to show that a specific method or a newly developed paramagnetic material could be applied to tumour oximetry [326,351,408,415–417]. Consequently, EPR oximetry has been compared to other methods that provide direct or indirect measurements of tumour oxygenation, such as; polarographic electrodes [331,418], the distribution of nitroimidazoles [419], perfusion-based MRI techniques [389,420,421], and pO_2 recordings using OxyLite® [384,422,423]. However, since oxygenation is of crucial importance in tumours to predict the outcome of a treatment, and since there is hope for manipulating local oxygenation to improve the efficacy of anti-cancer therapies; many efforts have been developed to apply EPR oximetry for the determination of tumour oxygenation in relation to a treatment regime.

For tumours, the ability to monitor changes in O_2 before and after treatment could have profound implications for the planning of effective treatment strategies [424]. In particular radiotherapy could benefit from modulated treatment based on regional variations in O_2. One way to increase the tumour pO_2 is the breathing of O_2 enriched gas. Generally, carbogen, a gas containing 95% O_2 and 5% CO_2, is preferred to pure O_2 to avoid the vasoconstrictive effects of O_2. Breathing carbogen (possibly combined with nicotinamide administration) is now applied successfully in the clinic together with irradiation [425]. Currently, raising pO_2 by inhalation of hyperoxic gases is the most effective way to decrease diffusion-limited hypoxia. The increase in pO_2 in tumours induced by breathing carbogen (and often

referred to as the carbogen challenge) was shown in several tumour lines using EPR spectroscopy [389,408,426,427]. This effect of carbogen on tumour pO_2 and on tumour regrowth delay is particularly interesting as a positive control for comparing the efficacy of other types of treatments [384,422,423]. Carbogen is also effective in human tumour models and patients as shown by the use of various different measures of tissue oxygenation [252,428–434]. Most studies found a significant decrease in hypoxia irrespective of the tumour type or method used. However, a few studies have observed no effect or even a worsening of the oxygenation status [435,436]. These studies of tumour oxygenation and re-oxygenation using EPR oximetry have been designed using both particulate and soluble spin probes. However, as mentioned previously, both categories have their advantages and disadvantages. In the case of tumour oximetry, a need for new spin probes which can meet the main requirements; excellent O_2 sensitivity *in vivo* with a narrow single EPR spectrum line which linearly corresponds to O_2 concentration, preparations which are stable and consistently produce similar products, good stability in biological media thus presenting no pharmacotoxicity issues, and capable of performing immediate measurements throughout the tumour mass; is of great need. Unfortunately, the particulate spin probes do not meet all these requirements but the soluble spin probes meet several. Both nitroxides and triarylmethyl radicals are chemically well-defined with well-established synthesis protocols, and benefit from being encapsulated as this confers protection to the radical (i.e. avoidance of metabolic conversion) as well as eliminating any possible toxicity the probe might confer to the tissue. Furthermore, nitroxides, such as TEMPO and TB, and triarylmethyl radicals, such as TAM (F15T-03), are capable of being encapsulated within a lipophilic environment (determined by their partition coefficient [log P] value) which is highly advantageous as this increases the sensitivity of the EPR radical because O_2 is highly soluble in lipids. A suitable encapsulation device is thus a priority. Several studies have involved the encapsulation of nitroxides within various carriers including microspheres, micelles, liposomes, and dendrimers [437–444], as well as the emulsification and encapsulation of triarylmethyl radicals in various organic materials including perfluorocarbons, liposomes, and even hydrogels [439,445–449]. These studies all indicate that the EPR radicals benefit from encapsulation. However, not all these encapsulation and emulsification methods can be applied *in vivo* as some concerns of biosafety [450] and sensitivity have been noted.

It is thus, to this end, that this body of work introduces the use of the biocompatible nanocarrier lipid nanocapsules (LNCs) as an encapsulation tool in **section 2.6**.

2.5 MAGNETIC RESONANCE IMAGING (MRI)

2.5.1 Development of MRI for determining oxygenation

MRI is based on the ability of hydrogen atoms to align and spin around an applied magnetic field, ŏ Upon application of a transverse RF pulse (ŏ, these protons are perturbed from ŏ The subsequent process through which these protons return to their original state is referred to as relaxation. Two independent processes, T_1 relaxation and T_2 relaxation, can be monitored and converted to generate an MR image. Notably, local variation in relaxation is due to the chemical and physical nature of the sample. In the case of T_1 relaxation – also termed spin-lattice or longitudinal relaxation – these perturbations are thermal based, in that they involve the transfer of energy from the nuclear spins to the surrounding molecular environment, which results in the recovery of the longitudinal magnetisation to its equilibrium. This energy transfer occurs because there are fluctuating fields associated with the 'lattice' or surrounding molecules. Conversely, T_2 relaxation – often called spin-spin relaxation – occurs due to internuclear and electron-nuclear interactions which result in the exponential decay of the transverse magnetisation. In a system of identical non-interacting nuclei such decay would not occur but, in reality, different nuclei precess at slightly different frequencies as a result of interactions between neighbouring nuclei, thus leading to a loss of overall transverse magnetisation. Notably, this decrease in signal occurs rapidly because the local magnetic field is always heterogeneous; either because the applied field is non-uniform or because of spatial variations in magnetic susceptibly. This is taken into account by another relaxation time, T_2*, and its relaxation is governed by the free induction decay (FID) resulting from the inhomogeneities of the magnetic field.

MR procedures for measurement of the oxygenation status of tumours have the advantage of allowing the assessment of hypoxia in deep-seated tumours in a non-invasive manner which does not disturb vasculature, and enables repeated measurements. MR techniques for hypoxia determination include perfusion and probe-based (both exogenous and endogenous) imaging and spectroscopy.

2.5.1.1 Perfusion-based MR methods

BOLD, or blood-oxygen level dependent, contrast is a functional MRI method able to measure blood oxygenation using gradient echo sequences sensitive to changes in transverse decay (also known as the effective T_2 or T_2*) [451]. Originally, the BOLD approach was

developed to investigate cerebral activity but, recently, its use has been extended to the assessment of tumour oxygenation in response to hyperoxic gas challenges (e.g. carbogen) [296,452]. BOLD-MRI relies on red blood cells to be delivered to the tissue of interest and provide information regarding tissue oxygenation [453] and is based on the paramagnetic nature of deoxyhaemoglobin; as the O_2 saturation of the haemoglobin increases, the iron within the haeme subunit changes from a paramagnetic high spin state, under low pO_2, to a diamagnetic low spin state under high pO_2. Therefore, changes in deoxyhaemoglobin content in blood will influence water relaxation (particularly T_2*), enabling blood oxygenation levels to be measured by MRI. Thus, BOLD-MRI is sensitive to oxygenation variation in the vascular compartment [454], as well as having high spatial and temporal resolution [455]. The major drawback, of course, is that BOLD does not provide actual pO_2 data but rather the change of O_2 tension in the vasculature, which is not directly correlated to blood oxygenation in tissue with poor blood perfusion such as in solid tumours and implantations [456]. Furthermore, a quantitative relationship between the BOLD effect and pO_2 has not been found, due to the complex relationship between these two parameters [457]. Indeed, in addition to oxygenation, the BOLD effect is influenced by other factors, including blood flow, haemoglobin levels, haematocrit levels, vasculature, temperature, and pH [454,455,457–459]. These circumstances prompted the use of FLOOD (flow and oxygenation dependent) to refer to the BOLD experiment when tissue oxygenation is measured and applied to the study of oxygenation in tumours [454].

Dynamic contrast-enhanced imaging techniques (DCE-MRI) characterises the physiological microenvironment of tumours via the uptake of contrast agent into tumour tissue. This imaging technique relies on repeated image acquisition before, during, and after the intravenous administration of a low-molecular-weight contrast agent, such as gadolinium-based (e.g. Gd-DOTA) [460]. DCE can be combined with computer tomography (CT) which enables the monitoring of temporal changes in the contrast enhancement. These changes can provide information regarding the perfusion, relative blood volume, and the microvasculature of the tumour [461]. DCE-MRI parameters reflecting heterogeneous tumour perfusion and subtle tumour volume change early during treatment were better predictors of tumour recurrence and death than clinically accepted prognostic factors (e.g., stage, lymph node status, and histology) [462]. From a clinical standpoint, several trials have investigated the relationship between various MRI parameters and more-specific markers of hypoxia [453,463–467]. DCE–MRI is the only MR technique whose measurements have been correlated with

radiotherapy outcome for patients with cervical tumours, concluding that patients with hypoxic tumours has a worse response to radiotherapy [468–470].

DCE-MRI is a rapid, minimally invasive technique with which repeated whole body imaging can be performed enabling the tracking of tumour heterogeneity with sub millimetre sized voxels for easily tracking chronic and acute hypoxia. However, although this technique has been used both pre-clinically and clinically, the technique provides only descriptive data pertaining to blood flow within the vascular compartment but not pO_2 measurements – much like BOLD. Furthermore, as with all the perfusion techniques, a complicated relationship between oxygenation, blood flow and blood supply exists in solid tumours, which must be accounted for using pharmacokinetic modelling to correctly interpret results.

2.5.1.2 Probe-based MR methods

Probe-based MR techniques include the use of exogenous probes (e.g. perfluorinated compounds [PFCs]) and endogenous probes (e.g. metabolic markers and lipids). PFCs are organic molecules, in which all the hydrogen atoms have been replaced by fluorine atoms, hence providing strong ^{19}F MR signal. PFCs possess a series of properties making them very suitable as an MR contrast agent [162], in particular they are; biologically inert, exhibit minimal toxicity, and are commercially available. Parhami and colleagues were the first to demonstrate that at a given magnetic field and temperature a linear relationship exists between ^{19}F MR T_1 relaxation of PFCs and O_2 tension, a circumstance attributed to the paramagnetic nature of O_2 [471]. The same paramagnetic effect has been reported in other molecules, including water [472–474]. However, in the latter case, many other factors, including metal ions, pH and temperature, also induce changes in water relaxivity *in vivo*, making the results observed more difficult to interpret exclusively in terms of pO_2 variations. In contrast, T_1 of PFCs is not usually affected by hydrophilic charged species [475] as these hydrophobic molecules do not mix with the surrounding aqueous phases, instead forming droplets that inhibit ions from entering the hydrophobic core [476]. Notably, O_2 solubility is greater in PFCs than in water, meaning these compounds could be considered as molecular amplifiers of O_2 tension but the differences in O_2 solubility between PFCs and the surrounding medium, pO_2 between both phases will become the same after a short (usually seconds) equilibration interval [473]. As a consequence, PFCs exhibit high sensitivity to O_2 changes and their detection and have been investigated for the measurement of oxygenation *in vivo* using O_2 maps

[473,477,478]. Standardisation of PFC probes for oxygenation determination in tumours have been attempted with microelectrodes but discrepancies have been found [479–481].

Several PFCs have been developed, including the cyclic hexafluorobenzene (HFB) [482] and perfluoro-15-crown-5-ether (PFCE) [483–485] (**Fig. 2-14**). The main limitation for HFB involves its relatively long T_1 relaxation rate, especially under hypoxic conditions, a circumstance which increases the acquisition time and causing potential data loss in hypoxic voxels. Two strategies were developed to circumvent this limitation, including two new procedures called alternating relaxation delays with variable acquisitions for reduction of clearance effects (ARDVARC) [486], and fluorocarbon relaxometry using echo planar imaging for dynamic oxygen mapping (FREDOM) [473], both to improve the efficiency and precision of the measurements [487]. Furthermore, a snapshot inversion recovery pulse sequence has been developed which allows for very fast HFB oxygenation mapping (~1.5 min) without sacrificing precision or spatial resolution [481].

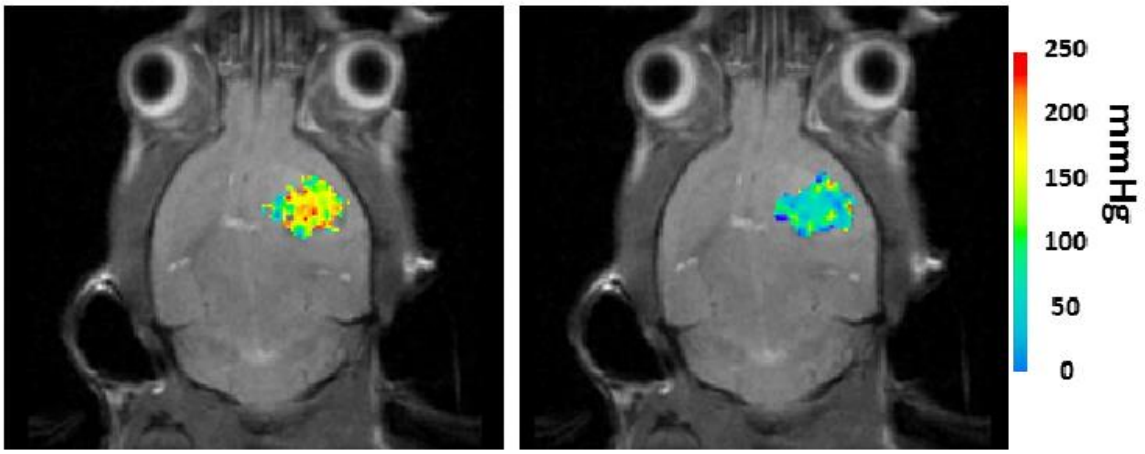

Figure 2-14. Measurement of tumour hypoxia (in mmHg) within a mouse brain after a single injection of a perfluorocarbon (perfluoro-15-crown-5-ether; PFCE) loaded within lipid nanocapsules (LNCs).Image reproduced from Lemaire et al. [485].

An important issue obstructing the use of PFCs is their method of administration. Initially, PFC emulsions were injected intravenously, but, under these conditions, most of the fluorinated agent becomes sequestered in the liver and spleen [488]. Even when sufficient PFC is present, measurements may become biased towards well-oxygenated values, as PFC is preferentially sequestered in the well-perfused zones [477,489]. Another option is the direct administration of the pure PFC at the site of measurement [473]. This ensures high PFC

concentration and spatial distribution, but can cause oedemas and haemorrhaging at the injection site. These two approaches allow pO_2 determination only during a limited period of time because of the clearance of PFCs; hours for HFB [487], days for perfluorooctylbromide [490], and weeks for perfluorotributylamine [491]. A third approach involves the encapsulation of the PFC in an oxygen-free diffusible material which allows for long-term measurements of pO_2 at the site of implantation [492]. The method, although promising, suffers from spatial resolution loss at measurements are restricted to only the area of implantation. Another type of probe developed for detecting tumour oxygenation by ^{19}F MRI comprises fluorinated-2-nitroimidazole compounds including hexafluoromisonidazole [493], EF5 [494], and SR-4554 [495]. SR-4554 has shown good results at detecting hypoxia in a Phase I clinical study by Lee et al. [495], and is being further developed for the detection of tumour hypoxia in some patients. However, the toxicity profile of nitroimidazole drugs is the major drawback; misonidazole showed neuropathy and acute central nervous system toxicity [496]. To circumvent some of the issues presented by PFCs, Kodibagkar et al. [474] developed a proton analogue to PFCs, hexamethyldisiloxane (HMDSO), as a novel ^{1}H MRS oximetry probe. HMDSO shares some important properties with PFCs: it is highly hydrophobic and non-toxic, shows high O_2 solubility, is biochemically inert *in vivo*, and is readily available and relatively inexpensive [497]. However, HMDSO also presents some disadvantages when compared with PFCs, mainly because of the strong background signal in ^{1}H NMR, a circumstance not occurring in ^{19}F NMR. To this end, proton imaging of siloxanes to map tissue oxygenation levels (PISTOL) was developed [498] but was hindered by poor spatial resolution.

Overall, PFCs enable the dynamic imaging and mapping of pO_2 in tumours but the utilisation of ^{19}F oximetry requires that clinical scanners are equipped with a specific ^{19}F-tuned probe. Furthermore, PFCs are subject to flow artefacts and the oxygen sensitivity of some ^{19}F MR imaging compounds are easily affected by temperature, dilution, pH, common proteins, and blood [499]. After intravenous injection, the majority of the PFC contrast agent is extensively ingested by the reticuloendothelial system (RES), and the slow clearance can have adverse effects. Intratumoural injection can also be risky as PFC emulsions could accidentally be injected into tumoral vein, leading to embolism [486]. Furthermore, although the technique allows for high anatomical resolution it cannot distinguish between necrotic areas and offers low sensitivity.

To circumvent the need for specially equipped scanners and the introduction of an exogenous probe for oximetry imaging, endogenous nuclei have been explored including the

change in water T_1 relaxation rates in tissues and CH_2 in the form of lipids. This technique includes the use of oxygen-enhanced MRI (OE-MRI). OE-MRI relies on the quantification of variation in water T_1 relaxation rate by the paramagnetic change in O_2 dissolved in blood plasma, interstitial tissue fluid and intracellular water under 100 % O_2 breathing. This technique can identify spatial heterogeneity in tumour hypoxia for renal [500] as well as murine glioma and human glioblastoma multiforme carcinomas [501]. OE-MRI enables repeated measurements with assessment of chronic and acute hypoxia. However, although the anatomical spatial resolution is well-defined and is not influenced by perfusion changes in the vascular compartment or haematocrit (such as BOLD); the technique is unable to identify necrotic regions, and relies on the use of hyperoxic gases which can be vasoactive and lead to difficulty in interpreting results. Furthermore, this technique is severely hindered by the heterogeneity of tumours; regions of tumours do not respond to gas challenges as the vasculature has collapsed making the gases inaccessible to the tumour [502].

It was to address this gap in tumour oxygenation determination that the use of CH_2 in the form of endogenous lipids were used to map oxygenation by T_1 relaxation rates (MOBILE; mapping of O_2 by imaging lipids relaxation enhancement) was developed.

2.5.2 Mapping of O_2 by imaging lipids relaxation enhancement (MOBILE)

While T_2* is sensitive to the relative changes in Hb/HbO_2 in vessels (exploited in BOLD [162,503]), it cannot provide a quantitative relationship between signal intensity and true changes in tissue pO_2. Likewise, although the OE-MRI method provides an alternative to the BOLD method as a non-invasive method for measuring O_2 level variations, unfortunately this technique suffers from poor sensitivity, and changes to relaxation times not only related to O_2 level but rather to alterations in blood flow and tissue H_2O content [504]. Arguably, methods which rely on measuring changes in tissue O_2 concentrations by monitoring the T_1 relaxation rate of water could be considered not sensitive enough [323,504,505].

Thus, Jordan and colleagues developed an MRI sequence which exploited the higher solubility of O_2 in lipids than in water [506]. The group demonstrated that the R_1 ($=1/T_1$) of lipids was more sensitive than the R_1 of water to variations in tissue oxygenation. In this technique, because dissolved O_2 acts as a T_1-shortening agent [507], monitoring the change in the R_1 relaxation rate of the lipid peak instead of the water, enabled the mapping of O_2 by imaging lipids relaxation enhancement (MOBILE [508]) (**Fig. 2-15**).

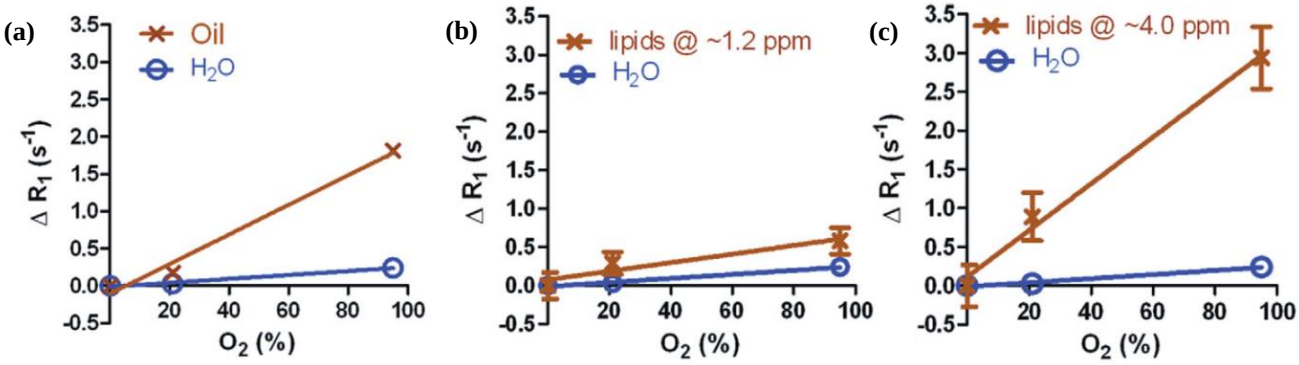

Figure 2-15. Relationship between changes in R_1 ($=1/T_1$) as compared to changes in pO_2 *in vitro* in **(a)** water and **(b & c)** pure oil measured at different chemical shifts (i.e. **[b]** 1.2 ppm and **[c]** 4.0 ppm). Image reproduced from Jordan et al. [508] .

The MOBILE sequence involves a segmented inversion-recovery fast imaging steady state precession (IR FISP) sequence [509]. This sequence can be used to acquire the time course of longitudinal magnetisation during its recovery after a single inversion pulse. Notably, most methods of T_1 quantification techniques are based on measuring the longitudinal magnetisation at different time intervals after an inversion or saturation pulse but such T_1 estimations are often erroneous because the excitation pulses perturbs the exponential recovery of T_1. However, for MOBILE, this is compensated for as the signal is acquired

continuously during its recovery using a fast low-angle snapshot (FLASH) sequence, and a series of images are obtained at different inversion times. To determine the T_1 relaxation of each pixel within the region of interest, Jordan and colleagues, used a home-made MatLab® script to fit the raw data acquired from the images according to the following equation wherein the relaxation behaviour of the magnetisation M_z is a function of the inversion time (TI):

$$M_z(TI) = A - B\exp(-TI/C), \text{ with}$$

$$A = M_0(T_1^*/T_1),\ B = M_0(1 + T_1^*/T_1), \text{ and } C = T_1^*$$

Here, the Look-Locker correction [510] is applied to calculate T_1 from the effective T_1 of the tissue, T_1^* with $T_1^* < T_1$. This correction is implemented to compensate for the T_1 shortening induced by imperfect inversion pulses. The T_1 is then calculated for each pixel using the following equation:

$$T_1 = T_1^*(B/A - 1).$$

In vivo assessment was achieved using several models of pathogeneses including severely hypoxic tumours, peripheral ischemia, cerebral ischemic stroke, and liver steatosis. The group also used normal human volunteers to demonstrate oxygenation mapping of adult brains before and after a hyperoxic carbogen challenge. Using MOBILE, the researchers were able to show the much greater sensitivity of the R_1 of lipids than water to O_2 variation, and succeeded in determining pO_2 values, comparable to OxyLite® and EPR oximetry methods, for all *in vivo* models (**Fig. 2-16**).

In fact, for the tumour oxygenation experiments, the R_1 of lipids was more sensitive to O_2 variation by a factor of 4.8 as compared to the R_1 of water. Notably, the correlation within the same tumoural experiments between the R_1 of H_2O and pO_2 was not significant, whilst a positive linear significant relationship was found for the R_1 of lipids and pO_2. Unfortunately, however, the MOBILE technique can only be applied to tissues which contains lipids at a sufficiently high enough intrinsic content. In the case of the aforementioned study, the mean value of total lipid content for human embryonal carcinoma-induced tumours at 6 mm in length was 106.1 ±20.4 μg/mg, and the normal adult human brain was 93.6 ±11.8 μg/mg. Thus, a signal-to-noise ratio (SNR) limitation is apparent; a sufficiently large enough amount of lipids is required in the tissue of interest otherwise the signal acquired by the MOBILE sequence would not be able to discern the lipid R_1 on a pixel-to-pixel basis as voxel size in MRI are limited. Thus, if no lipids, or insufficient amounts of lipids, occur in the tissue then

no oxygenation mapping could be determined or a very poor resolution of the map would be produced.

Thus, considering the potential use of MOBILE for mapping oxygenation *in vivo*, this body of work introduces the use of the highly lipidic nanoparticle, lipid nanocapsules (LNCs).

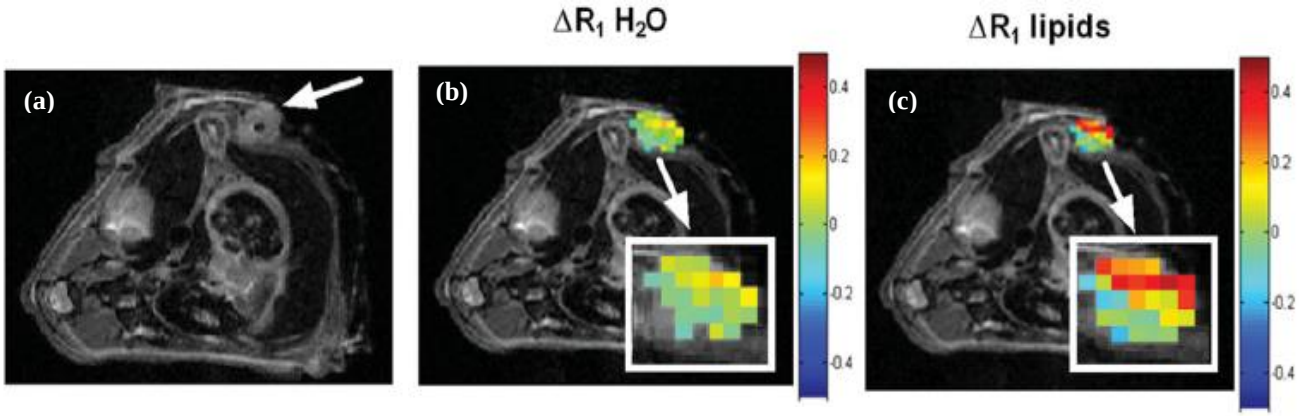

Figure 2-16. The sensitivity of the MOBILE sequence to variations in tumour oxygenation. Notably, **(a)** illustrates the anatomical transverse MR image of a mouse with a tumour (shown by arrow), wherein the dark spot within the tumour shows where the tip of the OxyLite® probe is situated. Following the carbogen gas challenge, maps of changes in relaxation times ($\Delta R_1 = R_{1\ carbogen} - R_{1\ air}$) in response to the challenge can be produced using the MOBILE sequence **(b & c)**. Colour scales highlight the higher sensitivity of the MOBILE technique wherein a higher proportion of the pixels are in the red zone indicating a greater change in R_1.

2.6 LIPID NANOCAPSULES (LNCS)

2.6.1 Formation and development of LNCs

Nanotechnology has emerged as an outstanding tool for the development of technologies for diagnosis, treatment and prevention of cancer [511]. Their applications in cancer treatment include molecular imaging, early detection, diagnosis, targeted therapy, overcoming drug resistance, and cancer bioinformatics [512–520]. Several nanomaterials have been developed as bioanalytical platforms in cancer for the detection, measuring and/or imaging of pH [521], apoptosis [522,523], ROS [524–526], and oxygen. Bioanalytical sensors specifically designed for oxygen determination include inorganic (e.g. quantum dots) and organic (e.g. polymer-based) nanoparticles which can be conjugated with phosphorescent metalloporphyrins [262,527–530] or near-infrared oxygen-sensitive dyes [531,532], wherein the nanoparticles can be embedded in hydrophobic matrices (such as organically modified silica) [533–536] or encapsulated into liposomes [537] or micelles [538]. An interesting application of nanotechnology is the preparation of dual-purpose nanomaterials used for simultaneous diagnosis and therapy. This dual-purpose targeted research has given rise to a new term: theranostics [539–542]. It is assumed that a combined technique will result in the acceleration of drug development, improved disease management, reduced risks and reduced cost.

Nanocarriers for drug delivery generally consist of 2 main components: the nanoparticle itself, which is used as the carrier agent, and the drug [543]. The drug can either be adsorbed, dissolved, or dispersed throughout the nanoparticle complex or, alternatively, it can be covalently attached to the surface. Studies using paclitaxel have shown that when compared with the conventional formulation, the nanoparticle formulation of the drug increases both its cytotoxicity profile in cell culture and its therapeutic efficiency in a living animal model [544]. This has been attributed to the nanoparticle formulation having greater bioavailability and a longer sustainable therapeutic time, which allows the drug concentration to remain above the minimum effective value for an extended period of time. There are several types of nanoparticle systems that have been used as carriers including liposomal [545,546], solid lipid [547–549], polymeric [550–552], mesoporous silica [553–555], and inorganic nanoparticles [556,557]. Among these carriers, Heurtault and colleagues [558–560] developed a nanoparticle characterised as a hybrid between polymer nanocapsules and liposomes called lipid nanocapsules (LNCs). These nanoparticles are classified as spherical, nanometre-sized biomimetic colloidal lipid emulsions, the core of which is composed of an oil surrounded by a thin amorphous shell (**Fig. 2-17**). These nanoparticles can be prepared in various sizes using

the low-energy phase inversion temperature (PIT) method which employs no organic solvents.

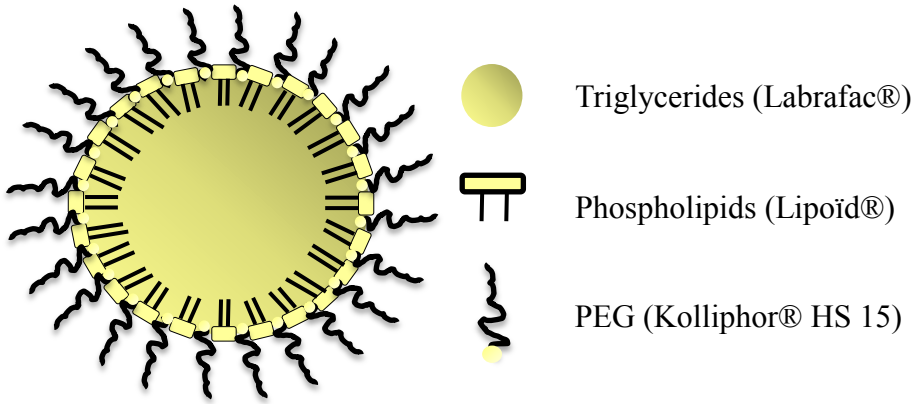

Figure 2-17. Schematic of the nanoparticle named LNCs including its constituent components.

LNCs are composed of a medium chain triglyceride core (i.e. lipids) known under the commercial name of Labrafac®, surrounded by a thin capsule consisting of non-ionic and amphiphile surfactants. This lipidic core is responsible for the size of the LNCs, as well as providing the oily reservoir in which lipophilic drugs are encapsulated. The surfactants of the system, both the non-ionic Kolliphor® and the lipophilic Lipoïd®, are the major influencers of LNC formation and stability [561,562]. Additionally, Kolliphor® provides a shell separating the loaded agent from the outside environment by a coating of polyethylene glycol (PEG) [561,563]. PEG is widely used material, as its addition lends increased stability to nanoparticles in biological fluids by creating a dynamic cloud of hydrophilic and neutral chains at the surface that reduces protein opsonisation, thereby preventing rapid clearance from the circulation system by mononuclear phagocytic cells from the RES [564,565]. A major drawback often arising in intravenous injection of drug carriers is the RES recognition of the nanoparticles and their subsequent removal from the vasculature system and accumulation in the liver and spleen. The PEGylation of a nanoparticle's shell thus serves to minimise the interaction of the nanoparticles with the RES by repelling plasma proteins [566], achieving the so-called Stealth® nanosystems [567–571]. This enables LNCs to have an increased half-life within the blood and cross certain biological barriers [572]. Notably, all the constituents of LNC synthesis are biocompatible and FDA approved.

During the phase inversion temperature (PIT) process (**Fig. 2-18, a**), a mixture of Kolliphor®, Lipoïd®, Labrafac®, NaCl and water (the proportions of which vary according

to the study) is heated under magnetic stirring from room temperature to 95 °C. This temperature is above the PIT and thus a water in oil (w/o) emulsion is obtained. This is followed by cooling to 50 °C (thus below the PIT) leading to the formation of an o/w emulsion. This temperature cycling is repeated several times, crossing the phase-inversion zone (PIZ) between high temperature and cooling repeatedly. During the final cooling phase, an irreversible cold dilution (4 °C) is added to the mixture during the PIZ (i.e. approximately 72 °C). This is done to break the microemulsion system obtained in the PIZ, and leads to the formation of stable nanocapsules [573]. Therefore, the formulation process is a function of the physiochemical properties of the components since the cycling of the temperature during the PIT method increases the quality of the nanoemulsions in terms of size and PDI by increasing the amount of surfactant at the water/oil interface [574]. Furthermore, it was necessary for the LNC formulation to be osmotically adjusted for *in vivo* administration in this thesis [562,575]. This involved the dialysis of the LNC formulation (MWCO = 100 kDa) with magnetic stirring, and occurred over several hours with continual water changes to allow for the maximal escape of the free components. Then, to reobtain the original concentration of LNCs, evaporation with N_2 was performed (**Fig. 2-18, b**).

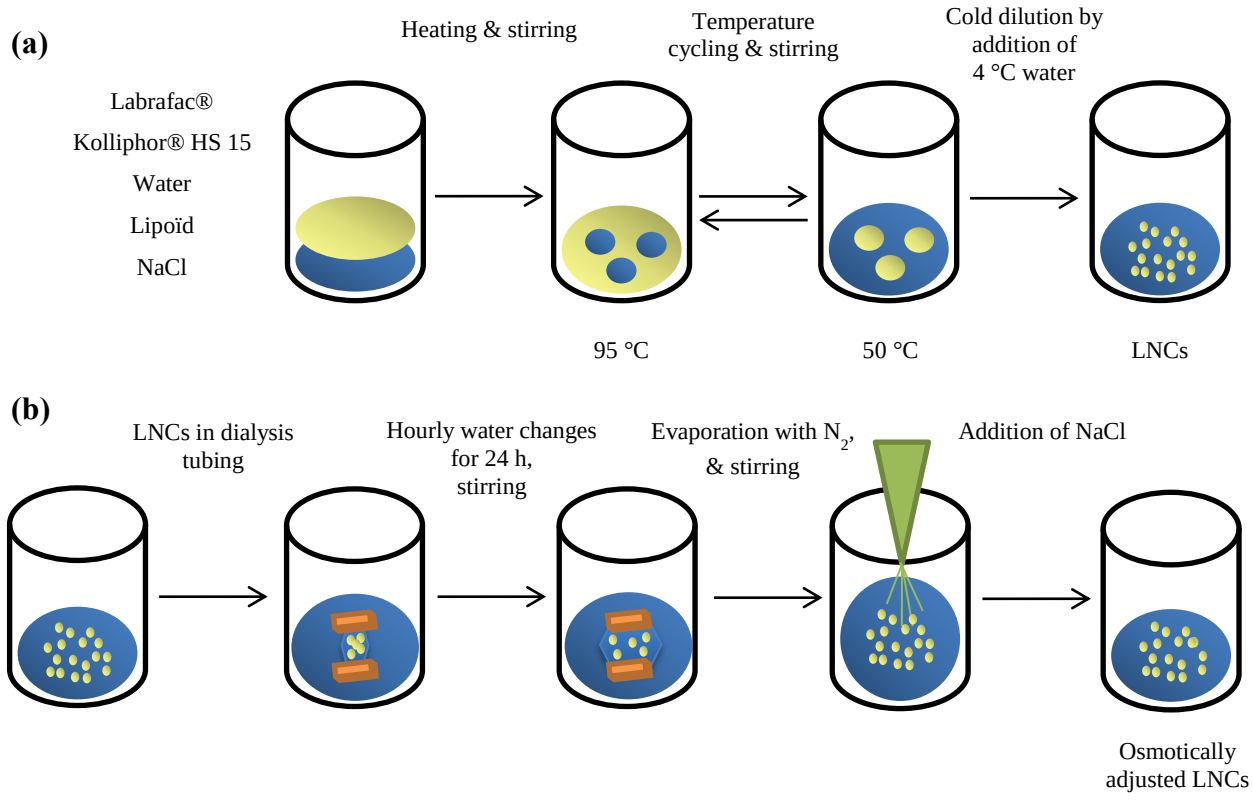

Figure 2-18. The use of the phase inversion temperature (PIT) method to formulation lipid nanocapsules (LNCs) **(a),** and their osmotic adjustment **(b)** for *in vivo* use.

Due to their very small size, in the range of 10 – 100 nm, and their capacity to encapsulate lipophilic agents, LNCs have undergone extensive investigation as drug carriers for improving therapeutic agent delivery [558,573,576–580]. LNCs have been applied to treatment of tumours by delivering known anti-cancer agents, such as docetaxel, paclitaxel, etc., loaded within the nanoparticles to malignancies including breast cancer, melanoma, small cell lung cancers, metastatic cancers, and most notably, glioblastomas [568,581–588]. Glioblastomas are highly malignant, aggressive and drug-resistant malignancies of the central nervous system which are often associated with high morbidity and mortality, and dismal prognosis [589–591]. Numerous studies involving LNCs loaded with various anti-cancer drugs specifically for glioblastoma treatment have been published [583–585,592–598]. These treatments have explored various strategies, including; passive [594,599–602] and active [586,592,603–605] targeting, direct introduction of the drug-loaded LNCs into the glioblastoma tumour using a convection-enhanced delivery (CED) protocol [585,606], the use of hydrogels imbedded with various drug-loaded LNCs specifically to address the recurrence issue of glioblastomas [596,597,607,608], as well as the introduction of drug-loaded LNCs into stem cells used for migration through the blood-brain-barrier for targeting glioblastoma [593,609]. LNCs have also been employed as carriers; to enhance the effect of radiopharmaceuticals for cancer treatments [594,610–612]; to test novel anti-cancer and cancer associated-symptom drugs including curcumin, artesunate, etc. [560,595,598,608,613–616]; as an oral [617,618] and aerosol [619] delivery nanomaterial; and as a diagnostic tool for monitoring hypoxia in glioblastomas [485]. All of these advances have been due to several factors of LNCs. Firstly, LNCs are synthesised with an organic solvent-free formation process using biocompatible constituents which are all FDA approved for oral, topical and parenteral *in vivo* administration in both animal models and human patients [620,621]. Also, LNCs exhibit adjuvant effects, such as the inhibition of the plasma membrane multi-drug resistance pump (such as glycoprotein P; P-gp), and generally have a slightly negatively charged surface, due to the phospholipid molecules and the presence of PEG dipoles in their shell. This enables the LNCs to cross membranes, become internalised within cells, and enables endo-lysosomal escape (ensuring the nanoparticles are not destroyed by the cells) thus offering increased bioavailability and protection of the LNCs' payload, as well as enabling the nanoparticles to avoid the immune system. LNCs also have an excellent drug loading capacity, as their oily core allows for the encapsulation of lipophilic and amphiphilic drugs, agents or compounds. Lastly, and most importantly for this thesis, LNCs have been shown to be permeable to O_2 [485].

Chapter 3:

Electron Paramagnetic Resonance and Lipid Nanocapsules

3.1 INTRODUCTION TO CHAPTER 3

From reviewing the literature in Chapter 2, it is apparent that EPR is an excellent tool for investigating tumour hypoxia as it is capable of providing non-invasive and repeatable oxygen measurements [341,622]. The application of EPR oximetry is accomplished through the use of paramagnetic spin probes. As described, two classes of oxygen-sensitive EPR spin probes have been developed both of which have certain advantages and drawbacks. In particular, soluble spin probes (e.g. nitroxides and trityl) have been chemically well-defined and demonstrated to distribute well within samples [322] but suffer when used in biological media due to signal intensity loss (from metabolic conversion and/or washout from the tissues) [373,623].

In this chapter, these limitations were addressed by the encapsulation of spin probes within LNCs. Encapsulation would provide several advantages including; improving the oxygen sensitivity [337,447,624,625], creating a defined microenvironment for the spin probe ensuring specificity, and providing a shell which might protect from bio-reductants [337,363,626] as well as prevent biocompatibility issues. In this regard, LNCs was good a candidate as not only could they provide the aforementioned advantages, but they are prepared using FDA approved constituents and have previously been employed in several studies of tumour therapeutics as an encapsulation agent (see **Chapter 2**). Thus, the incorporation of EPR spin probes within the oily-core of the LNCs were hypothesised to be able shield the spin probe from the tissue environment and provide an oxygen permeable shell, thus enabling the oxygen sensing mechanism of the EPR probe loaded-LNCs.

In this chapter, published data regarding the synthesis, characterisation and development of trityl-loaded LNCs as an EPR oxygen nanosensor is presented in **section 3.2**. The trityl-loaded LNCs (referred to as TAM-LNCs) were evaluated *in vitro* and *in vivo* to determine its O_2 sensing capabilities, and included the use of two animal models representing normal-functioning tissue and pathological tissue, i.e. subcutaneous fibrosarcoma. This tumoural model has well-characterised vasculature, a known response to the carbogen gas challenge, and established pO_2 values previously measured by EPR [384,422,627]. In **section 3.3**, unpublished data regarding the findings from the article in section 3.2 are presented. Herein, the kinetics of the TAM-LNCs within *in vivo* models is investigated regarding the sensor's pO_2 sensing reversibility and the possibility of an O_2 reservoir effect occurring *in vivo*.

3.2 ARTICLE

This section includes the article **Preparation and evaluation of trityl-loaded lipid nanocapsules as oxygen sensors for Electron Paramagnetic Resonance oximetry** published in the International Journal of Pharmaceutics (DOI: 10.1016/J.IJPHARM.2018.11.007).

Preparation and evaluation of trityl-loaded lipid nanocapsules as oxygen sensors for Electron Paramagnetic Resonance oximetry

Janske NEL [a,b], Céline M. DESMET [b], Benoit DRIESSCHAERT [b], Patrick SAULNIER [a], Laurent LEMAIRE [a] and Bernard GALLEZ [b*]

[a]*Micro et Nanomedecines translationnelles, MINT, Université Angers, INSERM 1066, CNRS 6021, 4 rue Larrey, Angers, France*
[b]*Biomedical Magnetic Resonance Unit (REMA), Louvain Drug Research Institute, Université catholique de Louvain, Avenue Mounier 73 bte B1.73.08, 1200 Brussels, Belgium*

Abstract

Oxygen is essential in physiology and pathophysiology. Electron Paramagnetic Resonance (EPR) oximetry, using oxygen sensitive paramagnetic materials, could be attractive for measuring oxygen in tissues. The aim of the present study was to assess the properties of lipid nanocapsules (LNCs) loaded with the nitroxide tempo-benzoate (TB) or tetrathiatriarylmethyl (TAM) radicals. LNCs loaded with the EPR probes were successfully prepared by the phase inversion process leading to nanocapsules of about 60 nm. LNCs protected the TB radical against reduction *in vitro*. The calibration of the EPR line width (LW) as a function of the pO_2 showed a two-fold increase in sensitivity with TAM-LNC compared to hydrophilic trityl radical. The TAM-LNCs were evaluated *in vivo*. Contrarily to unencapsulated TAM, for which a rapid decrease in EPR signal was observed, the half-life of TAM-LNCs administered in muscles or in tumours exceeded an hour. Carbogen-challenges in mice demonstrated that the TAM-LNCs responded well to changes in oxygen environment. However, the apparent pO_2 values acquired were higher than the expected physiological values. These results warrant further investigation in the formulation of stable nano-objects encapsulating EPR oxygen sensitive probes.

Keywords: Electron paramagnetic resonance, oximetry, hypoxia, lipid nanocapsules, trityl, nitroxide

1. INTRODUCTION

Tissue oxygenation is a key parameter in physiology and pathophysiological conditions, including wound healing, ischemia, peripheral vascular disease and cancer. In oncology, tumour hypoxia is known to decrease the response to radiation therapy [127,628], decrease the efficacy of cytotoxic drugs [129,629], and play a pivotal role in malignant progression including metastasis (reviewed in [4,101,630–633]). Therefore, appropriate knowledge of tumour oxygenation may help in guiding anti-cancer treatments. An assortment of different techniques has been developed for measuring tumour oxygenation, including electron paramagnetic resonance (EPR) oximetry. EPR oximetry is capable of producing real-time, repeated measurements of partial pressure of oxygen (pO_2) values in a non-invasive manner without consuming O_2. This technique uses paramagnetic spin probes which can be either in solutions or in particulate forms. Interactions between the unpaired electron spin centres [164,634] of the probes and oxygen molecules cause a shortening of relaxation times, producing a broadening effect on the EPR line width (LW) of the spin probes. Soluble probes have the advantage of diffusing throughout a tissue and providing estimates of pO_2 values. However, they are also prone to signal decrease due to rapid washout and/or metabolic biotransformation. The encapsulation of EPR spin probes could potentially circumvent these disadvantages [337,372,375,406,447,635,636].

The aim of the present study was to explore the possible use of lipid nanocapsules (LNCs) as an encapsulation entity for hydrophobic spin probes including nitroxides and tetrathiatriarylmethyl (TAM) free radicals. LNCs are core-shell based colloidal nano-structures where the core acts as an oily reservoir for loading hydrophobic molecules and/or drugs, and the shell acts as a protective, polymer membrane [573,605]. Furthermore, due to this polymeric shell, LNCs are capable of avoiding detection by the immune system thus increasing circulation time [566,575,637,638]. The encapsulation of lipophilic oxygen sensors in biocompatible, O_2 permeable LNCs [485] are of particular interest because the sensitivity of spin probes to oxygen can be enhanced by their encapsulation in a lipophilic carrier as the response is greatly increased by the high solubility of oxygen in lipids. Because nitroxides and TAM radicals could be used in *in vivo* EPR oximetry,

we sought to encapsulate 4-hydro-TEMPO benzoate (TB) and tetrathiatriarylmethyl (F15T-03, herein referred to as TAM) within LNCs (**Fig. 3-1**).

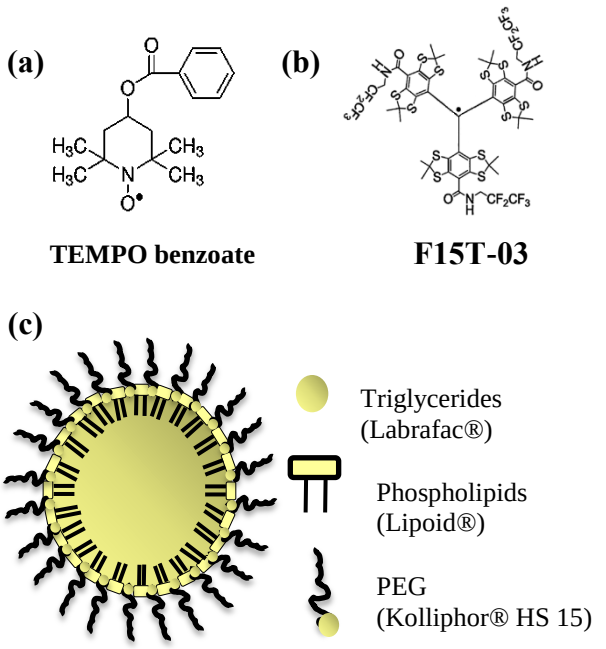

Figure 3-1. Chemical structure illustrations of **(a)** TEMPO benzoate and **(b)** F15T-03, and **(c)** a schematic of lipid nanocapsules (LNCs).

The probe-encapsulated LNCs were investigated regarding their physicochemical properties and oxygen sensitivity *in vitro*. *s*For *in vivo* experiments, the performances of TAM-loaded LNCs as oxygen sensors were assessed in muscles and in tumours during carbogen respiratory challenges.

2. Materials and Methods

2.1 Materials

Labrafac® WL 1349 (caprylic-capric acid triglycerides) was purchased from Gattefossé S.A. (Saint-Priest, France). Lipoïd S75-3 (soybean lecithin at 69 % of phosphatidylcholine) and Kolliphor® HS 15 (mixture of free polyethylene glycol 660 and polyethylene glycol 660 hydroxystearate) were provided by Lipoïd GmbH (Ludwigshafen, Germany) and BASF (Ludwigshafen, Germany), respectively. The nitroxide 4-hydroxy-TEMPO benzoate (TB) was supplied by Sigma Aldrich Chemie GmbH (Steinheim, Germany), whilst the TAM (tetrathiatriarylmethyl, F15T-03) radical was synthesised as previously described [374]. NaCl was purchased from Prolabo (Fontenay-sous-Bois, France). Water was obtained from a Milli-Q (Millipore) ultra-filtration system. No metal contaminates such as iron were observed in the EPR spectra.

2.2 Preparation of EPR probe encapsulated lipid nanocapsules

The preparation of nitroxide TB- and TAM-loaded LNCs (henceforth referred to as TB- and TAM-LNCs) was based on a phase inversion method [559]. In brief, the EPR probe was weighed, and dissolved in Labrafac® (oil phase) to reach a final concentration of 10 mM which produced a sufficient signal-to-noise ratio but did not exceed the self-induced line broadening threshold [367,639]. 1.028 g of Labrafac, containing the respective probe, was

mixed with water (2.962 g), NaCl (0.148 g), Kolliphor® HS 15 (0.846 g) and Lipoïd (0.075 g), and heated from ambient temperature to 95 °C whilst undergoing magnetic stirring. Subsequently, three heating and cooling cycles from 50 °C to 95 °C were performed. After the third cooling, once the temperature reached 72 °C, a rapid cold dilution was performed by adding 1 mL of 4 °C Milli-Q water.

2.2.1 Size characterisation

The average hydrodynamic size and polydispersity index (PDI) of the probe-loaded LNCs were determined by dynamic light scattering using a Malvern Zetasizer® (Nano Series DTS 1060, Malvern Instruments S.A., Worcestershire, UK) fitted with a 633 nm laser beam (helium–neon laser, 4 mW) at a fixed scattered angle of 173°. The formulations were diluted with pure water (dilution factor: 60) before measurement. Values are expressed as mean of three measurements ±standard deviation (SD).

2.2.2 Osmolarity adjustment of EPR probe loaded LNCs

Dialysis of the synthesised probe loaded LNCs (4 mL) was performed using dialysis tubing (Spectra Biotech Cellulose Ester Dialysis Membrane, MWCO = 100 kDa) for 24 h against pure water (obtained through a Milli-Q apparatus), changing the water hourly for the first 6 h. Then, to reobtain the original volume of LNCs (1 mL), the dilution factor of the dialysed solution was calculated and evaporation, using N_2, was applied under magnetic stirring. Once the initial volume was obtained, evaporation was ceased and 30 µL of a salt solution (320 mg/mL) was added to adjust the osmolarity of the formulation. Osmolarity measurements were performed using a 5520 Vapro vapour osmometer from Wescor (Logan, Utah, USA).

2.3 *In vitro* EPR measurements

2.3.1 *In vitro* EPR spectra acquisition

EPR spectra were acquired with a Bruker EMX-Plus spectrometer (Bruker, Rheinstetten, Germany), operating in X-band (9.85 GHz) and equipped with a PremiumX ultra low noise microwave bridge and a SHQ high sensitivity resonator. General settings were as follows: incident microwave power of 2.5 mW for TB and 0.3 mW for TAM; modulation frequency: 100 kHz; sweep width: 50 G for the nitroxide and 10 G for TAM; modulation amplitude: 0.6 G for TB and 0.2 G for TAM; scan time: 10 s.

2.3.2 Ascorbic acid assay

The protective properties of LNCs were investigated with an ascorbic acid reduction assay [640]. This was achieved by incubating the TB-LNCs in ascorbic acid, a compound known to reduce the

paramagnetic nitroxide into diamagnetic hydroxylamine. Nitroxide-loaded LNC formulations were combined 1:1 with a 2.5 mM ascorbic acid solution, and an aliquot of 100 µL was placed in an open quartz capillary tube (0.5 mm diameter). The non-encapsulated TB (dissolved in dimethyl sulfoxide (DMSO)) was used for comparison by mixing 1:1 with a 2.5 mM ascorbic acid solution diluted with Milli-Q water. EPR spectra were repeated over time to measure the decrease in signal intensity. All measurements were done in triplicate.

2.3.3 *In vitro* oxygen calibration curve

A calibration curve (LW as a function of pO_2) was obtained for both probe encapsulated-LNCs. LWs were obtained at various oxygen levels to determine the sensitivity of the LW to pO_2. Measurements were performed using the same spectrometer as mentioned in 2.3.1, equipped with a variable temperature controller (ER 4131 VT) equilibrated at 310 K. Samples were placed in a gas-permeable Teflon tube (0.625 mm inner diameter, 0.05 mm wall), which was folded and placed in a quartz open ended EPR tube. The oxygen content was varied between 0 % and 21 % O_2 by using an Aalborg gas mixer. The oxygen content in the mixed gas was measured by a Servomex MiniMP 5200 oxygen analyser (the precision of which is 0.1 % with oxygen content).

2.4 *In vivo* experiments

2.4.1 Animal models

The syngenic FSaII fibrosarcoma murine cell line was provided by ATCC and grown in Dulbecco's modified Eagle's medium (DMEM) high glucose GlutaMAX supplemented with 10 % horse serum and 1 % antibiotic and antimycotic solution (Gibco, Thermo Fisher Scientific). Animal studies were undertaken in accordance with Belgian and the Université catholique de Louvain ethical committee regulations (2014/UCL/MD/026). Two groups of male C3H mice (Janvier, Le Genest Saint Isle, France) were used; one group for intramuscular experiments (n = 17) and another for intratumoural (n = 14). For the tumour model, 2 x 10^6 FSaII cells in 100 µL serum-free DMEM were inoculated subcutaneously into the hind thigh (gastrocnemius muscle) of mice. Tumour size was measured daily and experiments were completed when tumours reached 8-10 mm in diameter.

2.4.2 Kinetic studies of TAM-LNCs

EPR spectra were acquired *in vivo* with a low-frequency microwave bridge operating at 1.2 GHz L-band EPR spectrometer (Magnettech, Berlin, Germany) with an extended loop resonator

possessing an inner diameter of 12.5 mm, and a thickness of 2 mm. Animals were anaesthetised using isoflurane (Forene, Abbot, Queensborough, UK): 3 % inhalation mixed with continuous air flow (2 L/min) for induction, and 1.5 % isoflurane for anaesthesia maintenance. A circulating water system was used for mouse-body temperature regulation. 50 µL injection of either TAM-LNCs or TAM dissolved in DMSO (10 mM) was injected intramuscularly or intratumourally (for intramuscularly; n = 5 encapsulated TAM-LNCs and n = 2 of unencapsulated TAM dissolved in DMSO, for intratumourally; n = 3 encapsulated TAM-LNCs and n = 2 of unencapsulated TAM dissolved in DMSO) in anaesthetised animals. Prior to the injection of TAM dissolved in DMSO, an occlusion of the femoral artery using a rubber band was performed to enable the measurement of the signal. The animal was placed in a side-way position to enable the access of the experimental gastrocnemius muscle, and the loop resonator was placed over the area of injection. The first EPR spectrum was acquired using the low-frequency EPR spectrometer 2 min after the injection, and this signal intensity was defined as the 100 % signal value. All other values were calculated relatively.

2.4.3 Intramuscular and intratumoural EPR measurements using TAM-LNCs during carbogen challenge

Animal anaesthesia and preparation for EPR spectra acquisition with an L-band EPR spectrometer was as previously described in 2.4.2. 50 µL of TAM-LNCs were injected intramuscularly (n = 10) or intratumourally (n = 9) into the anaesthetised animal. An EPR spectrum was recorded whilst the animal was breathing air (basal pO_2). Another EPR acquisition was performed after a 20 minutes carbogen (95 % O_2 and 5 % CO_2) challenge.

2.5 Statistical analysis

For the *in vitro* characterisation of probe loaded-LNCs, the data are presented as mean ±SD from triplicate experiments. For *in vivo* pO_2 measurements with TAM-LNCs, the paired Student's t-test was implemented, wherein a p value of < 0.05 was considered significant.

3. RESULTS AND DISCUSSION

3.1 Probe loaded-LNCs characterisation

The phase inversion process was exploited to obtain lipophilic EPR probes encapsulated within the lipidic core of the LNCs. The physicochemical properties of different types of the LNC

Table 3-1. Characteristics of EPR probe-loaded LNC preparations

Preparation	Particle size (nm) [1]	PDI [1]	LW_{air} (G)
TB-LNCs	60.8 ± 0.2	0.195 ± 0.007	1.92 [2]
TAM-LNCs	57.4 ± 0.9	0.165 ± 0.015	0.71

[1] mean ±SD (n = 3)
[2] measured on the central peak of the nitroxide

preparations are presented in **Table 3-1**. The size of TB-LNCs and TAM-LNCs were 60 nm and 57 nm, respectively with a PDI under 0.2. The size of the probe loaded-LNCs was comparable to previously studied standard blank LNCs which showed good stability stored at 4 °C from 12-18 months [641,642]. Both probe loaded-LNCs types exhibited an EPR signal demonstrating the effective inclusion of TB and TAM in the LNCs (**Fig. 3-2**). Of note, our attempt to prepare TEMPO loaded-LNCs was not successful as no EPR signal was recorded after the preparation. This could be due to the lower lipophilicity of TEMPO (log P = 1.40) compared to TB (log P = 3.10) [643]. Interestingly, the intensity of the three EPR lines in the EPR spectrum of TB-LNCs was not equivalent, with a reduced height of the third line (**Fig. 3-2**), indicative of motion restriction of TB within the LNCs. As expected the LW of the TAM-LNCs (equilibrated in air at room temperature) was narrow (0.71 G, under air) compared to the LW of the TB-LNCs (1.92 G, measured on the central peak of the nitroxide). To further ascertain the entrapment of the probes inside the LNCs, we used an ascorbic acid assay on TB-LNCs. It is well established that ascorbic acid rapidly reduces nitroxides in solution, and similarly it was found

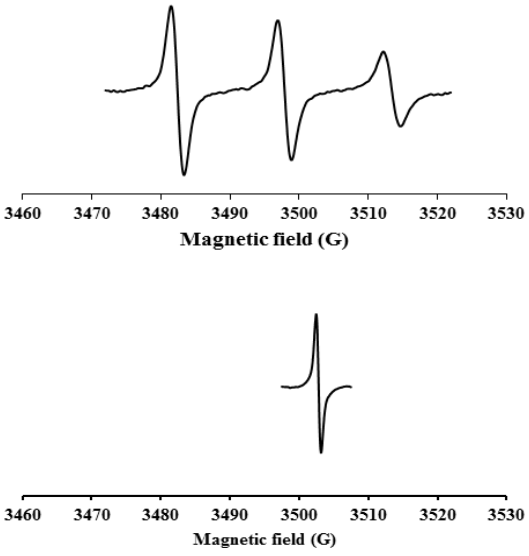

Figure 3-2. EPR spectra acquired *in vitro* (under air) of TB-LNCs **(top)** and TAM-LNCs **(bottom).**

for unencapsulated TB (**Fig. 3-3**): the signal intensity of TB completely disappeared within approximately 10 minutes in the presence of ascorbic acid.

Conversely, the signal intensity of TB-LNCs decreased much slower over time (**Fig. 3-3**) indicating that the TB was not directly exposed at the surface of the LNCs. Of note, we confirmed that there was no change in size and PDI when LNCs were exposed to ascorbic acid indicating that the integrity of LNCs was not affected by the presence of ascorbic acid.

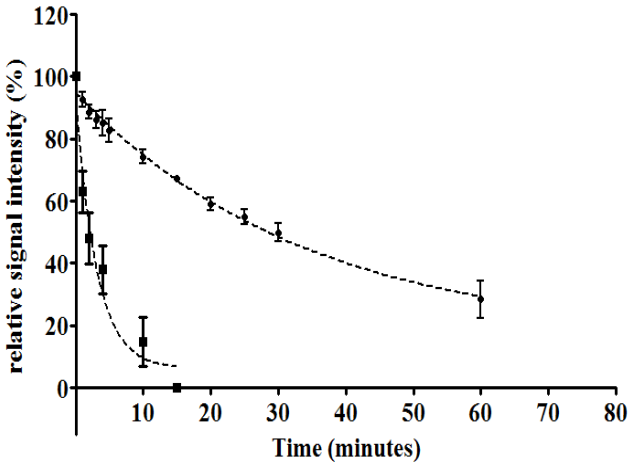

Figure 3-3. Evolution of EPR signal intensity over time of unencapsulated TB (squares) or TB-LNCs (circles) in the presence of ascorbic acid. Results are expressed as relative to the initial signal intensity (mean ±SD) (n = 3) wherein the dotted line indicates the trend

This is consistent with an encapsulation of TB into the lipidic core of the LNCs, with a slow exchange of a small fraction at the interfacial surface leading to a slow reduction of the nitroxide. TAM-LNCs were not tested using this protocol as trityls are not sensitive to the presence of ascorbic acid.

3.2 *In vitro* EPR oximetry with TB- and TAM-LNCs

The EPR LW (peak-to-peak) of TB- and TAM-LNCs increased linearly with pO_2. From nitrogen to air, the TB-LNCs LW (mean ±SD) increased from 1.621 ±0.001 to 1.846 ±0.011 G (presenting only a 14 % increase in LW) whilst TAM-LNCs increased from 0.511 ± 0.003 to 0.711 ±0.002 G (presenting a 39 % increase in LW) (**Fig. 3-4**), indicating that TAM-LNCs were more sensitive to change in O_2. The slope of the TAM-LNCs calibration curve (1.25 mG/mmHg) was about 2-fold increased by comparison with the sensitivity of the hydrophilic trityl CT-03 (0.64 mG/mmHg) [374]. This increase in oxygen sensitivity is consistent with the higher solubility of oxygen in lipophilic phases as predicted by the Smoluchowsky equation [337]. Of note, the sensitivity observed in LNCs was lower compared to previously developed nanocapsules containing F15T-03 in the perfluorocarbon hexafluorobenzene (14 mG/mmHg) [447]. Concerns about the biocompatibility of hexafluorobenzene [450] led us to consider other excipients such as

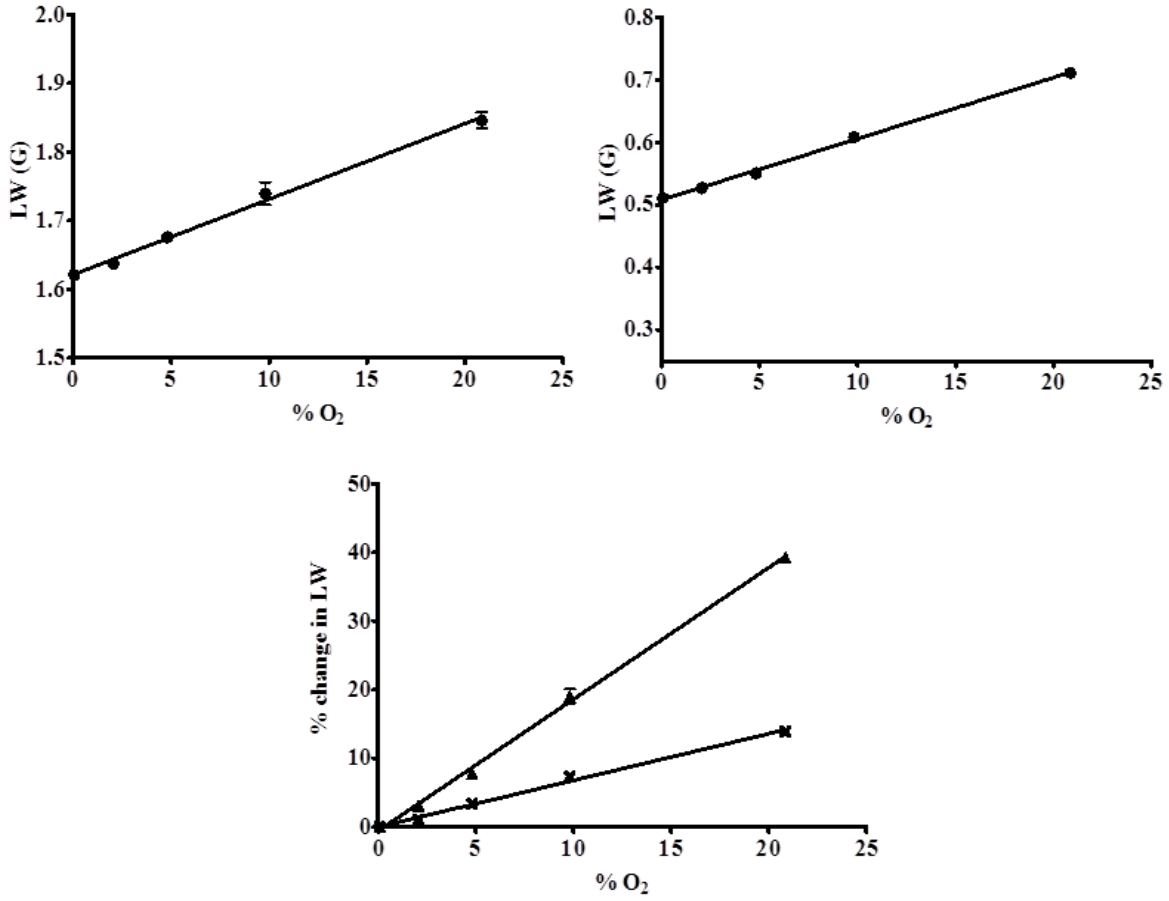

Figure 3-4. Calibration of the EPR LWs recorded with TB-LNCs **(top, left)** and TAM-LNCs **(top, right)** as a function of LW (G) over % O_2. Relative sensitivity to O_2 as % change in LW as a function of O_2 concentration **(bottom)** shown with both TB-LNCs (cross) and TAM-LNCs (triangle). Curves show an R^2 of 0.987 and 0.994, respectively.

LNCs based on Labrafac as the lipid core. While the oxygen sensitivity for TAM-LNCs remained limited, it was an improvement over hydrophilic trityls and deserved further consideration for *in vivo* applications. Thus, due to the characterisation and oximetry results obtained for the probe encapsulated-LNCs, TAM-LNCs were used for *in vivo* studies as it is more stable, has a narrower LW at lower O_2 concentrations, and has a better signal-to-noise ratio as compared to the nitroxide TB-LNCs.

3.3 *In vivo* measurements using TAM-LNCs

A low-frequency (1.2 GHz) EPR spectrometer was used for *in vivo* experiments as EPR spectra can be recorded in tissues at a depth of approximately 1 cm. After intramuscular or intratumoural administration of unencapsulated TAM, the EPR signal

decreased very rapidly (in approximately 10 min) (**Fig. 3-5**). By contrast, 1 hour after administration, the EPR signal intensity of TAM-LNCs was only reduced by 25 % in the muscle and 35 % in the tumours (**Fig. 3-5**).

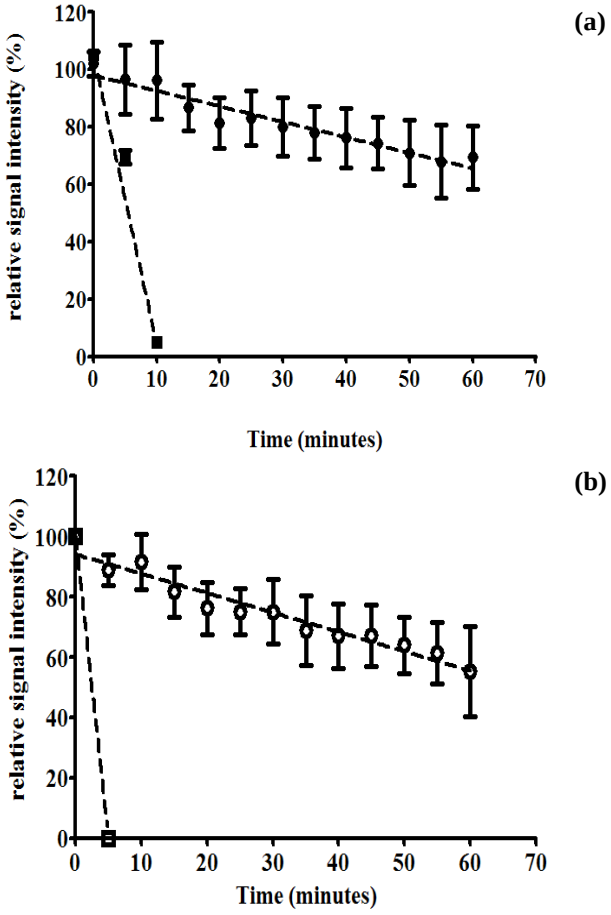

Figure 3-5. Evolution of the EPR intensity recorded in muscles or in tumours after administration of unencapsulated TAM or TAM-LNCs, wherein **(a)** indicates the injected muscle group with unencapsulated TAM shown as closed squares (n = 2) and TAM-LNCs shown as closed circles (n = 5), and **(b)** indicates the injected tumour group with unencapsulated TAM shown as open squares (n = 2) and TAM-LNCs shown as open circles (n = 3). Results are expressed as relative to the initial signal intensity (mean ±SD).

Due to this slow clearance of the EPR probes, it was possible to assess the sensitivity of TAM-LNCs to variations in tissue oxygenation. After administration of TAM-LNCs in the muscle, EPR spectra were acquired whilst the animals (n = 10) were breathing 21 % oxygen, then after a carbogen breathing challenge of 20 minutes. The LWs (mean ±SD) measured in the animals were 0.748 ±0.039 G in mice breathing air and 0.943 ±0.095 G in mice breathing carbogen (**Fig. 3-6**). The difference was statistically significant ($p < 0.0001$). TAM-LNCs were also injected into subcutaneous FSaII tumours (n = 9) The LWs (means ±SD) observed in the animals were 0.745 ±0.035 G during air breathing, and 0.912 ±0.196 G after carbogen challenge (individual changes in LWs are represented in **Fig. 3-7**). These values indicate a sensitivity of the EPR probe to the changing O_2 environment within the tumour, as indicated by the significant increase in LW (difference between means of -0.167 G, $p = 0.03$) following the application of carbogen. We observed a larger variation in the response to carbogen in tumours compared to the muscles. This observation is consistent with the heterogeneity in perfusion occurring in tumours, wherein the vascular network

is well hierarchized in muscles. While the TAM-LNCs were sensitive to variations in oxygen changes in muscles and in tumours, it should be noted that the transposition of the LWs into pO_2 values led to non-physiological estimates.

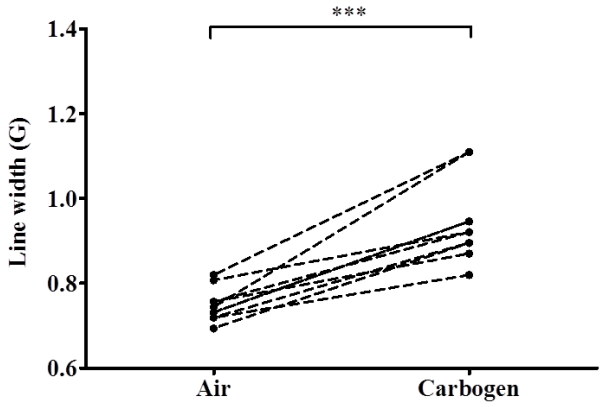

Figure 3-7. *In vivo* EPR LW from TAM-LNCs injected in the muscle (n = 10) when mice were breathing air or carbogen. *P* value of < 0.0001 indicated with *** as determined by the paired Student's t-test.

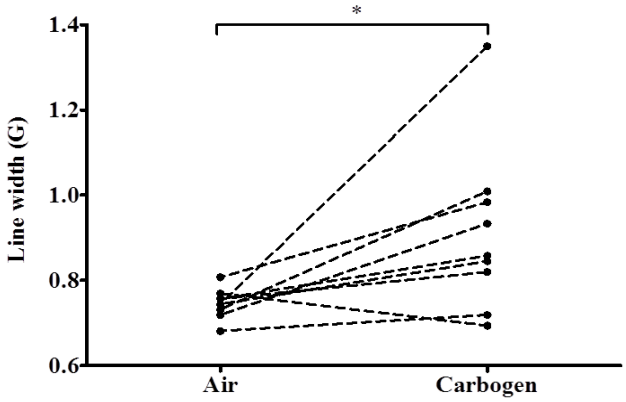

Figure 3-6. *In vivo* EPR LW from TAM-LNCs injected in the FSaII fibrosarcoma (n = 9) when mice were breathing air or carbogen. *P* value of 0.03 indicated with * as determined by the paired Student's t-test.

As an example, measurements in muscles while mice were breathing air provide estimates of pO_2 close to 150 mmHg which are higher than the expected physiological values. This is in contrast with pO_2 estimates that are routinely obtained in tissues when using the same EPR system and other EPR oxygen sensors such as charcoal particles and lithium phthalocyanine [409,644,645]. The higher sensitivity of these particulates probes to changes in oxygenation may potentially explain the lower uncertainty and better accuracy when trying to estimate the pO_2 *in vivo* using EPR. Another factor could be the potential instability of the LNCs *in vivo* that may lead to change in the viscosity around the trityls. It has been recently reported by Frank et al. that changes in viscosity may profoundly affect the LWs of trityl radicals [375].

4. CONCLUSION

LNCs loaded with EPR probes TB and TAM were successfully prepared by the phase inversion process leading to nanocapsules of about 60 nm. Experiments performed with TB-LNCs in the presence of ascorbic acid demonstrated that the encapsulation provided resistance against the reduction into hydroxylamine. The calibration of the EPR LW as a function of the

pO_2 showed a two-fold increase in sensitivity with TAM-LNCs compared to hydrophilic trityl radical. The TAM-LNCs were evaluated *in vivo*. Contrarily to unencapsulated TAM, for which a rapid decrease in EPR signal was observed, the half-life of TAM-LNCs administered in muscles or in tumours was longer than one hour. Carbogen challenges in mice demonstrated that the TAM-LNCs responded well to changes in oxygen environment. However, the apparent pO_2 values acquired were higher than the expected physiological values, which could be due to the instability of LNCs *in vivo* and potential changes in micro-viscosity surrounding the oxygen sensor. These developments and results warrant further investigation in the formulation of stable nano-objects encapsulating EPR oxygen sensitive probes.

ACKNOWLEDGEMENTS

The authors would like to thank the NanoFar Erasmus Mundus program, the "Fonds du Patrimoine" (Secteur des Sciences de la Santé, UCLouvain) and comité départemental de Maine and Loire de la Ligue Contre le Cancer (France) for providing the funding for this project.

3.3 KINETICS OF TAM-LNCS *IN VIVO*

3.3.1 Introduction

In this section, the unpublished work pertaining to the above article in section 3.2 will be discussed. Herein, the *in vivo* studies using normal and tumoural tissues were expanded upon to elucidate the ability of TAM-LNCs (**Fig. 3-8**) to reversibly respond to O_2 variation in tissue by using the carbogen challenge [323,646,647] and reversible occlusion of the femoral artery within the mouse muscle. Additionally, the possibility of LNCs introducing auxiliary O_2 within the tissue and thus acting as an "oxygen reservoir" was explored.

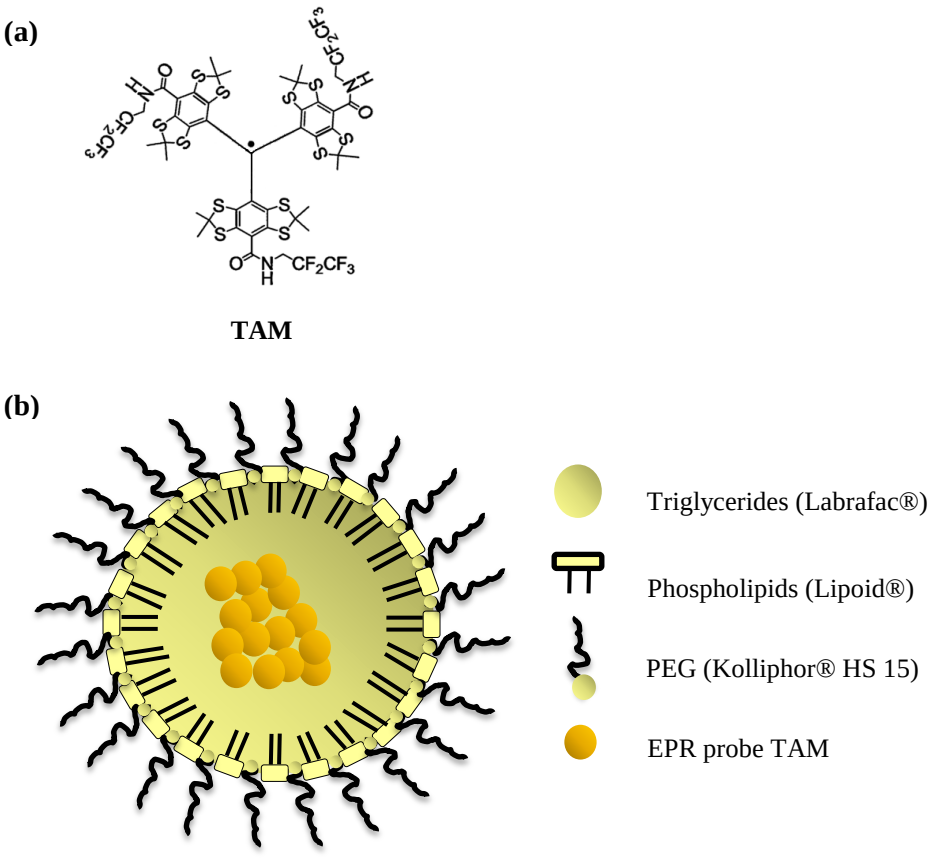

Figure 3-8. Chemical structure of the EPR probe **(a)** TAM, and a schematic of the EPR probe-loaded LNCs **(b)** representing the inclusion of the EPR probe within the LNC lipidic core.

3.3.2 Materials and Methods

3.3.2.1 Synthesis and characterisation of TAM-LNCs

Osmolarity adjusted LNCs loaded with TAM (herein referred to as TAM-LNCs) were prepared using the phase-inversion temperature (PIT) process [559] and the osmolarity adjustment protocol described in section 3.2. The average hydrodynamic size and polydispersity index (PDI) of the LNCs were determined by dynamic light scattering using a Malvern Zetasizer® (Nano Series DTS 1060, Malvern Instruments S.A., Worcestershire, UK).

3.3.2.2 *In vitro* EPR spectra acquisition

EPR spectra were acquired with a Bruker EMX-Plus spectrometer (Bruker, Rheinstetten, Germany), operating in X-band (9.85 GHz) and equipped with a PremiumX ultra low noise microwave bridge and a SHQ high sensitivity resonator. General settings were as previously described in section 3.2 for the TAM EPR probe.

3.3.2.3 *In vivo* EPR measurements

3.3.2.3.1 Animal models

For *in vivo* studies, two groups of male C3H mice (Janvier, Le Genest Saint Isle, France) were used; one group for intramuscular experiments (n = 13) and another for intratumoural (n = 12).

3.3.2.3.2 Intramuscular and intratumoural EPR measurements with TAM-LNCs

A bolus injection of 50 µL of TAM-LNCs were introduced intramuscularly (n = 10) or intratumourally (n = 9) into animals as previously described in section 3.2, and EPR spectra were recorded as per the following protocol (**Fig. 3-9**); firstly, during air breathing; then after 20 min of carbogen breathing; then, following a return to air breathing for 10 min, an occlusion of the ipsilateral femoral artery of the gastrocnemius muscle was applied for 5 min using a rubber band tied tightly above the knee of the animal. Total time taken for the full experiment was approximately 40 min.

EPR spectra were acquired *in vivo* with a low-frequency microwave bridge operating at 1.2 GHz L-band EPR spectrometer (Magnettech, Berlin, Germany) with an extended loop

resonator possessing an inner diameter of 12.5 mm, and a thickness of 2 mm. General settings were as follows: incident microwave power of 2.8 mW; modulation amplitude of 0.019 mT; modulation frequency: 100 kHz; sweep width: 1.0 mT; scan time: 30 s.

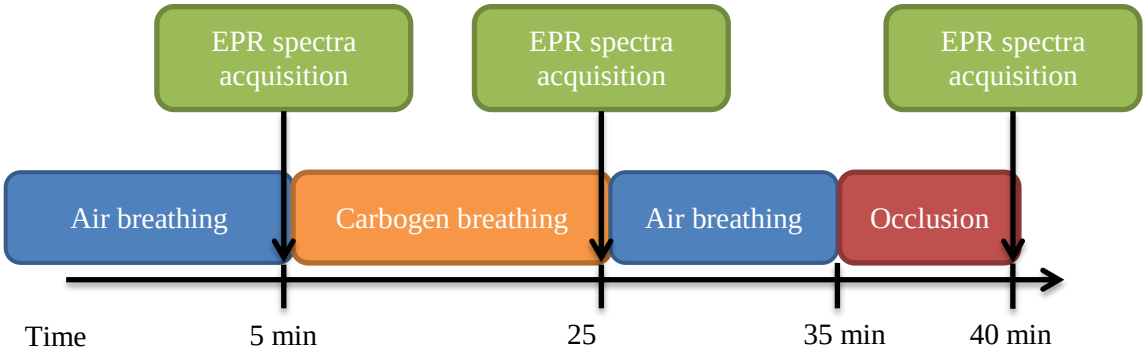

Figure 3-9. Experimental protocol for EPR spectra acquisition during *in vivo* experimentation with TAM-LNCs.

3.3.2.3.3 Evolution of LW over time

A 50 µL bolus injection of TAM-LNCs was injected intramuscularly (n = 3) or intratumourally (n = 3) in anaesthetised animals. The animal was placed as described previously in section 3.2 within the L-band EPR spectrometer.

3.3.3 Results

3.3.3.1 Intramuscular and intratumoural EPR measurements with TAM-LNCs

To further explore TAM-LNCs as an oxygen sensor, *in vivo* experiments were performed including normal tissue (gastrocnemius muscle) and pathological tissue (FSaII fibrosarcomas-induced subcutaneous tumour) animal models. After administration of TAM-LNCs in the muscle or subcutaneous tumours in the form of a bolus injection, three EPR spectra were acquired; during air breathing, carbogen breathing, and the occlusion. This experiment was applied to both the muscle (n = 10) and subcutaneous tumour (n = 9) models (**Fig. 3-10 (a) and (b)**, respectively).

The LWs (mean ±SD) measured in the muscles were 0.748 ±0.039 G in mice breathing air and 0.943 ±0.095 G in mice breathing carbogen, and 0.687 ±0.054 G after occlusion was

applied (**Fig. 3-10 (a)**). Similarly, the LWs were measured for subcutaneous tumours, 0.745 ±0.035 G during air breathing, 0.912 ±0.196 G after the carbogen challenge, and 0.649 ±0.054 G after occlusion (**Fig. 3-10 (b)**). For both muscles and tumours a significant difference between the means was determined using the one-way ANOVA, $p < 0.0001$ and $p < 0.0014$, respectively). Between the air and carbogen breathing a difference was noted ($p < 0.0001$ and $p < 0.05$, respectively) and between the carbogen breathing and occlusion ($p < 0.0001$ and $p < 0.01$, respectively). However, no significant difference ($p > 0.05$) was found between air and occlusion for either the muscle ($p = 0.1495$) or tumour ($p = 0.6856$) groups. It should also be noted, that the starting air LW values for muscles (0.748 ±0.039 G) and tumours (0.745 ±0.035 G) were similar.

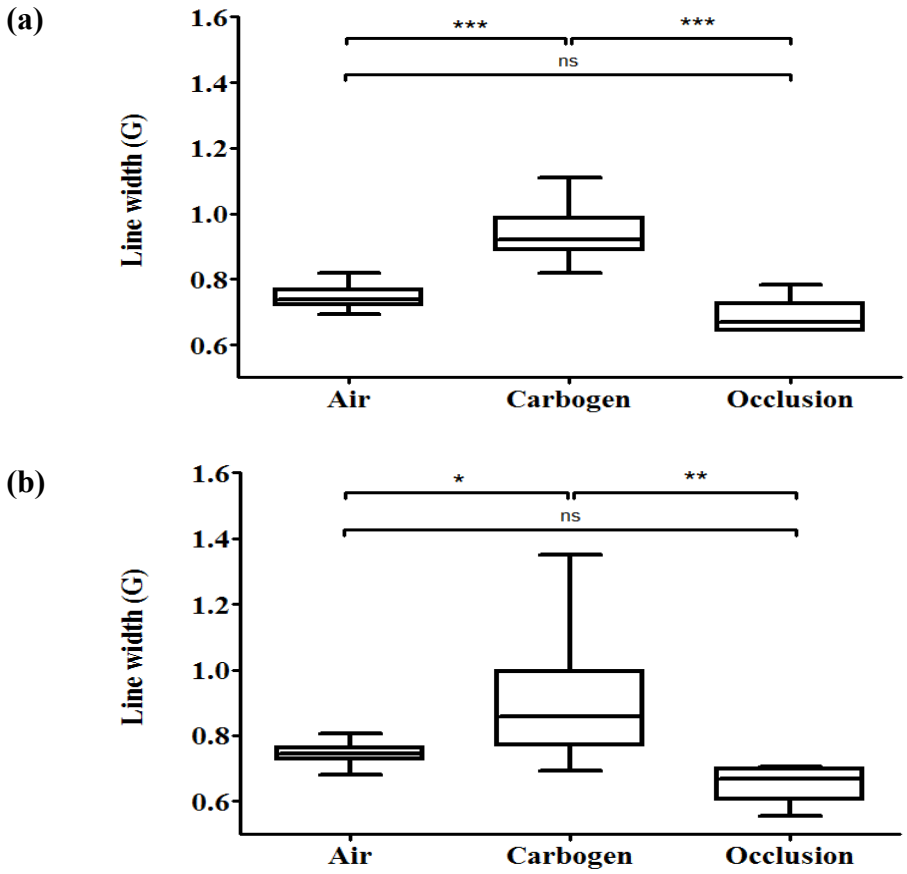

Figure 3-10. *In vivo* EPR LW from TAM-LNCs injected in the **(a)** muscle (n = 10) or **(b)** FSaII fibrosarcoma subcutaneous tumour (n = 9) when mice were breathing air or carbogen or underwent occlusion. For statistical analysis, the one-way analysis of variance (ANOVA) test, with the Tukey post-hoc test applied, was used, wherein a p value of < 0.05 indicated with *, p value of < 0.01 indicated with **, and p value < 0.001 indicated with ***. Notably, a non-significant result occurs when the p value is > 0.05.

3.3.3.2 Evolution of LW over time study

To address the issue of the 'reservoir effect', wherein O_2 is hypothesised to accumulate within the lipidic core of the LNCs (during formulation and handling) and be subsequently deposited *in vivo* during the LNC deposit; a kinetics study was done to note the evolution of the LW over time (**Fig. 3-11**).

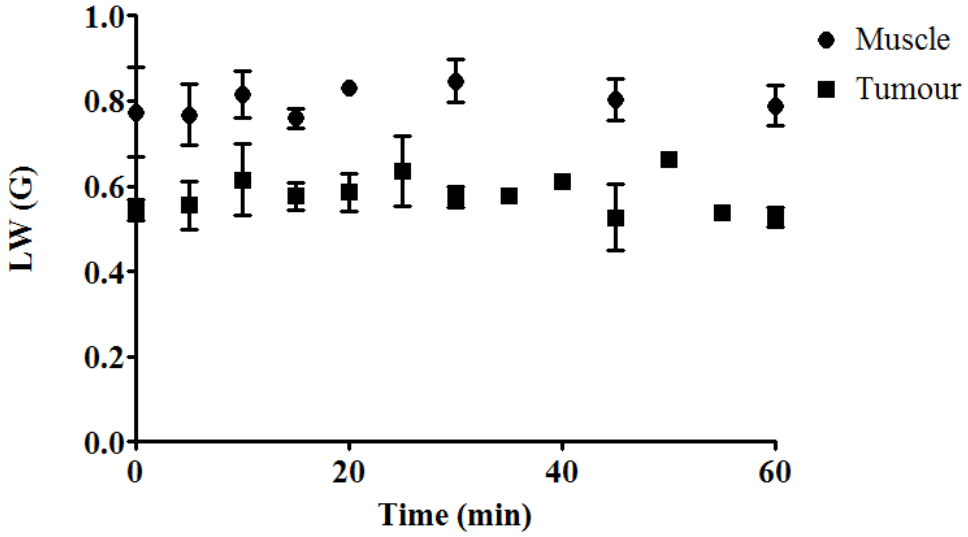

Figure 3-11. The change in EPR LW (mean ±SD) over time for muscle (n = 3, closed circle) and FSaII fibrosarcoma subcutaneous tumour (n = 3, closed square).

Indeed, if the 'reservoir effect' was occurring, a decrease and eventual plateau in the change in LW would be apparent over time thus indicating the diffusion of O_2 from the LNCs to the surrounding tissue. As shown in **Figure 3-11**, the LW did not decrease with time thus excluding the 'reservoir effect'.

3.3.4 Discussion and conclusions

A significant difference was observed in LWs measured during air and carbogen breathing as previously noted in the published article. Notable in this study, however, was the application of an ipsilateral occlusion of the femoral artery promoting the decrease in arterial blood flow – and thus the pO_2 – near the TAM-LNCs. Here, it was demonstrated that the TAM-LNCs could respond significantly and reversibly to a change in its O_2 environment in both a normal and tumoural tissue environment (**Fig. 3-10**). Unfortunately, no significant

difference was noted between the air breathing and the occlusion LWs in of the *in vivo* model group. This is surprising, as lower LWs were expected during occlusion due to the halt of arterial blood flow, and thus oxygen, towards the injected TAM-LNCs.

Furthermore, a potential limitation for the use of LNCs could be the 'reservoir effect' where an import of O_2 is dissolved in the lipid core which influences the pO_2 measurement during the experimental studies. If the 'reservoir effect' was occurring, a decrease in the LW would be apparent over time due to the distribution of O_2 from the LNCs into the tissue as the system equilibrates. However, this was not observed (**Fig. 3-11**). Instead a relatively stable difference throughout the experiment was noted, indicating this was not necessarily a factor attributing to the TAM-LNCs overestimation of pO_2. Another aspect contributing to the overestimated pO_2 values could be the system itself. Indeed, unlike for solid EPR probes, e.g. LiPc, the liquid probes are susceptible to viscosity; such as the difference between tissue and an aqueous environment [367], and the contribution from the choice of oil used (i.e. Labrafac®). Labrafac® was used as the oily-core constituent of LNCs, as described by Heurtault et al. [558], and is considered biologically inert and medically safe for use [620,621] but has a relatively high viscosity (25 – 33 mPa.s, 20 °C) [648] which could have a broadening effect on the EPR LW, thus effecting resolution and the conversion between LW and pO_2.

In conclusion, LNCs were capable of encapsulating lipophilic EPR probes, including both nitroxides and trityl. *In vitro* experiments, however, indicated that only TAM-LNCs could be used with *in vivo* animal models as the nitroxides suffered from EPR signal loss and incomplete incorporation of the EPR molecule within the LNCs. TAM-LNCs performed well as an oxygen sensor in both a normal tissue environment and in a pathological environment, with LNCs providing protection and *in vivo* biocompatibility for the EPR probe, and an O_2 permeable environment thus enabling the demonstration of its ability to respond to variations in pO_2. As a matter of fact, the LNCs were responsive enough to enable a reversible measurement of pO_2 within tissues. But an over estimation of pO_2 was apparent, thus only relative change in the level of oxygenation could be noted. These developments and results with TAM-LNCs warrant further investigation of the nanoplatform as an oxygen sensor.

Chapter 4:

Magnetic Resonance Imaging and Lipid Nanocapsules

4.1 INTRODUCTION TO CHAPTER 4

MRI is a non-invasive technique used extensively in oncology, as noted in Chapter 2, for imaging anatomical features and monitoring the growth of tumours. In the case of perfusion-based methods, however, this technique does not measure pO_2 directly. Furthermore, regarding probe-based methods such as PFCs, these techniques rely on specialised MR equipment. Thus, a different strategy for monitoring tumoural hypoxia via the mapping of oxygen by imaging lipid relaxation enhancement (MOBILE) was developed. This sequence enables the imaging of pO_2 variations within various *in vivo* models (see Chapter 2, section 2.5.2). However, due to signal-to-noise issues which require the intrinsic lipid content to be sufficiently high enough for the MOBILE sequence to produce a map of the area, the MOBILE sequence cannot be applied to all tissue.

Thus, in this chapter, the limitation of the MOBILE sequence is addressed by the use of LNCs. LNCs consists of a thin polymer coating surrounding a lipidic core, produced from entirely biocompatible components approved by the FDA for *in vivo* usage, and have been employed in treatment strategies of several cancer types, most notably the highly malignant and treatment resistant glioblastoma. The lipidic core of LNCs makes them an excellent tool for assessing and imaging O_2 in tissue, in regard to the MOBILE sequence, as the solubility of O_2 is much greater in lipids as compared to water [506]. Thus, the use of LNCs to increase the SNR will enable oxygenation mapping within tissues regardless of their intrinsic lipidic contents and will provide the basis of its usage as a theranostic tool.

In this chapter, data submitted for publication regarding the development of LNCs as an MRI O_2 sensor using the MOBILE sequence is presented in **section 4.2**. Herein, LNCs were evaluated for their ability to improve the SNR within both normal and pathological tissues, and produce pixel-by-pixel analysis of oxygenation maps. Importantly, the effect of using different techniques (i.e. bolus injection vs. convection-enhanced delivery [CED]) for introducing the LNCs into the tissues was examined. Of note was the choice of pathological tissue used; the subcutaneous fibrosarcoma and the intracerebral glioblastoma models. As previously described, the subcutaneous fibrosarcoma model is a well-known model in regards to its pO_2 values and response to the carbogen gas challenge [384,422,627]. Likewise, the intracerebral glioblastoma model is known to be highly vascularised yet hypoxic [649,650]. In the last sections, unpublished data regarding the *in vivo* fate of LNCs was investigated (**section 4.3**).

4.2 ARTICLE

This section includes the article **Lipid nanocapsules for tissue oxygenation determination using Magnetic Resonance Imaging** submitted for publication in the journal Materials Science and Engineering: C: Materials for Biological Applications.

Lipid nanocapsules as *in vivo* oxygen sensors using Magnetic Resonance Imaging

Janske NEL [a,b], Florence FRANCONI [a,c], Nicolas JOUDIOU [b,d], Patrick SAULNIER [a], Bernard GALLEZ [b], and Laurent LEMAIRE [a, c]

[a] *Micro et Nanomedecines translationnelles, MINT, Université Angers, INSERM 1066, CNRS 6021, 4 rue Larrey, Angers, France*
[b] *Biomedical Magnetic Resonance Unit (REMA), Louvain Drug Research Institute, Université Catholique de Louvain, Avenue Mounier 73 bte B1.73.08, 1200 Brussels, Belgium*
[c] *PRISM, Université d'Angers, 49933 4 rue Larrey, Angers, Fr*
[d] *Nuclear and Electron Spin Technologies Platform (NEST), Louvain Drug Research Institute, Université Catholique de Louvain, Avenue Mounier 73 bte B1.73.08, 1200 Brussels, Belgium*

Abstract

Hypoxia is common occurrence of the tumour microenvironment, wherein heterogeneous gradients of O_2 give rise to tumoural cells which are highly malignant, metastatic, and resistant to therapeutic efforts. Thus, the assessment and imaging of hypoxia is essential for tumour diagnosis and treatment. Magnetic resonance imaging and, more specifically, the quantitative assessment of longitudinal relaxation time enhancement, were shown to enable the mapping of oxygen in tumours with increased sensitivity for lipids as compared to water signal. Unfortunately, this can only be applied to tumours with high lipid content. To overcome this issue, we propose the use of lipid nanocapsules (LNCs). LNCs have been demonstrated as excellent core-shell nanocarriers, wherein the lipidic-core is used for lipophilic drug encapsulation, enabling treatment of highly malignant tumours. Herein, however, we exploited the lipidic-core of the LNCs to develop a simple but effective technique to increase the lipidic content within tissues to enable the assessment and mapping of pO_2. LNCs were prepared using the phase-inversion technique to produce 60 nm sized nanoparticles, and *in vitro* studies demonstrated the permeability and responsiveness of LNCs to O_2. To evaluate the ability of LNCs to respond to changes in pO_2 *in vivo*, after a hyperoxic challenge, three animal models, namely a normal tissue model (gastrocnemius muscle tissue) and two tumour tissue models (subcutaneous fibrosarcoma and intracerebral glioblastoma) were explored. LNCs were found to be responsive to variation of O_2 *in vivo*. Moreover, the use of MRI enabled the mapping of oxygen gradients and heterogeneity within tumours.

Keywords: hypoxia, lipid nanocapsules, carbogen challenge, magnetic resonance imaging

1. INTRODUCTION

Hypoxia is a key feature in solid tumours caused by abnormal and torturous vasculature which are unable to meet the O_2 demand of the tumour mass. This oxygen deprivation causes; a change in gene expression; leading to more aggressive tumours; and results in metastatic progression and resistance to radiation and chemotherapy [25,651]. Thus, a need has risen to combat the poor outcome of treatment interventions by developing techniques to image and assess the hypoxic tumour environment. Ideally, the imaging of hypoxia should be non-invasive, sensitive, robust, quantitative, widely available and able to reflect tumour heterogeneity. To this end, techniques such as electron paramagnetic resonance and positron emission tomography imaging have been developed, but magnetic resonance imaging (MRI) techniques are more appealing due to its ability to provide spatial information and its use of non-ionising probes.

The development of perfluorinated compounds began the use of ^{19}F-based MR oximetry and introduced the use of exogenous probes [471,652,653], however their *in vivo* application was limited by the need for specialist MR equipment regarding the ^{19}F-tuned probe. Endogenous probes, such as water and lipids, had no such limitation. Regardless the origin of the sensor, oxygen measurement is based on the change in longitudinal relaxation time (T_1). Indeed, molecular oxygen (O_2) possesses two unpaired electrons which enable its paramagnetic ability to act as a T_1-shortening agent in tissues [654], and therefore as a signal intensity enhancer on MR T_1-weighted sequences [323]. Therefore, the change of oxygenation is also directly correlated with the longitudinal relation rate ($1/T_1 = R_1$) [471,655]. Despite being attractive for oxygenation measurements, with respect to the high water content of biological tissues, water T_1 change with oxygen concentration is limited, and lower than the change observed with lipids, due the six times higher solubility of oxygen in lipids than in water [506]. This property was exploited by Jordan and colleagues who developed an MR sequence to map oxygen based on imaging of lipid relaxation rates (MOBILE; acronym for mapping of oxygen my imaging of lipid relaxation enhancement) [508].

The drawback of this method however, is that there is not always a sufficient amount of intrinsic lipids in the tissue of interest to enable the use of the MOBILE method. This limitation can be overcome by the use of lipid nanocapsules (LNCs) [559]: a nanocarrier with an oil-filled core surrounded by a protective polymer shell,

capable of encapsulating drugs, with proven treatment efficiency in preclinical glioblastoma cancer models [597,602,656]. Thus, while delivering therapy, an increase in lipid level can be reached allowing MR oxygenation mapping using the described MOBILE method. Notably, LNCs are also of particular interest due to their O_2 permeability [485], solvent free and FDA-approved constituents, and their ability to avoid the immune system [657]. Using the MOBILE MR sequence, LNCs were investigated for their ability to respond to changes in O_2 concentrations *in vitro*. For *in vivo* experiments, a muscle model and two tumour models were employed to assess the ability of the LNCs to act as an oxygen sensor during carbogen respiratory challenges.

2. MATERIALS AND METHODS

2.1 Reagents

The lipophilic Labrafac® WL 1349 (caprylic-capric acid triglycerides; European Pharmacopeia, IVth, 2002) was purchased from Gattefossé S.A. (Saint-Priest, France). Lipoïd S75-3 (soybean lecithin at 69 % of phosphatidylcholine) and Kolliphor® HS 15 (a mixture of free polyethylene glycol 660 and polyethylene glycol 660 hydroxystearate) were provided by Lipoïd GmbH (Ludwigshafen, Germany) and BASF (Ludwigshafen, Germany), respectively. NaCl was purchased from Prolabo (Fontenay-sous-Bois, France). Filtered and deionised water was obtained from a Milli-Q plus® system (Millipore).

2.2 Formulation and characterisation of LNCs

LNCs were prepared according to the phase inversion method [559]. Briefly, 1.028 g of Labrafac (oil phase), Lipoïd (0.075 g), Kolliphor® HS 15 (0.846 g), NaCl (0.148 g) and water (2.962 g) were mixed and heated to 95 °C with magnetic stirring. Thereafter the mixture underwent three cycles of cooling and heating between 50 °C and 95 °C. After the final heating phase, the solution was cooled to 72 °C and subjected to an irreversible shock induced by adding 1 mL of 4°C water. This fast cooling allowed for the formation of stable, core-shell LNCs. Thereafter, the osmolarity of the formulation was adjusted to be physiologically safe for *in vivo* administration. To achieve this, 1 mL of the LNC formulation was dialysed using dialysis tubing (Spectra Biotech Cellulose Ester Dialysis Membrane, MWCO = 100 kDa) for 24 h against pure water (Milli-Q plus® system, Millipore), changing the water hourly for 6 h. Then, to obtain the original volume of LNCs, the dilution factor of the dialysed solution was calculated and evaporation, using N_2, with

magnetic stirring was done. Once the initial volume was obtained, evaporation was ceased and 30 µL of a salt solution (320 mg/mL) was added. Osmolarity measurements were performed using a 5520 Vapro vapour osmometer from Wescor (Logan, Utah, USA). Osmolarity adjusted LNCs were used for all *in vivo* experiments. The average hydrodynamic size and polydispersity index (PDI) of the LNCs were determined by dynamic light scattering using a Malvern Zetasizer® (Nano Series DTS 1060, Malvern Instruments S.A., Worcestershire, UK) fitted with a 633 nm laser beam (helium–neon laser, 4 mW) at a fixed scattered angle of 173°. To ensure accuracy, LNCs were diluted 1:60 (v/v) in deionised water to produce scattering intensity values that were in the mid-range of the instrument's detector. Values are expressed as mean of three measurements ±standard deviation (SD) for five formulations.

2.3 *In vitro* sensitivity of LNCs to pO_2

To evaluate the response of LNCs to variations in O_2, the MOBILE sequence was applied wherein the T_1 of the methylene group (~1.2 ppm) of the lipid core of the LNCs was measured at 37 °C in sealed tubes bubbled with nitrogen (0 % O_2), air (21 % O_2) or pure oxygen (100 % O_2) for 30 min with magnetic stirring. Temperature of the samples was maintained using a warm water circulation system. MOBILE sequence acquisition parameters were as follows; TR: 1520 ms; mean echo time (TE): 0.8 ms, flip angle: 5°; bandwidth (BW): 200 kHz at 30 % echo position; matrix: 32 x 32, field of view (FOV): 5 x 5 cm; 16 segments, a series of 50 images spaced at TR 29.80 ms with a slice thickness of 4 mm, and a total acquisition time of approximately 35 min. Determination and acquisition of the lipid signal was performed as described by Jordan et al [508]. Briefly, the difference in frequency between the water and lipid peaks (i.e. 1.2 ppm for the methylene group of the lipid core of LNCs) in a ^1H proton spectrum was determined and used as the offset for the imaging frequency for the MOBILE sequence. A Gaussian saturation pulse of 2.74 ms with a 1000 Hz frequency range to spoil the water signal was applied.

2.4 Animal model care and preparation

Animal care and use were in accordance with the regulations of the French Ministry of Agriculture and approved by the Pays de la Loire Ethics in Animal Experimentation Committee under project number 01858.03. Animals were housed in a controlled and pathogen-free environment, with free access to food and water, at the University animal facility (SCAHU-Angers, France). Animal

anaesthesia was induced by a continuous flow of air (0.5-0.8 L/min) and 3 % isoflurane (Piramal Healthcare, UK Limited, Northumberland, UK) and maintained with 0.5-1 % isoflurane. Body temperature was maintained during MR acquisition using a heated water circulating system. Respiration was also monitored. Three animal models were used in this *in vivo* study; an intramuscular tissue model and two tumoural tissue models, namely subcutaneous fibrosarcoma and intracerebral glioblastoma tumours.

2.4.1 Normal gastrocnemius muscle animal model

Five 7-week old male C3H/HeJ mice (Janvier, Le Genest Saint Isle, France) were used for the intramuscular tissue study.

2.4.2 Cell culture for tumoural animal models

Two tumour models were used in this study; a subcutaneous fibrosarcoma model and an intracerebral glioblastoma model. Culture reagents were obtained from Thermo Fisher Scientific, Gibco and BioWhittaker (France). For the subcutaneous fibrosarcoma model, the syngenic FSaII fibrosarcoma murine cell line [658] was utilised and grown in Dulbecco's modified Eagle's medium (DMEM) high glucose GlutaMAX supplemented with 10 % bovine serum and 1 % Pen/Strep. For the intracerebral glioblastoma model, the C6 rat glioma cell line was purchased from ECACC and was grown in Ham's F12 medium, supplemented with 1 mM L-glutamine, 10 % bovine serum and 1 % Pen/Strep. Cells were grown in standard cell culture conditions (21 % O_2, 5 % CO_2 and 37 °C).

2.4.2.1 Subcutaneous fibrosarcoma tumour model

Seven male 7-week-old C3H/HeJ mice (Janvier, Le Genest Saint Isle, France) were inoculated subcutaneously into the hind thigh with 2 x 10^6 FSaII cells in 100 µL serum-free DMEM under isoflurane anaesthesia. MR experiments were undertaken once tumours reached 8-10 mm in diameter.

2.4.2.2 Intracerebral glioblastoma tumour model

Glioblastomas were induced in the caudate putamen of 10-12 week-old female Sprague-Dawley rats (n = 6) (SCAHU-Angers, France) via the stereotaxic inoculation of C6 rat glioma cells as previously described [659]. Briefly, under Rompun® (Xylazine, Bayer AG, Leverkusen,Germany) and Clorketam® (Kétamine, Vétoquinol, Lure, France) anaesthesia, rats were fixed in a stereotaxic

holder and placed on a heating pad to maintain the appropriate physiological temperature. Through a 1 mm drilled hole in the skull (anterior 5 mm, lateral 3 mm, depth 7 mm in respect to bregma), a 5 µL suspension of 4.0 x 10^4 C6 rat glioma cells were injected over a 10 min period into the caudate putamen of the right hemisphere. After surgery, rats received a single 30 µg/kg subcutaneous injection of Vetergesic® (buprenorphin, Sogeval, France) for pain management. Animals were monitored daily for grooming and mobility, and MR experiments commenced when tumours reached approximately 30 µL in volume.

2.5 MR experiments

MR imaging was performed using a 7T scanner (Biospec 70/20 Avance III, Bruker Wissembourg, France) equipped with BGA12S gradient system (675 mT/m). Emission was ensured by an 86 mm diameter resonator and reception by a 2 x 2 cm surface array coil positioned over the rat head for C6-glioma experiment and or a 2 cm diameter loop coil positioned under the mouse leg or tumour. For the duration of all MR experiments, animal temperature was regulated by a heated water-circulating system. For anatomical images, T_2-weighted rapid acquisition with refocused echoes (RARE) set of images was acquired to follow the volume of tumours (TR = 3200 ms; TE = 21.3 ms; RARE factor = 4; FOV = 4 x 4; matrix = 256 x 256; nine contiguous slices of 0.5 mm, Nex = 1). Thus, once tumours were of proper size, the LNC suspension was injected into the tissue. Animals were anaesthetised, and a bolus injection of 40 µL was injected intramuscularly in the normal tissue model, or intratumourally for the subcutaneous fibrosarcoma tumour model. For LNC delivery into the intracerebral glioblastoma tumour model, a convection-enhanced delivery (CED) protocol [606,660] was implemented to provide a well-diffused distribution of the 40 µL LNCs in the brain tumour. Once the LNC suspension was introduced into the animal model, T_1 was measured using the MOBILE MR sequence (with acquisition parameters described in section 2.3, with geometry changes for *in vivo* experiments adjusted as follows; SL of 3 mm, and a 1 x 1 cm FOV for mice and 3 x 3 cm for rats). LNC T_1 sensitivity to oxygen variation in the different animal models was assessed using a 20 min carbogen gas (95 % O_2, 5 % CO_2) breathing challenge [323].

2.5.1 T_1 lipid measurement using MOBILE

The MOBILE sequence, described by Jordan et al. [508] as a segmented inversion-recovery fast imaging with steady state precession (IR FISP), was used to acquire

images in order to calculate T_1 relaxation time maps whilst the animal was breathing air and carbogen. After the acquisition of the T_1-weighted MOBILE MR image set, the T_1 was calculated using a non-linear fit with a home-made program written in Matlab (The MathWorks, Inc., Natick, MA) for a global value of a manually drawn region of interest (ROI), and for each pixel within the same ROI, wherein the magnetisation M_z is a function of the inversion time (TI), according to: according to: $M_z(TI) = A - Bexp(-TI/C)$; with $A = M_0(T_1*/T_1)$; $B = M_0(1 + T_1*/T_1)$; and $C = T_1*$, and then $T_1 = (B/A - 1)T_1*$. The difference between R_1 ($= 1/T_1$) during carbogen and air breathing for each pixel was calculated and represented as oxygenation maps.

2.6 Statistical analysis

For the *in vivo* pO_2 measurements, one-tailed Wilcoxon tests were used to compare the mean changes between groups (air vs. carbogen breathing within the intramuscular, fibrosarcoma and glioblastoma groups). Histogram distributions, linear fits and Wilcoxon rank tests (for pixel-to-pixel analyses) with *p* values < 0.05 (*) were considered significant, and were calculated using Prism 5 software.

3. RESULTS

3.1 LNC preparation and characterisation

The phase inversion process was exploited to obtain LNCs consisting of a lipidic-core (i.e. Labrafac) enclosed within a polymer-based (i.e. PEG) shell. After osmolarity adjustment, the LNCs had an average size and PDI of 60.7 ±0.9 nm and 0.152 ±0.016, respectively. These physicochemical properties are comparable to previously studied LNCs [574,641,642].

3.2 *In vitro* validation of LNCs sensitivity to oxygen

To assess the ability and sensitivity of the LNCs to probe oxygenation variations *in vitro*, R_1 relaxation rates of the formulation's lipid component (i.e. Labrafac core) was assessed, in LNCs equilibrated in different oxygen environments (0 %, 21 % and 100 %) at 37 °C. As shown in **Figure 4-1**, the R_1 of the CH_2 backbone of Labrafac is sensitive to oxygen variation. This is demonstrated by the linear relationship between the change in oxygen from 0 to 100 % and the concurrent increase of R_1 by 30 % (R^2 = 0.9948).

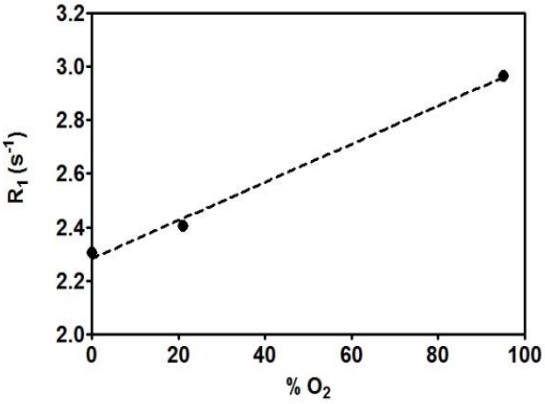

Figure 4-1. *In vitro* sensitivity of the lipid relaxation rate (R_1) arising from lipid nanocapsules (LNCs) to oxygenation as measured by using the MOBILE MR sequence (R^2 = 0.9948).

3.3 Intramuscular pO_2 measurements with LNCs

Following an intramuscular bolus injection of 40 µL of LNCs, a set of T_2-weighted RARE images was acquired to produce an anatomical image (**Fig. 4-2, a**), which was used to define the location wherein the LNCs were deposited. **Figure 4-2 (b)** presents the last image of the MOBILE set, and shows the lipid deposit. It should be noted that the bright areas of the MOBILE image in **Fig. 4-2 (b)** corresponds to the lipid deposit as well as to the subcutaneous fat surrounding the muscle tissue, while the dark areas within the muscle are where no LNCs were introduced. The absence of signal in the muscle highlights that basal muscular lipid content is too low to give rise to significant lipid signal. A ROI was drawn around the lipid hypersignal arising from the LNCs, and was used to calculate the global R_1 for each animal during air or carbogen breathing. Herein, the carbogen challenge was used to induce a transient increase in oxygenation within the normal and tumoural tissue, as previously demonstrated [323,646,647,649]. In the present study, an increase in oxygenation was observed through the increase in the global R_1 over the LNC area for all explored mice (**Fig. 4-2, c**: *p* value = 0.0313, n = 5) with an overall 6 % mean increase. Moreover, a pixel-to-pixel analysis of the LNC area was also performed. The insert in **Figure 4-2 (b)** shows the R_1 change in the lipid deposit area induced by the carbogen challenge on a pixel-to-pixel basis with the corresponding ΔR_1 distribution histogram shown in **Figure 4-2 (d)**. For all mice, a median of 61 % of pixels responded to the carbogen challenge and showed an increase in R_1. For the mouse presented in **Figure 4-2 (d)**, the median change in R_1 after the carbogen challenge was calculated at 0.1509 s^{-1} with 66 % of the pixels responding (for all mice = median change of 0.3450 s^{-1}). For data regarding all individuals in the intramuscular study, see the supplementary documentation (**Appendix A, Fig. 0-1**).

3.4 Intratumoural pO_2 measurements with LNCs

Two tumoural models; the subcutaneous fibrosarcoma and the intracerebral glioblastoma models were used in this study. These tumoural models were chosen to represent two types of severely hypoxic tissues (pO_2 < 10 mmHg [627,649]) and their associated heterogeneity, as well as two different conditions in which LNCs could be administered into tumours. On the one hand, the subcutaneous fibrosarcoma tumours which are easily accessible and in which a bolus injection of LNC solution was deposited; and on the other hand, the intracerebral glioblastoma tumours in which the LNC solution was infused into the tumoural tissue using CED [606,660]. For the subcutaneous fibrosarcoma model, a bolus injection was performed similarly to the intramuscular model. To verify the correct targeting of the injection, a T_2-weighted anatomical RARE image set was performed (**Fig. 4-3, a**), followed by the MOBILE sequence (**Fig. 4-3, b**). As with the intramuscular experiments, a ROI was drawn around the lipid LNC signal in the last image of the MOBILE image set, and was used to determine the global R_1 change after the carbogen challenge for all the animals. A significant global R_1 variation for subcutaneous tumours was induced by the carbogen challenge (**Fig. 4-3**, c; *p* value = 0.0452, n = 7) with a 3 % mean change for the responding animals (6 out of 7). To evaluate the response to the carbogen challenge more in depth, pixel-to-pixel R_1 variation maps illustrating the change in oxygenation was calculated, and an individual's response is illustrated in **Figures 4-3 (b & d)**. For all mice, a median of 71 % of pixels responded to the carbogen challenge and was associated with an increase in R_1. For the individual in **Figures 4-3 (b & d)**, the median change in R_1 after the carbogen challenge was calculated at 0.2034 s^{-1} with 71 % of the pixels responding (for all mice = median change of 0.1779 s^{-1}). Data regarding all individuals in the subcutaneous fibrosarcoma tumour study are presented in the supplementary documentation (**Appendix A, Fig. 0-2**). For the intracerebral glioblastoma tumour model, a CED protocol was used to introduce the LNCs into the brain tumour and the distribution of the solution is apparent in the T_2-weighted anatomical RARE image (**Fig. 4-4, a**). As in the two previous animal models, the MOBILE MR image (**Fig. 4-4, b**) was used to draw the global ROI to determine the change in R_1. Here, a similar pattern emerges as with the subcutaneous fibrosarcoma tumours; five out of the six intracerebral glioblastoma tumours responded with an average of 6 % increase in global R_1 (**Fig. 4-4, c**; *p* value

= 0.0313, n = 6). Pixel-to-pixel analysis of the change in global R_1 from air to carbogen (**Fig. 4-4, b insert**) highlights the response of an individual responding to the carbogen challenge, and all individuals in the intracerebral glioblastoma study are represented in the supplementary documentation (**Appendix A, Fig. 0-3**).

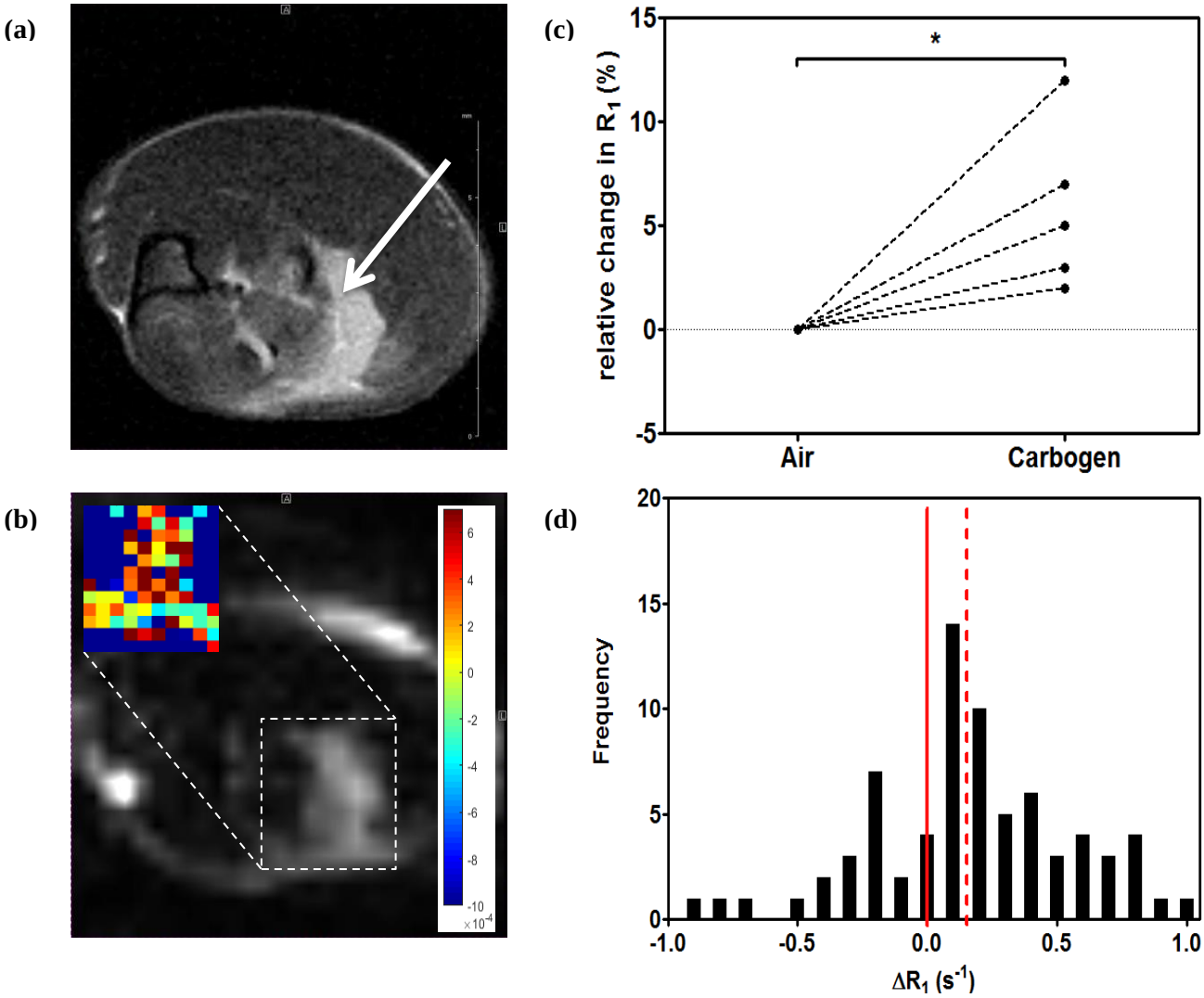

Figure 4-2. Application of lipid nanocapsules (LNCs) to assess variations of oxygenation in the intramuscular tissue of mice using lipid relaxation rate measured with the MOBILE MR sequence, wherein **(a)** shows the transversal anatomical image of a mouse gastrocnemius muscle and the injected LNCs (indicated by arrow) and **(b)** shows the lipid image issued from the set of images acquired with the MOBILE MR sequence wherein the lipids from the LNCs can be observed. The global R_1 measured over the entire lipid deposit signal for all mice (n = 5) is shown in **(c)** (*p* value = 0.0313 indicated by *). The insert in (b) indicates the change in R_1 ($\Delta R_1 = R_{1\ carbogen} - R_{1\ air}$) for each pixel of lipid signal in the MOBILE image and a colour scale highlights the more responsive pixels in red (s^{-1}). ΔR_1 distribution of all encompassing pixels in the lipid deposit region of interest is represented as a histogram **(d)**, wherein the median change of R_1 is indicated with a dotted red line.

In the intracerebral glioblastoma study, a median of 62 % of pixels for all animals responded to the carbogen challenge. For the individual in **Fig. 4-4 (d)**, 76 % of pixels responded to the carbogen challenge to produce a median change of 0.2475 s^{-1} (median change of 0.3187 s^{-1} for all rats).

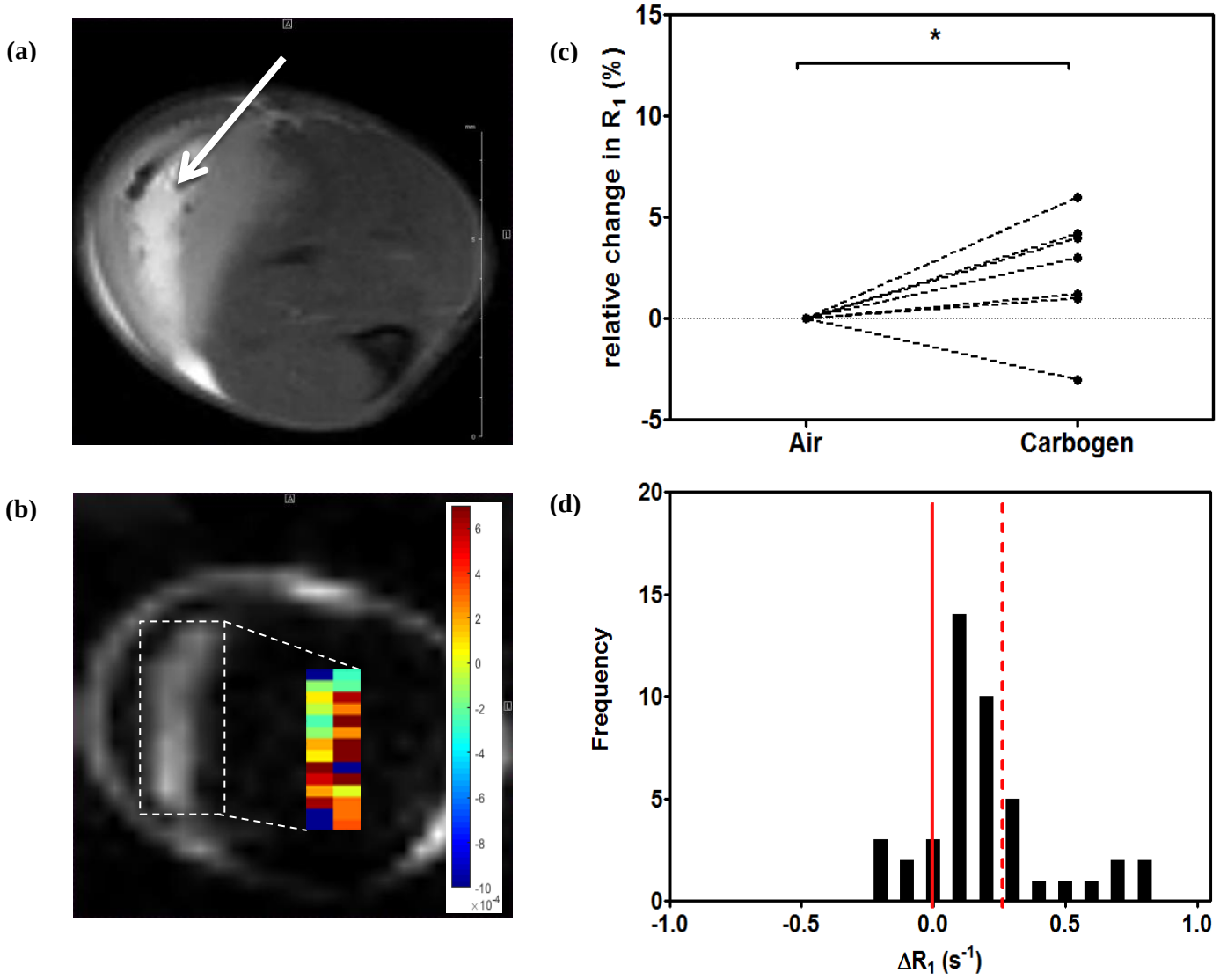

Figure 4-3. Application of lipid nanocapsules (LNCs) to assess variations of oxygenation in a subcutaneous FSaII fibrosarcoma tumour mouse model using lipid relaxation rate measured with the MOBILE MR sequence, wherein **(a)** shows the transversal anatomical image of a fibrosarcoma tumour and the injected LNCs (indicated by arrow) and **(b)** shows the lipid image issued from the set of images acquired with the MOBILE MR sequence wherein the lipids from the LNCs can be observed. The global R_1 measured over the entire lipid deposit signal for all mice (n = 7) is shown in **(c)** (*p* value = 0.0452 indicated by *). The insert in **(b)** indicates the change in R_1 ($\Delta R_1 = R_{1\ carbogen} - R_{1\ air}$) for each pixel of lipid signal in the MOBILE image and a colour scale highlights the more responsive pixels in red (s^{-1}). ΔR_1 distribution of all encompassing pixels in the lipid deposit region of interest is represented as a histogram **(d)**, wherein the median change of R_1 is indicated with a dotted red line.

It should also be noted, that for both the subcutaneous and glioblastoma models the MOBILE MR sequence was performed over the entire organ or leg. Thus, notwithstanding the bright area attributed to subcutaneous fat, other tissues appear as dark areas in the image sets (**Fig. 4-3, b & 4-4, b**) and illustrate that the intrinsic lipid

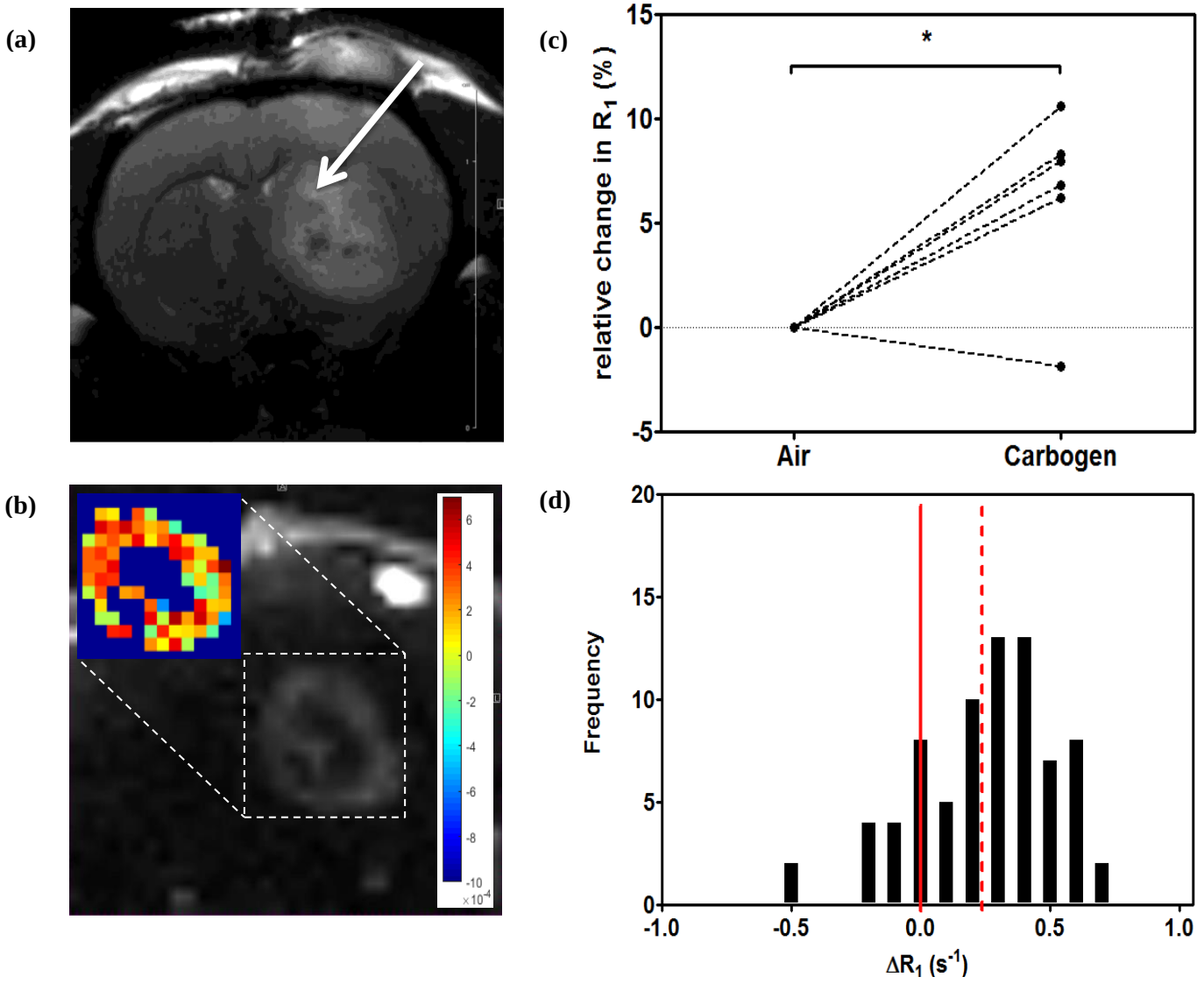

Figure 4-4. Application of lipid nanocapsules (LNCs) to assess variations of oxygenation in a glioblastoma tumour mouse rat using lipid relaxation rate measured with the MOBILE MR sequence, wherein **(a)** shows the transversal anatomical image of a glioblastoma tumour and the injected LNCs (indicated by arrow) and **(b)** shows the lipid image issued from the set of images acquired with the MOBILE MR sequence wherein the lipids from the LNCs can be observed. The global R_1 measured over the entire lipid deposit signal for all rats (n = 6) is shown in **(c)** (*p* value = 0.0313 indicated by *). The insert in (b) indicates the change in R_1 ($\Delta R_1 = R_{1\ carbogen} - R_{1\ air}$) for each pixel of lipid signal in the MOBILE image and a colour scale highlights the more responsive pixels in red (s^{-1}). ΔR_1 distribution of all encompassing pixels in the lipid deposit region of interest is represented as a histogram **(d)**, wherein the median change of R_1 is indicated with a dotted red line.

content was not high enough to be detected, demonstrating the necessary input of lipid provided by the LNCs.

4. DISCUSSION

In the present work, the main objective was to demonstrate the ability of LNCs to probe the oxygen level of normal and tumoural tissues. This was achieved using the MOBILE MR sequence [508] that was developed to assess oxygenation based on lipid longitudinal relaxation time. LNCs are excellent for use in tumour therapeutics as they are size tuneable, can avoid the immune system, have a neutral surface charge, are formulated with FDA approved constituents which make them suitable for *in vivo* administration, and they possess a large lipidic reservoir in which lipophilic agents and drugs can be embedded [596,661].

Thus LNCs, which are already used as a therapeutic nanocarrier [573,593,596,597,661], could also provide oxygenation information of tissues and double as a diagnostic tool thus becoming a theranostic platform. The ability of LNCs to respond to variations in oxygen was established using *in vitro* conditions wherein the oxygenation environment was controlled. Oxygen level variation accounts for a substantial change in R_1 and a linear relationship could be established (**Fig. 4-1**); as oxygenation increased, R_1 increased correspondingly. This relationship between the R_1 of lipids found in the LNCs and oxygen content could be reliably demonstrated and led to *in vivo* experimentation.

Thus, to further test the ability of the LNCs to probe oxygenation variation *in vivo*, a carbogen challenge was performed using three animal tissue models, namely a normal gastrocnemius muscle tissue model and two tumoural tissue models [428,650,662,663]. A bolus injection was used to introduce the LNC formulation into the muscle tissue, and the MOBILE MR image after the injection showed that the solution remained as a conglomeration, i.e. as a ‘drop’ (**Fig. 4-2 & 4-3, b**). This ‘drop’ of injected LNCs remained as is for the duration of the experiments and did not diffuse throughout the tissue. This can be attributed to the direct injection into the tissue; since the LNCs circumvent the washout and biodistribution associated with an intravenous injection [568,664–666] this allows for the formulation’s sustained presence within the tissue. Thus, the persistence of a ‘drop’ of injected LNCs within the tissue is to be expected, as the normal gastrocnemius muscle is a highly hierarchized tissue and the bolus injection takes place over a short period of time, thus not allowing the liquid to disperse throughout the tissue. Regardless of the

dispersion of the injected LNCs in the tissue, the lipids in the LNCs responded to the carbogen challenge and a map portraying the variation of the T_1 relaxation rate induced by percentage O_2 inhaled could be produced. This map enabled the visualisation of tissue pO_2 of the normal gastrocnemius muscle. Of note, the intrinsic muscular lipidic signal is too low to portray the effect of the challenge, thus making the LNC injection compulsory as no lipid signal can be observed outside the lipid drop (**Fig. 4-2, b**). This observation was also noted in the tumoural models used in this study (**Fig. 4-3 & 4-4, b**).

Within the subcutaneous fibrosarcoma tumours, an overall more limited response to the carbogen challenge was noted; an average R_1 increase of 3 %, as compared to the 6 % from both the gastrocnemius muscles and intracerebral glioblastomas (**Fig. 4-2 – 4-4, c**). This muted response could be attributed to the poor blood perfusion prevalent in this tumour model [384,422,627], which limits the blood's transportation of the carbogen gas to the tissue environment near the drop of LNCs. Similarly, this could explain the instance in which the R_1 decreased after the carbogen challenge in an individual animal. On the contrary, the intracerebral glioblastoma model, is associated with a heterogeneous tumour microenvironment which is highly vascularised [649]. This readily explains the increased response of this tumour model, comparative to the normal gastrocnemius muscle tissue, to the carbogen challenge. Furthermore, the methods of LNC introduction between the two tumour models should be noted. The CED protocol allowed for a more even distribution of the LNCs throughout the brain tumour tissue, whereas the bolus injection within the muscle and subcutaneous tumour model only allowed for the mapping of the LNCs within the drop.

Oxygenation mapping within the normal tissue and tumoural models showed that LNCs were able to improve the lipid signal-to-noise ratio to such an extent that pixel-to-pixel analysis of the area was achievable. Therefore, it was possible to image and analyse the response of each pixel to the carbogen challenge within all the animal models without using ionising probes or specialised ^{19}F-based MR equipment [294,485], thus making our system more widely applicable. Furthermore, in our study, the bolus injection allowed for a very specific site within the muscle and subcutaneous fibrosarcoma tumour to be analysed, whereas the CED diffusion of the LNCs throughout the intracerebral glioblastoma model allowed for the

mapping and analysis of the entire area of the injected LNCs. Using the pixel-to-pixel analysis, it was possible to map the heterogeneity of the response from air to carbogen breathing for each animal (**Fig. 4-2 – 4-4, c**) and the median overall change of the pixels could be calculated (**Fig. 4-2 – 4-4, d**).

Although mapping of pO_2 change in tissue was achievable and successful, the conversion of R_1 to pO_2 proved difficult *in vivo*. Direct conversion, on the basis of data presented in **Figure 4-1**, of R_1 into absolute pO_2 values cannot be done because although R_1 has been shown to be dependent on oxygenation it is also dependant on the heterogeneity of tissues, viscosity and iron content for example [667–670], all of which are variables that cannot be easily mimicked *in vitro*.

5. CONCLUSION

Herein, our aim was to demonstrate that LNCs, besides its proved therapeutic nanocarrier efficiency, could be used as a diagnostic tool in the form of an oxygen sensor for normal and tumoural tissue using the MOBILE MR sequence. LNCs were synthesised using the phase-inversion process, and the osmolarity of the formulation was adjusted for safe *in vivo* use. *In vitro* validation showed a linear relationship between oxygen variation and R_1, thus demonstrating the permeability and responsiveness of the LNCs to oxygen. For *in vivo* experimentation, three animal models; a normal muscle model and two tumoural tissue models (subcutaneous fibrosarcoma and intracerebral glioblastoma), were subjected to a carbogen challenge (95 % O_2, 5 % CO_2) to induce transient oxygenation changes within the tissue. From a single bolus injection of the LNCs, both a global R_1 value, as well as a pixel-to-pixel analysis was possible, due to the improved signal-to-noise provided by the lipid-core of the LNCs. However, because the bolus injection occurred over a short period of time, a limited area of tissue could be mapped. Thus, a CED injection was used to diffuse the LNCs throughout the intracerebral glioblastoma tumours to provide a more detailed oxygenation and heterogeneity map. Unfortunately, only relative pO_2 values were achievable from the LNC system as a myriad of parameters influence T_1 relaxation *in vivo*. Regardless, these developments and results indicate that LNCs could be used as both a therapeutic and diagnostic tool for cancer.

ACKNOWLEDGEMENTS

The authors would like to thank the NanoFar Erasmus Mundus program, le comité départemental de Maine et Loire de la Ligue Contre le Cancer (France), and la

Commission du Patrimoine (Université catholique de Louvain) for providing the funding for this project.

4.3 *IN VIVO* FATE OF LNCS AFTER DIRECT DEPOSIT IN TISSUE

4.3.1 Introduction

In this section the unpublished work pertaining to the above article in section 4.2, will be presented and discussed. Herein, the *in vivo* fate of the LNC formulation was explored as, according to literature and with respect to their therapeutical capabilities, they are broken apart or metabolised by cells and tissues over time. The objective of the experiments presented here was to address this issue.

4.3.2 Materials and methods

4.3.2.1 Synthesis of LNCs

Chemicals and formulation process for LNCs were as described in section 4.2.

4.3.2.2 Animal models

Three murine animal models were used in this *in vivo* study; two normal tissue models, i.e. a normal gastrocnemius muscle model in C3H/HeJ mice (Janvier, Le Genest Saint Isle, France) (n = 5), a normal brain model in female Sprague Dawley rats (SCAHU-Angers, France) (n = 6), and one tumoural tissue model, i.e. the C6 intracerebral glioblastoma tumour model in female Sprague Dawley rats (SCAHU-Angers, France) (n = 5) as described.

4.3.2.3 MR experiments

MR imaging was performed using a 7T scanner (Biospec 70/20 Avance III, Bruker Wissembourg, France) equipped with BGA12S gradient system (675 mT/m) as described in section 4.2. Lipid signal was attained from the described MOBILE sequence (acquisition parameters described in section 4.2).

LNC fate was evaluated after a 40 µL injection of the formulation using either a bolus injection in the normal gastrocnemius muscle or the CED protocol for the normal brain and the C6 intracerebral glioblastoma model. The CED protocol involved the injection of 40 µL of the LNC formulation at the coordinates of the tumour cells (or, in the case of the normal brain animals, in the same coordinates in which the cells would have been injected). Infusions were performed at the depth of 5 mm from the brain surface using a 40 µL Hamilton® syringe with a 22G needle. CED was performed with an osmotic pump PHD 2000 Infusion

(Harvard Apparatus, Les Ulis, France) at 0.5 µL/min rate for 80 min. Afterward, the needle was held in place for 5 additional minutes to avoid the expulsion of the LNC formulation from the brain during removal of the needle, which was withdrawn slowly (0.5 mm per 30 seconds). The incision was stitched and the animal was prepared for the MR experiments. Evaluation of the LNC formulations fate was assessed using point resolved spectroscopy (PRESS).

4.3.2.3.1 PRESS measurements

The PRESS sequence was used to determine the lipid content (CH_2 associated with the backbone of Labrafac®) of the injected LNCs. A single voxel of ~4 x 4 x 4 mm^3 was used for all the animal models. For each individual, the voxel was placed over the LNC area, avoiding vascular structures and subcutaneous fat tissue, and the spectra was recorded using the PRESS pulse sequence (TR = 3000 msec, TE = 10 msec) after water suppression using the variable power and optimised relaxation delays (VAPOR) pulse train [671]. The methylene signal, which represents CH_2 backbone of the Labrafac® within the LNCs, was measured at 1.2 ppm. This peak was measured in comparison to the water peak (4.7 ppm).

4.3.3 Results

4.3.3.1 Dispersion of LNC lipids over time

After the introduction of the LNC formulation, the PRESS MR sequence was used to acquire the spectra of the compounds present in the voxel within the animal models. An example of the constituents associated with the LNC formulation within the intracerebral brain tumour model is shown in **Figure 4-5**. In this example, the resonance associated with the water (chemical shift = 4.7 ppm) is unsuppressed and was used to determine the ratio between the water and CH_2 resonance (chemical shift = 1.2 ppm) associated with the LNC constituent Labrafac® over time. In the insert of **Figure 4-5**, the metabolites – creatine (chemical shift = 3.0) and choline (chemical shift = 3.2) – commonly associated with a tumour induced with C6 glioblastoma cells can be observed for both the spectra [672,673]. In both the water unsuppressed and suppressed spectra, a decrease in the resonances of PEG and CH_2 can be noted over time, with no PEG being measured after 24 h.

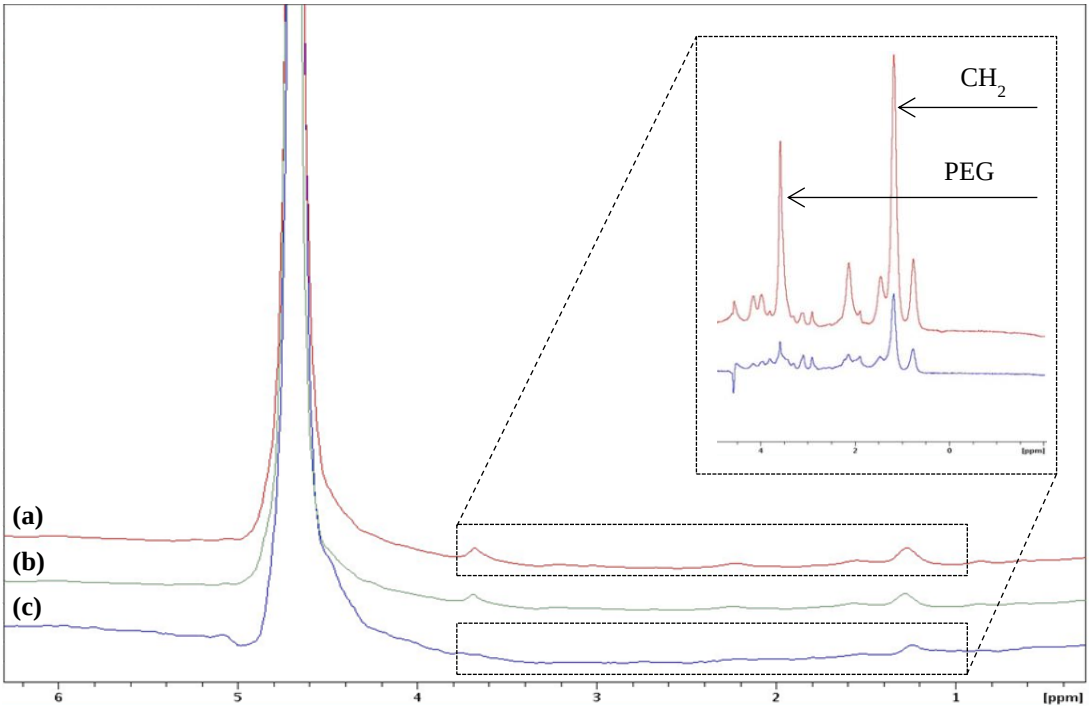

Figure 4-6. Spectra obtained using the MR PRESS sequence within the brain tumour animal model. The chemical shift for water is located at 4.7 ppm and the PEG and CH_2, associated with the LNCs, is located at 3.7 and 1.2 ppm, respectively. Spectra were acquired directly after the CED injection **(a)**, approximately one hour later **(b)** and 24 h after **(c)**. The insert shows the spectra acquired (with water suppression) directly after **(a, red)** and 24 h after **(c, blue)** the LNC introduction, and demonstrates the decrease of the LNC constituents, PEG and CH_2, over time.

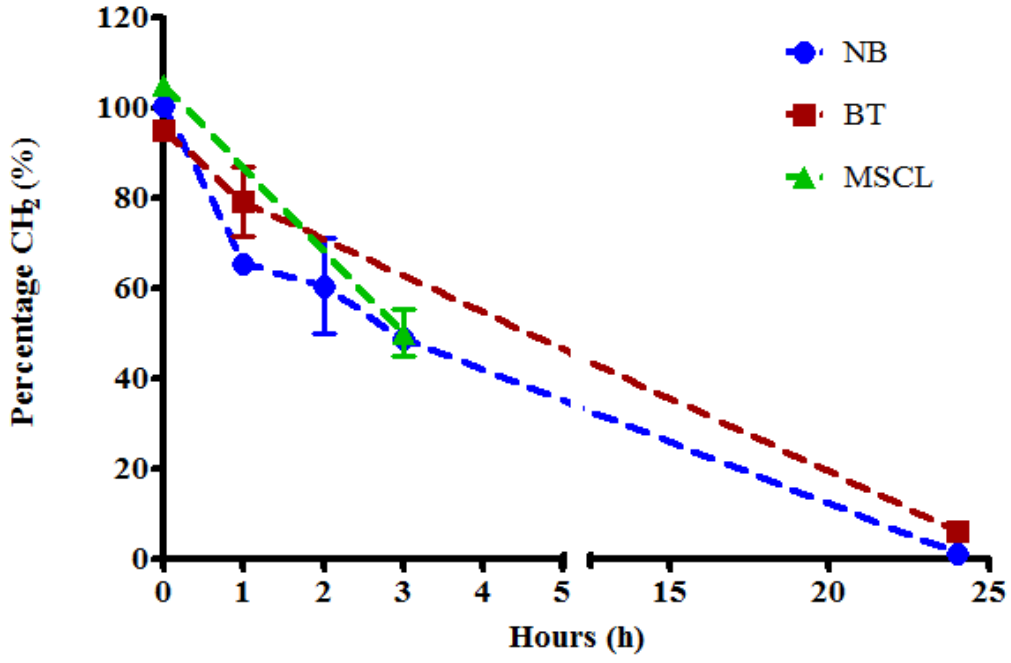

Figure 4-5. Percentage (%) of CH_2, associated with the lipids from LNCs, within the normal brain (NB, blue circle) model, the brain tumour (BT, red square) model and the normal muscle (MSCL, green triangle) model over time as compared to water.

A semi-quantitative analysis, using the ratio between the unsuppressed water and CH_2, was performed for all the animal models (**Fig. 4-6**). Here, the signal corresponding to the LNC, especially the CH_2 used for pO_2 estimation, decreases after one hour to about 80 % of the value measured just after injection for all the animal models explored. Two hours later, a further 25 % decrease is observed, and for two animals – one normal brain and one brain tumour – explored at 24 h after the initial injection, the CH_2 peak returns to pre-injection values.

Of note, and in complement to the main results included in the publication, the aforementioned *in vivo* LNC fate experiment enabled the response of the normal brain to the carbogen challenge to be measured. Interestingly, on both the RARE and MOBILE images it is apparent that a portion of the LNC formulation settled in the corpus callosum of the rat brain despite an injection into the striatum, thus showing a reflux of the LNC formulation from the well-organised normal brain. This phenomenon was noted in 5 of 6 animals. However, this did not impair the calculation of R_1 in the striatum before and after the carbogen challenge following the application of the MOBILE MR sequence, and as shown in **Figure 4-7**, an average increase of 9 % was observed ($p = 0.0469$, $n = 6$). For the data regarding all individuals in the normal brain tissue study, see the supplementary documentation (**Appendix B, Fig. 0-4**).

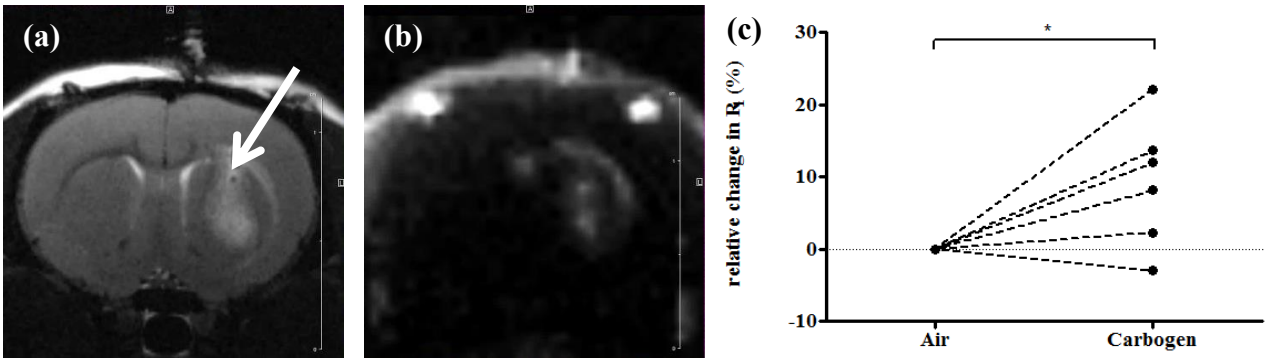

Figure 4-7. Application of LNCs to assess variations of oxygenation in the normal brain tissue of rats using lipid relaxation rate measured with the MOBILE MR sequence, wherein **(a)** shows the anatomical image of the rat brain and the injected LNCs (indicated by arrow) and **(b)** shows the lipid image from the set of images acquired with the MOBILE MR sequence wherein the lipids from the LNCs can be observed. The global R_1 measured over the entire lipid deposit signal for all rats ($n = 6$) is shown in **(c)**. A one-tailed Wilcoxon tests was used to compare the R_1 change between air vs. carbogen breathing, and *p* values < 0.05 (*) were considered significant, and were calculated using the Prism 5 software.

4.3.4 Discussion and conclusions

Assessing the fate of LNC after injection was an important factor to assess as this information has a direct impact in the time frame in which LNCs can be used as an O_2 sensor within the tissue. The semi-quantitative PRESS analysis revealed that the lipid signal arising from the LNCs decreased by 50 – 60 % for all the animal models tested. Most notable, however, was the decline in observable lipid (1.2 ppm) and PEG (3.7 ppm) resonances associated with the LNCs after 24 h. These results indicate that the LNCs cannot be used in the context of long-term (e.g. several days) oximetry measurements *in vivo*. Such a decline in LNCs could be associated with the metabolic degradation of the nanocapsules within the tissue, or the displacement of the LNCs from the measured area (i.e. the injected area).

Chapter 5:

Conclusions, Limitations and Perspectives

5.1 CONCLUSIONS

This thesis was focused on developing LNCs – which have already been established as a nanocarrier for cancer therapeutics – as an O_2 nanosensor capable of measuring and imaging pO_2 in hypoxic tissues, including tumours, using EPR and MRI methods.

EPR oximetry is potentially capable of producing real-time, repeated measurements of pO_2 values within tissues in a non-invasive manner without consuming O_2. The technique uses paramagnetic spin probes which can be either in solutions or in particulate forms. Among the soluble paramagnetic materials, two types of spin probes are particularly interesting: the nitroxides and the triarylmethyl radicals. The nitroxide spin probes have a rich history in EPR; the compounds have been used to measure numerous *in vivo* parameters, including pO_2, with accuracy and sensitivity [674]. However, although these compounds have been extensively modified to modulate their intracellular accumulation and tissue sensitivity [354,355] for improved *in vivo* use, upon contact with certain metabolic enzymes they are converted to the EPR-silent hydroxylamines which can hinder their usefulness. Alternatively, the triarylmethyl radicals – including the spin probe TAM – are considered to be less sensitive to metabolic enzymes with possible higher stability, although this has been re-evaluated in the literature [675]. TAM is also characterised by a narrower LW than nitroxides, such as TEMPO and TB **(Fig. 2-12 and 2-13)**, at 21 % O_2 thus indicating its increased O_2 sensitivity [676]. Altogether, the soluble spin probes have the advantage of diffusing throughout a tissue – as opposed to the particulate EPR spin probes which are implanted in an area – and providing measurements of O_2 values. Unfortunately, the soluble spin probes are prone to signal decrease due to rapid washout and metabolic biotransformation. Furthermore, soluble EPR probes are less sensitive to O_2 changes compared to particulate EPR probes which can be problematic for evaluating subtle changes in tissue oxygenation. To overcome this limitation, encapsulation within a lipophilic environment has been explored [442]. Consistent with the Smoluchowski equation, as O_2 is more soluble in lipophilic environment than in water, an increase in sensitivity can be achieved using these systems. Thus, the encapsulation of nitroxide probes – TEMPO and TB – and a triarylmethyl radical – TAM – within the lipophilic core of LNCs was proposed. The encapsulation was hypothesised to improve O_2 sensitivity, create a defined microenvironment for the spin probe which ensures specificity, and prevent biocompatibility issues *in vivo*.

In this regard, LNCs were an excellent candidate as not only could they provide the aforementioned advantages, but they are also prepared using FDA approved constituents and

have previously been employed in several studies of tumour therapeutics as an encapsulation agent **(see Chapter 2, section 2.6)**. In this body of work, it was demonstrated that LNCs could incorporate either the TB or TAM EPR spin probes within its lipophilic core and provide adequate EPR signal after formulation. The TAM-LNCs were found to be responsive to O_2 variation *in vitro* and demonstrated by a direct relationship between the LW and O_2 variation **(Fig. 3-4)**, thus indicating the permeability of LNCs to O_2. Notably, TB-LNCs were also found to be sensitive to O_2 variation but at a lower extent than the TAM-LNCs. TAM-LNCs were also applied to *in vivo* systems, both in normal muscle and subcutaneous fibrosarcoma tumour models, wherein they were noted to be responsive to an increase in the O_2 concentration within the tissues **(Fig. 3-6 and 3-7)** (following the carbogen challenge), as well as a decrease in the O_2 environment **(Fig. 3-12)** (following the temporary occlusion of an artery). This indicated that the TAM-LNCs were reversibly responsive to O_2 changes *in vivo*. The LNCs were also noted to protect the TB EPR spin probe it encapsulated from metabolic conversion **(Fig. 3-3)**. Interestingly, although the TAM-LNCs were protected within the LNCs (as demonstrated by the sustained TAM signal over time *in vivo*, **Fig. 3-5**), a decrease in the signal intensity is notable over time which was similar to the decrease of measurable signal over time noted for the LNCs in the MRI experiments.

MRI-based techniques are ideally suited for the assessment and imaging of tumour physiology and hypoxia as it is non-invasive, quantitative, widely available and able to reflect tumour heterogeneity. MRI techniques for hypoxia determination include perfusion- and probe-based (both exogenous and endogenous) imaging. Notably, however, perfusion-based techniques – such as BOLD, FLOOD or OE-MRI – do not provide direct pO_2 values but instead rely on relative changes in blood flow and Hb/HbO_2 ratio, furthermore these methods suffer from poor sensitivity, and changes to relaxation times not related to O_2 level [504]. Alternatively, probe-based methods rely on either exogenous or endogenous probes for pO_2 measurements. Notable exogenous probes include ^{19}F which, although sensitive to tumoural levels of O_2, requires specialised MR equipment. Of course, endogenous probes – such as water and lipids – have no such limitation. However, although water is an attractive option for monitoring tumoural pO_2 – due to its abundance in biological tissue – methods which monitor its relaxation rate could be considered as not sensitive enough for measuring hypoxia in tumours [323,504,505,677]. Notably, the water T_1 change with O_2 concentration is limited and lower than the change observed in lipids due to the six times higher solubility of O_2 in lipids than in water [506]. Thus, Jordan and colleagues developed the MOBILE MR sequence [508]

which exploited this phenomenon to map O_2 in tissues by imaging lipids relaxation enhancement. The drawback of this method, however, is that it requires a sufficient amount of lipids in the tissue of interest to enable the MOBILE sequence to produce a lipid image. This limitation was overcome by the use of LNCs – which possess an oily-core – which could thus serve to increase the SNR by strategically increasing the lipidic content within tissue.

Here, LNCs were assessed for their ability to respond to O_2 variations both *in vitro* and *in vivo* using the MOBILE MR sequence, and a direct relationship between the R_1 and O_2 % was observed **(Fig. 4-1)**. This coincided with the EPR results wherein the TAM within the LNCs could respond to O_2 changes, thus further demonstrating the permeability of the LNCs to O_2. To demonstrate the ability of the LNCs to respond *in vivo*, several animal models including both normal tissue and hypoxic tumoural tissues were used. LNCs were evaluated as a tool to assess and image the heterogeneity of hypoxia within tumours. Here, a bolus injection was used – similar to the EPR experiments – which deposited a lipid 'droplet' within normal muscle and subcutaneous fibrosarcoma tumour models. Using the MOBILE MR sequence it was possible to image the introduced lipids – in the form of LNCs – as well as measure their response to O_2 variation **(Fig. 4-2 and 4-3)** following a carbogen challenge. It was also possible to produce an oxygenation map wherein the ΔR_1 during air and carbogen breathing could be visualised **(Fig. 4-2 and 4-3, b insert)**. This was possible due to the increase in the SNR of lipids which enabled the pixel-to-pixel analysis of an oxygenation map. Interestingly, but not entirely unexpectedly, although an oxygenation map of the injected LNCs could be produced, the bolus injection – and thus the 'drop' of lipids – allowed for a limited area within the tissue to be mapped. Thus, a second method of introducing the LNCs within tumoural tissue was explored; local diffusion using a CED protocol. It should be noted, that LNCs have previously been introduced as a therapeutic agent nanocarrier into several cancer types – including the highly malignant glioblastoma **(see section Chapter 2)** – using the CED protocol. This is because CED allows for a direct, local delivery into the tissue of interest and enables an efficient distribution of the introduced LNC formulation. Hence, an intracerebral glioblastoma model was used for the CED introduction of the LNC formulation, and the MOBILE MR sequence was able to measure the R_1 change between air and carbogen breathing **(Fig.4-4)**. Furthermore, due to the large distribution of the LNCs, a map representing the oxygenation over the entire tumour was possible and the pixel-to-pixel analysis highlighted the heterogeneity of the glioblastoma tissue to the hyperoxic challenge **(Fig. 4-4, b insert)**. However, the signal was only

measurable for a few hours (2 – 3 h) after the LNC injection as the lipid signal decreased over time. To demonstrate this observation, the fate of the LNCs *in vivo* was explored using MR spectroscopy (PRESS) in the context of CED delivery in both normal brain and tumoural brain tissue. This semi-quantitative analysis indicated a decrease of approximately 50 - 60 % of the signal arising from the LNC formulation 3 h after its introduction in the tissue, and a return to base quantities after 24 h **(Fig. 4-6)**. This decline could be associated with the metabolic degradation of the LNCs within the tissue or the movement of the LNCs out of the area being studied.

In summation, this body of work showed that LNCs could serve as an O_2 sensor within tissues using both EPR and MRI. For the EPR spin probes, it served as an effective encapsulation device capable of protecting the TAM spin probes which proved to be O_2 permeable, allowing for pO_2 measurements to be determined for both normal and tumours tissues. Furthermore, the lipids within LNCs were not only detectable by the MOBILE MR sequence, but also increased the SNR sufficiently to allow for the pixel-to-pixel analysis of oxygenation maps within hypoxic tumoural tissue.

5.2 LIMITATIONS AND PERSPECTIVES

In this thesis, the feasibility and usefulness of LNCs as a diagnostic O_2 sensor using EPR and MRI within *in vitro* studies and *in vivo* models was demonstrated, showing that this system is a promising nanoplatform for combining cancer therapeutics and diagnostics. The LNC formulation is simple to synthesise and has been well-characterised, its constituents are FDA approved for *in vivo* use, and the therapeutic uses of drug-loaded LNCs have been demonstrated in several pre-clinical studies. Similarly, the magnetic resonance techniques used in this thesis, EPR and MRI, are frequently used for determining tumour physiology and oxygenation. These MR methods have well-understood limitations with respect to oxygen assessment – such as the degradation of the soluble EPR spin probes with time and the intrinsically low signal-to-noise ratio of the lipids assessed with the MOBILE MR sequence in MRI – which were addressed in this thesis by the use of the LNC formulations. However, there are still several limitations that should be addressed in regards to the application of LNCs as an O_2 sensor in tumours. Some of these limitations, and their associated perspectives, are evaluated and discussed in this section wherein **Tables 5-1** and **5-2** consider the *in vitro* parameters and **Tables 5-3** and **5-4** the *in vivo* parameters using a Strengths, Weakness, Opportunities and Threats (SWOT) analysis.

Table 5-1. SWOT analysis of the *in vitro* studies regarding the sensitivity curve.

Strengths	Weaknesses	Opportunities	Threats
***In vitro* studies: Sensitivity curve**			
TAM-LNCs are sensitive to O_2 variation as assessed by EPR (see Fig. 3-2 and 3-4)			
T_1 of lipid CH_2 backbone (Labrafac®) is detectable by the MOBILE sequence, demonstrated linear sensitivity to O_2 variation (see Fig. 4-1)	pO_2 values are overestimated	Develop an improved *ex vivo* model which mimics the *in vivo* situation	Cannot directly convert LW or T_1 to pO_2

Table 5-2. SWOT analysis of *in vitro* studies regarding the LNC formulation.

Strengths	Weaknesses	Opportunities	Threats
***In vitro* studies: LNC formulation**			
Soluble EPR spin probes (nitroxides and trityl) could be encapsulated in LNCs (see Table 3-1, Fig. 3-3 and Fig. 3-5)	Probes with low log P did not remain within lipidic core of LNCs	TB-LNC system could be used as a new tool for free radical scavenging in cells [678]	Bio-reduction of nitroxides; not suitable for oximetry studies
Osmolarity adjusted LNCs comparable to previously published formulations	Dialysis to eliminate salt, followed by re-concentration for *in vivo* use (time consuming)	Use of low energy process	Sterilisation of LNC formulation will require advanced processes

Table 5-3. SWOT analysis of the *in vivo* studies regarding the animal models.

Strengths	Weaknesses	Opportunities	Threats
***In vivo* studies: Animal models**			
No tissue damage (visible by MRI) when LNCs introduced into tissues (see Fig. 4-2, 4-3, 4-4 and 4-7)	No associated proof of tissue hypoxia	Use of immunohistochemistry techniques for hypoxia staining	LNC signal cannot be visualised in necrotic regions
pO_2 changes induced by the carbogen challenge tissue could be assessed using EPR and MRI techniques (see Fig. 3-6, 3-7, 4-2, 4-3, 4-4 and 4-7)		ΔpO_2 map indicating where O_2 diffuses during carbogen challenge; use in dose painting for radiation therapy	

Table 5-4. SWOT analysis of the *in vivo* studies regarding the applicability of LNCs as a theranostic tool

Strengths	Weaknesses	Opportunities	Threats
***In vivo* studies: LNCs as a theranostic tool**			
No 'reservoir effect' was observed for the LNCs (see Fig. 3-11)	Did not evaluate ability of LNCs to accumulate O_2 during carbogen challenge	Design of nanocarrier to sequester O_2	Synthesis of formulation capable of 'reservoir effect'
Increase in lipids and PEG was detectable *in vivo* after LNC introduction with MRI, and showed good SNR (see Fig. 4-9, insert for an example) **TAM-LNC signal measurable *in vivo* for at least 60 min (see Fig. 3-5)** **LNCs produce sufficient signal for MOBILE lipid measurements for 2 - 3 h *in vivo* (see Fig. 4-2, 4-3, 4-4, 4-9 and 4-7)**	Decrease of signal over time	Determination of the origin of the signal decreases: LNC biodegradation and/or formulation dispersion Modification of LNC formulation to limit biodegradation	Stabilisation of LNCs to keep the diagnostic valence may impair the therapeutic one

5.2.1 *In vitro* studies: Sensitivity curve

As noted for both the EPR and MRI studies, higher-than-expected pO_2 values were estimated when LW or T_1 were converted from the sensitivity curves. In Chapter 3, regarding the TAM-LNCs, the presented article noted a discrepancy between the *in vitro* pO_2 sensitivity curve and the pO_2 measured *in vivo*. A potential explanation for this observation, as shown by Frank et al. [375], could arise from local viscosity changes which was demonstrated to have an impact on LW and thus on the conversion to pO_2. Indeed in our study, the sensitivity curve was performed at 37 °C, and the *in vivo* measured LWs were converted to pO_2 on this basis. However, this conversion implies that the temperature of the tumour tissue was also 37 °C which, according to literature is not always the case as it is significantly dependent on the size of the tumour, blood flow, as well as the type and location of the tumour [679–681]. At reduced tumoural temperature, the viscosity of the formulation would be affected – which was not represented in the sensitivity curve – which could lead to the overestimation of pO_2 we encountered. This brought into question the nature of the medium in which the sensitivity curve was performed – for both the EPR and MRI experiments – and its relevance when converting T_1 and LW values into pO_2.

In regards to the MRI experiments, the *in vitro* sensitivity curve between the T_1 relaxation rate from the lipidic core of LNCs and O_2 variation demonstrated a linear relationship but, when R_1 was transposed to pO_2, a higher estimation of pO_2 was also noted within the *in vivo* models, and could be attributed to the environment surrounding the LNCs. Apart from O_2, various factors influence T_1 relaxation and many of which can be found – and must be taken into account – *in vivo*. Such factors include but are not limited to; temperature, viscosity, and iron content. Indeed, as for the EPR experiments, temperature was assumed to be 37 °C. However, as reported in literature [485], a decrease in temperature results in a an increase in R_1 and a proportional increase in pO_2. Thus, if the tumour temperature is lower than the temperature used for the sensitivity curve, converting the R_1 measured *in vivo* on this basis would lead to an overestimation. It could thus have been advantageous, and more representative, to measure the response of T_1 to O_2 and temperature variation in a step-wise fashion.

Another factor which influences T_1 relaxation is viscosity. The use of plasma as a medium – which has a higher viscosity than water at approximately 1.10 – 1.30 mPa.s [682] – could have been used to overcome this issue, however, it would not account for the

complexity encountered in tissue wherein iron could be present or the general organisation of the tissue with a multitude of cells, proteins, and macromolecules interacting with the LNCs which also affects the T_1 relaxation time.

Thus, the development of a more pertinent *ex vivo* model could be of interest. Unfortunately, however, this system presents its own issues as ensuring a homogenous perfusion of the gas throughout the tissue mass – to ensure good homogeneity for the sensitivity curve – and ensuring the LNCs interaction with the gas within the mass would be difficult with the system available during the MRI experiments. Thus, although the use of an aqueous system of LNCs was not the ideal experimental conditions it was used to demonstrate the feasibility of the LNCs system as an O_2 probe which responds well to O_2 variation both *in vitro* and *in vivo*.

5.2.2 *In vitro* studies: LNC formulation

Notably, for the encapsulation and retention of soluble EPR spin probes within LNCs, the use of compounds with a log P equal or less than 1.30 (i.e. TEMPO) is not recommended for oximetry use as presented in this thesis. In the case of the encapsulation of TEMPO, the molecule proved insufficiently lipophilic and separated from the LNCs during formulation. After the encapsulation of TB (log P = 3.10) within LNCs, an EPR spectrum with reduced height in the third line was noted and is indicative of an EPR spin probe whose motion is restricted with possible interaction with the LNC shell. Moreover, when the TB-LNCs were exposed to a reductive environment, the TB signal decreased with time, which is consistent if the TB probe was exposed from the LNC shell. Despite this being non-advantageous for long-term oxygenation measurements, the characteristics of the system could be further analysed using interface analysis techniques such as the pendant drop method. Our conclusion for this work was that a highly lipophilic molecule was required to remain within the O_2 soluble lipidic core of the LNCs whilst being protected by the PEGylated shell. However, for other work such as free radical scavenging within tumoural cells the exposure of the nitroxide to the biological milieu could be useful. As an example, nitroxide derivatives such as piperidine, pyrroline and pyrrolidine mimic the superoxide dismutase which scavenges reactive free radicals and is useful as an antioxidant against the oxidative stress induced by anti-cancer drugs as well as inhibiting tumoural proliferation [678]. If combined with LNCs, the system could provide a targeted delivery to tumoural cells through the use of a

functionalised shell [683]. But, for this thesis, only the use of lipophilic EPR spin probes, such as TAM which remained within the lipidic core of the LNCs, was useful.

As noted previously, the LNCs used in this thesis had comparable physio-chemical properties as previously used formulations (in terms of size, PDI and zeta potential, see **Chapter 2**) both before and after the osmolarity adjustment process. A notable exception, however, is sterility. Aqueous solutions of LNCs are commonly sterilised using mechanical filtration with a pore size of 0.22 µm [573]. This route of sterilisation removes any detectable bacteria, fungi and yeast and does not causes the nanocapsules to agglomerate, nor does it cause changes to their size or PDI (slight changes to zeta potential have been observed) [684]. However, although this method is effective, the use of highly concentrated LNC formulations – such as in this thesis – did not allow for such a sterilisation process and may require the use of a sterilised room with sterilised constituents. Furthermore, the use of such a highly concentrated LNC formulation injected *in vivo* raises concerns of toxicity. Although the LNCs were formulated using regulatory-approved components with similar characteristics (i.e. 50 nm-sized) as previous formulations which were well-tolerated *in vivo* in the past (see **Chapter 2, section 2.6**), an investigation at the cellular level to elucidate the effect of the highly concentrated formulation would be beneficial.

5.2.3 *In vivo* studies: Animal models

Notably, as a proof of concept for the sensitivity of LNCs to pO_2 an *in vivo* model of C6-induced intracerebral glioblastoma animal model was used. This model, although useful, highlighted a limitation for the use of the LNC formulation; if foci of necrosis of haemorrhaging were present, the lipid T_1 relaxation change following a carbogen challenge could not be measured and a qpR_1 map could not be produced in areas without blood perfusion or limited O_2 accessibility. This, however, could be an advantage for future work. The use of the a qpR_1 map produced from the LNC formulation following a carbogen challenge could be used as an indicator for poor O_2 accessibility and could be used as a tool for dose painting during IMRT [685–687]. It is also important to note, that although our work indicated a response within the tissue to carbogen challenge – reflected as changes in LW and T_1 relaxation time – no associated proof of hypoxia was presented. Thus, the use of immunohistochemical staining of tissue samples, such as a 2-nitroimidazole derivative, for hypoxia confirmation could be useful.

Lastly, in regard to the animal models, we demonstrated that TAM-LNCs could respond reversibly to pO_2 changes *in vivo* by using the carbogen challenge (to increase the pO_2) and the occlusion of the femoral artery performed by means of a rubber band tied tightly around the knee (to decrease the pO_2). Here, the LW values seemed to indicate that there was no difference between the two experimental conditions. This could indicate that the TAM-LNCs were not sensitive enough to discern the difference at such a low O_2 tension, however, the sensitivity curve demonstrates that the TAM-LNCs are capable of distinguishing between 0 – 5 % O_2 concentrations. Thus, the use of a different model to induce transient and severe hypoxia could be beneficial, such as the use of surgical severance of the femoral artery or for the animal to be sacrificed. In this way, the reversible response of the TAM-LNCs could be verified.

5.2.4 *In vivo* studies: LNCs as a theranostic tool

A concern, regarding the use of LNCs as an O_2 sensor in tissue, could be the possibility of the LNCs harbouring auxiliary O_2. In other words, during the formulation and handling process of the LNCs, O_2 accumulates in the lipidic core of the nanocapsules (due to the higher solubility of O_2 in lipids than in water) but once introduced *in vivo* the O_2 diffuses from the lipidic core into the tissue causing an initial large release of O_2 which equilibrates. Or, conversely, the O_2 from the tissue could accumulate within the LNC's lipidic core and reduce the O_2 available to the tissue. Indeed, Zhou et al. [688] recently demonstrated that PFC nanoparticles could be loaded with O_2 for release within tumours to induce an enhanced radio-therapeutic effect. In our studies, we did not evaluate the latter but did demonstrate the lack of the former, i.e. 'reservoir effect', occurring by means of measuring the TAM-LNCs LWs over time.

In **Chapter 4, section 4.2**, two routes of delivery for the LNC formulation was described, namely an intramuscular injection and the intracerebral CED protocol. The use of the intracerebral CED protocol has been used in clinic for glioblastoma multiforme drug delivery as a means to bypass the blood-brain barrier, reduce systemic toxicity, and to overcome the limitations of diffusion-mediated delivery of compounds with a larger molecular weight [660,689,690]. However, although this method is an effective strategy for drug delivery, it is still under development; a balance must be struck between the quantity of the therapeutic product delivered to the target site and the potential harmful side-effect. In this

regard, several new methods of drug delivery are being developed to both improve the current methods (e.g. multiport catheter designs approaches for CED protocols [691,692]) as well as develop new methods (e.g. miniaturised implantable systems [693,694]).

Lastly, it is also notable, that although LW or T_1 relaxation measurements could be performed for 1 – 3 h, respectively, a signal loss related to LNCs biodegradation and/or the dispersion was evident over time. This observation raises the question of the 'dual function' that is expected from a theranostic tool; i.e. the ability to treat and diagnose, and in our case, follow the change induced by therapy. Using the MR PRESS sequence, an increase in the CH_2 lipid peak (1.2 ppm) and the PEG peak (3.7 ppm) was notable after LNC introduction in all *in* models, and was associated with an increase in SNR enabling the production of lipid images by the MOBILE sequence. However, after 24 h this characteristic signal of LNCs (1.2 ppm lipid peak and 3.7 ppm PEG peak) could no longer be observed. Previous studies regarding the *in vivo* application of standard LNCs (with 15 units of HS-PEG within the shell) have determined that the nanocapsules are stable in the blood for up to 24 h (whereupon their hydrodynamic size increased dramatically) [695], however this study gave no quantitative indication. An attempt to discern the integrity of LNCs *in vivo* using two FRET embedded dyes within the nanocapsule has been studied, and demonstrated that LNCs can still be intact several days after introduction. Unfortunately, however, no information regarding the percentage of intact LNCs as compared to the introduced LNCs was determined [596]. As a consequence, if the use of LNCs in a diagnostic capacity is to be pursued, the issue of their integrity over time would have to be addressed. This could be achieved by avoiding their potential biodegradation (a different shell which is still O_2 permeable) or internalisation in cells (using different particle sizes).

Nevertheless, and considering these limitations, although the feasibility of the LNCs as an O_2 sensor within tissues have been demonstrated, their usefulness as a theranostic tool in long-term therapeutic regimes appears unlikely unless a mixture of LNC formulations is developed which possesses both diagnostic and therapeutic LNC formulations (assuming that the behaviour of the latter can be monitored by the former). Interestingly, measurements wherein the ability of the tissues to be oxygenated, i.e. an 'oxygen-ability map', is required could benefit from our system demonstrated in this thesis. Such applications include dose painting during IMRT. Here, the use of an O_2 sensor could be useful and act as a vehicle for radio-enhancers, such as oxygen-loaded PFCs or gold nanoparticles.

Bibliography

(1) Hanahan, D.; Weinberg, R. A. Hallmarks of Cancer: The Next Generation. *Cell* **2011**, *144* (5), 646–674.

(2) Vaupel, P.; Mayer, A.; Höckel, M. Tumor Hypoxia and Malignant Progression. *Methods Enzymol.* **2004**, *381*, 335–354.

(3) Vaupel, P.; Höckel, M.; Mayer, A. Detection and Characterization of Tumor Hypoxia Using PO2 Histography. *Antioxid. Redox Signal.* **2007**, *9* (8), 1221–1235.

(4) Brown, J. M.; Giaccia, A. J. The Unique Physiology of Solid Tumors: Opportunities (and Problems) for Cancer Therapy. *Cancer Res.* **1998**, *58* (7), 1408–1416.

(5) Vaupel, P.; Thews, O.; Hoeckel, M. Treatment Resistance of Solid Tumors: Role of Hypoxia and Anemia. *Med. Oncol.* **2001**, *18* (4), 243–259.

(6) Muz, B.; de la Puente, P.; Azab, F.; Azab, A. K. The Role of Hypoxia in Cancer Progression, Angiogenesis, Metastasis, and Resistance to Therapy. *Hypoxia (Auckland, N.Z.)* **2015**, *3*, 83–92.

(7) Semenza, G. L.; Wang, G. L. A Nuclear Factor Induced by Hypoxia via de Novo Protein Synthesis Binds to the Human Erythropoietin Gene Enhancer at a Site Required for Transcriptional Activation. *Mol. Cell. Biol.* **1992**, *12* (12), 5447–5454.

(8) Huang, L. E.; Arany, Z.; Livingston, D. M.; Bunn, H. F. Activation of Hypoxia-Inducible Transcription Factor Depends Primarily upon Redox-Sensitive Stabilization of Its Alpha Subunit. *J. Biol. Chem.* **1996**, *271* (50), 32253–32259.

(9) Bos, R.; van der Groep, P.; Greijer, A. E.; Shvarts, A.; Meijer, S.; Pinedo, H. M.; Semenza, G. L.; van Diest, P. J.; van der Wall, E. Levels of Hypoxia-Inducible Factor-1? Independently Predict Prognosis in Patients with Lymph Node Negative Breast Carcinoma. *Cancer* **2003**, *97* (6), 1573–1581.

(10) Gruber, G.; Greiner, R. H.; Hlushchuk, R.; Aebersold, D. M.; Altermatt, H. J.; Berclaz, G.; Djonov, V. Hypoxia-Inducible Factor 1 Alpha in High-Risk Breast Cancer: An Independent Prognostic Parameter? *Breast Cancer Res.* **2004**, *6* (3), R191.

(11) Vleugel, M. M.; Greijer, A. E.; Shvarts, A.; van der Groep, P.; van Berkel, M.; Aarbodem, Y.; van Tinteren, H.; Harris, A. L.; van Diest, P. J.; van der Wall, E.

Differential Prognostic Impact of Hypoxia Induced and Diffuse HIF-1alpha Expression in Invasive Breast Cancer. *J. Clin. Pathol.* **2005**, *58* (2), 172–177.

(12) Trastour, C.; Benizri, E.; Ettore, F.; Ramaioli, A.; Chamorey, E.; Pouysségur, J.; Berra, E. HIF-1α and CA IX Staining in Invasive Breast Carcinomas: Prognosis and Treatment Outcome. *Int. J. Cancer* **2007**, *120* (7), 1451–1458.

(13) Aebersold, D. M.; Burri, P.; Beer, K. T.; Laissue, J.; Djonov, V.; Greiner, R. H.; Semenza, G. L. Expression of Hypoxia-Inducible Factor-1alpha: A Novel Predictive and Prognostic Parameter in the Radiotherapy of Oropharyngeal Cancer. *Cancer Res.* **2001**, *61* (7), 2911–2916.

(14) Matsuyama, T.; Nakanishi, K.; Hayashi, T.; Yoshizumi, Y.; Aiko, S.; Sugiura, Y.; Tanimoto, T.; Uenoyama, M.; Ozeki, Y.; Maehara, T. Expression of Hypoxia-Inducible Factor-1alpha in Esophageal Squamous Cell Carcinoma. *Cancer Sci.* **2005**, *96* (3), 176–182.

(15) Griffiths, E. A.; Pritchard, S. A.; Valentine, H. R.; Whitchelo, N.; Bishop, P. W.; Ebert, M. P.; Price, P. M.; Welch, I. M.; West, C. M. L. Hypoxia-Inducible Factor-1α Expression in the Gastric Carcinogenesis Sequence and Its Prognostic Role in Gastric and Gastro-Oesophageal Adenocarcinomas. *Br. J. Cancer* **2007**, *96* (1), 95–103.

(16) Swinson, D. E. B.; Jones, J. L.; Cox, G.; Richardson, D.; Harris, A. L.; O'Byrne, K. J. Hypoxia-Inducible Factor-1? In Non Small Cell Lung Cancer: Relation to Growth Factor, Protease and Apoptosis Pathways. *Int. J. Cancer* **2004**, *111* (1), 43–50.

(17) Talks, K. L.; Turley, H.; Gatter, K. C.; Maxwell, P. H.; Pugh, C. W.; Ratcliffe, P. J.; Harris, A. L. The Expression and Distribution of the Hypoxia-Inducible Factors HIF-1alpha and HIF-2alpha in Normal Human Tissues, Cancers, and Tumor-Associated Macrophages. *Am. J. Pathol.* **2000**, *157* (2), 411–421.

(18) Zhong, H.; De Marzo, A. M.; Laughner, E.; Lim, M.; Hilton, D. A.; Zagzag, D.; Buechler, P.; Isaacs, W. B.; Semenza, G. L.; Simons, J. W. Overexpression of Hypoxia-Inducible Factor 1alpha in Common Human Cancers and Their Metastases. *Cancer Res.* **1999**, *59* (22), 5830–5835.

(19) Harris, A. L. Hypoxia — A Key Regulatory Factor in Tumour Growth. *Nat. Rev. Cancer* **2002**, *2* (1), 38–47.

(20) Denko, N.; Schindler, C.; Koong, A.; Laderoute, K.; Green, C.; Giaccia, A. Epigenetic

Regulation of Gene Expression in Cervical Cancer Cells by the Tumor Microenvironment. *Clin. Cancer Res.* **2000**, *6* (2), 480–487.

(21) Koong, A. C.; Denko, N. C.; Hudson, K. M.; Schindler, C.; Swiersz, L.; Koch, C.; Evans, S.; Ibrahim, H.; Le, Q. T.; Terris, D. J.; et al. Candidate Genes for the Hypoxic Tumor Phenotype. *Cancer Res.* **2000**, *60* (4), 883–887.

(22) Wykoff, C. C.; Beasley, N. J.; Watson, P. H.; Turner, K. J.; Pastorek, J.; Sibtain, A.; Wilson, G. D.; Turley, H.; Talks, K. L.; Maxwell, P. H.; et al. Hypoxia-Inducible Expression of Tumor-Associated Carbonic Anhydrases. *Cancer Res.* **2000**, *60* (24), 7075–7083.

(23) Lal, A.; Peters, H.; St Croix, B.; Haroon, Z. A.; Dewhirst, M. W.; Strausberg, R. L.; Kaanders, J. H.; van der Kogel, A. J.; Riggins, G. J. Transcriptional Response to Hypoxia in Human Tumors. *J. Natl. Cancer Inst.* **2001**, *93* (17), 1337–1343.

(24) Semenza, G. L.; Artemov, D.; Bedi, A.; Bhujwalla, Z.; Chiles, K.; Feldser, D.; Laughner, E.; Ravi, R.; Simons, J.; Taghavi, P.; et al. "The Metabolism of Tumours": 70 Years Later. *Novartis Found. Symp.* **2001**, *240*, 251-60; discussion 260-4.

(25) Vaupel, P.; Harrison, L. Tumor Hypoxia: Causative Factors, Compensatory Mechanisms, and Cellular Response. *Oncologist* **2004**, *9 Suppl 5* (Supplement 5), 4–9.

(26) Brown, J. M. Vasculogenesis: A Crucial Player in the Resistance of Solid Tumours to Radiotherapy. *Br. J. Radiol.* **2014**, *87* (1035), 20130686.

(27) Raica, M.; Cimpean, A. M.; Ribatti, D. Angiogenesis in Pre-Malignant Conditions. *Eur. J. Cancer* **2009**, *45* (11), 1924–1934.

(28) Baeriswyl, V.; Christofori, G. The Angiogenic Switch in Carcinogenesis. *Semin. Cancer Biol.* **2009**, *19* (5), 329–337.

(29) Bergers, G.; Benjamin, L. E. Tumorigenesis and the Angiogenic Switch. *Nat. Rev. Cancer* **2003**, *3* (6), 401–410.

(30) Goldmann, E. The Growth of Malignant Disease in Man and the Lower Animals, with Special Reference to the Vascular System. *Proc. R. Soc. Med.* **1908**, *1* (Surg Sect), 1–13.

(31) Hanahan, D.; Folkman, J. Patterns and Emerging Mechanisms of the Angiogenic Switch during Tumorigenesis. *Cell* **1996**, *86* (3), 353–364.

(32) Toi, M.; Matsumoto, T.; Bando, H. Vascular Endothelial Growth Factor: Its Prognostic, Predictive, and Therapeutic Implications. *Lancet Oncol.* **2001**, *2* (11), 667–673.

(33) McKeown, S. R. Defining Normoxia, Physoxia and Hypoxia in Tumours-Implications for Treatment Response. *Br. J. Radiol.* **2014**, *87* (1035), 20130676.

(34) Ballinger, J. R. Imaging Hypoxia in Tumors. *Semin. Nucl. Med.* **2001**, *31* (4), 321–329.

(35) Vaupel, P.; Briest, S.; Höckel, M. Hypoxia in Breast Cancer: Pathogenesis, Characterization and Biological/Therapeutic Implications. *Wien. Med. Wochenschr.* **2002**, *152* (13–14), 334–342.

(36) Vaupel, P.; Kallinowski, F.; Okunieff, P. Blood Flow, Oxygen and Nutrient Supply, and Metabolic Microenvironment of Human Tumors: A Review. *Cancer Res.* **1989**, *49* (23), 6449–6465.

(37) Dagogo-Jack, I.; Shaw, A. T. Tumour Heterogeneity and Resistance to Cancer Therapies. *Nat. Rev. Clin. Oncol.* **2017**, *15* (2), 81–94.

(38) Allison, K. H.; Sledge, G. W. Heterogeneity and Cancer. *Oncology (Williston Park).* **2014**, *28* (9), 772–778.

(39) Hendriksen, E. M.; Span, P. N.; Schuuring, J.; Peters, J. P. W.; Sweep, F. C. G. J.; van der Kogel, A. J.; Bussink, J. Angiogenesis, Hypoxia and VEGF Expression during Tumour Growth in a Human Xenograft Tumour Model. *Microvasc. Res.* **2009**, *77* (2), 96–103.

(40) Thomlinson, R. H.; Gray, L. H. The Histological Structure of Some Human Lung Cancers and the Possible Implications for Radiotherapy. *Br. J. Cancer* **1955**, *9* (4), 539–549.

(41) Less, J. R.; Skalak, T. C.; Sevick, E. M.; Jain, R. K. Microvascular Architecture in a Mammary Carcinoma: Branching Patterns and Vessel Dimensions. *Cancer Res.* **1991**, *51* (1), 265–273.

(42) Munn, L. L. Aberrant Vascular Architecture in Tumors and Its Importance in Drug-Based Therapies. *Drug Discov. Today* **2003**, *8* (9), 396–403.

(43) Carmeliet, P.; Jain, R. K. Angiogenesis in Cancer and Other Diseases. *Nature* **2000**,

407 (6801), 249–257.

(44) Hashizume, H.; Baluk, P.; Morikawa, S.; McLean, J. W.; Thurston, G.; Roberge, S.; Jain, R. K.; McDonald, D. M. Openings between Defective Endothelial Cells Explain Tumor Vessel Leakiness. *Am. J. Pathol.* **2000**, *156* (4), 1363–1380.

(45) McDonald, D. M.; Baluk, P. Significance of Blood Vessel Leakiness in Cancer. *Cancer Res.* **2002**, *62* (18), 5381–5385.

(46) Dvorak, H. F.; Nagy, J. A.; Feng, D.; Brown, L. F.; Dvorak, A. M. Vascular Permeability Factor/Vascular Endothelial Growth Factor and the Significance of Microvascular Hyperpermeability in Angiogenesis. *Curr. Top. Microbiol. Immunol.* **1999**, *237*, 97–132.

(47) Boucher, Y.; Leunig, M.; Jain, R. K. Tumor Angiogenesis and Interstitial Hypertension. *Cancer Res.* **1996**, *56* (18), 4264–4266.

(48) Vaupel, P. Tumor Microenvironmental Physiology and Its Implications for Radiation Oncology. *Semin. Radiat. Oncol.* **2004**, *14* (3), 198–206.

(49) Hielscher, A.; Gerecht, S. Hypoxia and Free Radicals: Role in Tumor Progression and the Use of Engineering-Based Platforms to Address These Relationships. *Free Radic. Biol. Med.* **2015**, *79*, 281–291.

(50) Prabhakar, N. R. Invited Review: Oxygen Sensing during Intermittent Hypoxia: Cellular and Molecular Mechanisms. *J. Appl. Physiol.* **2001**, *90* (5), 1986–1994.

(51) Wykoff, C. C.; Pugh, C. W.; Maxwell, P. H.; Harris, A. L.; Ratcliffe, P. J. Identification of Novel Hypoxia Dependent and Independent Target Genes of the von Hippel-Lindau (VHL) Tumour Suppressor by MRNA Differential Expression Profiling. *Oncogene* **2000**, *19* (54), 6297–6305.

(52) Semenza, G. L. Regulation of Hypoxia-Induced Angiogenesis: A Chaperone Escorts VEGF to the Dance. *J. Clin. Invest.* **2001**, *108* (1), 39–40.

(53) Kotch, L. E.; Iyer, N. V.; Laughner, E.; Semenza, G. L. Defective Vascularization of HIF-1α-Null Embryos Is Not Associated with VEGF Deficiency but with Mesenchymal Cell Death. *Dev. Biol.* **1999**, *209* (2), 254–267.

(54) Marjon, P. L.; Bobrovnikova-Marjon, E. V; Abcouwer, S. F. Expression of the Pro-Angiogenic Factors Vascular Endothelial Growth Factor and Interleukin-8/CXCL8 by

Human Breast Carcinomas Is Responsive to Nutrient Deprivation and Endoplasmic Reticulum Stress. *Mol. Cancer* **2004**, *3* (1), 4.

(55) Xu, L.; Fukumura, D.; Jain, R. K. Acidic Extracellular PH Induces Vascular Endothelial Growth Factor (VEGF) in Human Glioblastoma Cells via ERK1/2 MAPK Signaling Pathway. *J. Biol. Chem.* **2002**, *277* (13), 11368–11374.

(56) Warburg, O. The Metabolism of Carcinoma Cells. *J. Cancer Res.* **1925**, *9* (1), 148–163.

(57) Liberti, M. V; Locasale, J. W. The Warburg Effect: How Does It Benefit Cancer Cells? *Trends Biochem. Sci.* **2016**, *41* (3), 211–218.

(58) Vander Heiden, M. G.; Cantley, L. C.; Thompson, C. B. Understanding the Warburg Effect: The Metabolic Requirements of Cell Proliferation. *Science* **2009**, *324* (5930), 1029–1033.

(59) Rademakers, S. E.; Span, P. N.; Kaanders, J. H. A. M.; Sweep, F. C. G. J.; van der Kogel, A. J.; Bussink, J. Molecular Aspects of Tumour Hypoxia. *Mol. Oncol.* **2008**, *2* (1), 41–53.

(60) Dang, C. V; Semenza, G. L. Oncogenic Alterations of Metabolism. *Trends Biochem. Sci.* **1999**, *24* (2), 68–72.

(61) Seagroves, T. N.; Ryan, H. E.; Lu, H.; Wouters, B. G.; Knapp, M.; Thibault, P.; Laderoute, K.; Johnson, R. S. Transcription Factor HIF-1 Is a Necessary Mediator of the Pasteur Effect in Mammalian Cells. *Mol. Cell. Biol.* **2001**, *21* (10), 3436–3444.

(62) Semenza, G. L. Defining the Role of Hypoxia-Inducible Factor 1 in Cancer Biology and Therapeutics. *Oncogene* **2009**, *29* (5), 625–634.

(63) Lemaire, L.; Franconi, F.; Siegler, B.; Legendre, C.; Garcion, E. In Vitro Expansion of U87-MG Human Glioblastoma Cells under Hypoxic Conditions Affects Glucose Metabolism and Subsequent in Vivo Growth. *Tumour Biol.* **2015**, *36* (10), 7699–7710.

(64) Chen, C.; Pore, N.; Behrooz, A.; Ismail-Beigi, F.; Maity, A. Regulation of *Glut1* MRNA by Hypoxia-Inducible Factor-1. *J. Biol. Chem.* **2001**, *276* (12), 9519–9525.

(65) Kang, S. S.; Chun, Y. K.; Hur, M. H.; Lee, H. K.; Kim, Y. J.; Hong, S. R.; Lee, J. H.; Lee, S. G.; Park, Y. K. Clinical Significance of Glucose Transporter 1 (GLUT1) Expression in Human Breast Carcinoma. *Jpn. J. Cancer Res.* **2002**, *93* (10), 1123–

1128.

(66) Kunkel, M.; Reichert, T. E.; Benz, P.; Lehr, H.-A.; Jeong, J.-H.; Wieand, S.; Bartenstein, P.; Wagner, W.; Whiteside, T. L. Overexpression of Glut-1 and Increased Glucose Metabolism in Tumors Are Associated with a Poor Prognosis in Patients with Oral Squamous Cell Carcinoma. *Cancer* **2003**, *97* (4), 1015–1024.

(67) Tohma, T.; Okazumi, S.; Makino, H.; Cho, A.; Mochizuki, R.; Shuto, K.; Kudo, H.; Matsubara, K.; Gunji, H.; Matsubara, H.; et al. Overexpression of Glucose Transporter 1 in Esophageal Squamous Cell Carcinomas: A Marker for Poor Prognosis. *Dis. Esophagus* **2005**, *18* (3), 185–189.

(68) Hoskin, P. J.; Sibtain, A.; Daley, F. M.; Wilson, G. D. GLUT1 and CAIX as Intrinsic Markers of Hypoxia in Bladder Cancer: Relationship with Vascularity and Proliferation as Predictors of Outcome of ARCON. *Br. J. Cancer* **2003**, *89* (7), 1290–1297.

(69) Kawamura, T.; Kusakabe, T.; Sugino, T.; Watanabe, K.; Fukuda, T.; Nashimoto, A.; Honma, K.; Suzuki, T. Expression of Glucose Transporter-1 in Human Gastric Carcinoma: Association with Tumor Aggressiveness, Metastasis, and Patient Survival. *Cancer* **2001**, *92* (3), 634–641.

(70) Furudoi, A.; Tanaka, S.; Haruma, K.; Yoshihara, M.; Sumii, K.; Kajiyama, G.; Shimamoto, F. Clinical Significance of Human Erythrocyte Glucose Transporter 1 Expression at the Deepest Invasive Site of Advanced Colorectal Carcinoma. *Oncology* **2001**, *60* (2), 162–169.

(71) Cantuaria, G.; Fagotti, A.; Ferrandina, G.; Magalhaes, A.; Nadji, M.; Angioli, R.; Penalver, M.; Mancuso, S.; Scambia, G. GLUT-1 Expression in Ovarian Carcinoma: Association with Survival and Response to Chemotherapy. *Cancer* **2001**, *92* (5), 1144–1150.

(72) Younes, M.; Brown, R. W.; Stephenson, M.; Gondo, M.; Cagle, P. T. Overexpression of Glut1 and Glut3 in Stage I Nonsmall Cell Lung Carcinoma Is Associated with Poor Survival. *Cancer* **1997**, *80* (6), 1046–1051.

(73) Pescador, N.; Villar, D.; Cifuentes, D.; Garcia-Rocha, M.; Ortiz-Barahona, A.; Vazquez, S.; Ordoñez, A.; Cuevas, Y.; Saez-Morales, D.; Garcia-Bermejo, M. L.; et al. Hypoxia Promotes Glycogen Accumulation through Hypoxia Inducible Factor (HIF)-

Mediated Induction of Glycogen Synthase 1. *PLoS One* **2010**, *5* (3), e9644.

(74) Gatenby, R. A.; Gawlinski, E. T. Mathematical Models of Tumour Invasion Mediated by Transformation-Induced Alteration of Microenvironmental PH. *Novartis Found. Symp.* **2001**, *240*, 85-96; discussion 96-9.

(75) Robertson, N.; Potter, C.; Harris, A. L. Role of Carbonic Anhydrase IX in Human Tumor Cell Growth, Survival, and Invasion. *Cancer Res.* **2004**, *64* (17), 6160–6165.

(76) Parkkila, S.; Rajaniemi, H.; Parkkila, A. K.; Kivela, J.; Waheed, A.; Pastorekova, S.; Pastorek, J.; Sly, W. S. Carbonic Anhydrase Inhibitor Suppresses Invasion of Renal Cancer Cells in Vitro. *Proc. Natl. Acad. Sci. U. S. A.* **2000**, *97* (5), 2220–2224.

(77) Koukourakis, M. I.; Giatromanolaki, A.; Polychronidis, A.; Simopoulos, C.; Gatter, K. C.; Harris, A. L.; Sivridis, E. Endogenous Markers of Hypoxia/Anaerobic Metabolism and Anemia in Primary Colorectal Cancer. *Cancer Sci.* **2006**, *97* (7), 582–588.

(78) Loncaster, J. A.; Harris, A. L.; Davidson, S. E.; Logue, J. P.; Hunter, R. D.; Wycoff, C. C.; Pastorek, J.; Ratcliffe, P. J.; Stratford, I. J.; West, C. M. Carbonic Anhydrase (CA IX) Expression, a Potential New Intrinsic Marker of Hypoxia: Correlations with Tumor Oxygen Measurements and Prognosis in Locally Advanced Carcinoma of the Cervix. *Cancer Res.* **2001**, *61* (17), 6394–6399.

(79) Chia, S. K.; Wykoff, C. C.; Watson, P. H.; Han, C.; Leek, R. D.; Pastorek, J.; Gatter, K. C.; Ratcliffe, P.; Harris, A. L. Prognostic Significance of a Novel Hypoxia-Regulated Marker, Carbonic Anhydrase IX, in Invasive Breast Carcinoma. *J. Clin. Oncol.* **2001**, *19* (16), 3660–3668.

(80) Kon-no, H.; Ishii, G.; Nagai, K.; Yoshida, J.; Nishimura, M.; Nara, M.; Fujii, T.; Murata, Y.; Miyamoto, H.; Ochiai, A. Carbonic Anhydrase IX Expression Is Associated with Tumor Progression and a Poor Prognosis of Lung Adenocarcinoma. *Lung Cancer* **2006**, *54* (3), 409–418.

(81) Chen, J.; Röcken, C.; Hoffmann, J.; Krüger, S.; Lendeckel, U.; Rocco, A.; Pastorekova, S.; Malfertheiner, P.; Ebert, M. P. A. Expression of Carbonic Anhydrase 9 at the Invasion Front of Gastric Cancers. *Gut* **2005**, *54* (7), 920–927.

(82) Eales, K. L.; Hollinshead, K. E. R.; Tennant, D. A. Hypoxia and Metabolic Adaptation of Cancer Cells. *Oncogenesis* **2016**, *5* (1), e190.

(83) Potter, C.; Harris, A. L. Hypoxia Inducible Carbonic Anhydrase IX, Marker of Tumour

Hypoxia, Survival Pathway and Therapy Target. *Cell Cycle* **2004**, *3* (2), 164–167.

(84) Lagadic-Gossmann, D.; Huc, L.; Lecureur, V. Alterations of Intracellular PH Homeostasis in Apoptosis: Origins and Roles. *Cell Death Differ.* **2004**, *11* (9), 953–961.

(85) Seimiya, H.; Tanji, M.; Oh-hara, T.; Tomida, A.; Naasani, I.; Tsuruo, T. Hypoxia Up-Regulates Telomerase Activity via Mitogen-Activated Protein Kinase Signaling in Human Solid Tumor Cells. *Biochem. Biophys. Res. Commun.* **1999**, *260* (2), 365–370.

(86) Vande Velde, C.; Cizeau, J.; Dubik, D.; Alimonti, J.; Brown, T.; Israels, S.; Hakem, R.; Greenberg, A. H. BNIP3 and Genetic Control of Necrosis-like Cell Death through the Mitochondrial Permeability Transition Pore. *Mol. Cell. Biol.* **2000**, *20* (15), 5454–5468.

(87) Sowter, H. M.; Ratcliffe, P. J.; Watson, P.; Greenberg, A. H.; Harris, A. L. HIF-1-Dependent Regulation of Hypoxic Induction of the Cell Death Factors BNIP3 and NIX in Human Tumors. *Cancer Res.* **2001**, *61* (18), 6669–6673.

(88) Suzuki, H.; Tomida, A.; Tsuruo, T. Dephosphorylated Hypoxia-Inducible Factor 1α as a Mediator of P53-Dependent Apoptosis during Hypoxia. *Oncogene* **2001**, *20* (41), 5779–5788.

(89) Schmid, T.; Zhou, J.; Brüne, B. HIF-1 and P53: Communication of Transcription Factors under Hypoxia. *J. Cell. Mol. Med.* **2004**, *8* (4), 423–431.

(90) Hammond, E. M.; Giaccia, A. J. The Role of P53 in Hypoxia-Induced Apoptosis. *Biochem. Biophys. Res. Commun.* **2005**, *331* (3), 718–725.

(91) Chan, N.; Koritzinsky, M.; Zhao, H.; Bindra, R.; Glazer, P. M.; Powell, S.; Belmaaza, A.; Wouters, B.; Bristow, R. G. Chronic Hypoxia Decreases Synthesis of Homologous Recombination Proteins to Offset Chemoresistance and Radioresistance. *Cancer Res.* **2008**, *68* (2), 605–614.

(92) Luoto, K. R.; Kumareswaran, R.; Bristow, R. G. Tumor Hypoxia as a Driving Force in Genetic Instability. *Genome Integr.* **2013**, *4* (1), 1–15.

(93) Kondo, A.; Safaei, R.; Mishima, M.; Niedner, H.; Lin, X.; Howell, S. B. Hypoxia-Induced Enrichment and Mutagenesis of Cells That Have Lost DNA Mismatch Repair. *Cancer Res.* **2001**, *61* (20), 7603–7607.

(94) Pires, I. M.; Bencokova, Z.; Milani, M.; Folkes, L. K.; Li, J.-L.; Stratford, M. R.; Harris, A. L.; Hammond, E. M. Effects of Acute versus Chronic Hypoxia on DNA Damage Responses and Genomic Instability. *Cancer Res.* **2010**, *70* (3), 925–935.

(95) Terzi, M. Y.; Izmirli, M.; Gogebakan, B. The Cell Fate: Senescence or Quiescence. *Mol. Biol. Rep.* **2016**, *43* (11), 1213–1220.

(96) Das, B.; Tsuchida, R.; Malkin, D.; Koren, G.; Baruchel, S.; Yeger, H. Hypoxia Enhances Tumor Stemness by Increasing the Invasive and Tumorigenic Side Population Fraction. *Stem Cells* **2008**, *26* (7), 1818–1830.

(97) Vaupel, P.; Kelleher, D. K.; Höckel, M. Oxygen Status of Malignant Tumors: Pathogenesis of Hypoxia and Significance for Tumor Therapy. *Semin. Oncol.* **2001**, *28* (2 Suppl 8), 29–35.

(98) Collado, M.; Serrano, M. Senescence in Tumours: Evidence from Mice and Humans. *Nat. Rev. Cancer* **2010**, *10* (1), 51–57.

(99) Evan, G. I.; d'Adda di Fagagna, F. Cellular Senescence: Hot or What? *Curr. Opin. Genet. Dev.* **2009**, *19* (1), 25–31.

(100) Graeber, T. G.; Osmanian, C.; Jacks, T.; Housman, D. E.; Koch, C. J.; Lowe, S. W.; Giaccia, A. J. Hypoxia-Mediated Selection of Cells with Diminished Apoptotic Potential in Solid Tumours. *Nature* **1996**, *379* (6560), 88–91.

(101) Dachs, G. U.; Tozer, G. M. Hypoxia Modulated Gene Expression: Angiogenesis, Metastasis and Therapeutic Exploitation. *Eur. J. Cancer* **2000**, *36* (13), 1649–1660.

(102) Hammond, E. M.; Denko, N. C.; Dorie, M. J.; Abraham, R. T.; Giaccia, A. J. Hypoxia Links ATR and P53 through Replication Arrest. *Mol. Cell. Biol.* **2002**, *22* (6), 1834–1843.

(103) Agani, F.; Jiang, B.-H. Oxygen-Independent Regulation of HIF-1: Novel Involvement of PI3K/AKT/MTOR Pathway in Cancer. *Curr. Cancer Drug Targets* **2013**, *13* (3), 245–251.

(104) Courtnay, R.; Ngo, D. C.; Malik, N.; Ververis, K.; Tortorella, S. M.; Karagiannis, T. C. Cancer Metabolism and the Warburg Effect: The Role of HIF-1 and PI3K. *Mol. Biol. Rep.* **2015**, *42* (4), 841–851.

(105) Seta, K. A.; Spicer, Z.; Yuan, Y.; Lu, G.; Millhorn, D. E. Responding to Hypoxia:

Lessons From a Model Cell Line. *Sci. Signal.* **2002**, *2002* (146), re11-re11.

(106) Sanchez, A.; Tripathy, D.; Yin, X.; Desobry, K.; Martinez, J.; Riley, J.; Gay, D.; Luo, J.; Grammas, P. P38 MAPK: A Mediator of Hypoxia-Induced Cerebrovascular Inflammation. *J. Alzheimer ĝ Dis.* **2012**, *32* (3), 587–597.

(107) Minet, E.; Arnould, T.; Michel, G.; Roland, I.; Mottet, D.; Raes, M.; Remacle, J.; Michiels, C. ERK Activation upon Hypoxia: Involvement in HIF-1 Activation. *FEBS Lett.* **2000**, *468* (1), 53–58.

(108) Koong, A. C.; Chen, E. Y.; Giaccia, A. J. Hypoxia Causes the Activation of Nuclear Factor Kappa B through the Phosphorylation of I Kappa B Alpha on Tyrosine Residues. *Cancer Res.* **1994**, *54* (6), 1425–1430.

(109) Erler, J. T.; Bennewith, K. L.; Nicolau, M.; Dornhöfer, N.; Kong, C.; Le, Q.-T.; Chi, J.-T. A.; Jeffrey, S. S.; Giaccia, A. J. Lysyl Oxidase Is Essential for Hypoxia-Induced Metastasis. *Nature* **2006**, *440* (7088), 1222–1226.

(110) Erler, J. T.; Giaccia, A. J. Lysyl Oxidase Mediates Hypoxic Control of Metastasis. *Cancer Res.* **2006**, *66* (21), 10238–10241.

(111) Span, P. N.; Bussink, J. Biology of Hypoxia. *Semin. Nucl. Med.* **2015**, *45* (2), 101–109.

(112) Erler, J. T.; Bennewith, K. L.; Cox, T. R.; Lang, G.; Bird, D.; Koong, A.; Le, Q.-T.; Giaccia, A. J. Hypoxia-Induced Lysyl Oxidase Is a Critical Mediator of Bone Marrow Cell Recruitment to Form the Premetastatic Niche. *Cancer Cell* **2009**, *15* (1), 35–44.

(113) Lee, C.-T.; Mace, T.; Repasky, E. A. Hypoxia-Driven Immunosuppression: A New Reason to Use Thermal Therapy in the Treatment of Cancer? *Int. J. Hyperth.* **2010**, *26* (3), 232–246.

(114) Noman, M. Z.; Hasmim, M.; Messai, Y.; Terry, S.; Kieda, C.; Janji, B.; Chouaib, S. Hypoxia: A Key Player in Antitumor Immune Response. A Review in the Theme: Cellular Responses to Hypoxia. *Am. J. Physiol. Physiol.* **2015**, *309* (9), C569–C579.

(115) Vaupel, P.; Mayer, A. Hypoxia and Anemia: Effects on Tumor Biology and Treatment Resistance. *Transfus. Clin. Biol.* **2005**, *12* (1), 5–10.

(116) Nordsmark, M.; Høyer, M.; Keller, J.; Nielsen, O. S.; Jensen, O. M.; Overgaard, J. The Relationship between Tumor Oxygenation and Cell Proliferation in Human Soft Tissue Sarcomas. *Int. J. Radiat. Oncol. Biol. Phys.* **1996**, *35* (4), 701–708.

(117) Selvendiran, K.; Bratasz, A.; Kuppusamy, M. L.; Tazi, M. F.; Rivera, B. K.; Kuppusamy, P. Hypoxia Induces Chemoresistance in Ovarian Cancer Cells by Activation of Signal Transducer and Activator of Transcription 3. *Int. J. Cancer* **2009**, *125* (9), 2198–2204.

(118) Höckel, M.; Vaupel, P.; Hockel, M.; Vaupel, P. Tumor Hypoxia: Definitions and Current Clinical, Biologic, and Molecular Aspects. *J. Natl. Cancer Inst.* **2001**, *93* (4), 266–276.

(119) Gatenby, R. A.; Kessler, H. B.; Rosenblum, J. S.; Coia, L. R.; Moldofsky, P. J.; Hartz, W. H.; Broder, G. J. Oxygen Distribution in Squamous Cell Carcinoma Metastases and Its Relationship to Outcome of Radiation Therapy. *Int. J. Radiat. Oncol. Biol. Phys.* **1988**, *14* (5), 831–838.

(120) Okunieff, P.; Hoeckel, M.; Dunphy, E. P.; Schlenger, K.; Knoop, C.; Vaupel, P. Oxygen Tension Distributions Are Sufficient to Explain the Local Response of Human Breast Tumors Treated with Radiation Alone. *Int. J. Radiat. Oncol.* **1993**, *26* (4), 631–636.

(121) Stone, H. B.; Brown, J. M.; Phillips, T. L.; Sutherland, R. M. Oxygen in Human Tumors: Correlations between Methods of Measurement and Response to Therapy. Summary of a Workshop Held November 19-20, 1992, at the National Cancer Institute, Bethesda, Maryland. *Radiat. Res.* **1993**, *136* (3), 422–434.

(122) Thomas, C. D.; Chavaudra, N.; Martin, L.; Guichard, M. Correlation between Radiosensitivity, Percentage Hypoxic Cells and PO2 Measurements in One Rodent and Two Human Tumor Xenografts. *Radiat. Res.* **1994**, *139* (1), 1–8.

(123) Höckel, M.; Knoop, C.; Schlenger, K.; Vorndran, B.; Baußnann, E.; Mitze, M.; Knapstein, P. G.; Vaupel, P. Intratumoral PO2 Predicts Survival in Advanced Cancer of the Uterine Cervix. *Radiother. Oncol.* **1993**, *26* (1), 45–50.

(124) Höckel, M.; Vorndran, B.; Schlenger, K.; Baussmann, E.; Knapstein, P. G. Tumor Oxygenation: A New Predictive Parameter in Locally Advanced Cancer of the Uterine Cervix. *Gynecol. Oncol.* **1993**, *51* (2), 141–149.

(125) Höckel, M.; Schlenger, K.; Mitze, M.; Schäffer, U.; Vaupel, P. Hypoxia and Radiation Response in Human Tumors. *Semin. Radiat. Oncol.* **1996**, *6* (1), 3–9.

(126) Mundt, A. J.; Roeske, J. C.; Chung, T. D.; Weichselbaum, R. R. Biologic Basis of

Radiation Therapy. In *Holland-Frei Cancer Medicine*; Kufe, D. W., Pollock, R. E., Weichselbaum, R. R., Editors., et al., Eds.; BC Decker: Hamilton (ON), 2003.

(127) Gray, L. H.; Conger, A. D.; Ebert, M.; Hornsey, S.; Scott, O. C. A. The Concentration of Oxygen Dissolved in Tissues at the Time of Irradiation as a Factor in Radiotherapy. *Br. J. Radiol.* **1953**, *26* (312), 638–648.

(128) Durand, R. E. The Influence of Microenvironmental Factors during Cancer Therapy. *In Vivo* **1994**, *8* (5), 691–702.

(129) Teicher, B. A.; Holden, S. A.; Al-Achi, A.; Herman, T. S. Classification of Antineoplastic Treatments by Their Differential Toxicity toward Putative Oxygenated and Hypoxic Tumor Subpopulations in Vivo in the FSaIIC Murine Fibrosarcoma. *Cancer Res.* **1990**, *50* (11), 3339–3344.

(130) Campos, B.; Olsen, L. R.; Urup, T.; Poulsen, H. S. A Comprehensive Profile of Recurrent Glioblastoma. *Oncogene* **2016**, *35* (45), 5819–5825.

(131) Agnihotri, S.; Burrell, K. E.; Wolf, A.; Jalali, S.; Hawkins, C.; Rutka, J. T.; Zadeh, G. Glioblastoma, a Brief Review of History, Molecular Genetics, Animal Models and Novel Therapeutic Strategies. *Arch. Immunol. Ther. Exp. (Warsz).* **2013**, *61* (1), 25–41.

(132) Hervey-Jumper, S. L.; Berger, M. S. Maximizing Safe Resection of Low- and High-Grade Glioma. *J. Neurooncol.* **2016**, *130* (2), 269–282.

(133) Yong, R. L.; Lonser, R. R. Surgery for Glioblastoma Multiforme: Striking a Balance. *World Neurosurg.* **2011**, *76* (6), 528–530.

(134) Young, R. M.; Jamshidi, A.; Davis, G.; Sherman, J. H. Current Trends in the Surgical Management and Treatment of Adult Glioblastoma. *Ann. Transl. Med.* **2015**, *3* (9), 121.

(135) Mirimanoff, R.-O.; Gorlia, T.; Mason, W.; Van Den Bent, M. J.; Kortmann, R.-D.; Fisher, B.; Reni, M.; Brandes, A. A.; Curschmann, J.; Villa, S.; et al. Radiotherapy and Temozolomide for Newly Diagnosed Glioblastoma: Recursive Partitioning Analysis of the EORTC 26981/22981-NCIC CE3 Phase III Randomized Trial. *J Clin Oncol* **2006**, *24*, 2563–2569.

(136) Stupp, R.; Mason, W. P.; van den Bent, M. J.; Weller, M.; Fisher, B.; Taphoorn, M. J. B.; Belanger, K.; Brandes, A. A.; Marosi, C.; Bogdahn, U.; et al. Radiotherapy plus Concomitant and Adjuvant Temozolomide for Glioblastoma. *N. Engl. J. Med.* **2005**,

352 (10), 987–996.

(137) Bianco, J.; Bastiancich, C.; Jankovski, A.; des Rieux, A.; Préat, V.; Danhier, F. On Glioblastoma and the Search for a Cure: Where Do We Stand? *Cell. Mol. Life Sci.* **2017**, *74* (13), 2451–2466.

(138) Watanabe, M.; Tanaka, R.; Takeda, N. Magnetic Resonance Imaging and Histopathology of Cerebral Gliomas. *Neuroradiology* **1992**, *34* (6), 463–469.

(139) Drabycz, S.; Roldán, G.; de Robles, P.; Adler, D.; McIntyre, J. B.; Magliocco, A. M.; Cairncross, J. G.; Mitchell, J. R. An Analysis of Image Texture, Tumor Location, and MGMT Promoter Methylation in Glioblastoma Using Magnetic Resonance Imaging. *Neuroimage* **2010**, *49* (2), 1398–1405.

(140) Kalpathy-Cramer, J.; Gerstner, E. R.; Emblem, K. E.; Andronesi, O. C.; Rosen, B. Advanced Magnetic Resonance Imaging of the Physical Processes in Human Glioblastoma. *Cancer Res.* **2014**, *74* (17), 4622–4637.

(141) Ling, C. C.; Humm, J.; Larson, S.; Amols, H.; Fuks, Z.; Leibel, S.; Koutcher, J. A. Towards Multidimensional Radiotherapy (MD-CRT): Biological Imaging and Biological Conformality. *Int. J. Radiat. Oncol.* **2000**, *47* (3), 551–560.

(142) Rofstad, E. K. Microenvironment-Induced Cancer Metastasis. *Int. J. Radiat. Biol.* **2000**, *76* (5), 589–605.

(143) Hockel, M.; Schlenger, K.; Aral, B.; Mitze, M.; Schaffer, U.; Vaupel, P. Association between Tumor Hypoxia and Malignant Progression in Advanced Cancer of the Uterine Cervix. *Cancer Res.* **1996**, *56* (19), 4509–4515.

(144) Rofstad, E. K.; Danielsen, T. Hypoxia-Induced Metastasis of Human Melanoma Cells: Involvement of Vascular Endothelial Growth Factor-Mediated Angiogenesis. *Br. J. Cancer* **1999**, *80* (11), 1697–1707.

(145) Thiery, J. P.; Sleeman, J. P. Complex Networks Orchestrate Epithelial–mesenchymal Transitions. *Nat. Rev. Mol. Cell Biol.* **2006**, *7* (2), 131–142.

(146) Sakata, K.; Kwok, T. T.; Murphy, B. J.; Laderoute, K. R.; Gordon, G. R.; Sutherland, R. M. Hypoxia-Induced Drug Resistance: Comparison to P-Glycoprotein-Associated Drug Resistance. *Br. J. Cancer* **1991**, *64* (5), 809–814.

(147) Anthoney, D. A.; McIlwrath, A. J.; Gallagher, W. M.; Edlin, A. R.; Brown, R.

Microsatellite Instability, Apoptosis, and Loss of P53 Function in Drug-Resistant Tumor Cells. *Cancer Res.* **1996**, *56* (6), 1374–1381.

(148) Sethi, T.; Rintoul, R. C.; Moore, S. M.; MacKinnon, A. C.; Salter, D.; Choo, C.; Chilvers, E. R.; Dransfield, I.; Donnelly, S. C.; Strieter, R.; et al. Extracellular Matrix Proteins Protect Small Cell Lung Cancer Cells against Apoptosis: A Mechanism for Small Cell Lung Cancer Growth and Drug Resistance in Vivo. *Nat. Med.* **1999**, *5* (6), 662–668.

(149) Durand, R. E. Intermittent Blood Flow in Solid Tumours – an Under-Appreciated Source of 'Drug Resistance.' *Cancer Metastasis Rev.* **2001**, *20* (1/2), 57–61.

(150) Durand, R. E.; Aquino-Parsons, C. Clinical Relevance of Intermittent Tumour Blood Flow. *Acta Oncol. (Madr).* **2001**, *40* (8), 929–936.

(151) Vaupel, P. Metabolic Microenvironment of Tumor Cells: A Key Factor in Malignant Progression. *Exp. Oncol.* **2010**, *32* (3), 125–127.

(152) Jiang, J.; Tang, Y.; Liang, X. EMT: A New Vision of Hypoxia Promoting Cancer Progression. *Cancer Biol. Ther.* **2011**, *11* (8), 714–723.

(153) Bussink, J.; Kaanders, J. H.; Rijken, P. F.; Raleigh, J. A.; Van der Kogel, A. J. Changes in Blood Perfusion and Hypoxia after Irradiation of a Human Squamous Cell Carcinoma Xenograft Tumor Line. *Radiat. Res.* **2000**, *153* (4), 398–404.

(154) Overgaard, J. Clinical Evaluation of Nitroimidazoles as Modifiers of Hypoxia in Solid Tumors. *Oncol. Res.* **1994**, *6* (10–11), 509–518.

(155) Rijpkema, M.; Kaanders, J. H. A. .; Joosten, F. B. .; van der Kogel, A. J.; Heerschap, A. Effects of Breathing a Hyperoxic Hypercapnic Gas Mixture on Blood Oxygenation and Vascularity of Head-and-Neck Tumors as Measured by Magnetic Resonance Imaging. *Int. J. Radiat. Oncol.* **2002**, *53* (5), 1185–1191.

(156) Overgaard, J. Hypoxic Radiosensitization: Adored and Ignored. *J Clin Oncol* **2007**, *25*, 4066–4074.

(157) De Bree, R.; Van Der Kogel, A. J.; Span, P. N. Accelerated Radiotherapy With Carbogen and Nicotinamide for Laryngeal Cancer: Results of a Phase III Randomized Trial. *Artic. J. Clin. Oncol.* **2012**.

(158) Moen, I.; Stuhr, L. E. B. Hyperbaric Oxygen Therapy and Cancer--a Review. *Target.*

Oncol. **2012**, *7* (4), 233–242.

(159) Janssens, G. O.; Langendijk, J. A.; Terhaard, C. H.; Doornaert, P. A.; van den Ende, P.; de Jong, M. A.; Takes, R. P.; Span, P. N.; Kaanders, J. H. Quality-of-Life after Radiotherapy for Advanced Laryngeal Cancer: Results of a Phase III Trial of the Dutch Head and Neck Society. *Radiother. Oncol.* **2016**, *119* (2), 213–220.

(160) Janssens, G. O.; Rademakers, S. E.; Terhaard, C. H.; Doornaert, P. A.; Bijl, H. P.; van den Ende, P.; Chin, A.; Takes, R. P.; de Bree, R.; Hoogsteen, I. J.; et al. Improved Recurrence-Free Survival with ARCON for Anemic Patients with Laryngeal Cancer. *Clin. Cancer Res.* **2014**, *20* (5), 1345–1354.

(161) Mason, R. P.; Ran, S.; Thorpe, P. E. Quantitative Assessment of Tumor Oxygen Dynamics: Molecular Imaging for Prognostic Radiology. *J. Cell. Biochem. Suppl.* **2002**, *39*, 45–53.

(162) Pacheco-Torres, J.; López-Larrubia, P.; Ballesteros, P.; Cerdán, S. Imaging Tumor Hypoxia by Magnetic Resonance Methods. *NMR Biomed.* **2011**, *24* (1), 1–16.

(163) Vaupel, P.; Mayer, A. Hypoxia in Cancer: Significance and Impact on Clinical Outcome. *Cancer Metastasis Rev.* **2007**, *26* (2), 225–239.

(164) Springett, R.; Swartz, H. M. Measurements of Oxygen in Vivo: Overview and Perspectives on Methods to Measure Oxygen within Cells and Tissues. *Antioxid. Redox Signal.* **2007**, *9* (8), 1295–1302.

(165) Sun, X.; Niu, G.; Chan, N.; Shen, B.; Chen, X. Tumor Hypoxia Imaging. *Mol. imaging Biol.* **2011**, *13* (3), 399–410.

(166) Lee, C.-T.; Boss, M.-K.; Dewhirst, M. W. Imaging Tumor Hypoxia to Advance Radiation Oncology. *Antioxid. Redox Signal.* **2014**, *21* (2), 313–337.

(167) Clark, L. C.; Wolf, R.; Granger, D.; Taylor, Z. Continuous Recording of Blood Oxygen Tensions by Polarography. *J. Appl. Physiol.* **1953**, *6* (3), 189–193.

(168) Höckel, M.; Schlenger, K.; Höckel, S.; Vaupel, P. Hypoxic Cervical Cancers with Low Apoptotic Index Are Highly Aggressive. *Cancer Res.* **1999**, *59* (18), 4525–4528.

(169) Hofmann, J.; Meier, R. J.; Mahnke, A.; Schatz, V.; Brackmann, F.; Trollmann, R.; Bogdan, C.; Liebsch, G.; Wang, X.; Wolfbeis, O. S.; et al. Ratiometric Luminescence 2D *in Vivo* Imaging and Monitoring of Mouse Skin Oxygenation. *Methods Appl.*

Fluoresc. **2013**, *1* (4), 045002.

(170) Nozue, M.; Lee, I.; Yuan, F.; Teicher, B. A.; Brizel, D. M.; Dewhirst, M. W.; Milross, C. G.; Milas, L.; Song, C. W.; Thomas, C. D.; et al. Interlaboratory Variation in Oxygen Tension Measurement by Eppendorf Histograph and Comparison with Hypoxic Marker. *J. Surg. Oncol.* **1997**, *66* (1), 30–38.

(171) Buerk, D. G. Measuring Tissue PO2 with Microelectrodes. *Methods Enzymol.* **2004**, *381*, 665–690.

(172) Jang, K.-I.; Han, S. Y.; Xu, S.; Mathewson, K. E.; Zhang, Y.; Jeong, J.-W.; Kim, G.-T.; Webb, R. C.; Lee, J. W.; Dawidczyk, T. J.; et al. Rugged and Breathable Forms of Stretchable Electronics with Adherent Composite Substrates for Transcutaneous Monitoring. *Nat. Commun.* **2014**, *5* (1), 4779.

(173) Yip, W. L. Evaluation of the Clinimetrics of Transcutaneous Oxygen Measurement and Its Application in Wound Care. *Int. Wound J.* **2015**, *12* (6), 625–629.

(174) Maeda, K.; Osato, T.; Umezawa, H. A New Antibiotic, Azomycin. *J. Antibiot.* **1953**, *6* (4), 182.

(175) Irshad, K.; Mohapatra, S. K.; Srivastava, C.; Garg, H.; Mishra, S.; Dikshit, B.; Sarkar, C.; Gupta, D.; Chandra, P. S.; Chattopadhyay, P.; et al. A Combined Gene Signature of Hypoxia and Notch Pathway in Human Glioblastoma and Its Prognostic Relevance. *PLoS One* **2015**, *10* (3), e0118201.

(176) Seddon, B. M.; Workman, P. The Role of Functional and Molecular Imaging in Cancer Drug Discovery and Development. *Br. J. Radiol.* **2003**, *76 Spec No*, S128-38.

(177) Joseph, P.; Jaiswal, A. K.; Stobbe, C. C.; Chapman, J. D. The Role of Specific Reductases in the Intracellular Activation and Binding of 2-Nitroimidazoles. *Int. J. Radiat. Oncol. Biol. Phys.* **1994**, *29* (2), 351–355.

(178) Aboagye, E. O.; Lewis, A. D.; Tracy, M.; Workman, P. Bioreductive Metabolism of the Novel Fluorinated 2-Nitroimidazole Hypoxia Probe N-(2-Hydroxy-3,3,3-Trifluoropropyl)-2-(2-Nitroimidazolyl) Acetamide (SR-4554). *Biochem. Pharmacol.* **1997**, *54* (11), 1217–1224.

(179) Mahy, P.; De Bast, M.; Gallez, B.; Gueulette, J.; Koch, C. J.; Scalliet, P.; Grégoire, V. In Vivo Colocalization of 2-Nitroimidazole EF5 Fluorescence Intensity and Electron Paramagnetic Resonance Oximetry in Mouse Tumors. *Radiother. Oncol.* **2003**, *67* (1),

53–61.

(180) Evans, S. M.; Jenkins, K. W.; Jenkins, W. T.; Dilling, T.; Judy, K. D.; Schrlau, A.; Judkins, A.; Hahn, S. M.; Koch, C. J. Imaging and Analytical Methods as Applied to the Evaluation of Vasculature and Hypoxia in Human Brain Tumors. *Radiat. Res.* **2008**, *170* (6), 677–690.

(181) Evans, S. M.; Fraker, D.; Hahn, S. M.; Gleason, K.; Jenkins, W. T.; Jenkins, K.; Hwang, W.-T.; Zhang, P.; Mick, R.; Koch, C. J. EF5 Binding and Clinical Outcome in Human Soft Tissue Sarcomas. *Int. J. Radiat. Oncol. Biol. Phys.* **2006**, *64* (3), 922–927.

(182) Evans, S. M. Comparative Measurements of Hypoxia in Human Brain Tumors Using Needle Electrodes and EF5 Binding. *Cancer Res.* **2004**, *64* (5), 1886–1892.

(183) Kaanders, J. H. A. M.; Wijffels, K. I. E. M.; Marres, H. A. M.; Ljungkvist, A. S. E.; Pop, L. A. M.; van den Hoogen, F. J. A.; de Wilde, P. C. M.; Bussink, J.; Raleigh, J. A.; van der Kogel, A. J. Pimonidazole Binding and Tumor Vascularity Predict for Treatment Outcome in Head and Neck Cancer. *Cancer Res.* **2002**, *62* (23), 7066–7074.

(184) Nordsmark, M.; Loncaster, J.; Aquino-Parsons, C.; Chou, S.-C.; Gebski, V.; West, C.; Lindegaard, J. C.; Havsteen, H.; Davidson, S. E.; Hunter, R.; et al. The Prognostic Value of Pimonidazole and Tumour PO2 in Human Cervix Carcinomas after Radiation Therapy: A Prospective International Multi-Center Study. *Radiother. Oncol.* **2006**, *80* (2), 123–131.

(185) Young, R. J.; Möller, A. Immunohistochemical Detection of Tumour Hypoxia. *Methods Mol. Biol.* **2010**, *611*, 151–159.

(186) Whitmore, G. F.; Varghese, A. J. The Biological Properties of Reduced Nitroheterocyclics and Possible Underlying Biochemical Mechanisms. *Biochem. Pharmacol.* **1986**, *35* (1), 97–103.

(187) Kizaka-Kondoh, S.; Konse-Nagasawa, H. Significance of Nitroimidazole Compounds and Hypoxia-Inducible Factor-1 for Imaging Tumor Hypoxia. *Cancer Sci.* **2009**, *100* (8), 1366–1373.

(188) Shibata, T.; Giaccia, A. J.; Brown, J. M. Development of a Hypoxia-Responsive Vector for Tumor-Specific Gene Therapy. *Gene Ther.* **2000**, *7* (6), 493–498.

(189) Payen, E.; Bettan, M.; Henri, A.; Tomkiewitcz, E.; Houque, A.; Kuzniak, I.; Zuber, J.; Scherman, D.; Beuzard, Y. Oxygen Tension and a Pharmacological Switch in the

Regulation of Transgene Expression for Gene Therapy. *J. Gene Med.* **2001**, *3* (5), 498–504.

(190) Vordermark, D.; Shibata, T.; Brown, J. M. Green Fluorescent Protein Is a Suitable Reporter of Tumor Hypoxia despite an Oxygen Requirement for Chromophore Formation. *Neoplasia* **2001**, *3* (6), 527–534.

(191) Mayer, A.; Wree, A.; Höckel, M.; Leo, C.; Pilch, H.; Vaupel, P. Lack of Correlation between Expression of HIF-1alpha Protein and Oxygenation Status in Identical Tissue Areas of Squamous Cell Carcinomas of the Uterine Cervix. *Cancer Res.* **2004**, *64* (16), 5876–5881.

(192) Lehmann, S.; Stiehl, D. P.; Honer, M.; Dominietto, M.; Keist, R.; Kotevic, I.; Wollenick, K.; Ametamey, S.; Wenger, R. H.; Rudin, M. Longitudinal and Multimodal in Vivo Imaging of Tumor Hypoxia and Its Downstream Molecular Events. *Proc. Natl. Acad. Sci. U. S. A.* **2009**, *106* (33), 14004–14009.

(193) Russell, J.; Carlin, S.; Burke, S. A.; Wen, B.; Yang, K. M.; Ling, C. C. Immunohistochemical Detection of Changes in Tumor Hypoxia. *Int. J. Radiat. Oncol. Biol. Phys.* **2009**, *73* (4), 1177–1186.

(194) Kim, S. J.; Shin, H. J.; Jung, K.-Y.; Baek, S.-K.; Shin, B. K.; Choi, J.; Kim, B. S.; Shin, S. W.; Kim, Y. H.; Kim, J. S.; et al. Prognostic Value of Carbonic Anhydrase IX and Ki-67 Expression in Squamous Cell Carcinoma of the Tongue. *Jpn. J. Clin. Oncol.* **2007**, *37* (11), 812–819.

(195) Mayer, A.; Höckel, M.; Vaupel, P. Carbonic Anhydrase IX Expression and Tumor Oxygenation Status Do Not Correlate at the Microregional Level in Locally Advanced Cancers of the Uterine Cervix. *Clin. Cancer Res.* **2005**, *11* (20), 7220–7225.

(196) Westra, J.; Molema, G.; Kallenberg, C. G. M. Hypoxia-Inducible Factor-1 as Regulator of Angiogenesis in Rheumatoid Arthritis - Therapeutic Implications. *Curr. Med. Chem.* **2010**, *17* (3), 254–263.

(197) Macheda, M. L.; Rogers, S.; Best, J. D. Molecular and Cellular Regulation of Glucose Transporter (GLUT) Proteins in Cancer. *J. Cell. Physiol.* **2005**, *202* (3), 654–662.

(198) Rogers, S.; Macheda, M. L.; Docherty, S. E.; Carty, M. D.; Henderson, M. A.; Soeller, W. C.; Gibbs, E. M.; James, D. E.; Best, J. D. Identification of a Novel Glucose Transporter-like Protein-GLUT-12. *Am. J. Physiol. Endocrinol. Metab.* **2002**, *282* (3),

E733-8.

(199) Airley, R. E.; Loncaster, J.; Raleigh, J. A.; Harris, A. L.; Davidson, S. E.; Hunter, R. D.; West, C. M. L.; Stratford, I. J. GLUT-1 and CAIX as Intrinsic Markers of Hypoxia in Carcinoma of the Cervix: Relationship to Pimonidazole Binding. *Int. J. cancer* **2003**, *104* (1), 85–91.

(200) Jonathan, R. A.; Wijffels, K. I. E. M.; Peeters, W.; de Wilde, P. C. M.; Marres, H. A. M.; Merkx, M. A. W.; Oosterwijk, E.; van der Kogel, A. J.; Kaanders, J. H. A. M. The Prognostic Value of Endogenous Hypoxia-Related Markers for Head and Neck Squamous Cell Carcinomas Treated with ARCON. *Radiother. Oncol.* **2006**, *79* (3), 288–297.

(201) Janssen, H. L. K.; Hoebers, F. J.; Sprong, D.; Goethals, L.; Williams, K. J.; Stratford, I. J.; Haustermans, K. M.; Balm, A. J.; Begg, A. C. Differentiation-Associated Staining with Anti-Pimonidazole Antibodies in Head and Neck Tumors. *Radiother. Oncol.* **2004**, *70* (1), 91–97.

(202) Bennewith, K. L.; Durand, R. E. Quantifying Transient Hypoxia in Human Tumor Xenografts by Flow Cytometry. *Cancer Res.* **2004**, *64* (17), 6183–6189.

(203) Pagida, M. A.; Konstantinidou, A. E.; Malidelis, Y. I.; Ganou, V.; Tsekoura, E.; Patsouris, E.; Panayotacopoulou, M. T. The Human Neurosecretory Neurones under Perinatal Hypoxia: A Quantitative Immunohistochemical Study of the Supraoptic Nucleus in Autopsy Material. *J Neuroendocr.* **2013**, *25* (12), 1255–1263.

(204) Fung, A. S.; Jonkman, J.; Tannock, I. F. Quantitative Immunohistochemistry for Evaluating the Distribution of Ki67 and Other Biomarkers in Tumor Sections and Use of the Method to Study Repopulation in Xenografts after Treatment with Paclitaxel. *Neoplasia* **2012**, *14* (4), 324–334.

(205) Raleigh, J. A.; Chou, S.-C.; Bono, E. L.; Thrall, D. E.; Varia, M. A. Semiquantitative Immunohistochemical Analysis for Hypoxia in Human Tumors. *Int. J. Radiat. Oncol.* **2001**, *49* (2), 569–574.

(206) Leek, R. D.; Landers, R. J.; Harris, A. L.; Lewis, C. E. Necrosis Correlates with High Vascular Density and Focal Macrophage Infiltration in Invasive Carcinoma of the Breast. *Br. J. Cancer* **1999**, *79* (5–6), 991–995.

(207) Murdoch, C.; Giannoudis, A.; Lewis, C. E. Mechanisms Regulating the Recruitment of

Macrophages into Hypoxic Areas of Tumors and Other Ischemic Tissues. *Blood* **2004**, *104* (8), 2224–2234.

(208) Zijlstra, W. G.; Buursma, A.; Meeuwsen-van der Roest, W. P. Absorption Spectra of Human Fetal and Adult Oxyhemoglobin, de-Oxyhemoglobin, Carboxyhemoglobin, and Methemoglobin. *Clin. Chem.* **1991**, *37* (9), 1633–1638.

(209) Severinghaus, J. W. Simple, Accurate Equations for Human Blood O2 Dissociation Computations. *J. Appl. Physiol.* **1979**, *46* (3), 599–602.

(210) Leow, M. K.-S. Configuration of the Hemoglobin Oxygen Dissociation Curve Demystified: A Basic Mathematical Proof for Medical and Biological Sciences Undergraduates. *Adv. Physiol. Educ.* **2007**, *31* (2), 198–201.

(211) Intes, X.; Chance, B. Non-PET Functional Imaging Techniques: Optical. *Radiol. Clin. North Am.* **2005**, *43* (1), 221–34, xii.

(212) Brown, J. Q.; Vishwanath, K.; Palmer, G. M.; Ramanujam, N. Advances in Quantitative UV–visible Spectroscopy for Clinical and Pre-Clinical Application in Cancer. *Curr. Opin. Biotechnol.* **2009**, *20* (1), 119–131.

(213) Palmer, G. M.; Boruta, R. J.; Viglianti, B. L.; Lan, L.; Spasojevic, I.; Dewhirst, M. W. Non-Invasive Monitoring of Intra-Tumor Drug Concentration and Therapeutic Response Using Optical Spectroscopy. *J. Control. Release* **2010**, *142* (3), 457–464.

(214) Soliman, H.; Gunasekara, A.; Rycroft, M.; Zubovits, J.; Dent, R.; Spayne, J.; Yaffe, M. J.; Czarnota, G. J.; Mankoff, D.; Dunnwald, L.; et al. Functional Imaging Using Diffuse Optical Spectroscopy of Neoadjuvant Chemotherapy Response in Women with Locally Advanced Breast Cancer. *Clin. Cancer Res.* **2010**, *16* (9), 2605–2614.

(215) Shonat, R. D.; Wachman, E. S.; Niu, W.; Koretsky, A. P.; Farkas, D. L. Near-Simultaneous Hemoglobin Saturation and Oxygen Tension Maps in Mouse Brain Using an AOTF Microscope. *Biophys. J.* **1997**, *73* (3), 1223–1231.

(216) Sorg, B. S.; Moeller, B. J.; Donovan, O.; Cao, Y.; Dewhirst, M. W. Hyperspectral Imaging of Hemoglobin Saturation in Tumor Microvasculature and Tumor Hypoxia Development. *J. Biomed. Opt.* **2005**, *10* (4), 044004.

(217) Pittman, R. N.; Duling, B. R. Measurement of Percent Oxyhemoglobin in the Microvasculature. *J. Appl. Physiol.* **1975**, *38* (2), 321–327.

(218) Koizumi, H.; Yamamoto, T.; Maki, A.; Yamashita, Y.; Sato, H.; Kawaguchi, H.; Ichikawa, N. Optical Topography: Practical Problems and New Applications. *Appl. Opt.* **2003**, *42* (16), 3054–3062.

(219) Ferrari, M.; Mottola, L.; Quaresima, V. Principles, Techniques, and Limitations of Near Infrared Spectrscopy. *Can. J. Appl. Physiol.* **2004**, *29* (4), 463–487.

(220) Chung, S. H.; Feldman, M. D.; Martinez, D.; Kim, H.; Putt, M. E.; Busch, D. R.; Tchou, J.; Czerniecki, B. J.; Schnall, M. D.; Rosen, M. A.; et al. Macroscopic Optical Physiological Parameters Correlate with Microscopic Proliferation and Vessel Area Breast Cancer Signatures. *Breast Cancer Res.* **2015**, *17* (1), 72.

(221) Boushel, R.; Langberg, H.; Olesen, J.; Gonzales-Alonzo, J.; Bülow, J.; Kjaer, M. Monitoring Tissue Oxygen Availability with near Infrared Spectroscopy (NIRS) in Health and Disease. *Scand. J. Med. Sci. Sports* **2001**, *11* (4), 213–222.

(222) Faber, D. J.; Mik, E. G.; Aalders, M. C. G.; van Leeuwen, T. G. Toward Assessment of Blood Oxygen Saturation by Spectroscopic Optical Coherence Tomography. *Opt. Lett.* **2005**, *30* (9), 1015–1017.

(223) Lu, C.-W.; Lee, C.-K.; Tsai, M.-T.; Wang, Y.-M.; Yang, C. C. Measurement of the Hemoglobin Oxygen Saturation Level with Spectroscopic Spectral-Domain Optical Coherence Tomography. *Opt. Lett.* **2008**, *33* (5), 416–418.

(224) Villringer, A.; Chance, B. Non-Invasive Optical Spectroscopy and Imaging of Human Brain Function. *Trends Neurosci.* **1997**, *20* (10), 435–442.

(225) Boas, D. A.; Brooks, D. H.; Miller, E. L.; DiMarzio, C. A.; Kilmer, M.; Gaudette, R. J.; Quan Zhang. Imaging the Body with Diffuse Optical Tomography. *IEEE Signal Process. Mag.* **2001**, *18* (6), 57–75.

(226) Tromberg, B. J.; Pogue, B. W.; Paulsen, K. D.; Yodh, A. G.; Boas, D. A.; Cerussi, A. E. Assessing the Future of Diffuse Optical Imaging Technologies for Breast Cancer Management. *Med. Phys.* **2008**, *35* (6Part1), 2443–2451.

(227) Pogue, B. W.; Davis, S. C.; Song, X.; Brooksby, B. A.; Dehghani, H.; Paulsen, K. D. Image Analysis Methods for Diffuse Optical Tomography. *J. Biomed. Opt.* **2006**, *11* (3), 033001.

(228) Zhang, H. F.; Maslov, K.; Stoica, G.; Wang, L. V. Functional Photoacoustic Microscopy for High-Resolution and Noninvasive in Vivo Imaging. *Nat. Biotechnol.*

2006, *24* (7), 848–851.

(229) Siphanto, R. I.; Thumma, K. K.; Kolkman, R. G. M.; van Leeuwen, T. G.; de Mul, F. F. M.; van Neck, J. W.; van Adrichem, L. N. A.; Steenbergen, W. Serial Noninvasive Photoacoustic Imaging of Neovascularization in Tumor Angiogenesis. *Opt. Express* **2005**, *13* (1), 89–95.

(230) Sun, Z.-P.; Liu, L.; Zhang, L.; Jia, D.-Z. Rapid Synthesis of ZnO Nano-Rods by One-Step, Room-Temperature, Solid-State Reaction and Their Gas-Sensing Properties. *Nanotechnology* **2006**, *17* (9), 2266–2270.

(231) Emelianov, S. Y.; Aglyamov, S. R.; Karpiouk, A. B.; Mallidi, S.; Park, S.; Scott, W. G.; Sethuraman, S.; Shah, J.; Smalling, R. W.; Rubin, J. M.; et al. Synergy and Applications of Combined Ultrasound, Elasticity, and Photoacoustic Imaging. In *2006 IEEE Ultrasonics Symposium*; IEEE: Vancouver, BC, 2006; pp 405–415.

(232) Wang, L. V. Prospects of Photoacoustic Tomography. *Med. Phys.* **2008**, *35* (12), 5758–5767.

(233) Gerling, M.; Zhao, Y.; Nania, S.; Norberg, K. J.; Verbeke, C. S.; Englert, B.; Kuiper, R. V.; Bergström, A.; Hassan, M.; Neesse, A.; et al. Real-Time Assessment of Tissue Hypoxia in Vivo with Combined Photoacoustics and High-Frequency Ultrasound. *Theranostics* **2014**, *4* (6), 604–613.

(234) Mallidi, S.; Watanabe, K.; Timerman, D.; Schoenfeld, D.; Hasan, T. Prediction of Tumor Recurrence and Therapy Monitoring Using Ultrasound-Guided Photoacoustic Imaging. *Theranostics* **2015**, *5* (3), 289–301.

(235) Xu, M.; Wang, L. V. Photoacoustic Imaging in Biomedicine. *Rev. Sci. Instrum.* **2006**, *77* (4), 041101.

(236) Ku, G.; Wang, L. V. Deeply Penetrating Photoacoustic Tomography in Biological Tissues Enhanced with an Optical Contrast Agent. *Opt. Lett.* **2005**, *30* (5), 507–509.

(237) Shao, Q.; Morgounova, E.; Jiang, C.; Choi, J.; Bischof, J.; Ashkenazi, S. In Vivo Photoacoustic Lifetime Imaging of Tumor Hypoxia in Small Animals. *J. Biomed. Opt.* **2013**, *18* (7), 076019.

(238) Shao, Q.; Morgounova, E.; Choi, J.-H.; Jiang, C.; Bischof, J.; Ashkenazi, S. Mapping Tissue Oxygen *in Vivo* by Photoacoustic Lifetime Imaging; Oraevsky, A. A., Wang, L. V., Eds.; International Society for Optics and Photonics, 2013; p 85811S.

(239) Shao, Q.; Biel, M. A.; Ashkenazi, S. Noninvasive Tumor Oxygen Imaging by Photoacoustic Lifetime Imaging Integrated with Photodynamic Therapy; Kessel, D. H., Hasan, T., Eds.; International Society for Optics and Photonics, 2014; p 89310H.

(240) Wu, D.; Huang, L.; Jiang, M. S.; Jiang, H. Contrast Agents for Photoacoustic and Thermoacoustic Imaging: A Review. *Int. J. Mol. Sci.* **2014**, *15* (12), 23616–23639.

(241) Dmitriev, R. I.; Papkovsky, D. B. Optical Probes and Techniques for O2 Measurement in Live Cells and Tissue. *Cell. Mol. Life Sci.* **2012**, *69* (12), 2025–2039.

(242) Quaranta, M.; Borisov, S. M.; Klimant, I. Indicators for Optical Oxygen Sensors. *Bioanal. Rev.* **2012**, *4* (2–4), 115–157.

(243) Papkovsky, D. B.; Dmitriev, R. I.; Morris, R. L.; Schmidt, T. M.; Fenchel, T.; Finlay, B.; Nelson, N.; Ball, S.; Colleoni, C.; Cenci, U.; et al. Biological Detection by Optical Oxygen Sensing. *Chem. Soc. Rev.* **2013**, *42* (22), 8700.

(244) Wang, X.-D.; Wolfbeis, O. S. Optical Methods for Sensing and Imaging Oxygen: Materials, Spectroscopies and Applications. *Chem. Soc. Rev.* **2014**, *43* (10), 3666–3761.

(245) Rumsey, W. L.; Vanderkooi, J. M.; Wilson, D. F. Imaging of Phosphorescence: A Novel Method for Measuring Oxygen Distribution in Perfused Tissue. *Science* **1988**, *241* (4873), 1649–1651.

(246) Vanderkooi, J.; Maniara, G.; Green, T.; Wilson, D. An Optical Method for Measurement of Dioxygen Concentration Based upon Quenching of Phosphorescence. *J. Biol. Chem.* **1987**, *262* (12), 5476–5482.

(247) Ranji, M.; Jaggard, D. L.; Apreleva, S. V.; Vinogradov, S. A.; Chance, B. Simultaneous Fluorometry and Phosphorometry of Langendorff Perfused Rat Heart: Ex Vivo Animal Studies. *Opt. Lett.* **2006**, *31* (20), 2995.

(248) Shonat, R. D.; Kight, A. C. Oxygen Tension Imaging in the Mouse Retina. *Ann. Biomed. Eng.* **2003**, *31* (9), 1084–1096.

(249) Sakadžić, S.; Roussakis, E.; Yaseen, M. A.; Mandeville, E. T.; Srinivasan, V. J.; Arai, K.; Ruvinskaya, S.; Devor, A.; Lo, E. H.; Vinogradov, S. A.; et al. Two-Photon High-Resolution Measurement of Partial Pressure of Oxygen in Cerebral Vasculature and Tissue. *Nat. Methods* **2010**, *7* (9), 755–759.

(250) Ziemer, L. S.; Lee, W. M. F.; Vinogradov, S. A.; Sehgal, C.; Wilson, D. F. Oxygen Distribution in Murine Tumors: Characterization Using Oxygen-Dependent Quenching of Phosphorescence. *J. Appl. Physiol.* **2005**, *98* (4), 1503–1510.

(251) Collingridge, D. R.; Young, W. K.; Vojnovic, B.; Wardman, P.; Lynch, E. M.; Hill, S. A.; Chaplin, D. J. Measurement of Tumor Oxygenation: A Comparison between Polarographic Needle Electrodes and a Time-Resolved Luminescence-Based Optical Sensor. *Radiat. Res.* **1997**, *147* (3), 329.

(252) Bussink, J.; Kaanders, J. H. A. .; Strik, A. M.; van der Kogel, A. J. Effects of Nicotinamide and Carbogen on Oxygenation in Human Tumor Xenografts Measured with Luminescense Based Fiber-Optic Probes. *Radiother. Oncol.* **2000**, *57* (1), 21–30.

(253) Young, W. K.; Vojnovic, B.; Wardman, P. Measurement of Oxygen Tension in Tumours by Time-Resolved Fluorescence. *Br. J. Cancer. Suppl.* **1996**, *27*, S256-9.

(254) Plant, R. L.; Burns, D. H. Quantitative, Depth-Resolved Imaging of Oxygen Concentration by Phosphorescence Lifetime Measurement. *Appl. Spectrosc. Vol. 47, Issue 10, pp. 1594-1599* **1993**, *47* (10), 1594–1599.

(255) Apreleva, S. V.; Wilson, D. F.; Vinogradov, S. A. Tomographic Imaging of Oxygen by Phosphorescence Lifetime. *Appl. Opt.* **2006**, *45* (33), 8547.

(256) Cárdenas-Navia, L. I.; Mace, D.; Richardson, R. A.; Wilson, D. F.; Shan, S.; Dewhirst, M. W. The Pervasive Presence of Fluctuating Oxygenation in Tumors. *Cancer Res.* **2008**, *68* (14), 5812–5819.

(257) Spencer, J. A.; Ferraro, F.; Roussakis, E.; Klein, A.; Wu, J.; Runnels, J. M.; Zaher, W.; Mortensen, L. J.; Alt, C.; Turcotte, R.; et al. Direct Measurement of Local Oxygen Concentration in the Bone Marrow of Live Animals. *Nature* **2014**, *508* (7495), 269–273.

(258) Lecoq, J.; Parpaleix, A.; Roussakis, E.; Ducros, M.; Houssen, Y. G.; Vinogradov, S. A.; Charpak, S. Simultaneous Two-Photon Imaging of Oxygen and Blood Flow in Deep Cerebral Vessels. *Nat. Med.* **2011**, *17* (7), 893–898.

(259) Dobrucki, J. W. Interaction of Oxygen-Sensitive Luminescent Probes Ru(Phen)(3)(2+) and Ru(Bipy)(3)(2+) with Animal and Plant Cells in Vitro. Mechanism of Phototoxicity and Conditions for Non-Invasive Oxygen Measurements. *J. Photochem. Photobiol. B.* **2001**, *65* (2–3), 136–144.

(260) Komatsu, H.; Yoshihara, K.; Yamada, H.; Kimura, Y.; Son, A.; Nishimoto, S.; Tanabe, K. Ruthenium Complexes with Hydrophobic Ligands That Are Key Factors for the Optical Imaging of Physiological Hypoxia. *Chem. - A Eur. J.* **2013**, *19* (6), 1971–1977.

(261) You, Y. Recent Progress on the Exploration of the Biological Utility of Cyclometalated Iridium(III) Complexes. *J. Chinese Chem. Soc.* **2018**, *65* (3), 352–367.

(262) Zhang, S.; Hosaka, M.; Yoshihara, T.; Negishi, K.; Iida, Y.; Tobita, S.; Takeuchi, T.; Brahimi-Horn, C.; Berra, E.; Pouysségur, J.; et al. Phosphorescent Light-Emitting Iridium Complexes Serve as a Hypoxia-Sensing Probe for Tumor Imaging in Living Animals. *Cancer Res.* **2010**, *70* (11), 4490–4498.

(263) Sun, W.; Guo, S.; Hu, C.; Fan, J.; Peng, X. Recent Development of Chemosensors Based on Cyanine Platforms. *Chem. Rev.* **2016**, *116* (14), 7768–7817.

(264) Kim, H. N.; Lee, M. H.; Kim, H. J.; Kim, J. S.; Yoon, J. A New Trend in Rhodamine-Based Chemosensors: Application of Spirolactam Ring-Opening to Sensing Ions. *Chem. Soc. Rev.* **2008**, *37* (8), 1465–1472.

(265) Qian, X.; Xiao, Y.; Xu, Y.; Guo, X.; Qian, J.; Zhu, W. "Alive" Dyes as Fluorescent Sensors: Fluorophore, Mechanism, Receptor and Images in Living Cells. *Chem. Commun.* **2010**, *46* (35), 6418–6436.

(266) Lepock, J. R.; Thompson, J. E.; Kruuv, J.; Wallach, D. F. H. Photoinduced Crosslinking of Membrane Proteins by Fluorescein Isothiocyanate. *Biochem. Biophys. Res. Commun.* **1978**, *85* (1), 344–350.

(267) Johnson, G. D.; Davidson, R. S.; McNamee, K. C.; Russell, G.; Goodwin, D.; Holborow, E. J. Fading of Immunofluorescence during Microscopy: A Study of the Phenomenon and Its Remedy. *J. Immunol. Methods* **1982**, *55* (2), 231–242.

(268) Sun, W.-C.; Gee, K. R.; Klaubert, D. H.; Haugland, R. P. Synthesis of Fluorinated Fluoresceins. *J. Org. Chem.* **1997**, *62* (19), 6469–6475.

(269) Elliott, K. A.; Baker, Z. The Effects of Oxidation-Reduction Potential Indicator Dyes on the Metabolism of Tumour and Normal Tissues. *Biochem. J.* **1935**, *29* (10), 2396–2404.

(270) Bastos, A. L.; Marques, D.; Affra, M. A. Dye-Induced Fluorescence of Tumour Cells: Photochemical Action Spectra. *Histochem. J.* **1974**, *6* (3), 237–243.

(271) Esipova, T. V.; Karagodov, A.; Miller, J.; Wilson, D. F.; Busch, T. M.; Vinogradov, S. A. Two New "Protected" Oxyphors for Biological Oximetry: Properties and Application in Tumor Imaging. *Anal. Chem.* **2011**, *83* (22), 8756–8765.

(272) Dunphy, I.; Vinogradov, S. A.; Wilson, D. F. Oxyphor R2 and G2: Phosphors for Measuring Oxygen by Oxygen-Dependent Quenching of Phosphorescence. *Anal Biochem* **2002**, *310* (2), 191–198.

(273) Erickson, K.; Braun, R. D.; Yu, D.; Lanzen, J.; Wilson, D.; Brizel, D. M.; Secomb, T. W.; Biaglow, J. E.; Dewhirst, M. W. Effect of Longitudinal Oxygen Gradients on Effectiveness of Manipulation of Tumor Oxygenation. *Cancer Res.* **2003**, *63* (15), 4705–4712.

(274) Wang, X.; Chen, H.; Zhao, Y.; Chen, X.; Wang, X.; Chen, X. Optical Oxygen Sensors Move towards Colorimetric Determination. *TrAC Trends Anal. Chem.* **2010**, *29* (4), 319–338.

(275) Rasey, J. S.; Koh, W. J.; Evans, M. L.; Peterson, L. M.; Lewellen, T. K.; Graham, M. M.; Krohn, K. A. Quantifying Regional Hypoxia in Human Tumors with Positron Emission Tomography of [18F]Fluoromisonidazole: A Pretherapy Study of 37 Patients. *Int. J. Radiat. Oncol. Biol. Phys.* **1996**, *36* (2), 417–428.

(276) Souvatzoglou, M.; Grosu, A. L.; Röper, B.; Krause, B. J.; Beck, R.; Reischl, G.; Picchio, M.; Machulla, H.-J.; Wester, H.-J.; Piert, M. Tumour Hypoxia Imaging with [18F]FAZA PET in Head and Neck Cancer Patients: A Pilot Study. *Eur. J. Nucl. Med. Mol. Imaging* **2007**, *34* (10), 1566–1575.

(277) Lehtiö, K.; Eskola, O.; Viljanen, T.; Oikonen, V.; Grönroos, T.; Sillanmäki, L.; Grénman, R.; Minn, H. Imaging Perfusion and Hypoxia with PET to Predict Radiotherapy Response in Head-and-Neck Cancer. *Int. J. Radiat. Oncol. Biol. Phys.* **2004**, *59* (4), 971–982.

(278) Koh, W. J.; Rasey, J. S.; Evans, M. L.; Grierson, J. R.; Lewellen, T. K.; Graham, M. M.; Krohn, K. A.; Griffin, T. W. Imaging of Hypoxia in Human Tumors with [F-18]Fluoromisonidazole. *Int. J. Radiat. Oncol. Biol. Phys.* **1992**, *22* (1), 199–212.

(279) Lee, S. T.; Scott, A. M. Hypoxia Positron Emission Tomography Imaging with 18f-Fluoromisonidazole. *Semin. Nucl. Med.* **2007**, *37* (6), 451–461.

(280) Gagel, B.; Reinartz, P.; Demirel, C.; Kaiser, H. J.; Zimny, M.; Piroth, M.; Pinkawa,

M.; Stanzel, S.; Asadpour, B.; Hamacher, K.; et al. [18F] Fluoromisonidazole and [18F] Fluorodeoxyglucose Positron Emission Tomography in Response Evaluation after Chemo-/Radiotherapy of Non-Small-Cell Lung Cancer: A Feasibility Study. *BMC Cancer* **2006**, *6* (51), 1–8.

(281) Eschmann, S.-M.; Paulsen, F.; Reimold, M.; Dittmann, H.; Welz, S.; Reischl, G.; Machulla, H.-J.; Bares, R. Prognostic Impact of Hypoxia Imaging with 18F-Misonidazole PET in Non-Small Cell Lung Cancer and Head and Neck Cancer before Radiotherapy. *J. Nucl. Med.* **2005**, *46* (2), 253–260.

(282) Bentzen, L.; Keiding, S.; Nordsmark, M.; Falborg, L.; Hansen, S. B.; Keller, J.; Nielsen, O. S.; Overgaard, J. Tumour Oxygenation Assessed by 18F-Fluoromisonidazole PET and Polarographic Needle Electrodes in Human Soft Tissue Tumours. *Radiother. Oncol.* **2003**, *67* (3), 339–344.

(283) Bell, C.; Dowson, N.; Fay, M.; Thomas, P.; Puttick, S.; Gal, Y.; Rose, S. Hypoxia Imaging in Gliomas With 18F-Fluoromisonidazole PET: Toward Clinical Translation. *Semin. Nucl. Med.* **2015**, *45* (2), 136–150.

(284) Valk, P. E.; Mathis, C. A.; Prados, M. D.; Gilbert, J. C.; Budinger, T. F. Hypoxia in Human Gliomas: Demonstration by PET with Fluorine-18-Fluoromisonidazole. *J. Nucl. Med.* **1992**, *33* (12), 2133–2137.

(285) Lehtio, K.; Oikonen, V.; Gronroos, T.; Eskola, O.; Kalliokoski, K.; Bergman, J.; Solin, O.; Grenman, R.; Nuutila, P.; Minn, H. Imaging of Blood Flow and Hypoxia in Head and Neck Cancer: Initial Evaluation with [15O]H2O and [18F]Fluoroerythronitroimidazole PET. *J. Nucl. Med.* **2001**, *42* (11), 1643–1652.

(286) Yang, D. J.; Wallace, S.; Cherif, A.; Li, C.; Gretzer, M. B.; Kim, E. E.; Podoloff, D. A. Development of F-18-Labeled Fluoroerythronitroimidazole as a PET Agent for Imaging Tumor Hypoxia. *Radiology* **1995**, *194* (3), 795–800.

(287) Barthel, H.; Wilson, H.; Collingridge, D. R.; Brown, G.; Osman, S.; Luthra, S. K.; Brady, F.; Workman, P.; Price, P. M.; Aboagye, E. O. In Vivo Evaluation of [18F]Fluoroetanidazole as a New Marker for Imaging Tumour Hypoxia with Positron Emission Tomography. *Br. J. Cancer* **2004**, *90* (11), 2232–2242.

(288) Sorger, D.; Patt, M.; Kumar, P.; Wiebe, L. I.; Barthel, H.; Seese, A.; Dannenberg, C.; Tannapfel, A.; Kluge, R.; Sabri, O. [18F]Fluoroazomycinarabinofuranoside (18FAZA)

and [18F]Fluoromisonidazole (18FMISO): A Comparative Study of Their Selective Uptake in Hypoxic Cells and PET Imaging in Experimental Rat Tumors. *Nucl. Med. Biol.* **2003**, *30* (3), 317–326.

(289) Kachur, A. V; Dolbier, W. R.; Evans, S. M.; Shiue, C. Y.; Shiue, G. G.; Skov, K. A.; Baird, I. R.; James, B. R.; Li, A. R.; Roche, A.; et al. Synthesis of New Hypoxia Markers EF1 and [18F]-EF1. *Appl. Radiat. Isot.* **1999**, *51* (6), 643–650.

(290) Evans, S. M.; Kachur, A. V; Shiue, C. Y.; Hustinx, R.; Jenkins, W. T.; Shive, G. G.; Karp, J. S.; Alavi, A.; Lord, E. M.; Dolbier, W. R.; et al. Noninvasive Detection of Tumor Hypoxia Using the 2-Nitroimidazole [18F]EF1. *J. Nucl. Med.* **2000**, *41* (2), 327–336.

(291) Ziemer, L. S.; Evans, S. M.; Kachur, A. V; Shuman, A. L.; Cardi, C. A.; Jenkins, W. T.; Karp, J. S.; Alavi, A.; Dolbier, W. R.; Koch, C. J. Noninvasive Imaging of Tumor Hypoxia in Rats Using the 2-Nitroimidazole 18F-EF5. *Eur. J. Nucl. Med. Mol. Imaging* **2003**, *30* (2), 259–266.

(292) Horsman, M. R.; Mortensen, L. S.; Petersen, J. B.; Busk, M.; Overgaard, J. Imaging Hypoxia to Improve Radiotherapy Outcome. *Nat. Rev. Clin. Oncol.* **2012**, *9* (12), 674–687.

(293) Riedl, C. C.; Brader, P.; Zanzonico, P. B.; Chun, Y. S.; Woo, Y.; Singh, P.; Carlin, S.; Wen, B.; Ling, C. C.; Hricak, H.; et al. Imaging Hypoxia in Orthotopic Rat Liver Tumors with Iodine 124-Labeled Iodoazomycin Galactopyranoside PET. *Radiology* **2008**, *248* (2), 561–570.

(294) Zanzonico, P.; O'Donoghue, J.; Chapman, J. D.; Schneider, R.; Cai, S.; Larson, S.; Wen, B.; Chen, Y.; Finn, R.; Ruan, S.; et al. Iodine-124-Labeled Iodo-Azomycin-Galactoside Imaging of Tumor Hypoxia in Mice with Serial MicroPET Scanning. *Eur. J. Nucl. Med. Mol. Imaging* **2004**, *31* (1), 117–128.

(295) Vāvere, A. L.; Lewis, J. S. Cu-ATSM: A Radiopharmaceutical for the PET Imaging of Hypoxia. *Dalton Trans.* **2007**, No. 43, 4893–4902.

(296) Padhani, A. R.; Krohn, K. A.; Lewis, J. S.; Alber, M. Imaging Oxygenation of Human Tumours. *Eur. Radiol.* **2007**, *17* (4), 861–872.

(297) Lewis, J. S.; Herrero, P.; Sharp, T. L.; Engelbach, J. A.; Fujibayashi, Y.; Laforest, R.; Kovacs, A.; Gropler, R. J.; Welch, M. J. Delineation of Hypoxia in Canine

Myocardium Using PET and Copper(II)-Diacetyl-Bis(N(4)-Methylthiosemicarbazone). *J. Nucl. Med.* **2002**, *43* (11), 1557–1569.

(298) Arabi, M.; Piert, M. Hypoxia PET/CT Imaging: Implications for Radiation Oncology. *Q. J. Nucl. Med. Mol. Imaging* **2010**, *54* (5), 500–509.

(299) Lewis, J. S.; McCarthy, D. W.; McCarthy, T. J.; Fujibayashi, Y.; Welch, M. J. Evaluation of 64Cu-ATSM in Vitro and in Vivo in a Hypoxic Tumor Model. *J. Nucl. Med.* **1999**, *40* (1), 177–183.

(300) Takahashi, N.; Fujibayashi, Y.; Yonekura, Y.; Welch, M. J.; Waki, A.; Tsuchida, T.; Sadato, N.; Sugimoto, K.; Itoh, H. Evaluation of 62Cu Labeled Diacetyl-Bis(N4-Methylthiosemicarbazone) as a Hypoxic Tissue Tracer in Patients with Lung Cancer. *Ann. Nucl. Med.* **2000**, *14* (5), 323–328.

(301) Dehdashti, F.; Grigsby, P. W.; Mintun, M. A.; Lewis, J. S.; Siegel, B. A.; Welch, M. J. Assessing Tumor Hypoxia in Cervical Cancer by Positron Emission Tomography with 60Cu-ATSM: Relationship to Therapeutic Response-a Preliminary Report. *Int. J. Radiat. Oncol. Biol. Phys.* **2003**, *55* (5), 1233–1238.

(302) Minagawa, Y.; Shizukuishi, K.; Koike, I.; Horiuchi, C.; Watanuki, K.; Hata, M.; Omura, M.; Odagiri, K.; Tohnai, I.; Inoue, T.; et al. Assessment of Tumor Hypoxia by 62Cu-ATSM PET/CT as a Predictor of Response in Head and Neck Cancer: A Pilot Study. *Ann. Nucl. Med.* **2011**, *25* (5), 339–345.

(303) Tateishi, K.; Tateishi, U.; Sato, M.; Yamanaka, S.; Kanno, H.; Murata, H.; Inoue, T.; Kawahara, N. Application of ^{62} Cu-Diacetyl-Bis (N ^{4} -Methylthiosemicarbazone) PET Imaging to Predict Highly Malignant Tumor Grades and Hypoxia-Inducible Factor-1α Expression in Patients with Glioma. *Am. J. Neuroradiol.* **2013**, *34* (1), 92–99.

(304) Vāvere, A. L.; Lewis, J. S. Examining the Relationship between Cu-ATSM Hypoxia Selectivity and Fatty Acid Synthase Expression in Human Prostate Cancer Cell Lines. *Nucl. Med. Biol.* **2008**, *35* (3), 273–279.

(305) Cho, H.; Ackerstaff, E.; Carlin, S.; Lupu, M. E.; Wang, Y.; Rizwan, A.; O'Donoghue, J.; Ling, C. C.; Humm, J. L.; Zanzonico, P. B.; et al. Noninvasive Multimodality Imaging of the Tumor Microenvironment: Registered Dynamic Magnetic Resonance Imaging and Positron Emission Tomography Studies of a Preclinical Tumor Model of Tumor Hypoxia. *Neoplasia* **2009**, *11* (3), 247–259.

(306) Yuan, H.; Schroeder, T.; Bowsher, J. E.; Hedlund, L. W.; Wong, T.; Dewhirst, M. W. Intertumoral Differences in Hypoxia Selectivity of the PET Imaging Agent 64Cu(II)-Diacetyl-Bis(N4-Methylthiosemicarbazone). *J. Nucl. Med.* **2006**, *47* (6), 989–998.

(307) Jalilian, A.; Rostampour, N.; Rowshanfarzad, P.; Shafaii, K.; Kamali-Dehghan, M.; Akhlaghi, M. Preclinical Studies of [61Cu]ATSM as a PET Radiopharmaceutical for Fibrosarcoma Imaging. *Acta Pharm.* **2009**, *59* (1), 45–55.

(308) Busk, M.; Horsman, M. R.; Kristjansen, P. E. G.; van der Kogel, A. J.; Bussink, J.; Overgaard, J. Aerobic Glycolysis in Cancers: Implications for the Usability of Oxygen-Responsive Genes and Fluorodeoxyglucose-PET as Markers of Tissue Hypoxia. *Int. J. cancer* **2008**, *122* (12), 2726–2734.

(309) Christian, N.; Deheneffe, S.; Bol, A.; De Bast, M.; Labar, D.; Lee, J. A.; Grégoire, V. Is (18)F-FDG a Surrogate Tracer to Measure Tumor Hypoxia? Comparison with the Hypoxic Tracer (14)C-EF3 in Animal Tumor Models. *Radiother. Oncol.* **2010**, *97* (2), 183–188.

(310) Kimura, H.; Braun, R. D.; Ong, E. T.; Hsu, R.; Secomb, T. W.; Papahadjopoulos, D.; Hong, K.; Dewhirst, M. W. Fluctuations in Red Cell Flux in Tumor Microvessels Can Lead to Transient Hypoxia and Reoxygenation in Tumor Parenchyma. *Cancer Res.* **1996**, *56* (23), 5522–5528.

(311) Komar, G.; Seppänen, M.; Eskola, O.; Lindholm, P.; Grönroos, T. J.; Forsback, S.; Sipilä, H.; Evans, S. M.; Solin, O.; Minn, H. 18F-EF5: A New PET Tracer for Imaging Hypoxia in Head and Neck Cancer. *J. Nucl. Med.* **2008**, *49* (12), 1944–1951.

(312) Stypinski, D.; McQuarrie, S. A.; Wiebe, L. I.; Tam, Y. K.; Mercer, J. R.; McEwan, A. J. Dosimetry Estimations for 123I-IAZA in Healthy Volunteers. *J. Nucl. Med.* **2001**, *42* (9), 1418–1423.

(313) Stypinski, D.; Wiebe, L. I.; McEwan, A. J.; Schmidt, R. P.; Tam, Y. K.; Mercer, J. R. Clinical Pharmacokinetics of 123I-IAZA in Healthy Volunteers. *Nucl. Med. Commun.* **1999**, *20* (6), 559–567.

(314) Iyer, R. V; Kim, E.; Schneider, R. F.; Chapman, J. D. A Dual Hypoxic Marker Technique for Measuring Oxygenation Change within Individual Tumors. *Br. J. Cancer* **1998**, *78* (2), 163–169.

(315) Mees, G.; Dierckx, R.; Vangestel, C.; Van de Wiele, C. Molecular Imaging of Hypoxia

with Radiolabelled Agents. *Eur. J. Nucl. Med. Mol. Imaging* **2009**, *36* (10), 1674–1686.

(316) Ballinger, J. R.; Kee, J. W.; Rauth, A. M. In Vitro and in Vivo Evaluation of a Technetium-99m-Labeled 2-Nitroimidazole (BMS181321) as a Marker of Tumor Hypoxia. *J. Nucl. Med.* **1996**, *37* (6), 1023–1031.

(317) Hoebers, F. J. P.; Janssen, H. L. K.; Olmos, A. V.; Sprong, D.; Nunn, A. D.; Balm, A. J. M.; Hoefnagel, C. A.; Begg, A. C.; Haustermans, K. M. G. Phase 1 Study to Identify Tumour Hypoxia in Patients with Head and Neck Cancer Using Technetium-99m BRU 59-21. *Eur. J. Nucl. Med. Mol. Imaging* **2002**, *29* (9), 1206–1211.

(318) Yutani, K.; Kusuoka, H.; Fukuchi, K.; Tatsumi, M.; Nishimura, T. Applicability of 99mTc-HL91, a Putative Hypoxic Tracer, to Detection of Tumor Hypoxia. *J. Nucl. Med.* **1999**, *40* (5), 854–861.

(319) Bloch, F.; Hansen, W. W.; Packard, M. Nuclear Induction. *Phys. Rev.* **1946**, *69* (3–4), 127–127.

(320) Zavoisky, E. Spin-Magnetic Resonance in Paramagnetics. *J Phys E* **1945**, *9*, 245–249.

(321) Rabi, I. I.; Zacharias, J. R.; Millman, S.; Kusch, P. A New Method of Measuring Nuclear Magnetic Moment. *Phys. Rev.* **1938**, *53* (4), 318–318.

(322) Ahmad, R.; Kuppusamy, P. Theory, Instrumentation, and Applications of Electron Paramagnetic Resonance Oximetry. *Chem. Rev.* **2010**, *110* (5), 3212–3236.

(323) O'Connor, J. P. B.; Jackson, A.; Buonaccorsi, G. A.; Buckley, D. L.; Roberts, C.; Watson, Y.; Cheung, S.; McGrath, D. M.; Naish, J. H.; Rose, C. J.; et al. Organ-Specific Effects of Oxygen and Carbogen Gas Inhalation on Tissue Longitudinal Relaxation Times. *Magn. Reson. Med.* **2007**, *58* (3), 490–496.

(324) Hyde, J. S.; Subczynski, W. K. Spin-Label Oximetry; 1989; pp 399–425.

(325) Teng, C.-L.; Hong, H.; Kiihne, S.; Bryant, R. G. Molecular Oxygen Spin–Lattice Relaxation in Solutions Measured by Proton Magnetic Relaxation Dispersion. *J. Magn. Reson.* **2001**, *148* (1), 31–34.

(326) Gallez, B.; Bacic, G.; Goda, F.; Jiang, J.; O′Hara, J. A.; Dunn, J. F.; Swartz, H. M. Use of Nitroxides for Assessing Perfusion, Oxygenation, and Viability of Tissues:In Vivo EPR and MRI Studies. *Magn. Reson. Med.* **1996**, *35* (1), 97–106.

(327) Halpern, H. J.; Yu, C.; Peric, M.; Barth, E. D.; Karczmar, G. S.; River, J. N.; Grdina, D. J.; Teicher, B. A. Measurement of Differences in PO 2 in Response to Perfluorocarbon/Carbogen in FSa and NFSa Murine Fibrosarcomas with Low-Frequency Electron Paramagnetic Resonance Oximetry. *Radiat. Res.* **1996**, *145* (5), 610–618.

(328) Hou, H.; Dong, R.; Li, H.; Williams, B.; Lariviere, J. P.; Hekmatyar, S. K.; Kauppinen, R. A.; Khan, N.; Swartz, H. Dynamic Changes in Oxygenation of Intracranial Tumor and Contralateral Brain during Tumor Growth and Carbogen Breathing: A Multisite EPR Oximetry with Implantable Resonators. *J. Magn. Reson.* **2012**, *214*, 22–28.

(329) Ilangovan, G.; Liebgott, T.; Kutala, V. K.; Petryakov, S.; Zweier, J. L.; Kuppusamy, P. EPR Oximetry in the Beating Heart: Myocardial Oxygen Consumption Rate as an Index of Postischemic Recovery. *Magn. Reson. Med.* **2004**, *51* (4), 835–842.

(330) Kuppusamy, P.; Afeworki, M.; Shankar, R. A.; Coffin, D.; Kirshna, M. C.; Hahn, S. M.; Mitchell, J. B.; Zweier, J. L.; Krishna, M. C.; Hahn, S. M.; et al. In Vivo Electron Paramagnetic Resonance Imaging of Tumor Heterogeneity and Oxygenation in a Murine Model. *Cancer Res.* **1998**, *58* (7), 1562–1568.

(331) Krishna, M. C.; English, S.; Yamada, K.; Yoo, J.; Murugesan, R.; Devasahayam, N.; Cook, J. A.; Golman, K.; Ardenkjaer-Larsen, J. H.; Subramanian, S.; et al. Overhauser Enhanced Magnetic Resonance Imaging for Tumor Oximetry: Coregistration of Tumor Anatomy and Tissue Oxygen Concentration. *Proc. Natl. Acad. Sci. U. S. A.* **2002**, *99* (4), 2216–2221.

(332) Matsumoto, A.; Matsumoto, K.; Matsumoto, S.; Hyodo, F.; Sowers, A. L.; Koscielniak, J. W.; Devasahayam, N.; Subramanian, S.; Mitchell, J. B.; Krishna, M. C. Intracellular Hypoxia of Tumor Tissue Estimated by Noninvasive Electron Paramagnetic Resonance Oximetry Technique Using Paramagnetic Probes. *Biol. Pharm. Bull.* **2011**, *34* (1), 142–145.

(333) Elas, M.; Bell, R.; Hleihel, D.; Barth, E. D.; McFaul, C.; Haney, C. R.; Bielanska, J.; Pustelny, K.; Ahn, K.-H.; Pelizzari, C. A.; et al. Electron Paramagnetic Resonance Oxygen Image Hypoxic Fraction plus Radiation Dose Strongly Correlates with Tumor Cure in FSa Fibrosarcomas. *Int. J. Radiat. Oncol. Biol. Phys.* **2008**, *71* (2), 542–549.

(334) Desmet, C. M.; Lafosse, A.; Vériter, S.; Porporato, P. E.; Sonveaux, P.; Dufrane, D.; Levêque, P.; Gallez, B. Application of Electron Paramagnetic Resonance (EPR)

Oximetry to Monitor Oxygen in Wounds in Diabetic Models. *PLoS One* **2015**, *10* (12), e0144914.

(335) Swartz, H. M.; Glockner, J. F. Measurement of Oxygen by EPRI and EPRS. In *EPR Imaging and In Vivo EPR*; Eaton, G. R., Eaton, S. S., Ohno, K., Eds.; CRC Press: Boca Raton (FL), 1991; pp 261–290.

(336) Turek, P.; Moussavi, M.; André, J.-J. Magnetic Properties of the Lithium Phthalocyanine π-Radical. Role of Dioxygen. *Europhys. Lett.* **1989**, *8* (3), 275–280.

(337) Liu, K. J.; Grinstaff, M. W.; Jiang, J.; Suslick, K. S.; Swartz, H. M.; Wang, W. In Vivo Measurement of Oxygen Concentration Using Sonochemically Synthesized Microspheres. *Biophys. J.* **1994**, *67* (2), 896–901.

(338) Kusumi, A.; Subczynski, W. K.; Hyde, J. S. Oxygen Transport Parameter in Membranes as Deduced by Saturation Recovery Measurements of Spin-Lattice Relaxation Times of Spin Labels. *Proc. Natl. Acad. Sci. U. S. A.* **1982**, *79* (6), 1854–1858.

(339) Liu, K. J.; Gast, P.; Moussavi, M.; Norby, S. W.; Vahidi, N.; Walczak, T.; Wu, M.; Swartz, H. M. Lithium Phthalocyanine: A Probe for Electron Paramagnetic Resonance Oximetry in Viable Biological Systems. *Proc. Natl. Acad. Sci. U. S. A.* **1993**, *90* (12), 5438–5442.

(340) Swartz, H. M. The Measurement of Oxygen in Vivo Using EPR Techniques. In *In Vivo EPR (ESR)*; Berliner, L. J., Ed.; Springer US: New York, 2003; pp 403–440.

(341) Gallez, B.; Baudelet, C.; Jordan, B. F. Assessment of Tumor Oxygenation by Electron Paramagnetic Resonance: Principles and Applications. *NMR Biomed.* **2004**, *17* (5), 240–262.

(342) Vahidi, N.; Clarkson, R. B.; Liu, K. J.; Norby, S. W.; Wu, M.; Swartz, H. M. In Vivo and in Vitro EPR Oximetry with Fusinite: A New Coal-Derived, Particulate EPR Probe. *Magn. Reson. Med.* **1994**, *31* (2), 139–146.

(343) Swartz, H. M.; Boyer, S.; Gast, P.; Glockner, J. F.; Hu, H.; Liu, K. J.; Moussavi, M.; Norby, S. W.; Vahidi, N.; Walczak, T. Measurements of Pertinent Concentrations of Oxygen in Vivo. *Magn. Reson. Med.* **1991**, *20* (2), 333–339.

(344) James, P. E.; Grinberg, O. Y.; Goda, F.; Panz, T.; O'Hara, J. A.; Swartz, H. M. Gloxy: An Oxygen-Sensitive Coal for Accurate Measurement of Low Oxygen Tensions in

Biological Systems. *Magn. Reson. Med.* **1997**, *38* (1), 48–58.

(345) Zweier, J. L.; Chzhan, M.; Ewert, U.; Schneider, G.; Kuppusamy, P. Development of a Highly Sensitive Probe for Measuring Oxygen in Biological Tissues. *J. Magn. Reson. B* **1994**, *105* (1), 52–57.

(346) Smirnov, A. I.; Norby, S. W.; Clarkson, R. B.; Walczak, T.; Swartz, H. M. Simultaneous Multi-Site EPR Spectroscopy in Vivo. *Magn. Reson. Med.* **1993**, *30* (2), 213–220.

(347) Swartz, H. M.; Liu, K. J.; Goda, F.; Walczak, T. India Ink: A Potential Clinically Applicable EPR Oximetry Probe. *Magn. Reson. Med.* **1994**, *31* (2), 229–232.

(348) Williams, B. B.; Khan, N.; Zaki, B.; Hartford, A.; Ernstoff, M. S.; Swartz, H. M. Clinical Electron Paramagnetic Resonance (EPR) Oximetry Using India Ink. *Adv. Exp. Med. Biol.* **2010**, *662*, 149–156.

(349) Swartz, H. M.; Williams, B. B.; Zaki, B. I.; Hartford, A. C.; Jarvis, L. A.; Chen, E. Y.; Comi, R. J.; Ernstoff, M. S.; Hou, H.; Khan, N.; et al. Clinical EPR. *Acad. Radiol.* **2014**, *21* (2), 197–206.

(350) Swartz, H. M.; Williams, B. B.; Hou, H.; Khan, N.; Jarvis, L. A.; Chen, E. Y.; Schaner, P. E.; Ali, A.; Gallez, B.; Kuppusamy, P.; et al. Direct and Repeated Clinical Measurements of PO2 for Enhancing Cancer Therapy and Other Applications; Springer, Cham, 2016; pp 95–104.

(351) Gallez, B.; Debuyst, R.; Dejehet, F.; Liu, K. J.; Walczak, T.; Goda, F.; Demeure, R.; Taper, H.; Swartz, H. M. Small Particles of Fusinite and Carbohydrate Chars Coated with Aqueous Soluble Polymers: Preparation and Applications Forin Vivo EPR Oximetry. *Magn. Reson. Med.* **1998**, *40* (1), 152–159.

(352) O'Hara, J. a; Khan, N.; Hou, H.; Wilmot, C. M.; Demidenko, E.; Dunn, J. F.; Swartz, H. M.; Wilmo, C. M.; Demidenko, E.; Dunn, J. F.; et al. Comparison of EPR Oximetry and Eppendorf Polarographic Electrode Assessments of Rat Brain PtO2. *Physiol. Meas.* **2004**, *25* (6), 1413–1423.

(353) Kocherginsky, N.; Swartz, H. M. Terminology, Classification and Distribution of the Nitroxides in Cells. In *Nitroxide spin labels fl reactions in biology and chemistry*; Kocherginsky, N., Swartz, H. M., Eds.; CRC Press: Boca Raton (FL), 1995; pp 15–26.

(354) Gallez, B.; Debuyst, R.; Demeure, R.; Dejehet, F.; Grandin, C.; Van Beers, B.; Taper,

H.; Pringot, J.; Dumont, P. Evaluation of a Nitroxyl Fatty Acid as Liver Contrast Agent for Magnetic Resonance Imaging. *Magn. Reson. Med.* **1993**, *30* (5), 592–599.

(355) Gallez, B.; Lacour, V.; Demeure, R.; Debuyst, R.; Dejehet, F.; De Keyser, J.-L.; Dumont, P. Spin Labelled Arabinogalactan as MRI Contrast Agent. *Magn. Reson. Imaging* **1994**, *12* (1), 61–69.

(356) Halpern, H. J.; Yu, C.; Peric, M.; Barth, E.; Grdina, D. J.; Teicher, B. A. Oxymetry Deep in Tissues with Low-Frequency Electron Paramagnetic Resonance. *Proc. Natl. Acad. Sci.* **1994**, *91* (26), 13047–13051.

(357) Chen, K.; Glockner, J. F.; Morse, P. D.; Swartz, H. M. Effects of Oxygen on the Metabolism of Nitroxide Spin Labels in Cells. *Biochemistry* **1989**, *28* (6), 2496–2501.

(358) Pals, M. A.; Swartz, H. M. Oxygen-Dependent Metabolism of Potential Magnetic Resonance Contrast Agents. *Invest. Radiol.* **1987**, *22* (6), 497–501.

(359) Swartz, H. M. Use of Nitroxides to Measure Redox Metabolism in Cells and Tissues. *J. Chem. Soc. Faraday Trans. 1 Phys. Chem. Condens. Phases* **1987**, *83* (1), 191.

(360) Swartz, H. M.; Chen, K.; Pals, M.; Sentjurc, M.; Morse, P. D. Hypoxia-Sensitive NMR Contrast Agents. *Magn. Reson. Med.* **1986**, *3* (1), 169–174.

(361) Gomberg, M. On the Preparation of Triphenylchlormethane. *J. Am. Chem. Soc.* **1900**, *22* (11), 752–757.

(362) Andersson, A.; Radner, F.; Rydbeek, A.; Servin, R.; Wistrand, L.-G. Free Radicals. US5530140A, March 31, 1994.

(363) Liu, Y.; Villamena, F. A.; Zweier, J. L. Highly Stable Dendritic Trityl Radicals as Oxygen and PH Probe. *Chem. Commun.* **2008**, *0* (36), 4336.

(364) Dhimitruka, I.; Velayutham, M.; Bobko, A. A.; Khramtsov, V. V.; Villamena, F. A.; Hadad, C. M.; Zweier, J. L. Large-Scale Synthesis of a Persistent Trityl Radical for Use in Biomedical EPR Applications and Imaging. *Bioorg. Med. Chem. Lett.* **2007**, *17* (24), 6801–6805.

(365) Ardenkjaer-Larsen, J. H.; Laursen, I.; Leunbach, I.; Ehnholm, G.; Wistrand, L.-G. G.; Petersson, J. S. S.; Golman, K.; Ardenkj?r-Larsen, J. H.; Laursen, I.; Leunbach, I.; et al. EPR and DNP Properties of Certain Novel Single Electron Contrast Agents Intended for Oximetric Imaging. *J. Magn. Reson.* **1998**, *133* (1), 1–12.

(366) Liu, Y.; Villamena, F. A.; Sun, J.; Wang, T.-S. T.; Zweier, J. L. Esterified Trityl Radicals as Intracellular Oxygen Probes. *Free Radic Biol Med* **2009**, *46* (7), 876–883.

(367) Dang, V.; Wang, J.; Feng, S.; Buron, C.; Villamena, F. A.; Wang, P. G.; Kuppusamy, P. Synthesis and Characterization of a Perchlorotriphenylmethyl (Trityl) Triester Radical: A Potential Sensor for Superoxide and Oxygen in Biological Systems. *Bioorganic Med. Chem. Lett.* **2007**, *17* (14), 4062–4065.

(368) Bobko, A. A.; Dhimitruka, I.; Komarov, D. A.; Khramtsov, V. V. Dual-Function PH and Oxygen Phosphonated Trityl Probe. *Anal. Chem.* **2012**, *84* (14), 6054–6060.

(369) Liu, Y.; Villamena, F. A.; Sun, J.; Xu, Y.; Dhimitruka, I.; Zweier, J. L. Synthesis and Characterization of Ester-Derivatized Tetrathiatriarylmethyl Radicals as Intracellular Oxygen Probes. *J. Org. Chem.* **2008**, *73*, 1490–1497.

(370) Panagiotelis, I.; Nicholson, I.; Hutchison, J. M. S. Electron Spin Relaxation Time Measurements Using Radiofrequency Longitudinally Detected ESR and Application in Oximetry. *J. Magn. Reson.* **2001**, *149* (1), 74–84.

(371) Yong, L.; Harbridge, J.; Quine, R. W.; Rinard, G. A.; Eaton, S. S.; Eaton, G. R.; Mailer, C.; Barth, E.; Halpern, H. J. Electron Spin Relaxation of Triarylmethyl Radicals in Fluid Solution. *J. Magn. Reson.* **2001**, *152* (1), 156–161.

(372) Gallez, B.; Mäder, K. Accurate and Sensitive Measurements of PO2 in Vivo Using Low Frequency EPR Spectroscopy: How to Confer Biocompatibility to the Oxygen Sensors. *Free Radic. Biol. Med.* **2000**, *29* (11), 1078–1084.

(373) Song, Y.; Liu, Y.; Liu, W.; Villamena, F. A.; Zweier, J. L. Characterization of the Binding of the Finland Trityl Radical with Bovine Serum Albumin. *RSC Adv.* **2014**, *4* (88), 47649–47656.

(374) Driesschaert, B.; Charlier, N.; Gallez, B.; Marchand-Brynaert, J. Synthesis of Two Persistent Fluorinated Tetrathiatriarylmethyl (TAM) Radicals for Biomedical EPR Applications. *Bioorg. Med. Chem. Lett.* **2008**, *18*, 4291–4293.

(375) Frank, J.; Elewa, M.; Said, M. M.; El Shihawy, H. A.; El-Sadek, M.; Müller, D.; Meister, A.; Hause, G.; Drescher, S.; Metz, H.; et al. Synthesis, Characterization, and Nanoencapsulation of Tetrathiatriarylmethyl and Tetrachlorotriarylmethyl (Trityl) Radical Derivatives - A Study To Advance Their Applicability as in Vivo EPR Oxygen Sensors. *J. Org. Chem.* **2015**, *80* (13), 6754–6766.

(376) Bratasz, A.; Pandian, R. P.; Deng, Y.; Petryakov, S.; Grecula, J. C.; Gupta, N.; Kuppusamy, P. In Vivo Imaging of Changes in Tumor Oxygenation during Growth and after Treatment. *Magn. Reson. Med.* **2007**, *57* (5), 950–959.

(377) Hou, H.; Lariviere, J. P.; Demidenko, E.; Gladstone, D.; Swartz, H.; Khan, N. Repeated Tumor PO(2) Measurements by Multi-Site EPR Oximetry as a Prognostic Marker for Enhanced Therapeutic Efficacy of Fractionated Radiotherapy. *Radiother. Oncol.* **2009**, *91* (1), 126–131.

(378) Hou, H.; Abramovic, Z.; Lariviere, J. P.; Sentjurc, M.; Swartz, H.; Khan, N. Effect of a Topical Vasodilator on Tumor Hypoxia and Tumor Oxygen Guided Radiotherapy Using EPR Oximetry. *Radiat. Res.* **2010**, *173* (5), 651–658.

(379) Hou, H.; Dong, R.; Lariviere, J. P.; Mupparaju, S. P.; Swartz, H. M.; Khan, N. Synergistic Combination of Hyperoxygenation and Radiotherapy by Repeated Assessments of Tumor PO2 with EPR Oximetry. *J. Radiat. Res.* **2011**, *52* (5), 568–574.

(380) Goda, F.; Bacic, G.; O'Hara, J. A.; Gallez, B.; Swartz, H. M.; Dunn, J. F. The Relationship between Partial Pressure of Oxygen and Perfusion in Two Murine Tumors after X-Ray Irradiation: A Combined Gadopentetate Dimeglumine Dynamic Magnetic Resonance Imaging and in Vivo Electron Paramagnetic Resonance Oximetry Study. *Cancer Res.* **1996**, *56* (14), 3344–3349.

(381) Goda, F.; O'Hara, J. A.; Rhodes, E. S.; Liu, K. J.; Dunn, J. F.; Bacic, G.; Swartz, H. M. Changes of Oxygen Tension in Experimental Tumors after a Single Dose of X-Ray Irradiation. *Cancer Res.* **1995**, *55* (11), 2249–2252.

(382) Hou, H.; Mupparaju, S. P.; Lariviere, J. P.; Hodge, S.; Gui, J.; Swartz, H. M.; Khan, N. Assessment of the Changes in 9L and C6 Glioma PO2 by EPR Oximetry as a Prognostic Indicator of Differential Response to Radiotherapy. *Radiat. Res.* **2013**, *179* (3), 343–351.

(383) Ansiaux, R.; Baudelet, C.; Jordan, B. F.; Beghein, N.; Sonveaux, P.; De Wever, J.; Martinive, P.; Grégoire, V.; Feron, O.; Gallez, B. Thalidomide Radiosensitizes Tumors through Early Changes in the Tumor Microenvironment. *Clin. Cancer Res.* **2005**, *11*, 743–750.

(384) Jordan, B. F.; Grégoire, V.; Demeure, R. J.; Sonveaux, P.; Feron, O.; O'Hara, J.;

Vanhulle, V. P.; Delzenne, N.; Gallez, B. Insulin Increases the Sensitivity of Tumors to Irradiation: Involvement of an Increase in Tumor Oxygenation Mediated by a Nitric Oxide-Dependent Decrease of the Tumor Cells Oxygen Consumption. *Cancer Res.* **2002**, *62* (12), 3555–3561.

(385) Sarna, T.; Duleba, A.; Korytowski, W.; Swartz, H. Interaction of Melanin with Oxygen. *Arch. Biochem. Biophys.* **1980**, *200* (1), 140–148.

(386) Hou, H.; Grinberg, O.; Williams, B.; Grinberg, S.; Yu, H.; Alvarenga, D. L.; Wallach, H.; Buckey, J.; Swartz, H. M. The Effect of Oxygen Therapy on Brain Damage and Cerebral PO_2 in Transient Focal Cerebral Ischemia in the Rat. *Physiol. Meas.* **2007**, *28* (8), 963–976.

(387) Liu, K. J.; Bacic, G.; Jack Hoopes, P.; Jiang, J.; Du, H.; Ou, L. C.; Dunn, J. F.; Swartz, H. M. Assessment of Cerebral PO2 by EPR Oximetry in Rodents: Effects of Anesthesia, Ischemia, and Breathing Gas. *Brain Res.* **1995**, *685* (1–2), 91–98.

(388) Lei, H.; Grinberg, O.; Nwaigwe, C. I.; Hou, H. G.; Williams, H.; Swartz, H. M.; Dunn, J. F. The Effects of Ketamine-Xylazine Anesthesia on Cerebral Blood Flow and Oxygenation Observed Using Nuclear Magnetic Resonance Perfusion Imaging and Electron Paramagnetic Resonance Oximetry. *Brain Res.* **2001**, *913* (2), 174–179.

(389) Dunn, J. F.; O'Hara, J. A.; Zaim-Wadghiri, Y.; Lei, H.; Meyerand, M. E.; Grinberg, O. Y.; Hou, H.; Hoopes, P. J.; Demidenko, E.; Swartz, H. M. Changes in Oxygenation of Intracranial Tumors with Carbogen: A BOLD MRI and EPR Oximetry Study. *J. Magn. Reson. Imaging* **2002**, *16* (5), 511–521.

(390) Hou, H.; Grinberg, O. Y.; Taie, S.; Leichtweis, S.; Miyake, M.; Grinberg, S.; Xie, H.; Csete, M.; Swartz, H. M. Electron Paramagnetic Resonance Assessment of Brain Tissue Oxygen Tension in Anesthetized Rats. *Anesth. Analg.* **2003**, *96* (5), 1467–72, table of contents.

(391) Zweier, J. L.; Kuppusamy, P. Electron Paramagnetic Resonance Measurements of Free Radicals in the Intact Beating Heart: A Technique for Detection and Characterization of Free Radicals in Whole Biological Tissues. *Proc. Natl. Acad. Sci. U. S. A.* **1988**, *85* (15), 5703–5707.

(392) Grinberg, O. Y.; Grinberg, S. A.; Friedman, B. J.; Swartz, H. M. Myocardial Oxygen Tension and Capillary Density in the Isolated Perfused Rat Heart during

Pharmacological Intervention. *Adv. Exp. Med. Biol.* **1997**, *411*, 171–181.

(393) Zweier, J. L.; Samouilov, A.; Kuppusamy, P. Cardiac Applications of in Vivo EPR Spectroscopy and Imaging; Springer, Boston, MA, 2003; pp 441–468.

(394) Zweier, J. L.; Thompson-Gorman, S.; Kuppusamy, P. Measurement of Oxygen Concentrations in the Intact Beating Heart Using Electron Paramagnetic Resonance Spectroscopy: A Technique for Measuring Oxygen Concentrationsin Situ. *J. Bioenerg. Biomembr.* **1991**, *23* (6), 855–871.

(395) Friedman, B. J.; Grinberg, O. Y.; Isaacs, K. A.; Ruuge, E. K.; Swartz, H. M. Effect of Repetitive Ischemia on Myocardial Oxygen Tension in Isolated Perfused and Hypoperfused Rat Hearts. *Magn. Reson. Med.* **1996**, *35* (2), 214–220.

(396) Friedman, B.; Grinberg, O. Y.; Isaacs, K. A.; Walczak, T. M.; Swartz, H. M. Myocardial Oxygen Tension and Relative Capillary Density in Isolated Perfused Rat Hearts. *J. Mol. Cell. Cardiol.* **1995**, *27* (12), 2551–2558.

(397) Kuppusamy, P.; Chzhan, M.; Vij, K.; Shteynbuk, M.; Lefer, D. J.; Giannella, E.; Zweier, J. L. Three-Dimensional Spectral-Spatial EPR Imaging of Free Radicals in the Heart: A Technique for Imaging Tissue Metabolism and Oxygenation. *Proc. Natl. Acad. Sci. U. S. A.* **1994**, *91* (8), 3388–3392.

(398) Goda, F.; Liu, K. J.; Walczak, T.; O'Hara, J. A.; Jiang, J.; Swartz, H. M. In Vivo Oximetry Using EPR and India Ink. *Magn. Reson. Med.* **1995**, *33* (2), 237–245.

(399) Jiang, J.; Nakashima, T.; Liu, K. J.; Goda, F.; Shima, T.; Swartz, H. M. Measurement of PO2 in Liver Using EPR Oximetry. *J. Appl. Physiol.* **1996**, *80* (2), 552–558.

(400) James, P. E.; Miyake, M.; Swartz, H. M. Simultaneous Measurement of NO• and PO2 from Tissue by in Vivo EPR. *Nitric Oxide* **1999**, *3* (4), 292–301.

(401) James, P. E.; Madhani, M.; Roebuck, W.; Jackson, S. K.; Swartz, H. M. Endotoxin-Induced Liver Hypoxia: Defective Oxygen Delivery versus Oxygen Consumption. *Nitric Oxide* **2002**, *6* (1), 18–28.

(402) Madhani, M.; Barchowsky, A.; Klei, L.; Ross, C. R.; Jackson, S. K.; Swartz, H. M.; James, P. E. Antibacterial Peptide PR-39 Affects Local Nitric Oxide and Preserves Tissue Oxygenation in the Liver during Septic Shock. *Biochim. Biophys. Acta* **2002**, *1588* (3), 232–240.

(403) Nakashima, T.; Goda, F.; Jiang, J.; Shima, T.; Swartz, H. M. Use of EPR Oximetry with India Ink to Measure the PO2 in the Liver in Vivo in Mice. *Magn. Reson. Med.* **1995**, *34* (6), 888–892.

(404) James, P. E.; Bacic, G.; Grinberg, O. Y.; Goda, F.; Dunn, J. F.; Jackson, S. K.; Swartz, H. M. Endotoxin-Induced Changes in Intrarenal PO2, Measured by in Vivo Electron Paramagnetic Resonance Oximetry and Magnetic Resonance Imaging. *Free Radic. Biol. Med.* **1996**, *21* (1), 25–34.

(405) He, G.; Shankar, R. A.; Chzhan, M.; Samouilov, A.; Kuppusamy, P.; Zweier, J. L. Noninvasive Measurement of Anatomic Structure and Intraluminal Oxygenation in the Gastrointestinal Tract of Living Mice with Spatial and Spectral EPR Imaging. *Proc. Natl. Acad. Sci. U. S. A.* **1999**, *96* (8), 4586–4591.

(406) Glockner, J. F.; Chan, H.-C.; Swartz, H. M. In Vivo Oximetry Using a Nitroxide-Liposome System. *Magn. Reson. Med.* **1991**, *20* (1), 123–133.

(407) Norby, S. W.; Swartz, H. M.; Clarkson, R. B. Electron and Light Microscopy Studies on Particulate EPR Spin Probes Lithium Phthalocyanine, Fusinite and Synthetic Chars. *J. Microsc.* **1998**, *192* (Pt 2), 172–185.

(408) Lan, M.; Beghein, N.; Charlier, N.; Gallez, B. Carbon Blacks as EPR Sensors for Localized Measurements of Tissue Oxygenation. *Magn. Reson. Med.* **2004**, *51* (6), 1272–1278.

(409) Jordan, B. F.; Baudelet, C.; Gallez, B. Carbon-Centered Radicals as Oxygen Sensors for in Vivo Electron Paramagnetic Resonance: Screening for an Optimal Probe among Commercially Available Charcoals. **1998**, *7* (2), 121–129.

(410) Ilangovan, G.; Manivannan, A.; Li, H.; Yanagi, H.; Zweier, J. L.; Kuppusamy, P. A Naphthalocyanine-Based EPR Probe for Localized Measurements of Tissue Oxygenation. *Free Radic. Biol. Med.* **2002**, *32* (2), 139–147.

(411) Kržič, M.; Šentjurc, M.; Kristl, J. Improved Skin Oxygenation after Benzyl Nicotinate Application in Different Carriers as Measured by EPR Oximetry in Vivo. *J. Control. Release* **2001**, *70* (1–2), 203–211.

(412) He, G.; Kutala, V. K.; Kuppusamy, P.; Zweier, J. L. In Vivo Measurement and Mapping of Skin Redox Stress Induced by Ultraviolet Light Exposure. *Free Radic. Biol. Med.* **2004**, *36* (5), 665–672.

(413) Lu, C.; Rollins, M.; Hou, H.; Swartz, H. M.; Hopf, H.; Miclau, T.; Marcucio, R. S. Tibial Fracture Decreases Oxygen Levels at the Site of Injury. *Iowa Orthop. J.* **2008**, *28*, 14–21.

(414) Schugart, R. C.; Friedman, A.; Zhao, R.; Sen, C. K. Wound Angiogenesis as a Function of Tissue Oxygen Tension: A Mathematical Model. *Proc. Natl. Acad. Sci.* **2008**, *105* (7), 2628–2633.

(415) Pandian, R. P.; Parinandi, N. L.; Ilangovan, G.; Zweier, J. L.; Kuppusamy, P. Novel Particulate Spin Probe for Targeted Determination of Oxygen in Cells and Tissues. *Free Radic. Biol. Med.* **2003**, *35* (9), 1138–1148.

(416) Bacić, G.; Liu, K. J.; O'Hara, J. A.; Harris, R. D.; Szybinski, K.; Goda, F.; Swartz, H. M. Oxygen Tension in a Murine Tumor: A Combined EPR and MRI Study. *Magn. Reson. Med.* **1993**, *30* (5), 568–572.

(417) Elas, M.; Williams, B. B.; Parasca, A.; Mailer, C.; Pelizzari, C. A.; Lewis, M. A.; River, J. N.; Karczmar, G. S.; Barth, E. D.; Halpern, H. J. Quantitative Tumor Oxymetric Images from 4D Electron Paramagnetic Resonance Imaging (EPRI): Methodology and Comparison with Blood Oxygen Level-Dependent (BOLD) MRI. *Magn. Reson. Med.* **2003**, *49* (4), 682–691.

(418) Goda, F.; O'Hara, J. A.; Liu, K. J.; Rhodes, E. S.; Dunn, J. F.; Swartz, H. M. Comparisons of Measurements of PO2 in Tissue In Vivo by EPR Oximetry and Micro-Electrodes; Springer, Boston, MA, 1997; pp 543–549.

(419) Josse, O.; Labar, D.; Georges, B.; Grégoire, V.; Marchand-Brynaert, J. Synthesis of [18F]-Labeled EF3 [2-(2-Nitroimidazol-1-Yl)-N-(3,3,3-Trifluoropropyl)-Acetamide], a Marker for PET Detection of Hypoxia. *Bioorg. Med. Chem.* **2001**, *9* (3), 665–675.

(420) Jordan, B. F.; Misson, P.-D.; Demeure, R.; Baudelet, C.; Beghein, N.; Gallez, B. Changes in Tumor Oxygenation/Perfusion Induced by the No Donor, Isosorbide Dinitrate, in Comparison with Carbogen: Monitoring by EPR and MRI. *Int. J. Radiat. Oncol.* **2000**, *48* (2), 565–570.

(421) Matsumoto, K.; Chandrika, B.; Lohman, J. A. B.; Mitchell, J. B.; Krishna, M. C.; Subramanian, S. Application of Continuous-Wave EPR Spectral-Spatial Image Reconstruction Techniques for in Vivo Oxymetry: Comparison of Projection Reconstruction and Constant-Time Modalities. *Magn. Reson. Med.* **2003**, *50* (4), 865–

874.

(422) Jordan, B. F.; Beghein, N.; Aubry, M.; Grégoire, V.; Gallez, B. Potentiation of Radiation-Induced Regrowth Delay by Isosorbide Dinitrate in FSaII Murine Tumors. *Int. J. Cancer* **2003**, *103* (1), 138–141.

(423) Jordan, B. F.; Sonveaux, P.; Feron, O.; Grégoire, V.; Beghein, N.; Gallez, B. Nitric Oxide–mediated Increase in Tumor Blood Flow and Oxygenation of Tumors Implanted in Muscles Stimulated by Electric Pulses. *Int. J. Radiat. Oncol.* **2003**, *55* (4), 1066–1073.

(424) Evans, S. M.; Du, K. L.; Chalian, A. A.; Mick, R.; Zhang, P. J.; Hahn, S. M.; Quon, H.; Lustig, R.; Weinstein, G. S.; Koch, C. J. Patterns and Levels of Hypoxia in Head and Neck Squamous Cell Carcinomas and Their Relationship to Patient Outcome. *Int. J. Radiat. Oncol.* **2007**, *69* (4), 1024–1031.

(425) Kaanders, J. H.; Bussink, J.; van der Kogel, A. J. ARCON: A Novel Biology-Based Approach in Radiotherapy. *Lancet Oncol.* **2002**, *3* (12), 728–737.

(426) Jordan, B. F.; Misson, P.-D.; Demeure, R.; Baudelet, C.; Beghein, N.; Gallez, B. Changes in Tumor Oxygenation/Perfusion Induced by the No Donor, Isosorbide Dinitrate, in Comparison with Carbogen: Monitoring by EPR and MRI. *Int. J. Radiat. Oncol.* **2000**, *48* (2), 565–570.

(427) Gallez, B.; Jordan, B. F.; Baudelet, C.; Misson, P.-D. P.-D. Pharmacological Modifications of the Partial Pressure of Oxygen in Murine Tumors: Evaluation Using in Vivo EPR Oximetry. *Magn. Reson. Med.* **1999**, *42* (4), 627–630.

(428) Siemann, D. W.; Hill, R. P.; Bush, R. S. The Importance of the Pre-Irradiation Breathing Times of Oxygen and Carbogen (5% CO2: 95% O2) on the in Vivo Radiation Response of a Murine Sarcoma. *Int. J. Radiat. Oncol. ÅBiol. ÅPhys.* **1977**, *2* (9), 903–911.

(429) Thews, O.; Kelleher, D. K.; Vaupel, P. Dynamics of Tumor Oxygenation and Red Blood Cell Flux in Response to Inspiratory Hyperoxia Combined with Different Levels of Inspiratory Hypercapnia. *Radiother. Oncol.* **2002**, *62* (1), 77–85.

(430) Ljungkvist, A. S. .; Bussink, J.; Rijken, P. F. J. .; Raleigh, J. A.; Denekamp, J.; Van Der Kogel, A. J. Changes in Tumor Hypoxia Measured with a Double Hypoxic Marker Technique. *Int. J. Radiat. Oncol.* **2000**, *48* (5), 1529–1538.

(431) Hill, S. A.; Collingridge, D. R.; Vojnovic, B.; Chaplin, D. J. Tumour Radiosensitization by High-Oxygen–Content Gases: Influence of the Carbon Dioxide Content of the Inspired Gas on PO2, Microcirculatory Function and Radiosensitivity. *Int. J. Radiat. Oncol.* **1998**, *40* (4), 943–951.

(432) Rijpkema, M.; Kaanders, J. H. A. M.; Joosten, F. B. M.; van der Kogel, A. J.; Heerschap, A. Effects of Breathing a Hyperoxic Hypercapnic Gas Mixture on Blood Oxygenation and Vascularity of Head-and-Neck Tumors as Measured by Magnetic Resonance Imaging. *Int. J. Radiat. Oncol. Biol. Phys.* **2002**, *53* (5), 1185–1191.

(433) Powell, M. E.; Collingridge, D. R.; Saunders, M. I.; Hoskin, P. J.; Hill, S. A.; Chaplin, D. J. Improvement in Human Tumour Oxygenation with Carbogen of Varying Carbon Dioxide Concentrations. *Radiother. Oncol.* **1999**, *50* (2), 167–171.

(434) Aquino-Parsons, C.; Green, A.; Minchinton, A. I. Oxygen Tension in Primary Gynaecological Tumours: The Influence of Carbon Dioxide Concentration. *Radiother. Oncol.* **2000**, *57* (1), 45–51.

(435) Brizel, D.; Lin, S.; Johnson, J.; Brooks, J.; Dewhirst, M.; Piantadosi, C. The Mechanisms by Which Hyperbaric Oxygen and Carbogen Improve Tumour Oxygenation. *Br. J. Cancer* **1995**, *72* (5), 1120–1124.

(436) Robinson, S.; Rodrigues, L.; Ojugo, A.; McSheehy, P.; Howe, F.; Griffiths, J. The Response to Carbogen Breathing in Experimental Tumour Models Monitored by Gradient-Recalled Echo Magnetic Resonance Imaging. *Br. J. Cancer* **1997**, *75* (7), 1000–1006.

(437) Glockner, J. F.; Norby, S.-W.; Swartz, H. M. Simultaneous Measurement of Intracellular and Extracellular Oxygen Concentrations Using a Nitroxide-Liposome System. *Magn. Reson. Med.* **1993**, *29* (1), 12–18.

(438) Woldman YYu; Khramtsov, V. V; Grigor'ev, I. A.; Kiriljuk, I. A.; Utepbergenov, D. I. Spin Trapping of Nitric Oxide by Nitronylnitroxides: Measurement of the Activity of No Synthase from Rat Cerebellum. *Biochem. Biophys. Res. Commun.* **1994**, *202* (1), 195–203.

(439) Woldman, Y. Y.; Semenov, S. V.; Bobko, A. A.; Kirilyuk, I. A.; Polienko, J. F.; Voinov, M. A.; Bagryanskaya, E. G.; Khramtsov, V. V. Design of Liposome-Based PH Sensitive NanoSPIN Probes: Nano-Sized Particles with Incorporated Nitroxides.

Analyst **2009**, *134* (5), 904–910.

(440) Bobko, A. A.; Ivanov, A.; Khramtsov, V. V. Discriminative EPR Detection of NO and HNO by Encapsulated Nitronyl Nitroxides. *Free Radic. Res.* **2013**, *47* (2), 74–81.

(441) Burks, S. R.; Legenzov, E. A.; Rosen, G. M.; Kao, J. P. Y. Clearance and Biodistribution of Liposomally Encapsulated Nitroxides: A Model for Targeted Delivery of Electron Paramagnetic Resonance Imaging Probes to Tumors. *Drug Metab. Dispos.* **2011**, *39* (10), 1961–1966.

(442) Liu, K. J.; Grinstaff, M. W.; Jiang, J.; Suslick, K. S.; Swartz, H. M.; Wang, W. In Vivo Measurement of Oxygen Concentration Using Sonochemically Synthesized Microspheres. *Biophys. J.* **1994**, *67* (2), 896–901.

(443) Rosen, G. M.; Porasuphatana, S.; Tsai, P.; Ambulos, N. P.; Galtsev, V. E.; Ichikawa, K.; Halpern, H. J. Dendrimeric-Containing Nitronyl Nitroxides as Spin Traps for Nitric Oxide: Synthesis, Kinetic, and Stability Studies. *Macromolecules* **2003**, *36* (4), 1012–1027.

(444) Baker, J. E.; Froncisz, W.; Joseph, J.; Kalyanaraman, B. Spin Label Oximetry to Assess Extracellular Oxygen During Myocardial Ischemia. *Free Radic. Biol. Med.* **1997**, *22* (1–2), 109–115.

(445) Frank, J.; Elewa, M.; M. Said, M.; El Shihawy, H. A.; El-Sadek, M.; Müller, D.; Meister, A.; Hause, G.; Drescher, S.; Metz, H.; et al. Synthesis, Characterization, and Nanoencapsulation of Tetrathiatriarylmethyl and Tetrachlorotriarylmethyl (Trityl) Radical Derivatives—A Study To Advance Their Applicability as in Vivo EPR Oxygen Sensors. *J. Org. Chem.* **2015**, *80* (13), 6754–6766.

(446) Liu, J.; Bu, W.; Shi, J. Chemical Design and Synthesis of Functionalized Probes for Imaging and Treating Tumor Hypoxia. *Chem. Rev.* **2017**, *117* (9), 6160–6224.

(447) Charlier, N.; Driesschaert, B.; Wauthoz, N.; Beghein, N.; Préat, V.; Amighi, K.; Marchand-Brynaert, J.; Gallez, B. Nano-Emulsions of Fluorinated Trityl Radicals as Sensors for EPR Oximetry. *J. Magn. Reson.* **2009**, *197* (2), 176–180.

(448) Song, Y.; Liu, Y.; Hemann, C.; Villamena, F. A.; Zweier, J. L. Esterified Dendritic TAM Radicals with Very High Stability and Enhanced Oxygen Sensitivity. *J. Org. Chem.* **2013**, *78* (4), 1371–1376.

(449) Abbas, K.; Boutier-Pischon, A.; Auger, F.; Françon, D.; Almario, A.; Frapart, Y.-M. In

Vivo Triarylmethyl Radical Stabilization through Encapsulation in Pluronic F-127 Hydrogel. *J. Magn. Reson.* **2016**, *270*, 147–156.

(450) Mignion, L.; Magat, J.; Schakman, O.; Marbaix, E.; Gallez, B.; Jordan, B. F. Hexafluorobenzene in Comparison with Perfluoro-15-Crown-5-Ether for Repeated Monitoring of Oxygenation Using 19F MRI in a Mouse Model. *Magn Reson Med.* **2013**, *69* (1), 248–254.

(451) Robinson, S. P.; Howe, F. A.; Rodrigues, L. M.; Stubbs, M.; Griffiths, J. R. Magnetic Resonance Imaging Techniques for Monitoring Changes in Tumor Oxygenation and Blood Flow. *Semin. Radiat. Oncol.* **1998**, *8* (3), 197–207.

(452) Ndubuizu, O.; LaManna, J. C. Brain Tissue Oxygen Concentration Measurements. *Antioxid. Redox Signal.* **2007**, *9* (8), 1207–1219.

(453) Hoskin, P. J.; Carnell, D. M.; Taylor, N. J.; Smith, R. E.; Stirling, J. J.; Daley, F. M.; Saunders, M. I.; Bentzen, S. M.; Collins, D. J.; d'Arcy, J. A.; et al. Hypoxia in Prostate Cancer: Correlation of BOLD-MRI with Pimonidazole Immunohistochemistry-Initial Observations. *Int. J. Radiat. Oncol. Biol. Phys.* **2007**, *68* (4), 1065–1071.

(454) Howe, F. A.; Robinson, S. P.; McIntyre, D. J. O.; Stubbs, M.; Griffiths, J. R. Issues in Flow and Oxygenation Dependent Contrast (FLOOD) Imaging of Tumours. *NMR Biomed.* **2001**, *14* (7–8), 497–506.

(455) Padhani, A. Science to Practice: What Does MR Oxygenation Imaging Tell Us about Human Breast Cancer Hypoxia? *Radiology* **2010**, *254* (1), 1–3.

(456) Shao, Q.; Ashkenazi, S. Photoacoustic Lifetime Imaging for Direct in Vivo Tissue Oxygen Monitoring. *J. Biomed. Opt.* **2015**, *20* (3), 036004.

(457) Baudelet, C.; Gallez, B. How Does Blood Oxygen Level-Dependent (BOLD) Contrast Correlate with Oxygen Partial Pressure (PO2) inside Tumors? *Magn. Reson. Med.* **2002**, *48* (6), 980–986.

(458) Mason, R. P. Non-Invasive Assessment of Kidney Oxygenation: A Role for BOLD MRI. *Kidney Int.* **2006**, *70* (1), 10–11.

(459) McPhail, L. D.; Robinson, S. P. Intrinsic Susceptibility MR Imaging of Chemically Induced Rat Mammary Tumors: Relationship to Histologic Assessment of Hypoxia and Fibrosis. *Radiology* **2010**, *254* (1), 110–118.

(460) Türkbey, B.; Thomasson, D.; Pang, Y.; Bernardo, M.; Choyke, P. L. The Role of Dynamic Contrast-Enhanced MRI in Cancer Diagnosis and Treatment. *Diagn. Interv. Radiol.* **2010**, *16* (3), 186–192.

(461) Choyke, P. L.; Dwyer, A. J.; Knopp, M. V. Functional Tumor Imaging with Dynamic Contrast-Enhanced Magnetic Resonance Imaging. *J. Magn. Reson. Imaging* **2003**, *17* (5), 509–520.

(462) Mayr, N. A.; Yuh, W. T. C.; Jajoura, D.; Wang, J. Z.; Lo, S. S.; Montebello, J. F.; Porter, K.; Zhang, D.; McMeekin, D. S.; Buatti, J. M. Ultra-Early Predictive Assay for Treatment Failure Using Functional Magnetic Resonance Imaging and Clinical Prognostic Parameters in Cervical Cancer. *Cancer* **2010**, *116* (4), 903–912.

(463) Newbold, K.; Castellano, I.; Charles-Edwards, E.; Mears, D.; Sohaib, A.; Leach, M.; Rhys-Evans, P.; Clarke, P.; Fisher, C.; Harrington, K.; et al. An Exploratory Study into the Role of Dynamic Contrast-Enhanced Magnetic Resonance Imaging or Perfusion Computed Tomography for Detection of Intratumoral Hypoxia in Head-and-Neck Cancer. *Int. J. Radiat. Oncol. ÅBiol. ÅPhys* **2009**, *74* (1), 29–37.

(464) Cooper, R. A.; Carrington, B. M.; Loncaster, J. A.; Todd, S. M.; Davidson, S. E.; Logue, J. P.; Luthra, A. D.; Jones, A. P.; Stratford, I.; Hunter, R. D.; et al. Tumour Oxygenation Levels Correlate with Dynamic Contrast-Enhanced Magnetic Resonance Imaging Parameters in Carcinoma of the Cervix. *Radiother. Oncol.* **2000**, *57* (1), 53–59.

(465) Donaldson, S. B.; Betts, G.; Bonington, S. C.; Homer, J. J.; Slevin, N. J.; Kershaw, L. E.; Valentine, H.; West, C. M. L.; Buckley, D. L. Perfusion Estimated with Rapid Dynamic Contrast-Enhanced Magnetic Resonance Imaging Correlates Inversely with Vascular Endothelial Growth Factor Expression and Pimonidazole Staining in Head-and-Neck Cancer: A Pilot Study. *Int. J. Radiat. Oncol. ÅBiol. ÅPhys* **2011**, *81* (4), 1176–1183.

(466) Swanson, K. R.; Chakraborty, G.; Wang, C. H.; Rockne, R.; Harpold, H. L. P.; Muzi, M.; Adamsen, T. C. H.; Krohn, K. A.; Spence, A. M. Complementary but Distinct Roles for MRI and 18F-Fluoromisonidazole PET in the Assessment of Human Glioblastomas. *J. Nucl. Med.* **2009**, *50* (1), 36–44.

(467) Jansen, J. F. A.; Schöder, H.; Lee, N. Y.; Wang, Y.; Pfister, D. G.; Fury, M. G.; Stambuk, H. E.; Humm, J. L.; Koutcher, J. A.; Shukla-Dave, A. Noninvasive

Assessment of Tumor Microenvironment Using Dynamic Contrast-Enhanced Magnetic Resonance Imaging and 18F-Fluoromisonidazole Positron Emission Tomography Imaging in Neck Nodal Metastases. *Int. J. Radiat. Oncol. ÅBiol. ÅPhys* **2010**, *77* (5), 1403–1410.

(468) Loncaster, J. A.; Carrington, B. M.; Sykes, J. R.; Jones, A. P.; Todd, S. M.; Cooper, R.; Buckley, D. L.; Davidson, S. E.; Logue, J. P.; Hunter, R. D.; et al. Prediction of Radiotherapy Outcome Using Dynamic Contrast Enhanced MRI of Carcinoma of the Cervix. *Int. J. Radiat. Oncol. ÅBiol. ÅPhys* **2002**, *54* (3), 759–767.

(469) Mayr, N. A.; Wang, J. Z.; Zhang, D.; Grecula, J. C.; Lo, S. S.; Jaroura, D.; Montebello, J.; Zhang, H.; Li, K.; Lu, L.; et al. Longitudinal Changes in Tumor Perfusion Pattern during the Radiation Therapy Course and Its Clinical Impact in Cervical Cancer. *Int. J. Radiat. Oncol. ÅBiol. ÅPhys* **2010**, *77* (2), 502–508.

(470) Andersen, E. K. F.; Hole, K. H.; Lund, K. V; Sundfør, K.; Kristensen, G. B.; Lyng, H.; Malinen, E. Dynamic Contrast-Enhanced MRI of Cervical Cancers: Temporal Percentile Screening of Contrast Enhancement Identifies Parameters for Prediction of Chemoradioresistance. *Int. J. Radiat. Oncol. ÅBiol. ÅPhys* **2012**, *82* (3), e485-92.

(471) Parhami, P.; Fung, B. M. Fluorine-19 Relaxation Study of Perfluoro Chemicals as Oxygen Carriers. *J. Phys. Chem.* **1983**, *87*, 1928–1931.

(472) Lewa, C. J.; Majewska, Z. Temperature Relationships of Proton Spin-Lattice Relaxation Time T1 in Biological Tissues. *Bull. Cancer* **1980**, *67* (5), 525–530.

(473) Zhao, D.; Jiang, L.; P. Mason, R. Measuring Changes in Tumor Oxygenation. *Methods Enzymol.* **2004**, *386*, 378–418.

(474) Kodibagkar, V. D.; Cui, W.; Merritt, M. E.; Mason, R. P. Novel1H NMR Approach to Quantitative Tissue Oximetry Using Hexamethyldisiloxane. *Magn. Reson. Med.* **2006**, *55* (4), 743–748.

(475) Neubauer, A. M.; Myerson, J.; Caruthers, S. D.; Hockett, F. D.; Winter, P. M.; Chen, J.; Gaffney, P. J.; Robertson, J. D.; Lanza, G. M.; Wickline, S. A. Gadolinium-Modulated ^{19} F Signals from Perfluorocarbon Nanoparticles as a New Strategy for Molecular Imaging. *Magn. Reson. Med.* **2008**, *60* (5), 1066–1072.

(476) Thomas, S. R.; Pratt, R. G.; Millard, R. W.; Samaratunga, R. C.; Shiferaw, Y.; Clark, L. C.; Hoffmann, R. E. Evaluation of the Influence of the Aqueous Phase

Bioconstituent Environment on the F-19 T1 of Perfluorocarbon Blood Substitute Emulsions. *J. Magn. Reson. Imaging* **1994**, *4* (4), 631–635.

(477) McIntyre, D. J. O.; McCoy, C. L.; Griffiths, J. R. Tumour Oxygenation Measurements by 19F Magnetic Resonance Imaging of Perfluorocarbons B. *Curr. Sci.* **1999**, *76* (6), 753–762.

(478) Mason, R. P.; Shukla, H.; Antich, P. P. In Vivo Oxygen Tension and Temperature: Simultaneous Determination Using 19F NMR Spectroscopy of Perfluorocarbon. *Magn. Reson. Med.* **1993**, *29* (3), 296–302.

(479) Mason, R. P.; Hunjan, S.; Constantinescu, A.; Song, Y.; Zhao, D.; Hahn, E. W.; Antich, P. P.; Peschke, P. Tumor Oximetry: Comparison of 19F MR EPI and Electrodes. *Adv. Exp. Med. Biol.* **2003**, *530*, 19–27.

(480) Robinson, S. P.; Griffiths, J. R. Current Issues in the Utility of 19F Nuclear Magnetic Resonance Methodologies for the Assessment of Tumour Hypoxia. *Philos. Trans. R. Soc. Lond. B. Biol. Sci.* **2004**, *359* (1446), 987–996.

(481) Jordan, B. F.; Cron, G. O.; Gallez, B. Rapid Monitoring of Oxygenation by 19F Magnetic Resonance Imaging: Simultaneous Comparison with Fluorescence Quenching. *Magn. Reson. Med.* **2009**, *61* (3), 634–638.

(482) Zhao, D.; Ran, S.; Constantinescu, A.; Hahn, E. W.; Mason, R. P. Tumor Oxygen Dynamics: Correlation of In Vivo MRI with Histological Findings. *Neoplasia* **2003**, *5* (4), 308–318.

(483) van der Sanden, B. P.; Heerschap, A.; Simonetti, A. W.; Rijken, P. F.; Peters, H. P.; Stüben, G.; van der Kogel, A. J. Characterization and Validation of Noninvasive Oxygen Tension Measurements in Human Glioma Xenografts by 19F-MR Relaxometry. *Int J Radiat Oncol Biol Phys* **1999**, *44* (3), 649–658.

(484) McNab, J. A.; Yung, A. C.; Kozlowski, P. Tissue Oxygen Tension Measurements in the Shionogi Model of Prostate Cancer Using 19F MRS and MRI. *Magn. Reson. Mater. Physics, Biol. Med.* **2004**, *17* (3–6), 288–295.

(485) Lemaire, L.; Bastiat, G.; Franconi, F.; Lautram, N.; Duong Thi Dan, T.; Garcion, E.; Saulnier, P.; Benoit, J. P. Perfluorocarbon-Loaded Lipid Nanocapsules as Oxygen Sensors for Tumor Tissue PO2 Assessment. *Eur. J. Pharm. Biopharm.* **2013**, *84* (3), 479–486.

(486) Hunjan, S.; Zhao, D.; Constantinescu, A.; Hahn, E. W.; Antich, P. P.; Mason, R. P. Tumor Oximetry: Demonstration of an Enhanced Dynamic Mapping Procedure Using Fluorine-19 Echo Planar Magnetic Resonance Imaging in the Dunning Prostate R3327-AT1 Rat Tumor. *Int. J. Radiat. Oncol.* **2001**, *49* (4), 1097–1108.

(487) Mason, R. P.; Rodbumrung, W.; Antich, P. P. Hexafluorobenzene: A Sensitive 19F NMR Indicator of Tumor Oxygenation. *NMR Biomed.* **1996**, *9* (3), 125–134.

(488) Mason, R. P.; Antich, P. P.; Babcock, E. E.; Gerberich, J. L.; Nunnally, R. L. Perfluorocarbon Imaging in Vivo: A 19F MRI Study in Tumor-Bearing Mice. *Magn. Reson. Imaging* **1989**, *7* (5), 475–485.

(489) Mason, R. P.; Antich, P. P.; Babcock, E. E.; Constantinescu, A.; Peschke, P.; Hahn, E. W. Non-Invasive Determination of Tumor Oxygen Tension and Local Variation with Growth. *Int J Radiat Oncol Biol Phys.* **1994**, *29* (1), 95–103.

(490) Jäger, L. J.; Nöth, U.; Haase, A.; Lutz, J. Half-Life of Perfluorooctylbromide in Inner Organs Determined by Fast 19F-NMR Imaging. *Adv. Exp. Med. Biol.* **1994**, *361*, 129–134.

(491) Krohn, K. A.; Link, J. M.; Mason, R. P. Molecular Imaging of Hypoxia. *J. Nucl. Med.* **2008**, *49 Suppl 2* (Suppl_2), 129S–48S.

(492) Nöth, U.; Rodrigues, L. M.; Robinson, S. P.; Jork, A.; Zimmermann, U.; Newell, B.; Griffiths, J. R. In Vivo Determination of Tumor Oxygenation during Growth and in Response to Carbogen Breathing Using 15C5-Loaded Alginate Capsules as Fluorine-19 Magnetic Resonance Imaging Oxygen Sensors. *Int. J. Radiat. Oncol. ÅBiol. ÅPhys* **2004**, *60* (3), 909–919.

(493) Kwock, L.; Gill, M.; McMurry, H. L.; Beckman, W.; Raleigh, J. A.; Joseph, A. P. Evaluation of a Fluorinated 2-Nitroimidazole Binding to Hypoxic Cells in Tumor-Bearing Rats by 19F Magnetic Resonance Spectroscopy and Immunohistochemistry. *Radiat. Res.* **1992**, *129* (1), 71–78.

(494) Salmon, H. W.; Siemann, D. W. Utility of 19F MRS Detection of the Hypoxic Cell Marker EF5 to Assess Cellular Hypoxia in Solid Tumors. *Radiother Oncol* **2004**, *73* (3), 359–366.

(495) Lee, C. P.; Payne, G. S.; Oregioni, A.; Ruddle, R.; Tan, S.; Raynaud, F. I.; Eaton, D.; Campbell, M. J.; Cross, K.; Halbert, G.; et al. A Phase I Study of the Nitroimidazole

Hypoxia Marker SR4554 Using 19F Magnetic Resonance Spectroscopy. *Br. J. Cancer* **2009**, *101* (11), 1860–1868.

(496) Davda, S.; Bezabeh, T. Advances in Methods for Assessing Tumor Hypoxia in Vivo: Implications for Treatment Planning. *Cancer Metastasis Rev.* **2006**, *25* (3), 469–480.

(497) Kodibagkar, V. D.; Wang, X.; Mason, R. P. Physical Principles of Quantitative Nuclear Magnetic Resonance Oximetry. *Front. Biosci.* **2008**, *13*, 1371–1384.

(498) Kodibagkar, V. D.; Wang, X.; Pacheco-Torres, J.; Gulaka, P.; Mason, R. P. Proton Imaging of Siloxanes to Map Tissue Oxygenation Levels (PISTOL): A Tool for Quantitative Tissue Oximetry. *NMR Biomed.* **2008**, *21* (8), 899–907.

(499) Yu, J.; Kodibagkar, V. D.; Cui, W.; Mason, R. P. 19F: A Versatile Reporter for Non-Invasive Physiology and Pharmacology Using Magnetic Resonance. *Curr. Med. Chem.* **2005**, *12* (7), 819–848.

(500) O'Connor, J. P. B.; Boult, J. K.; Jamin, Y.; Babur, M.; Finegan, K. G.; Williams, K. J.; Little, R. A.; Jackson, A.; Parker, G. J. M.; Reynolds, A. R.; et al. Oxygen Enhanced MRI Accurately Identifies, Quantifies, and Maps Hypoxia in Preclinical Cancer Models. *Cancer Res.* **2016**, *76* (4), 789–795.

(501) Linnik, I. V.; Scott, M. L. J.; Holliday, K. F.; Woodhouse, N.; Waterton, J. C.; O'Connor, J. P. B.; Barjat, H.; Liess, C.; Ulloa, J.; Young, H.; et al. Noninvasive Tumor Hypoxia Measurement Using Magnetic Resonance Imaging in Murine U87 Glioma Xenografts and in Patients with Glioblastoma. *Magn. Reson. Med.* **2014**, *71* (5), 1854–1862.

(502) Dewhirst, M. W.; Birer, S. R. Oxygen-Enhanced MRI Is a Major Advance in Tumor Hypoxia Imaging. *Cancer Res.* **2016**, *76* (4), 769–772.

(503) Ogawa, S.; Lee, T. M.; Kay, A. R.; Tank, D. W. Brain Magnetic Resonance Imaging with Contrast Dependent on Blood Oxygenation. *Proc. Natl. Acad. Sci. U. S. A.* **1990**, *87* (24), 9868–9872.

(504) O'Connor, J. P. B.; Naish, J. H.; Parker, G. J. M.; Waterton, J. C.; Watson, Y.; Jayson, G. C.; Buonaccorsi, G. A.; Cheung, S.; Buckley, D. L.; McGrath, D. M.; et al. Preliminary Study of Oxygen-Enhanced Longitudinal Relaxation in MRI: A Potential Novel Biomarker of Oxygenation Changes in Solid Tumors. *Int. J. Radiat. Oncol. Biol. Phys.* **2009**, *75* (4), 1209–1215.

(505) Winter, J. D.; Estrada, M.; Cheng, H.-L. M. Normal Tissue Quantitative T1 and T2 ᶻ MRI Relaxation Time Responses to Hypercapnic and Hyperoxic Gases. *Acad. Radiol.* **2011**, *18* (9), 1159–1167.

(506) Bennett, H. F.; Swartz, H. M.; Brown, R. D.; Koenig, S. H. Modification of Relaxation of Lipid Protons by Molecular Oxygen and Nitroxides. *Invest. Radiol.* **1987**, *22* (6), 502–507.

(507) Matsumoto, K.; Bernardo, M.; Subramanian, S.; Choyke, P.; Mitchell, J. B.; Krishna, M. C.; Lizak, M. J. MR Assessment of Changes of Tumor in Response to Hyperbaric Oxygen Treatment. *Magn. Reson. Med.* **2006**, *56* (2), 240–246.

(508) Jordan, B. F.; Magat, J.; Colliez, F.; Ozel, E.; Fruytier, A. C.; Marchand, V.; Mignion, L.; Bouzin, C.; Cani, P. D.; Vandeputte, C.; et al. Mapping of Oxygen by Imaging Lipids Relaxation Enhancement: A Potential Sensitive Endogenous MRI Contrast to Map Variations in Tissue Oxygenation. *Magn. Reson. Med.* **2013**, *70* (3), 732–744.

(509) Scheffler, K.; Hennig, J. T1 Quantification with Inversion Recovery TrueFISP. *Magn. Reson. Med.* **2001**, *45* (4), 720–723.

(510) Kellman, P.; Herzka, D. A.; Hansen, M. S. Adiabatic Inversion Pulses for Myocardial T1 Mapping. *Magn. Reson. Med.* **2014**, *71* (4), 1428–1434.

(511) Jain, K. K. Advances in the Field of Nanooncology. *BMC Med.* **2010**, *8*, 83.

(512) Brannon-Peppas, L.; Blanchette, J. O. Nanoparticle and Targeted Systems for Cancer Therapy. *Adv. Drug Deliv. Rev.* **2012**, *64*, 206–212.

(513) Cho, K.; Wang, X.; Nie, S.; Chen, Z. (G); Shin, D. M. Therapeutic Nanoparticles for Drug Delivery in Cancer. *Clin. Cancer Res.* **2008**, *14* (5), 1310–1316.

(514) Danhier, F.; Feron, O.; Préat, V. To Exploit the Tumor Microenvironment: Passive and Active Tumor Targeting of Nanocarriers for Anti-Cancer Drug Delivery. *J. Control. Release* **2010**, *148* (2), 135–146.

(515) Yu, M. K.; Park, J.; Jon, S. Targeting Strategies for Multifunctional Nanoparticles in Cancer Imaging and Therapy. *Theranostics* **2012**, *2* (1), 3–44.

(516) Huang, H.-C.; Barua, S.; Sharma, G.; Dey, S. K.; Rege, K. Inorganic Nanoparticles for Cancer Imaging and Therapy. *J. Control. Release* **2011**, *155* (3), 344–357.

(517) Brigger, I.; Dubernet, C.; Couvreur, P. Nanoparticles in Cancer Therapy and

Diagnosis. *Adv. Drug Deliv. Rev.* **2012**, *64*, 24–36.

(518) Peer, D.; Karp, J. M.; Hong, S.; Farokhzad, O. C.; Margalit, R.; Langer, R. Nanocarriers as an Emerging Platform for Cancer Therapy. *Nat. Nanotechnol.* **2007**, *2* (12), 751–760.

(519) Phan, J. H.; Moffitt, R. A.; Stokes, T. H.; Liu, J.; Young, A. N.; Nie, S.; Wang, M. D. Convergence of Biomarkers, Bioinformatics and Nanotechnology for Individualized Cancer Treatment. *Trends Biotechnol.* **2009**, *27* (6), 350–358.

(520) Ahmed, N.; Fessi, H.; Elaissari, A. Theranostic Applications of Nanoparticles in Cancer. *Drug Discov. Today* **2012**, *17* (17–18), 928–934.

(521) Arppe, R.; Näreoja, T.; Nylund, S.; Mattsson, L.; Koho, S.; Rosenholm, J. M.; Soukka, T.; Schäferling, M. Photon Upconversion Sensitized Nanoprobes for Sensing and Imaging of PH. *Nanoscale* **2014**, *6* (12), 6837–6843.

(522) Huang, X.; Lee, S.; Chen, X. Design of "Smart" Probes for Optical Imaging of Apoptosis. *Am. J. Nucl. Med. Mol. Imaging* **2011**, *1* (1), 3–17.

(523) Kang, B.; Austin, L. A.; El-Sayed, M. A. Observing Real-Time Molecular Event Dynamics of Apoptosis in Living Cancer Cells Using Nuclear-Targeted Plasmonically Enhanced Raman Nanoprobes. *ACS Nano* **2014**, *8* (5), 4883–4892.

(524) Josefsen, L. B.; Aylott, J. W.; Beeby, A.; Warburton, P.; Boyle, J. P.; Peers, C.; Boyle, R. W. Porphyrin-Nanosensor Conjugates. New Tools for the Measurement of Intracellular Response to Reactive Oxygen Species. *Photochem. Photobiol. Sci.* **2010**, *9* (6), 801.

(525) Woolley, J. F.; Stanicka, J.; Cotter, T. G. Recent Advances in Reactive Oxygen Species Measurement in Biological Systems. *Trends Biochem. Sci.* **2013**, *38* (11), 556–565.

(526) Adegoke, O.; Forbes, P. B. C. Challenges and Advances in Quantum Dot Fluorescent Probes to Detect Reactive Oxygen and Nitrogen Species: A Review. *Anal. Chim. Acta* **2015**, *862*, 1–13.

(527) Park, J.; Lee, J.; Kwag, J.; Baek, Y.; Kim, B.; Yoon, C. J.; Bok, S.; Cho, S.-H.; Kim, K. H.; Ahn, G.-O.; et al. Quantum Dots in an Amphiphilic Polyethyleneimine Derivative Platform for Cellular Labeling, Targeting, Gene Delivery, and Ratiometric Oxygen Sensing. *ACS Nano* **2015**, *9* (6), 6511–6521.

(528) Liu, J.; Wu, Y.; Yu, Y.; Li, K.; Ji, Y.; Wu, D. Quantitative Ratiometric Phosphorescence Hypoxia–sensing Nanoprobes Based on Quantum Dots/Ir(III) Glycerol Monoolein Cubic-Phase Nanoparticles. *Biosens. Bioelectron.* **2017**, *98*, 119–125.

(529) Lemon, C. M.; Karnas, E.; Bawendi, M. G.; Nocera, D. G. Two-Photon Oxygen Sensing with Quantum Dot-Porphyrin Conjugates. *Inorg. Chem.* **2013**, *52* (18), 10394–10406.

(530) Zhou, X.; Liang, H.; Jiang, P.; Zhang, K. Y.; Liu, S.; Yang, T.; Zhao, Q.; Yang, L.; Lv, W.; Yu, Q.; et al. Multifunctional Phosphorescent Conjugated Polymer Dots for Hypoxia Imaging and Photodynamic Therapy of Cancer Cells. *Adv. Sci.* **2016**, *3* (2), 1500155.

(531) Wu, J. B.; Shao, C.; Li, X.; Shi, C.; Li, Q.; Hu, P.; Chen, Y.-T.; Dou, X.; Sahu, D.; Li, W.; et al. Near-Infrared Fluorescence Imaging of Cancer Mediated by Tumor Hypoxia and HIF1α/OATPs Signaling Axis. *Biomaterials* **2014**, *35* (28), 8175–8185.

(532) Napp, J.; Behnke, T.; Fischer, L.; Würth, C.; Wottawa, M.; Katschinski, D. M.; Alves, F.; Resch-Genger, U.; Schäferling, M. Targeted Luminescent Near-Infrared Polymer-Nanoprobes for in Vivo Imaging of Tumor Hypoxia. *Anal. Chem.* **2011**, *83* (23), 9039–9046.

(533) Xu, H.; Aylott, J. W.; Kopelman, R.; Miller, T. J.; Philbert, M. A. A Real-Time Ratiometric Method for the Determination of Molecular Oxygen Inside Living Cells Using Sol−Gel-Based Spherical Optical Nanosensors with Applications to Rat C6 Glioma. *Anal. Chem.* **2001**, *73* (17), 4124–4133.

(534) Koo, Y.; Cao, Y.; Kopelman, R.; Koo, S. M.; Brasuel, M.; Philbert, M. A. Real-Time Measurements of Dissolved Oxygen Inside Live Cells by Organically Modified Silicate Fluorescent Nanosensors. **2004**.

(535) Clark, H. A.; Barker, S. L. .; Brasuel, M.; Miller, M. T.; Monson, E.; Parus, S.; Shi, Z.-Y.; Song, A.; Thorsrud, B.; Kopelman, R.; et al. Subcellular Optochemical Nanobiosensors: Probes Encapsulated by Biologically Localised Embedding (PEBBLEs). *Sensors Actuators B Chem.* **1998**, *51* (1–3), 12–16.

(536) Sasaki, K.; Shi, Z.-Y.; Kopelman, R.; Masuhara, H. Three-Dimensional PH Microprobing with an Optically-Manipulated Fluorescent Particle. *Chem. Lett.* **1996**,

25 (2), 141–142.

(537) Cheng, Z.; Aspinwall, C. A. Nanometre-Sized Molecular Oxygen Sensors Prepared from Polymer Stabilized Phospholipid Vesicles. *Analyst* **2006**, *131* (2), 236–243.

(538) Lemon, C. M.; Karnas, E.; Han, X.; Bruns, O. T.; Kempa, T. J.; Fukumura, D.; Bawendi, M. G.; Jain, R. K.; Duda, D. G.; Nocera, D. G. Micelle-Encapsulated Quantum Dot-Porphyrin Assemblies as in Vivo Two-Photon Oxygen Sensors. *J. Am. Chem. Soc.* **2015**, *137* (31), 9832–9842.

(539) Liong, M.; Lu, J.; Kovochich, M.; Xia, T.; Ruehm, S. G.; Nel, A. E.; Tamanoi, F.; Zink, J. I. Multifunctional Inorganic Nanoparticles for Imaging, Targeting, and Drug Delivery. *ACS Nano* **2008**, *2* (5), 889–896.

(540) Veiseh, O.; Gunn, J. W.; Zhang, M. Design and Fabrication of Magnetic Nanoparticles for Targeted Drug Delivery and Imaging. *Adv. Drug Deliv. Rev.* **2010**, *62* (3), 284–304.

(541) Janib, S. M.; Moses, A. S.; MacKay, J. A. Imaging and Drug Delivery Using Theranostic Nanoparticles. *Adv. Drug Deliv. Rev.* **2010**, *62* (11), 1052–1063.

(542) Wang, C.; Cheng, L.; Liu, Z. Drug Delivery with Upconversion Nanoparticles for Multi-Functional Targeted Cancer Cell Imaging and Therapy. *Biomaterials* **2011**, *32* (4), 1110–1120.

(543) Ferrari, M. Cancer Nanotechnology: Oppurtunities and Challenges. *Nat. Rev. Cancer* **2005**, *5* (3), 161–171.

(544) Win, K. Y.; Feng, S.-S. In Vitro and in Vivo Studies on Vitamin E TPGS-Emulsified Poly(d,l-Lactic-Co-Glycolic Acid) Nanoparticles for Paclitaxel Formulation. *Biomaterials* **2006**, *27* (10), 2285–2291.

(545) Bozzuto, G.; Molinari, A. Liposomes as Nanomedical Devices. *Int. J. Nanomedicine* **2015**, *10*, 975–999.

(546) Daraee, H.; Etemadi, A.; Kouhi, M.; Alimirzalu, S.; Akbarzadeh, A. Application of Liposomes in Medicine and Drug Delivery. *Artif. Cells, Nanomedicine, Biotechnol.* **2016**, *44* (1), 381–391.

(547) Ekambaram, P.; Abdul, A.; Sathali, H.; Priyanka, K. Solid Lipid Nanoparticles: A Review. *Sci. Revs. Chem. Commun* **2012**, *2* (1), 80–102.

(548) Muller, R. H.; Keck, C. M. Challenges and Solutions for the Delivery of Biotech Drugs - a Review of Drug Nanocrystal Technology and Lipid Nanoparticles. *J. Biotechnol.* **2004**, *113* (1–3), 151–170.

(549) Mehnert, W.; Mäder, K. Solid Lipid Nanoparticles: Production, Characterization and Applications. *Adv. Drug Deliv. Rev.* **2012**, *64*, 83–101.

(550) Kumari, A.; Yadav, S. K.; Yadav, S. C. Biodegradable Polymeric Nanoparticles Based Drug Delivery Systems. *Colloids Surfaces B Biointerfaces* **2010**, *75* (1), 1–18.

(551) Cheng, R.; Meng, F.; Deng, C.; Klok, H.-A.; Zhong, Z. Dual and Multi-Stimuli Responsive Polymeric Nanoparticles for Programmed Site-Specific Drug Delivery. *Biomaterials* **2013**, *34* (14), 3647–3657.

(552) Soppimath, K. S.; Aminabhavi, T. M.; Kulkarni, A. R.; Rudzinski, W. E. Biodegradable Polymeric Nanoparticles as Drug Delivery Devices. *J. Control. Release* **2001**, *70* (1–2), 1–20.

(553) Slowing, I. I.; Vivero-Escoto, J. L.; Wu, C.-W.; Lin, V. S.-Y. Mesoporous Silica Nanoparticles as Controlled Release Drug Delivery and Gene Transfection Carriers. *Adv. Drug Deliv. Rev.* **2008**, *60* (11), 1278–1288.

(554) Tang, F.; Li, L.; Chen, D. Mesoporous Silica Nanoparticles: Synthesis, Biocompatibility and Drug Delivery. *Adv. Mater.* **2012**, *24* (12), 1504–1534.

(555) Zhang, Q.; Liu, F.; Nguyen, K. T.; Ma, X.; Wang, X.; Xing, B.; Zhao, Y. Multifunctional Mesoporous Silica Nanoparticles for Cancer-Targeted and Controlled Drug Delivery. *Adv. Funct. Mater.* **2012**, *22* (24), 5144–5156.

(556) Huang, H.-C.; Barua, S.; Sharma, G.; Dey, S. K.; Rege, K. Inorganic Nanoparticles for Cancer Imaging and Therapy. *J. Control. Release* **2011**, *155* (3), 344–357.

(557) Bhattacharyya, S.; Kudgus, R. A.; Bhattacharya, R.; Mukherjee, P. Inorganic Nanoparticles in Cancer Therapy. *Pharm. Res.* **2011**, *28* (2), 237–259.

(558) Heurtault, B.; Saulnier, P.; Pech, B.; Proust, B. E.; Richard, J. Lipidic Nanocapsules: Preparation Process and Use as Drug Delivery Systems. WO02688000, 2000.

(559) Heurtault, B.; Saulnier, P.; Pech, B.; Proust, J.-E.; Benoit, J.-P. A Novel Phase Inversion-Based Process for the Preparation of Lipid Nanocarriers. *Pharm. Res.* **2002**, *19* (6), 875–880.

(560) Lamprecht, A.; Bouligand, Y.; Benoit, J.-P. New Lipid Nanocapsules Exhibit Sustained Release Properties for Amiodarone. *J. Control. Release* **2002**, *84* (1–2), 59–68.

(561) Minkov, I.; Ivanova, T.; Panaiotov, I.; Proust, J.; Saulnier, P. Reorganization of Lipid Nanocapsules at Air-Water Interface: Part 2. Properties of the Formed Surface Film. *Colloids Surf B Biointerfaces* **2005**, *44* (4), 194–203.

(562) Vonarbourg, A.; Saulnier, P.; Passirani, C.; Benoit, J.-P. Electrokinetic Properties of Noncharged Lipid Nanocapsules: Influence of the Dipolar Distribution at the Interface. *Electrophoresis* **2005**, *26* (11), 2066–2075.

(563) Minkov, I.; Ivanova, T.; Panaiotov, I.; Proust, J.; Saulnier, P.; Verger, R.; Saulnier, P. Reorganization of Lipid Nanocapsules at Air–water Interface. *Colloids Surfaces B Biointerfaces* **2005**, *44* (4), 197–203.

(564) Owens, D. E.; Peppas, N. A. Opsonization, Biodistribution, and Pharmacokinetics of Polymeric Nanoparticles. *Int. J. Pharm.* **2006**, *307* (1), 93–102.

(565) Brigger, I.; Dubernet, C.; Couvreur, P. Nanoparticles in Cancer Therapy and Diagnosis. *Adv Drug Deliv Rev* **2002**, *54* (5), 631–651.

(566) Mohanraj, V. J.; Chen, Y. Nanoparticles - A Review. *Trop. J. Pharm. Res.* **2006**, *5* (1), 561–573.

(567) Malam, Y.; Loizidou, M.; Seifalian, A. M. Liposomes and Nanoparticles: Nanosized Vehicles for Drug Delivery in Cancer. *Trends Pharmacol. Sci.* **2009**, *30* (11), 592–599.

(568) Khalid, M. N.; Simard, P.; Hoarau, D.; Dragomir, A.; Leroux, J.-C. Long Circulating Poly(Ethylene Glycol)-Decorated Lipid Nanocapsules Deliver Docetaxel to Solid Tumors. *Pharm. Res.* **2006**, *23* (4), 752–758.

(569) Mosqueira, V. C. F.; Legrand, P.; Barratt, G. Surface-Modified and Conventional Nanocapsules as Novel Formulations for Parenteral Delivery of Halofantrine. *J. Nanosci. Nanotechnol.* **2006**, *6* (9), 3193–3202.

(570) Kwon, G. S.; Okano, T. Polymeric Micelles as New Drug Carriers. *Adv. Drug Deliv. Rev.* **1996**, *21* (2), 107–116.

(571) Goutayer, M.; Dufort, S.; Josserand, V.; Royère, A.; Heinrich, E.; Vinet, F.; Bibette, J.; Coll, J.-L.; Texier, I. Tumor Targeting of Functionalized Lipid Nanoparticles:

Assessment by in Vivo Fluorescence Imaging. *Eur. J. Pharm. Biopharm.* **2010**, *75* (2), 137–147.

(572) Ambruosi, A.; Gelperina, S.; Khalansky, A.; Tanski, S.; Theisen, A.; Kreuter, J. Influence of Surfactants, Polymer and Doxorubicin Loading on the Anti-Tumour Effect of Poly(Butyl Cyanoacrylate) Nanoparticles in a Rat Glioma Model. *J. Microencapsul.* **2006**, *23* (5), 582–592.

(573) Huynh, N. T.; Passirani, C.; Saulnier, P.; Benoit, J. P. Lipid Nanocapsules: A New Platform for Nanomedicine. *Int. J. Pharm.* **2009**, *379* (2), 201–209.

(574) Anton, N.; Gayet, P.; Benoit, J.-P.; Saulnier, P. Nano-Emulsions and Nanocapsules by the PIT Method: An Investigation on the Role of the Temperature Cycling on the Emulsion Phase Inversion. *Int. J. Pharm.* **2007**, *344* (1–2), 44–52.

(575) Hureaux, J.; Lagarce, F.; Gagnadoux, F.; Clavreul, A.; Benoit, J.-P.; Urban, T. The Adaptation of Lipid Nanocapsule Formulations for Blood Administration in Animals. *Int. J. Pharm.* **2009**, *379* (2), 266–269.

(576) Heurtault, B.; Saulnier, P.; Benoit, J. P.; Proust, J.-E.; Pech, B.; Richard, J. Lipid Nanocapsules, Preparation Process and Use as Medicine. US10220506, March 2, 2001.

(577) Hirsjärvi, S.; Sancey, L.; Dufort, S.; Belloche, C.; Vanpouille-Box, C.; Garcion, E.; Coll, J.-L.; Hindré, F.; Benoît, J.-P. Effect of Particle Size on the Biodistribution of Lipid Nanocapsules: Comparison between Nuclear and Fluorescence Imaging and Counting. *Int. J. Pharm.* **2013**, *453* (2), 594–600.

(578) Paillard, A.; Hindré, F.; Vignes-Colombeix, C.; Benoit, J.-P.; Garcion, E. The Importance of Endo-Lysosomal Escape with Lipid Nanocapsules for Drug Subcellular Bioavailability. *Biomaterials* **2010**, *31* (29), 7542–7554.

(579) Garcion, E.; Lamprecht, A.; Heurtault, B.; Paillard, A.; Aubert-Pouessel, A.; Denizot, B.; Menei, P.; Benoît, J.-P. A New Generation of Anticancer, Drug-Loaded, Colloidal Vectors Reverses Multidrug Resistance in Glioma and Reduces Tumor Progression in Rats. *Mol. Cancer. Ther.* **2006**, *5* (7), 1710–1722.

(580) Roger, E.; Lagarce, F.; Garcion, E.; Benoit, J.-P. Lipid Nanocarriers Improve Paclitaxel Transport throughout Human Intestinal Epithelial Cells by Using Vesicle-Mediated Transcytosis. *J. Control. Release* **2009**, *140* (2), 174–181.

(581) Malzert-Fréon, A.; Vrignaud, S.; Saulnier, P.; Lisowski, V.; Benoît, J. P.; Rault, S. Formulation of Sustained Release Nanoparticles Loaded with a Tripentone, a New Anticancer Agent. *Int. J. Pharm.* **2006**, *320* (1–2), 157–164.

(582) Lamprecht, A.; Benoit, J.-P. Etoposide Nanocarriers Suppress Glioma Cell Growth by Intracellular Drug Delivery and Simultaneous P-Glycoprotein Inhibition. *J. Control. Release* **2006**, *112* (2), 208–213.

(583) Allard, E.; Passirani, C.; Garcion, E.; Pigeon, P.; Vessières, A.; Jaouen, G.; Benoit, J.-P. Lipid Nanocapsules Loaded with an Organometallic Tamoxifen Derivative as a Novel Drug-Carrier System for Experimental Malignant Gliomas. *J. Control. Release* **2008**, *130* (2), 146–153.

(584) Allard, E.; Huynh, N. T.; Vessières, A.; Pigeon, P.; Jaouen, G.; Benoit, J.-P.; Passirani, C. Dose Effect Activity of Ferrocifen-Loaded Lipid Nanocapsules on a 9L-Glioma Model. *Int. J. Pharm.* **2009**, *379* (2), 317–323.

(585) Allard, E.; Jarnet, D.; Vessières, A.; Vinchon-Petit, S.; Jaouen, G.; Benoit, J.-P.; Passirani, C. Local Delivery of Ferrociphenol Lipid Nanocapsules Followed by External Radiotherapy as a Synergistic Treatment Against Intracranial 9L Glioma Xenograft. *Pharm. Res.* **2010**, *27* (1), 56–64.

(586) Dhanikula, A. B.; Khalid, N. M.; Lee, S. D.; Yeung, R.; Risovic, V.; Wasan, K. M.; Leroux, J.-C. Long Circulating Lipid Nanocapsules for Drug Detoxification. *Biomaterials* **2007**, *28* (6), 1248–1257.

(587) Saliou, B.; Thomas, O.; Lautram, N.; Clavreul, A.; Hureaux, J.; Urban, T.; Benoit, J.-P.; Lagarce, F. Development and in Vitro Evaluation of a Novel Lipid Nanocapsule Formulation of Etoposide. *Eur. J. Pharm. Sci.* **2013**, *50* (2), 172–180.

(588) Roger, E.; Lagarce, F.; Benoit, J.-P. Development and Characterization of a Novel Lipid Nanocapsule Formulation of Sn38 for Oral Administration. *Eur. J. Pharm. Biopharm.* **2011**, *79* (1), 181–188.

(589) Woehrer, A.; Bauchet, L.; Barnholtz-Sloan, J. S. Glioblastoma Survival. *Curr. Opin. Neurol.* **2014**, 1.

(590) Ribeiro, M. de C.; Coutinho, L. M. B.; Hilbig, A. The Role of Apoptosis, Cell Proliferation Index, Bcl-2, and P53 in Glioblastoma Prognosis. *Arq. Neuropsiquiatr.* **2004**, *62* (2a), 262–270.

(591) Chinot, O. L.; Wick, W.; Mason, W.; Henriksson, R.; Saran, F.; Nishikawa, R.; Carpentier, A. F.; Hoang-Xuan, K.; Kavan, P.; Cernea, D.; et al. Bevacizumab plus Radiotherapy–Temozolomide for Newly Diagnosed Glioblastoma. *N. Engl. J. Med.* **2014**, *370* (8), 709–722.

(592) Weyland, M.; Griveau, A.; Bejaud, J.; Benoit, J.-P.; Coursaget, P.; Garcion, E. Lipid Nanocapsule Functionalization by Lipopeptides Derived from Human Papillomavirus Type-16 Capsid for Nucleic Acid Delivery into Cancer Cells. *Int. J. Pharm.* **2013**, *454* (2), 756–764.

(593) Clavreul, A.; Lautram, N.; Franconi, F.; Passirani, C.; Montero-Menei, C.; Menei, P.; Tetaud, C.; Montagu, A.; Laine, A.-L.; Vessieres, A. Targeting and Treatment of Glioblastomas with Human Mesenchymal Stem Cells Carrying Ferrociphenol Lipid Nanocapsules. *Int. J. Nanomedicine* **2015**, *10* (1), 1259–1271.

(594) Griveau, A.; Bejaud, J.; Anthiya, S.; Avril, S.; Autret, D.; Garcion, E. Silencing of MiR-21 by Locked Nucleic Acid–lipid Nanocapsule Complexes Sensitize Human Glioblastoma Cells to Radiation-Induced Cell Death. *Int. J. Pharm.* **2013**, *454* (2), 765–774.

(595) Bernardi, A.; Frozza, R. L.; Hoppe, J. B.; Salbego, C.; Pohlmann, A. R.; Battastini, A. M. O.; Guterres, S. S. The Antiproliferative Effect of Indomethacin-Loaded Lipid-Core Nanocapsules in Glioma Cells Is Mediated by Cell Cycle Regulation, Differentiation, and the Inhibition of Survival Pathways. *Int. J. Nanomedicine* **2013**, *8*, 711–728.

(596) Bastiancich, C.; Lemaire, L.; Bianco, J.; Franconi, F.; Danhier, F.; Préat, V.; Bastiat, G.; Lagarce, F. Evaluation of Lauroyl-Gemcitabine-Loaded Hydrogel Efficacy in Glioblastoma Rat Models. *Nanomedicine* **2018**, *13* (16), 1999–2013.

(597) Bastiancich, C.; Vanvarenberg, K.; Ucakar, B.; Pitorre, M.; Bastiat, G.; Lagarce, F.; Préat, V.; Danhier, F. Lauroyl-Gemcitabine-Loaded Lipid Nanocapsule Hydrogel for the Treatment of Glioblastoma. *J. Control. Release* **2016**, *225*, 283–293.

(598) Zanotto-Filho, A.; Coradini, K.; Braganhol, E.; Schröder, R.; de Oliveira, C. M.; Simões-Pires, A.; Battastini, A. M. O.; Pohlmann, A. R.; Guterres, S. S.; Forcelini, C. M.; et al. Curcumin-Loaded Lipid-Core Nanocapsules as a Strategy to Improve Pharmacological Efficacy of Curcumin in Glioma Treatment. *Eur. J. Pharm. Biopharm.* **2013**, *83* (2), 156–167.

(599) Morille, M.; Montier, T.; Legras, P.; Carmoy, N.; Brodin, P.; Pitard, B.; Benoît, J. P.; Passirani, C. Long-Circulating DNA Lipid Nanocapsules as New Vector for Passive Tumor Targeting. *Biomaterials* **2010**, *31* (2), 321–329.

(600) Morille, M.; Passirani, C.; Dufort, S.; Bastiat, G.; Pitard, B.; Coll, J. L.; Benoit, J. P. Tumor Transfection after Systemic Injection of DNA Lipid Nanocapsules. *Biomaterials* **2011**, *32* (9), 2327–2333.

(601) Huynh, N. T.; Morille, M.; Bejaud, J.; Legras, P.; Vessieres, A.; Jaouen, G.; Benoit, J.; Passirani, C. Treatment of 9L Gliosarcoma in Rats by Ferrociphenol-Loaded Lipid Nanocapsules Based on a Passive Targeting Strategy via the EPR Effect. *Pharm Res* **2011**, *28* (12), 3189–3198.

(602) Huynh, N. T.; Passirani, C.; Allard-Vannier, E.; Lemaire, L.; Roux, J.; Garcion, E.; Vessieres, A.; Benoit, J. Administration-Dependent Efficacy of Ferrociphenol Lipid Nanocapsules for the Treatment of Intracranial 9L Rat Gliosarcoma. *Int. J. Pharm.* **2012**, *423* (1), 55–62.

(603) Morille, M.; Passirani, C.; Letrou-Bonneval, E.; Benoit, J.-P.; Pitard, B. Galactosylated DNA Lipid Nanocapsules for Efficient Hepatocyte Targeting. *Int. J. Pharm.* **2009**, *379* (2), 293–300.

(604) Béduneau, A.; Saulnier, P.; Benoit, J.-P. Active Targeting of Brain Tumors Using Nanocarriers. *Biomaterials* **2007**, *28* (33), 4947–4967.

(605) Sánchez-Moreno, P.; Ortega-Vinuesa, J. L.; Martín-Rodríguez, A.; Boulaiz, H.; Marchal-Corrales, J. A.; Peula-García, J. M. Characterization of Different Functionalized Lipidic Nanocapsules as Potential Drug Carriers. *Int. J. Mol. Sci.* **2012**, *13* (2), 2405–2424.

(606) Allard, E.; Passirani, C.; Benoit, J.-P. Convection-Enhanced Delivery of Nanocarriers for the Treatment of Brain Tumors. *Biomaterials* **2009**, *30* (12), 2302–2318.

(607) Wauthoz, N.; Bastiat, G.; Moysan, E.; Cieślak, A.; Kondo, K.; Zandecki, M.; Moal, V.; Rousselet, M.-C.; Hureaux, J.; Benoit, J.-P. Safe Lipid Nanocapsule-Based Gel Technology to Target Lymph Nodes and Combat Mediastinal Metastases from an Orthotopic Non-Small-Cell Lung Cancer Model in SCID-CB17 Mice. *Nanomedicine* **2015**, *11* (5), 1237–1245.

(608) Varshosaz, J.; Hajhashemi, V.; Soltanzadeh, S. Lipid Nanocapsule-Based Gels for

Enhancement of Transdermal Delivery of Ketorolac Tromethamine. *J. Drug Deliv.* **2011**, *2011*, 571272.

(609) Roger, M.; Clavreul, A.; Huynh, N. T.; Passirani, C.; Schiller, P.; Vessières, A.; Montero-Menei, C.; Menei, P. Ferrociphenol Lipid Nanocapsule Delivery by Mesenchymal Stromal Cells in Brain Tumor Therapy. *Int. J. Pharm.* **2012**, *423* (1), 63–68.

(610) Allard, E.; Hindre, F.; Passirani, C.; Lemaire, L.; Lepareur, N.; Noiret, N.; Menei, P.; Benoit, J.-P. 188Re-Loaded Lipid Nanocapsules as a Promising Radiopharmaceutical Carrier for Internal Radiotherapy of Malignant Gliomas. *Eur. J. Nucl. Med. Mol. Imaging* **2008**, *35* (10), 1838–1846.

(611) Ballot, S.; Noiret, N.; Hindré, F.; Denizot, B.; Garin, E.; Rajerison, H.; Benoit, J.-P. 99mTc/188Re-Labelled Lipid Nanocapsules as Promising Radiotracers for Imaging and Therapy: Formulation and Biodistribution. *Eur. J. Nucl. Med. Mol. Imaging* **2006**, *33* (5), 602–607.

(612) Yang, Y.-S.; Carney, R. P.; Stellacci, F.; Irvine, D. J. Enhancing Radiotherapy by Lipid Nanocapsule-Mediated Delivery of Amphiphilic Gold Nanoparticles to Intracellular Membranes. *ACS Nano* **2014**, *8* (9), 8992–9002.

(613) Tran, T. H.; Nguyen, T. D.; Poudel, B. K.; Nguyen, H. T.; Kim, J. O.; Yong, C. S.; Nguyen, C. N. Development and Evaluation of Artesunate-Loaded Chitosan-Coated Lipid Nanocapsule as a Potential Drug Delivery System Against Breast Cancer. *AAPS PharmSciTech* **2015**, *16* (6), 1307–1316.

(614) Figueiró, F.; Bernardi, A.; Frozza, R. L.; Terroso, T.; Zanotto-Filho, A.; Jandrey, E. H. F.; Moreira, J. C. F.; Salbego, C. G.; Edelweiss, M. I.; Pohlmann, A. R.; et al. Resveratrol-Loaded Lipid-Core Nanocapsules Treatment Reduces In Vitro and In Vivo Glioma Growth. *J. Biomed. Nanotechnol.* **2013**, *9* (3), 516–526.

(615) Lamprecht, A.; Saumet, J.-L.; Roux, J.; Benoit, J.-P. Lipid Nanocarriers as Drug Delivery System for Ibuprofen in Pain Treatment. *Int. J. Pharm.* **2004**, *278* (2), 407–414.

(616) Frozza, R. L.; Bernardi, A.; Paese, K.; Hoppe, J. B.; Silva, T. da; Battastini, A. M. O.; Pohlmann, A. R.; Guterres, S. S.; Salbego, C. Characterization of Trans-Resveratrol-Loaded Lipid-Core Nanocapsules and Tissue Distribution Studies in Rats. *J. Biomed.*

Nanotechnol. **2010**, *6* (6), 694–703.

(617) Peltier, S.; Oger, J.-M.; Lagarce, F.; Couet, W.; Benoît, J.-P. Enhanced Oral Paclitaxel Bioavailability After Administration of Paclitaxel-Loaded Lipid Nanocapsules. *Pharm. Res.* **2006**, *23* (6), 1243–1250.

(618) Groo, A.-C.; Saulnier, P.; Gimel, J.-C.; Gravier, J.; Ailhas, C.; Benoit, J.-P.; Lagarce, F. Fate of Paclitaxel Lipid Nanocapsules in Intestinal Mucus in View of Their Oral Delivery. *Int. J. Nanomedicine* **2013**, *8*, 4291–4302.

(619) Hureaux, J.; Lagarce, F.; Gagnadoux, F.; Vecellio, L.; Clavreul, A.; Roger, E.; Kempf, M.; Racineux, J.-L.; Diot, P.; Benoit, J.-P.; et al. Lipid Nanocapsules: Ready-to-Use Nanovectors for the Aerosol Delivery of Paclitaxel. *Eur. J. Pharm. Biopharm.* **2009**, *73* (2), 239–246.

(620) Strickley, R. G. Solubilizing Excipients in Oral and Injectable Formulations. *Pharm. Res.* **2004**, *21* (2), 201–230.

(621) Nanjwade, B. K.; Patel, D. J.; Udhani, R. A.; Manvi, F. V. Functions of Lipids for Enhancement of Oral Bioavailability of Poorly Water-Soluble Drugs. *Sci. Pharm.* **2011**, *79* (4), 705–727.

(622) Khan, N.; Williams, B. B.; Hou, H.; Li, H.; Swartz, H. M. Repetitive Tissue PO2 Measurements by Electron Paramagnetic Resonance Oximetry: Current Status and Future Potential for Experimental and Clinical Studies. *Antioxid. Redox Signal.* **2007**, *9* (8), 1169–1182.

(623) Gallez, B.; Mäder, K. Accurate and Sensitive Measurements of PO(2) in Vivo Using Low Frequency EPR Spectroscopy: How to Confer Biocompatibility to the Oxygen Sensors. *Free Radic. Biol. Med.* **2000**, *29* (11), 1078–1084.

(624) Bratasz, A.; Kulkarni, A. C.; Kuppusamy, P. A Highly Sensitive Biocompatible Spin Probe for Imaging of Oxygen Concentration in Tissues. *Biophys. J.* **2007**, *92* (8), 2918–2925.

(625) Meenakshisundaram, G.; Eteshola, E.; Blank, A.; Lee, S. C.; Kuppusamy, P. A Molecular Paramagnetic Spin-Doped Biopolymeric Oxygen Sensor. *Biosens. Bioelectron.* **2010**, *25* (10), 2283–2289.

(626) Jagtap, A. P.; Krstic, I.; Kunjir, N. C.; Hänsel, R.; Prisner, T. F.; Sigurdsson, S. T. Sterically Shielded Spin Labels for In-Cell EPR Spectroscopy: Analysis of Stability in

Reducing Environment. *Free Radic. Res.* **2015**, *49* (1), 78–85.

(627) Ansiaux, R.; Baudelet, C.; Jordan, B. F.; Beghein, N.; Sonveaux, P.; De Wever, J.; Martinive, P.; Grégoire, V.; Feron, O.; Gallez, B. Thalidomide Radiosensitizes Tumors through Early Changes in the Tumor Microenvironment. *Clin. cancer Res.* **2005**, *11*, 743–750.

(628) Mottram, J. C. A Factor of Importance in the Radio Sensitivity of Tumours. *Br J Radiol.* **1931**, *9* (105), 606–614.

(629) Littlewood, T. J. The Impact of Hemoglobin Levels on Treatment Outcomes in Patients with Cancer. *Semin. Oncol.* **2001**, *28*, 49–53.

(630) Sutherland, R. M. Tumor Hypoxia and Gene Expression - Implications for Malignant Progression and Therapy. *Acta Oncol.* **1998**, *37* (6), 567–574.

(631) Semenza, G. L. Hypoxia-Inducible Factor 1 and Cancer Pathogenesis. *IUBMB Life.* **2008**, *60* (9), 591–597.

(632) Lu, X.; Kang, Y. Hypoxia and Hypoxia-Inducible Factors: Master Regulators of Metastasis. *Clin Cancer Res.* **2010**, *16* (24), 5928–5935.

(633) Semenza, G. L. HIF-1: Mediator of Physiological and Pathophysiological Responses to Hypoxia. *J Appl Physiol.* **2000**, *88* (4), 1474–1480.

(634) Swartz, H. M.; Williams, B. B.; Zaki, B. I.; Hartford, A. C.; Jarvis, L. A.; Chen, E. Y.; Comi, R. J.; Ernstoff, M. S.; Hou, H.; Khan, N.; et al. Clinical EPR: Unique Opportunities and Some Challenges. *Acad Radiol.* **2014**, *21* (2), 197–206.

(635) Sostaric, J. Z.; Pandian, R. P.; Bratasz, A.; Kuppusamy, P. Encapsulation of a Highly Sensitive EPR Active Oxygen Probe into Sonochemically Prepared Microspheres. *Phys Chem B.* **2007**, *111* (12), 3298–3303.

(636) Dhimitruka, I.; Alzarie, Y. A.; Hemann, C.; Samouilov, A.; Zweier, J. L. Trityl Radicals in Perfluorocarbon Emulsions as Stable, Sensitive, and Biocompatible Oximetry Probes. *Bioorganic Med. Chem. Lett.* **2016**, *26* (23), 5685–5688.

(637) Hirsjärvi, S.; Dufort, S.; Gravier, J.; Texier, I.; Yan, Q.; Bibette, J.; Sancey, L.; Josserand, V.; Passirani, C.; Benoit, J.-P.; et al. Influence of Size, Surface Coating and Fine Chemical Composition on the in Vitro Reactivity and in Vivo Biodistribution of Lipid Nanocapsules versus Lipid Nanoemulsions in Cancer Models. *Nanomedicine.*

2013, *9* (3), 375–387.

(638) Basile, L.; Passirani, C.; Huynh, N.-T.; Béjaud, J.; Benoit, J.; Puglisi, G.; Pignatello, R. Serum-Stable , Long-Circulating Paclitaxel-Loaded Colloidal Carriers Decorated with a New Amphiphilic PEG Derivative. *Int. J. Pharm.* **2012**, *426* (1–2), 231–238.

(639) Khramtsov, V. V. In Vivo Spectroscopy and Imaging of Nitroxide Probes. In *Nitroxides - Theory, Experiment and Applications*; InTech, 2012.

(640) Rübe, A.; Mäder, K. Electron Spin Resonance Study on the Dynamics of Polymeric Nanocapsules. *J. Biomed. Nanotechnol.* **2005**, *1* (2), 208–213.

(641) Heurtault, B.; Saulnier, P.; Pech, B.; Benoit, J.-P.; Proust, J.-E. Interfacial Stability of Lipid Nanocapsules. *Colloids Surf B Biointerfaces.* **2003**, *30* (3), 225–235.

(642) Thomas, O.; Lagarce, F. Lipid Nanocapsules: A Nanocarrier Suitable for Scale-Up Process. *J. Drug Deliv. Sci. Technol.* **2013**, *23* (6), 555–559.

(643) Kim, S.; Thiessen, P.; Bolton, E.; Chen, J.; Fu, G.; Gindulyte, A.; Han, L.; He, J.; He, S.; Shoemaker, B.; et al. PubChem Substance and Compound Databases. *Nucleic Acids Res.* **2016**, *44* (D1), D1202–D1213.

(644) Diepart, C.; Jordan, B. F.; Gallez, B. A New EPR Oximetry Protocol to Estimate the Tissue Oxygen Consumption in Vivo. *Radiat. Res.* **2009**, *172* (2), 220–225.

(645) Dinguizli, M.; Jeumont, S.; Beghein, N.; He, J.; Walczak, T.; Lesniewski, P. N. N.; Hou, H.; Grinberg, O. Y. Y.; Sucheta, A.; Swartz, H. M. M.; et al. Development and Evaluation of Biocompatible Films of Polytetrafluoroethylene Polymers Holding Lithium Phthalocyanine Crystals for Their Use in EPR Oximetry. *Biosens. Bioelectron.* **2006**, *21* (7), 1015–1022.

(646) Robinson, S. P.; Howe, F. A.; Griffiths, J. R. Noninvasive Monitoring of Carbogen-Induced Changes in Tumor Blood Flow and Oxygenation by Functional Magnetic Resonance Imaging. *Int J Radiat Oncol Biol Phys.* **1995**, *33* (4), 855–859.

(647) Karczmar, G. S.; Kuperman, V. Y.; River, J. N.; Lewis, M. Z.; Lipton, M. J. Magnetic Resonance Measurement of Response to Hyperoxia Differentiates Tumors from Normal Tissue and May Be Sensitive to Oxygen Consumption. *Invest. Radiol.* **1994**, *29*, S161–S163.

(648) Ghosh, P. K.; Majithiya, R. J.; Umrethia, M. L.; Murthy, R. S. R. Design and

Development of Microemulsion Drug Delivery System of Acyclovir for Improvement of Oral Bioavailability. *AAPS PharmSciTech* **2006**, *7* (3), 77.

(649) Valable, S.; Lemasson, B.; Farion, R.; Beaumont, M.; Segebarth, C.; Remy, C.; Barbier, E. L. Assessment of Blood Volume, Vessel Size, and the Expression of Angiogenic Factors in Two Rat Glioma Models: A Longitudinal in Vivo and Ex Vivo Study. *NMR Biomed.* **2008**, *21* (10), 1043–1056.

(650) Khan, N.; Li, H.; Hou, H.; Lariviere, J. P.; Gladstone, D. J.; Demidenko, E.; Swartz, H. M. Tissue PO2 of Orthotopic 9L and C6 Gliomas and Tumor-Specific Response to Radiotherapy and Hyperoxygenation. *Int. J. Radiat. Oncol. Biol. Phys.* **2009**, *73* (3), 878–885.

(651) Ramachandran, S.; Ient, J.; Göttgens, E.-L.; Krieg, A.; Hammond, E. Epigenetic Therapy for Solid Tumors: Highlighting the Impact of Tumor Hypoxia. *Genes (Basel).* **2015**, *6* (4), 935–956.

(652) Riess, J. G.; Le Blanc, M. Perfluoro Compounds as Blood Substitutes. *Angew. Chemie Int. Ed. English* **1978**, *17* (9), 621–634.

(653) Ruiz-Cabello, J.; Barnett, B. P.; Bottomley, P. A.; Bulte, J. W. M. M. Fluorine (19F) MRS and MRI in Biomedicine. *NMR Biomed.* **2011**, *24* (2), 114–129.

(654) Lauffer, R. B. Paramagnetic Metal Complexes as Water Proton Relaxation Agents for NMR Imaging: Theory and Design. *Chem. Rev.* **1987**, *87* (5), 901–927.

(655) Sotak, C. H.; Hees, P. S.; Huang, H.-N.; Hung, M.-H.; Krespan, C. G.; Raynolds, S. A New Perfluorocarbon for Use in Fluorine-19 Magnetic Resonance Imaging and Spectroscopy. *Magn. Reson. Med.* **1993**, *29* (2), 188–195.

(656) Vanpouille-Box, C.; Lacoeuille, F.; Belloche, C.; Lepareur, N.; Lemaire, L.; LeJeune, J. J.; Benoit, J. P.; Menei, P.; Couturier, O. F.; Garcion, E.; et al. Tumor Eradication in Rat Glioma and Bypass of Immunosuppressive Barriers Using Internal Radiation with (188)Re-Lipid Nanocapsules. *Biomaterials* **2011**, *32* (28), 6781–6790.

(657) Vonarbourg, A.; Passirani, C.; Saulnier, P.; Simard, P.; Leroux, J. C.; Benoit, J.-P. Evaluation of Pegylated Lipid Nanocapsules versus Complement System Activation and Macrophage Uptake. *Wiley Period.* **2006**, *78* (3), 620–628.

(658) Volpe, J. P.; Hunter, N.; Basic, I.; Milas, L. Metastatic Properties of Murine Sarcomas and Carcinomas I. Positive Correlation with Lung Colonization and Lack of

Correlation with s.c. Tumor Take. *Clin. Exp. Metastasis* **1985**, *3* (4), 281–294.

(659) Lemaire, L.; Franconi, F.; Saint-André, J. P.; Roullin, V.-G.; Jallet, P.; Le Jeune, J.-J. High-Field Quantitative Transverse Relaxation Time, Magnetization Transfer and Apparent Water Diffusion in Experimental Rat Brain Tumour. *NMR Biomed.* **2000**, *13* (3), 116–123.

(660) Bobo, R. H.; Laske, D. W.; Akbasak, A.; Morrison, P. F.; Dedrick, R. L.; Oldfield, E. H. Convection-Enhanced Delivery of Macromolecules in the Brain. *Proc. Natl. Acad. Sci. U. S. A.* **1994**, *91* (6), 2076–2080.

(661) Lollo, G.; Vincent, M.; Ullio-Gamboa, G.; Lemaire, L.; Franconi, F.; Couez, D.; Benoit, J.-P. Development of Multifunctional Lipid Nanocapsules for the Co-Delivery of Paclitaxel and CpG-ODN in the Treatment of Glioblastoma. *Int. J. Pharm.* **2015**, *495* (2), 972–980.

(662) Kruuv, J. A.; Inch, W. R.; McCredie, J. A. Blood Flow and Oxygenation of Tumors in Mice. I. Effects of Breathing Gases Containing Carbon Dioxide at Atmospheric Pressure. *Cancer* **1967**, *20* (1), 51–59.

(663) Lanzen, J. L.; Braun, R. D.; Ong, A. L.; Dewhirst, M. W. Variability in Blood Flow and PO2 in Tumors in Response to Carbogen Breathing. *Int. J. Radiat. Oncol. Biol. Phys.* **1998**, *42* (4), 855–859.

(664) Ballot, S.; Noiret, N.; Hindré, F.; Denizot, B.; Garin, E.; Rajerison, H.; Benoit, J.-P. 99mTc/188Re-Labelled Lipid Nanocapsules as Promising Radiotracers for Imaging and Therapy: Formulation and Biodistribution. *Eur. J. Nucl. Med. Mol. Imaging* **2006**, *33* (5), 602–607.

(665) Lacoeuille, F.; Hindre, F.; Moal, F.; Roux, J.; Passirani, C.; Couturier, O.; Cales, P.; Le Jeune, J. J.; Lamprecht, A.; Benoit, J. P. In Vivo Evaluation of Lipid Nanocapsules as a Promising Colloidal Carrier for Paclitaxel. *Int. J. Pharm.* **2007**, *344* (1–2), 143–149.

(666) Cahouet, A.; Denizot, B.; Hindré, F.; Passirani, C.; Heurtault, B.; Moreau, M.; Le Jeune, J. .; Benoît, J. . Biodistribution of Dual Radiolabeled Lipidic Nanocapsules in the Rat Using Scintigraphy and γ Counting. *Int. J. Pharm.* **2002**, *242* (1–2), 367–371.

(667) Hernando, D.; Sharma, S. D.; Kramer, H.; Reeder, S. B. On the Confounding Effect of Temperature on Chemical Shift-Encoded Fat Quantification. *Magn. Reson. Med.* **2014**, *72* (2), 464–470.

(668) Hoad, C. L.; Palaniyappan, N.; Kaye, P.; Chernova, Y.; James, M. W.; Costigan, C.; Austin, A.; Marciani, L.; Gowland, P. A.; Guha, I. N.; et al. A Study of T1 Relaxation Time as a Measure of Liver Fibrosis and the Influence of Confounding Histological Factors. *NMR Biomed.* **2015**, *28* (6), 706–714.

(669) Donahue, K. M.; Weisskoff, R. M.; Burstein, D. Water Diffusion and Exchange as They Influence Contrast Enhancement. *J. Magn. Reson. Imaging* **1997**, *7* (1), 102–110.

(670) Kellman, P.; Hansen, M. S. T1-Mapping in the Heart: Accuracy and Precision. *J. Cardiovasc. Magn. Reson.* **2014**, *16* (1), 1–20.

(671) Tkác, I.; Starcuk, Z.; Choi, I. Y.; Gruetter, R. In Vivo 1H NMR Spectroscopy of Rat Brain at 1 Ms Echo Time. *Magn. Reson. Med.* **1999**, *41* (4), 649–656.

(672) Sankar, T.; Caramanos, Z.; Assina, R.; Villemure, J.-G.; Leblanc, R.; Langleben, A.; Arnold, D. L.; Preul, M. C. Prospective Serial Proton MR Spectroscopic Assessment of Response to Tamoxifen for Recurrent Malignant Glioma. *J. Neurooncol.* **2008**, *90* (1), 63–76.

(673) McKnight, T. R.; von dem Bussche, M. H.; Vigneron, D. B.; Lu, Y.; Berger, M. S.; McDermott, M. W.; Dillon, W. P.; Graves, E. E.; Pirzkall, A.; Nelson, S. J. Histopathological Validation of a Three-Dimensional Magnetic Resonance Spectroscopy Index as a Predictor of Tumor Presence. *J. Neurosurg.* **2002**, *97* (4), 794–802.

(674) Swartz, H. M.; Khan, N.; Buckey, J.; Comi, R.; Gould, L.; Grinberg, O.; Hartford, A.; Hopf, H.; Hou, H.; Hug, E.; et al. Clinical Applications of EPR: Overview and Perspectives. *NMR Biomed.* **2004**, *17* (5), 335–351.

(675) Decroos, C.; Li, Y.; Bertho, G.; Frapart, Y.; Mansuy, D.; Boucher, J.-L. Oxidative and Reductive Metabolism of Tris(*p* -Carboxyltetrathiaaryl)Methyl Radicals by Liver Microsomes. *Chem. Res. Toxicol.* **2009**, *22* (7), 1342–1350.

(676) Ardenkjær-Larsen, J. H.; Laursen, I.; Leunbach, I.; Ehnholm, G.; Wistrand, L.-G.; Petersson, J. S.; Golman, K. EPR and DNP Properties of Certain Novel Single Electron Contrast Agents Intended for Oximetric Imaging. *J. Magn. Reson.* **1998**, *133* (1), 1–12.

(677) Cao-Pham, T.-T.; Tran, L.-B.-A.; Colliez, F.; Joudiou, N.; El Bachiri, S.; Grégoire, V.; Levêque, P.; Gallez, B.; Jordan, B. F. Monitoring Tumor Response to Carbogen

Breathing by Oxygen-Sensitive Magnetic Resonance Parameters to Predict the Outcome of Radiation Therapy: A Preclinical Study. *Int. J. Radiat. Oncol.* **2016**, *96* (1), 149–160.

(678) Lewandowski, M.; Gwozdzinski, K. Nitroxides as Antioxidants and Anticancer Drugs. *Int. J. Mol. Sci.* **2017**, *18* (11), 2490.

(679) Song, C. W.; Lokshina, A.; Rhee, J. G.; Patten, M.; Levitt, S. H. Implication of Blood Flow in Hyperthermic Treatment of Tumors. *IEEE Trans. Biomed. Eng.* **1984**, *BME-31* (1), 9–16.

(680) Repasky, E. A.; Evans, S. S.; Dewhirst, M. W. Temperature Matters! And Why It Should Matter to Tumor Immunologists. *Cancer Immunol. Res.* **2013**, *1* (4), 210–216.

(681) Prasad, B.; Kim, S.; Cho, W.; Kim, S.; Kim, J. K. Effect of Tumor Properties on Energy Absorption, Temperature Mapping, and Thermal Dose in 13.56-MHz Radiofrequency Hyperthermia. *J. Therm. Biol.* **2018**, *74*, 281–289.

(682) Késmárky, G.; Kenyeres, P.; Rábai, M.; Tóth, K. Plasma Viscosity: A Forgotten Variable. *Clin. Hemorheol. Microcirc.* **2008**, *39* (1–4), 243–246.

(683) Balzeau, J.; Pinier, M.; Berges, R.; Saulnier, P.; Benoit, J.-P.; Eyer, J. The Effect of Functionalizing Lipid Nanocapsules with NFL-TBS.40-63 Peptide on Their Uptake by Glioblastoma Cells. *Biomaterials* **2013**, *34* (13), 3381–3389.

(684) Vetten, M. A.; Yah, C. S.; Singh, T.; Gulumian, M. Challenges Facing Sterilization and Depyrogenation of Nanoparticles: Effects on Structural Stability and Biomedical Applications. *Nanomedicine Nanotechnology, Biol. Med.* **2014**, *10* (7), 1391–1399.

(685) Bentzen, S. M. Theragnostic Imaging for Radiation Oncology: Dose-Painting by Numbers. *Lancet Oncol.* **2005**, *6* (2), 112–117.

(686) Grosu, A.-L.; Souvatzoglou, M.; Röper, B.; Dobritz, M.; Wiedenmann, N.; Jacob, V.; Wester, H.-J.; Reischl, G.; Machulla, H.-J.; Schwaiger, M.; et al. Hypoxia Imaging With FAZA-PET and Theoretical Considerations With Regard to Dose Painting for Individualization of Radiotherapy in Patients With Head and Neck Cancer. *Int. J. Radiat. Oncol.* **2007**, *69* (2), 541–551.

(687) Yang, J. C.; Wexler, L. H.; Meyers, P. A.; Happersett, L.; LaQuaglia, M. P.; Wolden, S. L. Dose-Painting Intensity Modulated Radiation Therapy for Pediatric Sarcomas With Lung Metastases. *Int. J. Radiat. Oncol.* **2012**, *84* (3), S638.

(688) Zhou, Z.; Zhang, B.; Wang, H.; Yuan, A.; Hu, Y.; Wu, J. Two-Stage Oxygen Delivery for Enhanced Radiotherapy by Perfluorocarbon Nanoparticles. *Theranostics* **2018**, *8* (18), 4898–4911.

(689) Jahangiri, A.; Chin, A. T.; Flanigan, P. M.; Chen, R.; Bankiewicz, K.; Aghi, M. K. Convection-Enhanced Delivery in Glioblastoma: A Review of Preclinical and Clinical Studies. *J. Neurosurg.* **2017**, *126* (1), 191–200.

(690) Jain, R. K. Delivery of Novel Therapeutic Agents in Tumors: Physiological Barriers and Strategies. *J. Natl. Cancer Inst.* **1989**, *81* (8), 570–576.

(691) Vogelbaum, M. A.; Aghi, M. K. Convection-Enhanced Delivery for the Treatment of Glioblastoma. *Neuro. Oncol.* **2015**, *17* (suppl 2), ii3-ii8.

(692) Vogelbaum, M. A.; Brewer, C.; Barnett, G. H.; Mohammadi, A. M.; Peereboom, D. M.; Ahluwalia, M. S.; Gao, S. First-in-Human Evaluation of the Cleveland Multiport Catheter for Convection-Enhanced Delivery of Topotecan in Recurrent High-Grade Glioma: Results of Pilot Trial 1. *J. Neurosurg.* **2018**, 1–10.

(693) Dagdeviren, C.; Ramadi, K. B.; Joe, P.; Spencer, K.; Schwerdt, H. N.; Shimazu, H.; Delcasso, S.; Amemori, K.-I.; Nunez-Lopez, C.; Graybiel, A. M.; et al. Miniaturized Neural System for Chronic, Local Intracerebral Drug Delivery. *Sci. Transl. Med.* **2018**, *10* (425), eaan2742.

(694) Alphandéry, E. Glioblastoma Treatments: An Account of Recent Industrial Developments. *Front. Pharmacol.* **2018**, *9*, 879.

(695) Lainé, A.-L.; Gravier, J.; Henry, M.; Sancey, L.; Béjaud, J.; Pancani, E.; Wiber, M.; Texier, I.; Coll, J.-L.; Benoit, J.-P.; et al. Conventional versus Stealth Lipid Nanoparticles: Formulation and in Vivo Fate Prediction through FRET Monitoring. *J. Control. Release* **2014**, *188*, 1–8.

Author Contributions

LIST OF PUBLICATIONS

Nel, J.; Desmet, C. M.; Driesschaert, B.; Saulnier, P.; Lemaire, L.; Gallez, B. Preparation and evaluation of trityl-loaded lipid nanocapsules as oxygen sensors for electron paramagnetic resonance oximetry. *Int. J. Pharm.* **2019**, *554*, 87-92. DOI: 10.1016/J.IJPHARM.2018.11.007

Nel, J.; Franconi, F.; Joudiou, N.; Saulnier, P.; Gallez, B.; Lemaire, L. Lipid nanocapsules as *in vivo* oxygen sensors using Magnetic Resonance Imaging.

Publication submitted in journal of Materials Science & Engineering C: Materials for Biological Applications.

Nel, J.; Gallez, B.; Lemaire, L. Nanoparticles for hypoxia determination and imaging in tumours. Publication in preparation.

Lemaire, L.; **Nel, J.**; Franconi, F.; Guillaume, B.; Saulnier, P. Perfluorocarbon-Loaded Lipid Nanocapsules to Assess the Dependence of U87-Human Glioblastoma Tumor pO_2 on *In Vitro* Expansion Conditions. *PLoS ONE*. **2016**, *11 (10),* e0165479. DOI: 10.1371/journal.pone.0165479

LIST OF CONFERENCE CONTRIBUTIONS

1. **Nel, J.**, Franconi, F., Desmet, C. M., Joudiou, N., Gallez, B., Lemaire, L. Lipid nanocapsules for tissue O_2 determination using EPR and MRI, SFNano 2018, Marseilles (France) (2018)
2. **Nel, J.**, Franconi, F., Joudiou, N., Gallez, B., Lemaire, L. Lipid nanocapsules for tissue pO_2 determination using MRI, Joint meeting of ISMRM-ESMRMB, Paris (France) (2018)
3. **Nel, J.**, Franconi, F., Gallez, B., Lemaire, L. Measuring oxygen variations in tumours with EPR and MRI, 6th NanoFar Summer school, Modena (Italy) (2018)
4. **Nel, J.**, Desmet, C. M., Franconi, F., Joudiou, N., Driesschaert, B., Gallez, B., Lemaire, L. Challenging oxygen variations in tumours with EPR and MRI techniques, SFR 4208, Angers (France) (2018)
5. **Nel, J.**, Gallez, B., Lemaire, L. Lipid nanocapsules as a prognostic tool in cancer, ESMRMB, Barcelona (Spain) (2017)
6. **Nel, J.**, Franconi, F., Gallez, B., Lemaire, L. Lipid nanocapsules : An innovative oxygen sensor, Les 7e estivales de la plate-forme PRISM, Angers (France) (2017)
7. Nel, J., Franconi, F., Gallez, B., **Lemaire, L.** Les nanocapsules lipidiques comme senseur d'oxygénation, SFR 4208, Angers (France) (2017)
8. **Nel, J.**, Gallez, B., Franconi, F., Lemaire, L. Lipid nanocapsules as a prognostic tool in cancer, 5th NanoFar Autumn school, Nottingham (United Kingdom) (2017)
9. **Nel, J.**, Gallez, B., Lemaire, L. Lipid nanocapsules as a prognostic tool in cancer, Journées Scientifique ED BS UBL, Nantes (France) (2016)
10. **Nel, J.**, Gallez, B., Lemaire, L. Lipid nanocapsules as a prognostic tool in cancer, SFNano 2016, Paris (France) (2016)
11. **Nel, J.**, Gallez, B., Lemaire, L. Lipid nanocapsule as a theranostic tool in cancer, 4th NanoFar Autumn school, Nantes (France) 2015

LIST OF TRAINING FORMATIONS AND MOBILITIES

1. 26-30 October (2015), **4th NanoFar Autumn School** in Nantes (France); 15 h
2. 01-03 March (2016), **Imagerie par Résonance Magnétique préclinique** in Angers (France); 6 h
3. 03-11 October (2016), **Formation à l'Expérimentation Animale Niveau 1** in ONIRIS-Nantes (France); 28 h
4. March – September (2017), **Mobility to Université catholique de Louvain** in Woluwe-Louvain (Belgium); 7 months
5. 24-28 April (2017), **5th NanoFar Autumn School** in Nottingham (United Kingdom); 15 h
6. 19-21 October (2017), **Small Animal Imaging Course** in Barcelona (Spain); 3 days
7. 11-15 June (2018), **6th NanoFar Summer School** in Modena (Italy); 13 h

Supplementary

APPENDIX A

SUPPLEMENTARY DATA REGARDING SECTION 4.2

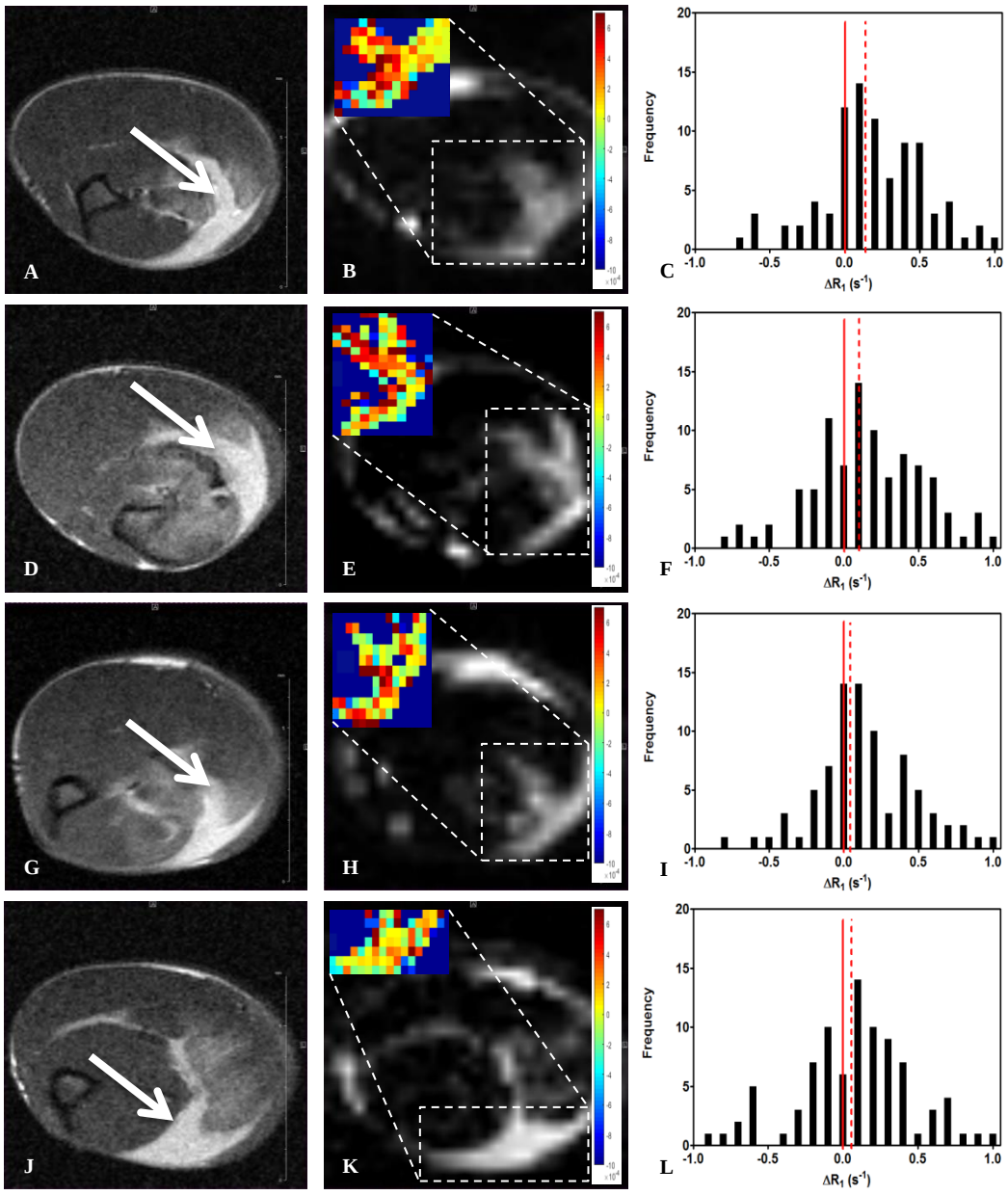

Figure 0-1. Supplementary data regarding the intramuscular normal muscle model experiments. Application of LNCs to assess variations of oxygenation in the intramuscular tissue of mice using lipid relaxation rate measured with the MOBILE MR sequence, wherein **(a)**, **(d)**, **(g)** and **(j)** show the transversal anatomical images of mice gastrocnemius muscles and the injected LNCs (indicated by an arrow). Images **(b)**, **(e)**, **(h)** and **(k)** show the lipid image issued from the set of images acquired with the MOBILE MR sequence wherein the lipids from the LNCs can be observed. The insert indicates the change in R_1 ($\Delta R_1 = R_{carbogen} - R_{air}$) for each pixel of lipid signal in the MOBILE image and a colour scale highlights the more responsive pixels in red (s^{-1}). ΔR_1 distribution of all encompassing pixels in the lipid deposit region of interest is represented as a histogram in **(c)**, **(f)**, **(i)** and **(l)**, wherein the median change of R_1 is indicated with a dotted red line.

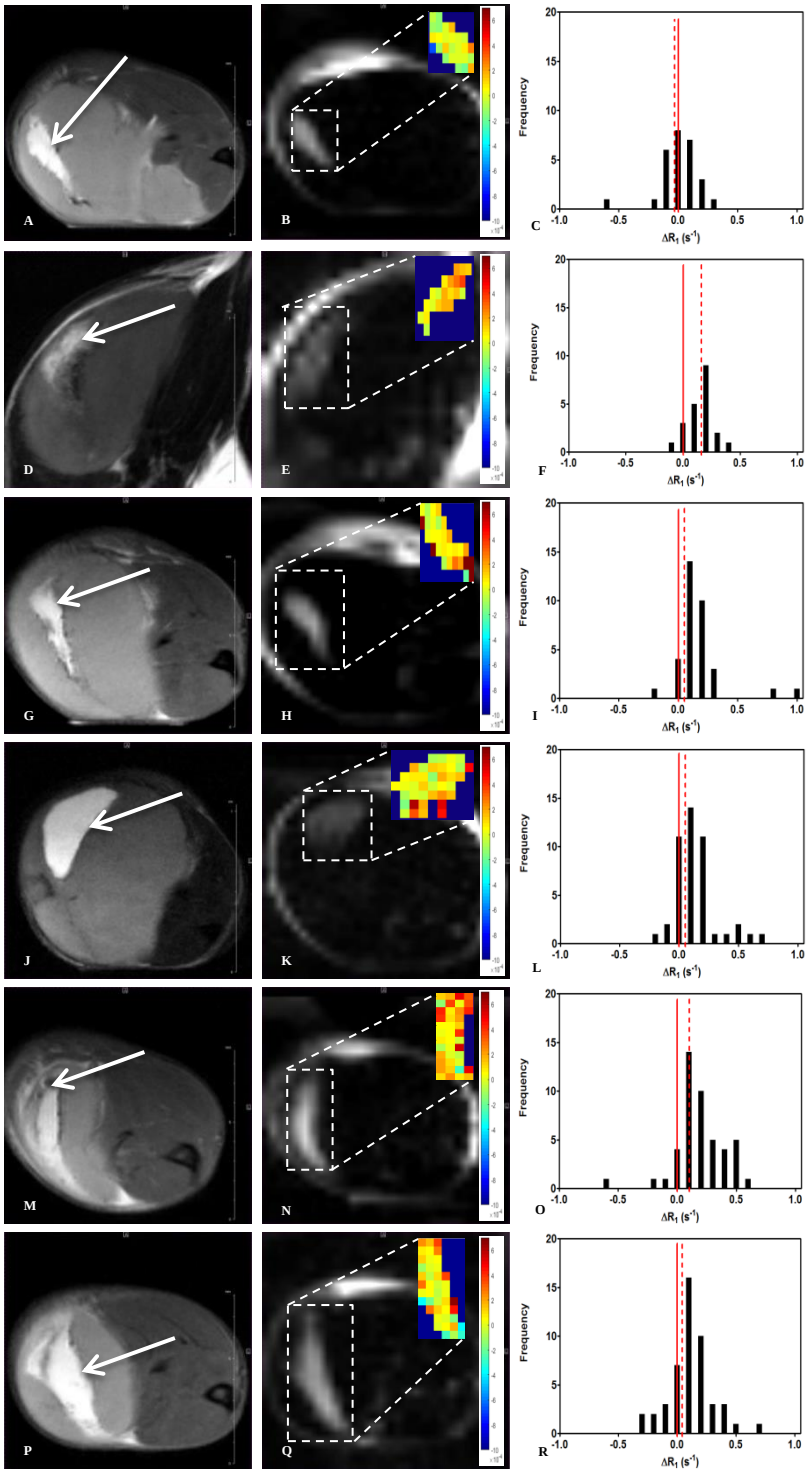

Figure 0-2. Supplementary data regarding the intratumoural subcutaneous FSaII fibrosarcoma tumour experiments. Application of LNCs to asses variations of oxygenation in a mouse subcutaneous tumour model with the MOBILE MR sequence, wherein **(a)**, **(d)**, **(g)**, **(j)**, **(m)**, and **(p)** show the transversal anatomical image of the mouse leg and the fibrosarcoma tumour and the injected LNCs (indicated by an arrow). Images **(b)**, **(e)**, **(h)**, **(k)**, **(n)**, and **(q)** show the lipid image issued from the set of images acquired with the MOBILE MR sequence wherein the lipids from the LNCs can be observed. The insert indicates the change in R_1 ($\Delta R_1 = R_{carbogen} - R_{air}$) for each pixel of lipid signal in the MOBILE image and a colour scale highlights the more responsive pixels in red (s^{-1}). ΔR_1 distribution of all encompassing pixels in the lipid deposit region of interest is represented as a histogram in **(c)**, **(f)**, **(i)**, **(l)**, **(o)** and **(r)**, wherein the median change of R_1 is indicated with a dotted red line

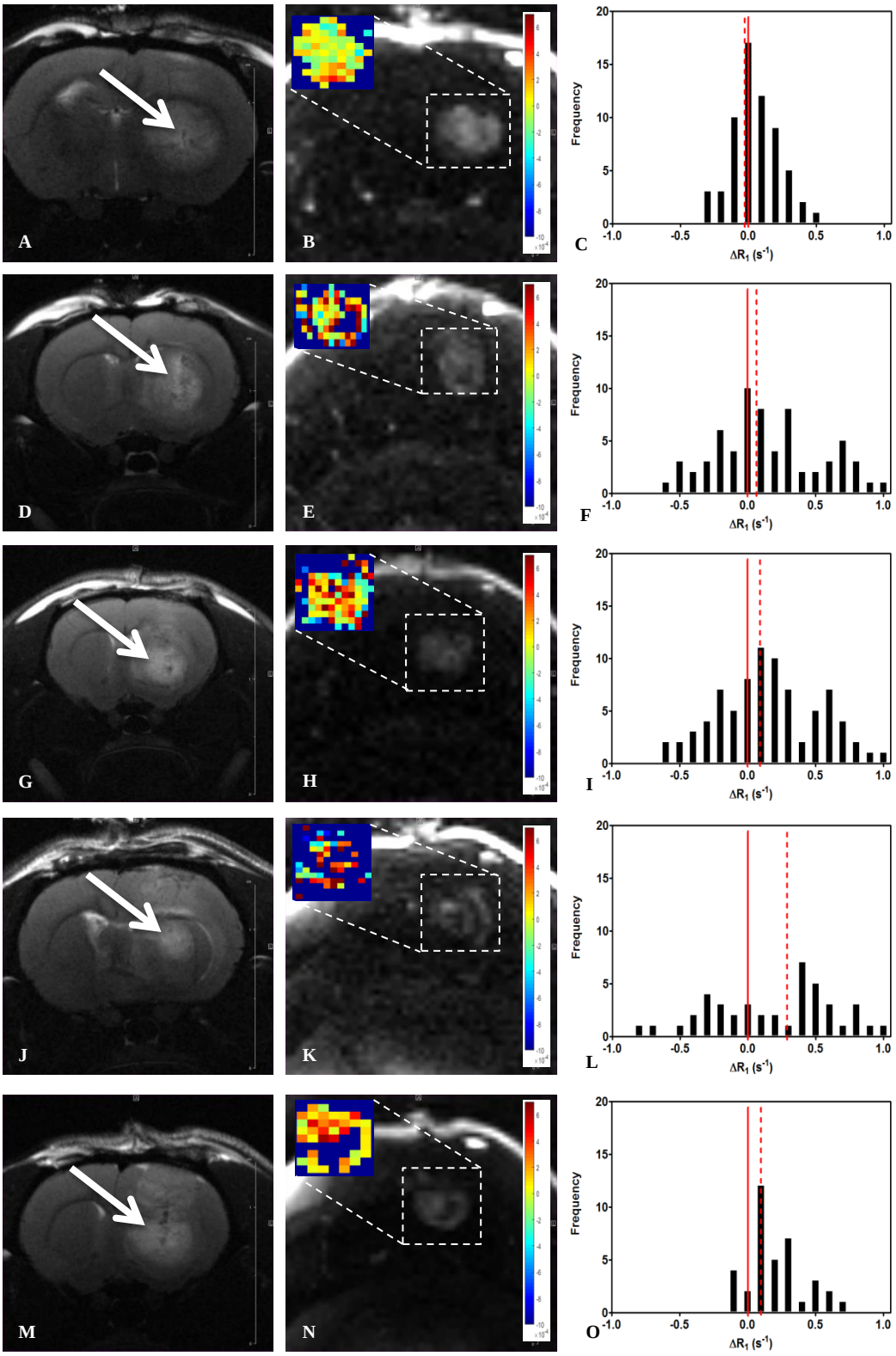

Figure 0-3. Supplementary data regarding the intratumoural glioblastoma C6 model experiments. Application of LNCs to assess variations of oxygenation in a glioblastoma tumour model with the MOBILE MR sequence, wherein **(a)**, **(d)**, **(g)**, **(j)** and **(m)** show the transversal anatomical image of the rat brain and the brain tumour and the injected LNCs (indicated by an arrow). Images **(b)**, **(e)**, **(h)**, **(k)** and **(n)** show the lipid image issued from the set of images acquired with the MOBILE MR sequence wherein the lipids from the LNCs can be observed. The insert indicates the change in R_1 ($\Delta R_1 = R_{carbogen} - R_{air}$) for each pixel of lipid signal in the MOBILE image and a colour scale highlights the more responsive pixels in red (s^{-1}). ΔR_1 distribution of all encompassing pixels in the lipid deposit region of interest is represented as a histogram in **(c)**, **(f)**, **(i)**, **(l)**, and **(o)**, wherein the median change of R_1 is indicated with a dotted red line.

APPENDIX B

SUPPLEMENTARY DATA REGARDING SECTION 4.3

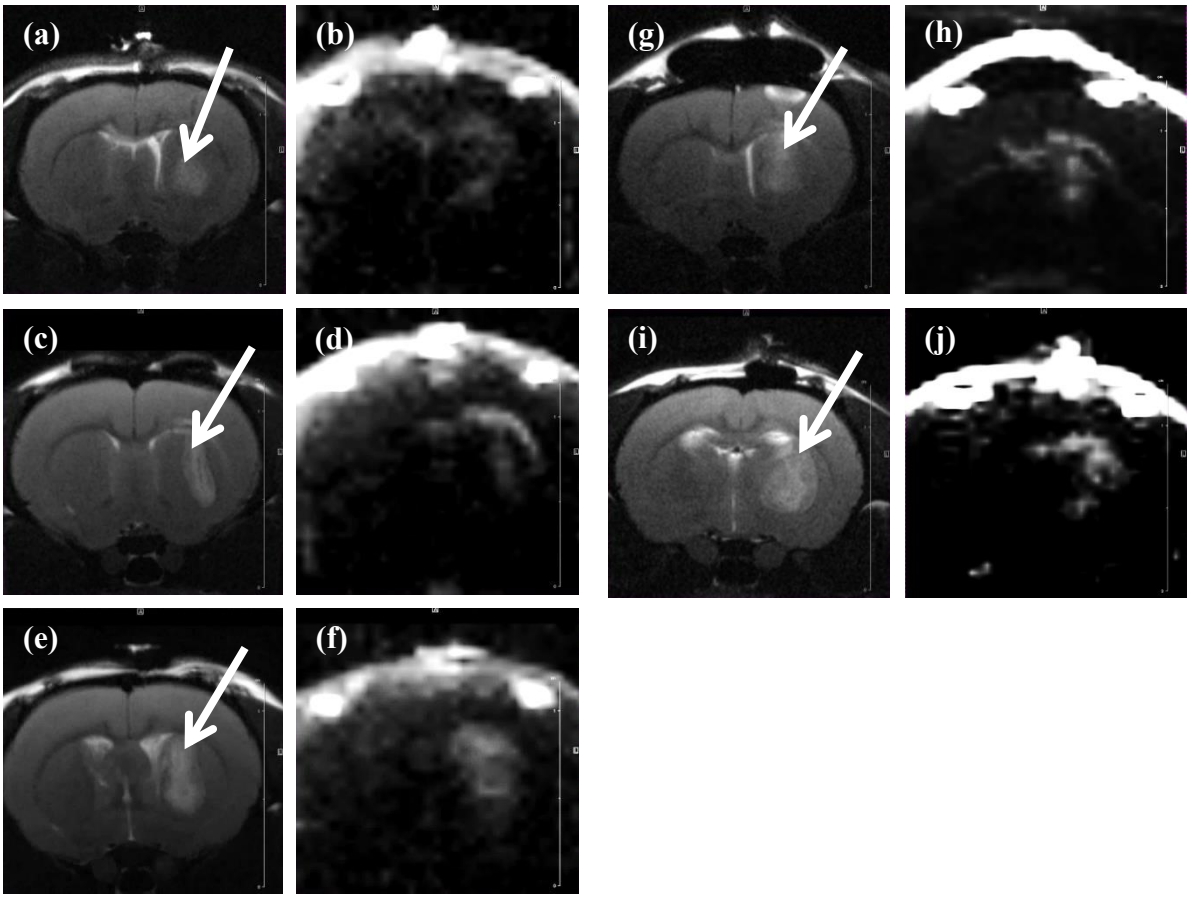

Figure 0-4. Supplementary data regarding the intracerebral normal brain model experiments. Application of LNCs to assess variations of oxygenation in a normal brain model with the MOBILE MR sequence, wherein **(a)**, **(c)**, **(e)**, **(g)** and **(i)** show the transversal anatomical image of the rat brain and the injected LNCs (indicated by an arrow). Images **(b)**, **(d), (f)**, **(h)** and **(j)** show the lipid image issued from the set of images acquired with the MOBILE MR sequence wherein the lipids from the LNCs can be observed.

UNIVERSITE BIOLOGIE BRETAGNE SANTE LOIRE

université angers

UCLouvain

Titre: **Les nanocapsules lipidiques en tant qu'outil théranostique**

Mots clés: hypoxie ; nanocapsules lipidiques ; résonance paramagnétique électronique ; imagerie par résonance magnétique

Résumé: L'hypoxie est l'un des aspects les plus importants dans le microenvironnement tumoral. Ce phénomène, causé par une structure vasculaire anormale et un métabolisme perturbé, conduit à la formation de cellules hautement malignes résistantes aux thérapies cyto- et radio-toxiques. De ce fait, l'hypoxie est une préoccupation majeure et est à la base de notre nouvelle approche qui utilise des nanocapsules lipidiques (LNC) en tant que senseur d'oxygène. Il a été montré que les LNC sont d'excellents nanocarriers capables d'encapsuler des principes actifs à l'intérieur de leur cœur lipidiques et d'éviter le système immunitaire grâce au PEG de leur coque, permettant ainsi le traitement de tumeurs agressives. Nous avons émis l'hypothèse que le cœur lipidique des LNC pouvait être utilisé pour cartographier l'O_2 dans l'environnement tissulaire. En effet, la solubilité de l'O_2 étant supérieure dans les lipides que dans l'eau, le moindre changement d'oxygénation dans les tissus sera amplifié dans le cœur lipidique des LNC. Par conséquent, nous avons encapsulé une sonde paramagnétique lipophile, e.g. le tetrathiatriarylmethyl (TAM), et montré sa réponse *in vitro* à des variations en O_2 en utilisant la résonance paramagnétique électronique (RPE) montrant de ce fait la perméabilité des LNC à l'O_2.

Nous avons utilisé les TAM-LNC dans un modèle *in vivo* de tissu normal (muscle murin gastrocnémien) et pathologique (sarcome). Sans LNC, le TAM a rapidement été réduit et aucune mesure en O_2 n'a été possible toutefois, notre système TAM-LNC présentait une demi-vie supérieure à une heure et permettait la mesure en temps réel lorsque les animaux respiraient soit de l'air soit du carbogène (95 % O_2, 5 % CO_2). Par ailleurs, la nature lipidique du cœur des LNC a été exploitée pour cartographier l'oxygénation des tissus grâce à l'imagerie par résonance magnétique (IRM) et plus précisément par l'utilisation de la séquence MOBILE qui permet d'imager la variation du temps de relaxation T1 induite par l'O_2 dans les lipides. Avec une dose unique de LNC, nous avons été capables de représenter les changements de T_1 entre les différents modes de respiration et l'hétérogénéité de l'hypoxie dans des modèles de tissus murins sain et pathologique. En conclusion, nous avons apporté la preuve de faisabilité de l'utilisation des LNC en tant qu'outil diagnostique pour cartographier l'hypoxie dans des tissus sains et pathologiques.

Title: **Lipid nanocapsules as a theranostic tool**

Keywords: hypoxia ; lipid nanocapsules ; electron paramagnetic resonance ; magnetic resonance imaging

Abstract: Hypoxia is one of the most challenging aspects of the tumour microenvironment. The phenomenon occurs due to abnormal vasculature and an exacerbated metabolism, and leads to highly malignant cells resistant to radio- and cyto-toxic therapy. As such, hypoxia is of major concern and prompted our novel approach in using lipid nanocapsules (LNCs) as an oxygen sensor. LNCs have been demonstrated as excellent core-shell nanocarriers, capable of encapsulating drugs within their lipidic core and avoiding the immune system due to their PEGylated shell, thus enabling treatment of highly aggressive tumours. We hypothesised that the lipidic-core of LNCs could also be used to assess the O_2 environment in tissue. Indeed, because O_2 solubility is greater in lipids than in water, any subtle changes in tissue O_2 will be heightened in the lipidic LNC core. Consequently, we encapsulated a lipophilic paramagnetic probe, e.g. tetrathiatriarylmethyl (TAM), and demonstrated its response to variations in O_2 *in vitro*, using Electron Paramagnetic Resonance (EPR), indicating the permeability of LNCs to O_2.

We applied the TAM-LNCs to an *in vivo* normal tissue model (gastrocnemius mouse muscle) and pathological model (sarcoma tumour). Herein, free TAM was rapidly reduced and no O_2 measurement was possible, however, our TAM-LNC system exhibited a half-life of over an hour and enabled real-time measurements whilst animals were breathing air and during a carbogen (95 % O_2, 5 % CO_2) breathing challenge. Moreover, the lipidic-core nature of the LNCs was exploited to image tissue oxygenation using Magnetic Resonance Imaging (MRI), specifically the MOBILE sequence which enabled the mapping of O_2-induced T_1 relaxation rate changes in lipids. Using a single dose of LNCs, we were able to portray the change in T_1 between air breathing and the carbogen challenge, and image the heterogeneous nature of hypoxia in murine normal tissue and pathological tumour models. In conclusion, we demonstrated the feasibility of using LNCs as a diagnostic tool for assessing hypoxia in both normal and pathological tissues.